Single- and Cross-Hole Pneumatic Tests in Unsaturated Fractured Tuffs at the Apache Leap Research Site: Phenomenology, Spatial Variability, Connectivity and Scale

Prepared by
W.A. Illman, D.L. Thompson, V.V. Vesselinov,
G. Chen, S.P. Neuman

Department of Hydrology and Water Resources
The University of Arizona

Single- and Cross-Hole Pneumatic Tests in Unsaturated Fractured Tuffs at the Apache Leap Research Site: Phenomenology, Spatial Variability, Connectivity and Scale

Prepared by
W.A. Illman, D.L. Thompson, V.V. Vesselinov,
G. Chen, S.P. Neuman

Department of Hydrology and Water Resources
The University of Arizona
Tucson, AZ 85721

ABSTRACT

This report documents methods, analyses and results of single-hole and cross-hole pneumatic injection tests recently completed by The University of Arizona in unsaturated fractured tuffs at the Apache Leap Research Site (ALRS) near Superior, Arizona. The research was designed to investigate, test and confirm methods and models that can be used to determine the role of fractures and fracture zones in flow and transport through partially saturated porous rocks. We summarize briefly previous analyses of steady state pressure data from single-hole tests, and describe more recent type-curve and inverse analyses of transient data from the same tests. The latter yield information about air permeability, air-filled porosity, skin factor, borehole storage, phenomenology and dimensionality of the flow regime on a nominal scale of 1 m in the vicinity of each test interval. Transient air permeabilities agree well with steady state values but correlate poorly with fracture density. Larger scale cross-hole pneumatic tests were conducted by injecting air into a relatively short borehole interval of length 1 - 2 m while monitoring a) air pressure and temperature in the injection interval; b) barometric pressure, air temperature and relative humidity at the surface; and c) air pressure and temperature in 13 short (0.5 - 2 m) and 24 longer (4 - 20 m) intervals within the injection and surrounding boreholes. Only one of these tests was fully analyzed to date, by means of newly-developed pressure and pressure-derivative type-curves, and a three-dimensional parameter estimation method. Analyses of pressure data from individual monitoring intervals by the two methods, under the assumption that the rock acts as a uniform and isotropic fractured porous continuum, yield comparable results. These results include information about pneumatic connections between the injection and monitoring intervals, corresponding directional air permeabilities, and air-filled porosities. All of these quantities are found to vary considerably from one monitoring interval to another on scales ranging from a few meters to over 20 meters. Together with the results of earlier site investigations our single- and cross-hole test analyses reveal that, at the ALRS, a) the pneumatic pressure behavior of fractured tuff is amenable to analysis by methods that treat the rock as a continuum on scales ranging from meters to tens of meters; b) this continuum is representative primarily of interconnected fractures; c) its pneumatic properties vary strongly with location, direction and scale; in particular, the mean of pneumatic permeabilities increases, and their variance decreases, with scale; d) this scale effect is most probably due to the presence in the rock of various size fractures that are interconnected on a variety of scales; and e) given a sufficiently large sample of spatially varying pneumatic rock properties on a given scale of measurement, these properties are amenable to analysis by geostatistical methods, which treat them as correlated random fields defined over a continuum.

CONTENTS

LIST OF FIGURES

LIST OF TABLES

EXECUTIVE SUMMARY

This report documents methods, analyses and results of single-hole and cross-hole pneumatic injection tests recently completed in unsaturated fractured tuffs at the Apache Leap Research Site (ALRS) near Superior, Arizona. The research was designed to investigate, test and confirm methods and models that can be used to determine the role of fractures and fracture zones in flow and transport through partially saturated porous rocks, with emphasis on the characterization of fracture connectivity, permeability, porosity, and their dependence on location, direction and scale. Its results are relevant to site characterization and performance confirmation issues related to high-level radioactive waste (HLW) facilities located in unsaturated fractured tuff. However, unsaturated fractured porous rocks similar to tuffs are found at many locations, including some low-level radioactive waste disposal sites, nuclear decommissioning facilities and sites contaminated with radioactive as well as other hazardous materials. The test methodologies described in this report, and the new understanding that the report provides regarding flow and transport phenomena in, and properties of, fractured tuffs at the ALRS are directly relevant to such facilities and sites.

Issues associated with the site characterization of fractured rock terrains, the analysis of fluid flow and contaminant transport in such terrains, and the efficient handling of contaminated sites are typically very difficult to resolve. A major source of this difficulty is the complex nature of the subsurface "plumbing systems" of pores and fractures through which flow and transport in rocks take place. There is at present no well-established field methodology to characterize the fluid flow and contaminant transport properties of unsaturated fractured rocks. In order to characterize the ability of such rocks to conduct water, and to transport dissolved or suspended contaminants, one would ideally want to observe these phenomena directly by conducting controlled field hydraulic injection and tracer experiments within the rock. In order to characterize the ability of unsaturated fractured rocks to conduct non-aqueous phase liquids such as chlorinated solvents, one would ideally want to observe the movement of such liquids under controlled conditions in the field. In practice, there are severe logistical obstacles to the injection of water into unsaturated geologic media, and logistical as well as regulatory obstacles to the injection of non-aqueous liquids. There also are important technical reasons why the injection of liquids, and dissolved or suspended tracers, into fractured rocks may not be the most feasible approach to site characterization when the rock is partially saturated with water. Many of these limitations can be overcome by conducting field tests with gases rather than with liquids, and with gaseous tracers instead of chemicals dissolved in water.

This report focuses on single-hole and cross-hole pneumatic injection at the ALRS. Over 270 single-hole tests have been conducted in six shallow vertical and inclined boreholes at the site by Guzman et al. (1996). These authors used steady state formulae to obtain permeability values for borehole test intervals of various lengths, based solely on late pressure data from each test. This report summarizes briefly the results of their work and describes more recent pressure and pressure-derivative type-curve analyses, as well as numerical inverse interpretations, of transient data from some of the single-hole tests. The transient analyses yield information about air permeability,

air-filled porosity, skin factor, phenomenology and dimensionality of the flow regime on a nominal scale of 1 m.

Single-hole air injection tests provide information only about a small volume of rock in the close vicinity of the injection interval. Rock properties measured on such small scales vary rapidly and erratically in space in a manner that renders the rock strongly and randomly heterogeneous. To determine the properties of the rock on larger scales ranging from meters to tens of meters, 44 cross-hole pneumatic interference tests have been conducted at the ALRS during the years 1995 – 1997. In most of these tests, air was injected at a constant mass flow rate into a relatively short borehole interval of length 1 - 2 m while monitoring a) air pressure and temperature in the injection interval; b) barometric pressure, air temperature and relative humidity at the surface; and c) air pressure and temperature in 13 short (0.5 - 2 m) and 24 longer (4 - 20 m) intervals within the injection and surrounding boreholes. Only one of these tests, labeled PP4, was fully analyzed to date. During this test, which the report describes in detail, pressure responses were detected in 12 of the 13 short monitoring intervals and 20 of the 24 longer intervals. Of the 16 boreholes utilized in cross-hole testing, 6 had been previously subjected to single-hole testing. The results of single-hole tests (primarily spatial distribution of air permeabilities and local flow geometry) together with other site information (primarily core data and borehole televiewer images) served as useful guides in the design of cross-hole tests.

The earlier work of Guzman *et al.* (1994, 1996) and Guzman and Neuman (1996), together with the work described in this report, suggest strongly that air injection tests yield properties of the fracture system, which are relevant to both unsaturated and saturated conditions. In particular, whereas the pneumatic permeability and air-filled porosity of fractures one determines from such tests tend to be somewhat lower than their intrinsic (fluid-independent) counterparts, the former nevertheless approach the latter as the applied pressure goes up. This is so because capillary forces tend to draw water from fractures into the porous (matrix) blocks of rock between the fractures, thereby leaving the latter saturated primarily with air. Water saturation in the matrix blocks is therefore typically much higher than that within the fractures, making it relatively difficult for air to flow through such blocks. It follows that, during a pneumatic injection test, the air moves primarily through fractures (most of which contain relatively little water) and the test therefore yields flow and transport parameters which closely reflect (though somewhat underestimate) the intrinsic properties of these largely air-filled fractures. The displacement of water by air under a constant rate of injection manifests itself in a rapid increase in pressure within the injection interval, followed by a gradual decrease. Two-phase flow of water and air additionally causes air permeabilities from single-hole pneumatic injection tests to exhibit a hysteretic variation with applied pressure.

In most single-hole pneumatic injection tests at the ALRS, pneumatic permeabilities increase systematically with applied pressure as air displaces water under two-phase flow. In a few single-hole tests, where the injection intervals are intersected by widely open fractures, air permeabilities decrease with applied pressure due to inertial effects. This pressure-dependence of air permeability suggests that it is advisable to conduct single-hole air injection tests at several applied flow rates and/or pressures. Pneumatic parameters derived from pressure data recorded in monitoring intervals during cross-hole tests appear to be much less sensitive to the rate of injection, suggesting that

two-phase flow and inertial phenomena decay rapidly with distance from the injection interval. Enhanced permeability due to slip flow (the Klinkenberg effect) appears to be of little relevance to the interpretation of single-hole or cross-hole air injection tests at the ALRS.

The report demonstrates that it is possible to interpret both single-hole and cross-hole pneumatic injection tests at the ALRS by means of analytically derived type-curves, and a numerical inverse model, which account only for single-phase airflow through the rock while treating water as if it was immobile. Type-curves are presented which represent linearized solutions to nonlinear partial differential equations that govern single-phase airflow in uniform, isotropic porous continua under three regimes: three-dimensional flow with spherical symmetry, two-dimensional flow with radial symmetry, and flow in a continuum with an embedded high-permeability planar feature (a major fracture). The method of linearization appears to have only a minor impact on test results obtained by means of these type-curves. The type-curves account for effects of compressible air storage and skin in the injection interval during single-hole tests, and in monitoring intervals during cross-hole tests. Type-curves of pressure derivative versus the logarithm of time are included to accentuate phenomena that might otherwise be missed (such as dual continuum), help diagnose the prevailing flow regime (distinguish between radial and spherical flow regimes), and aid in constraining the calculation of corresponding flow parameters.

The numerical inverse model simulates pneumatic tests at the ALRS on the computer using a three-dimensional finite volume code, FEHM (Zyvoloski *et al.*, 1988, 1996, 1997). It automatically estimates the pneumatic properties of the rock, as well as the effective storage volume of the injection borehole interval, by means of the inverse code PEST (Doherty *et al.*, 1994). The decision to use FEHM was based in part on its ability to simulate two-phase flow of air and water in dual porosity and/or permeability continua, and to account for discrete fractures. However, it was found possible to interpret pneumatic tests at the ALRS successfully without the need to activate any of these features of the code. The inverse model is able to represent pneumatic test conditions at the site more realistically than do type-curves by incorporating medium heterogeneity and the effects that vertical and inclined boreholes have on pressure propagation through the system. Yet the two methods of interpretation yield comparable results.

Steady state interpretations of single-hole pneumatic tests yield air permeability values for the rock in the immediate vicinity of the test interval. Transient type-curve analyses of such tests provide additional information about the phenomenology and dimensionality of the corresponding flow regime, skin factors and compressible air storage effects. Under radial flow, or in the absence of a significant borehole storage effect, transient type-curve analyses may also yield values of air-filled porosity. At the ALRS, air permeabilities obtained from steady state and transient type-curve interpretations of single-hole pneumatic injection tests, conducted in borehole intervals of 1 *m*, agree closely with each other but correlate poorly with fracture density data. Airflow around the vast majority of these relatively short test intervals appears to be three-dimensional; borehole storage due to air compressibility is pronounced; and skin effects are minimal. The combined effects of three-dimensional flow and borehole

storage make it difficult to obtain reliable air-filled porosity values from these tests by means of type-curves, but do allow obtaining such values by means of the inverse model.

Flow in the vicinity of most 1-*m* single-hole pneumatic test intervals at the ALRS appears to be three-dimensional regardless of the number or orientation of fractures in the surrounding rock. This suggests that such flow is controlled by a single continuum, representative of a three-dimensional network of interconnected fractures, rather than by discrete planar features. Indeed, most single-hole and cross-hole pneumatic test data at the ALRS have proven amenable to analysis by means of a single fracture-dominated continuum representation of the fractured-porous tuff at the site. Only in a small number of single-hole test intervals, known to be intersected by widely open fractures, have the latter dominated flow as evidenced by the development of an early half-slope on logarithmic plots of pressure versus time; unfortunately, the corresponding data do not fully conform to available type-curve models of fracture flow. Some pressure records conform to the radial flow model during early and intermediate times, but none do so unambiguously at late time.

Work at the ALRS clearly demonstrates that it is generally not possible to distinguish between the permeabilities of individual fractures, and the bulk permeability of the fractured rock in the immediate vicinity of a test interval, by means of pneumatic injection tests. Hence there is little justification for attempting to model flow through individual fractures at the site. The explicit modeling of discrete features appears to be justified only when one can distinguish clearly between layers, faults, fracture zones, or major individual fractures on scales not much smaller than the domain of interest.

Air permeabilities obtained from single-hole tests at the ALRS are poorly correlated with fracture densities. The same is known to be the case for hydraulic conductivities at many water-saturated fractured rock sites worldwide (Neuman, 1987). This provides support for Neuman's decade-old assertion that the permeability of fractured rocks cannot be reliably predicted from information about fracture geometry (density, trace lengths, orientations, apertures and their roughness) but must be determined directly by means of hydraulic and/or pneumatic tests.

Core and single-hole measurements, conducted over short segments of a borehole, provide information only about a small volume of rock in the immediate vicinity of each measurement interval. Available data from the ALRS indicate that rock properties, measured on such small scales, vary erratically in space in a manner, which renders the rock randomly heterogeneous and pneumatically anisotropic. Local-scale air permeabilities from single-hole tests vary by orders of magnitude between test intervals across the site; their spatial variability is much more pronounced than their dependence on applied pressure. The report demonstrates that it is possible to interpolate some of the core and single-hole measurements at the ALRS between boreholes by means of geostatistical methods, which view the corresponding variables as correlated random fields defined over a continuum. This is especially true about air permeability, porosity, fracture density, water content, and the van Genuchten water retention parameter α, for each of which there are enough site data to constitute a workable geostatistical sample. To differentiate between geostatistical models that appear to fit these data equally well, the report uses formal model discrimination criteria based on maximum likelihood and the principle of parsimony (which places a premium on simplicity and penalizes models having an excessive number of parameters). Standard geostatistical analysis provides

best (minimum variance) linear unbiased estimates of how each such quantity varies in three-dimensional space, together with information about the quality of these estimates.

The finding in this report that core and single-hole test data are amenable to continuum geostatistical analysis supports the application of continuum flow and transport theories and models to unsaturated fractured porous tuffs at the ALRS on scales of one meter or more. It implies that the data can be viewed as samples from a random field, or stochastic continuum, as proposed for fractured rocks by Neuman (1987) and affirmed more recently by Tsang *et al.* (1996). This is so despite the fact that the rock is fractured and therefore mechanically discontinuous.

Estimates of hydrogeologic variables, obtained by geostatistical methods such as kriging, are smooth relative to their random counterparts. The report illustrates how one can generate less smooth and more realistic images of log air permeability, fracture density, log porosity, water content, and log α values in three dimensions that honor the available data, by means of a sequential Gaussian conditional simulation code due to Gómez-Hernández and Cassiraga (1994).

Cross-hole pneumatic injection test data from individual monitoring intervals at the ALRS have proven amenable to analysis by type-curve and numerical inverse models which treat the rock as a uniform and isotropic fractured porous continuum. Analyses of pressure data from individual monitoring intervals by the two methods gave comparable results concerning pneumatic connections between injection and monitoring intervals, corresponding directional air permeabilities, and air-filled porosities. All of these quantities were found to vary considerably from one monitoring interval to another in a given cross-hole test on scales ranging from a few meters to over 20 meters. Thus, even when the analysis treats the rock as if it was pneumatically uniform and isotropic, it ultimately yields information about the spatial and directional dependence of pneumatic permeability and connectivity across the site.

Some cross-hole pressure records reveal an inflection that is characteristic of dual continuum behavior. The prevailing interpretation of dual continua is that one represents the fracture network and the other embedded blocks of rock matrix. This report advocates a broader view according to which multiple (including dual) continua may represent fractures on a multiplicity of scales, not necessarily fractures and matrix.

The pneumatic permeabilities of unsaturated fractured tuffs at the ALRS are revealed to vary strongly with location, direction and scale. In particular, the mean of pneumatic permeabilities increases, and their variance decreases, with distance between packers in a single-hole injection test, and with distance between injection and monitoring intervals in cross-hole injection tests. This scale effect is most probably due to the presence in the rock of various size fractures that are interconnected on a variety of scales.

ACKNOWLEDGEMENTS

FOREWORD

This final technical report, NUREG/CR-5559, was prepared by the Department of Hydrology and Water Resources at The University of Arizona under their research contract (NRC-04-95-038) with the Waste Management Branch, Office of Nuclear Regulatory Research, U.S. Nuclear Regulatory Commission (JOB CODE W6388). This report documents research results from a series of field experiments and analyses conducted over a three-year period at the Apache Leap Research Site. The research was designed to: (1) investigate, test and confirm methods used to determine the role of fractures and fracture zones in flow and transport through partially saturated rock; (2) identify and test alternative conceptual models of flow and transport in fractured rock at the site scale with emphasis on characterizing fracture connectivity and permeability; and (3) investigate a range of models for interpreting single- and cross-hole pneumatic injection tests in partially saturated, fractured rock over a range of moisture contents with a focus on scaling and spatial variability of flow properties.

The research results are relevant to site characterization and performance confirmation issues related to high-level radioactive waste (HLW) facilities located in unsaturated, fractured tuff. Specifically, this report provides technical bases for review of: (1) air permeability testing, and (2) analysis of fractured rock that may be used to estimate flow and transport parameters and fracture connectivity at the candidate HLW sites, where the repository would be located in a deep unsaturated zone. The report summarizes the experimental design, including borehole configuration and testing schedules, data collection system, interpretive models developed and tested, results, and significant research conclusions. Data summaries and detailed discussions of the interpretive models developed and used to analyze the field testing results are provided in the appendices.

NUREG/CR-5559 is not a substitute for NRC regulations, and compliance is not required. The approaches and/or methods described in this NUREG/CR are provided for information only. Publication of this report does not necessarily constitute NRC approval or agreement with the information contained herein. Use of product or trade names is for identification purposes only and does not constitute endorsement by the NRC or The University of Arizona.

Dr. Sher Bahadur, Chief
Waste Management Branch
Division of Regulatory Applications
Office of Nuclear Regulatory Research

1. INTRODUCTION

1.1 ROLE OF PNEUMATIC TESTS IN SITE CHARACTERIZATION

Issues associated with the site characterization of fractured rock terrains, the analysis of fluid flow and contaminant transport in such terrains and the efficient handling of contaminated sites are typically very difficult to resolve. A major source of this difficulty is the complex nature of the subsurface "plumbing systems" of pores and fractures through which flow and transport in rocks take place. There is at present no well-established field methodology to characterize the fluid flow and contaminant transport properties of unsaturated fractured rocks. In order to characterize the ability of such rocks to conduct water, and to transport dissolved or suspended contaminants, one would ideally want to observe these phenomena directly by conducting controlled field hydraulic injection and tracer experiments within the rock. In order to characterize the ability of unsaturated fractured rocks to conduct non-aqueous phase liquids such as chlorinated solvents, one would ideally want to observe the movement of such liquids under controlled conditions in the field. In practice, there are severe logistical obstacles to the injection of water into unsaturated geologic media, and logistical as well as regulatory obstacles to the injection of non-aqueous liquids. There also are important technical reasons why the injection of liquids, and dissolved or suspended tracers, into fractured rocks may not be the most feasible approach to site characterization when the rock is partially saturated with water. Injecting liquids and dissolved or suspended tracers into an unsaturated rock would cause them to move predominantly downward under the influence of gravity, and would therefore yield at best limited information about the ability of the rock to conduct liquids and chemical constituents in directions other than the vertical. It would further make it difficult to conduct more than a single test at any location because the injection of liquid modifies the ambient saturation of the rock, and the time required to recover ambient conditions may be exceedingly long.

Many of these limitations can be overcome by conducting field tests with gases rather than with liquids, and with gaseous tracers instead of chemicals dissolved in water. Experience with pneumatic injection and gaseous tracer experiments in fractured rocks is limited. Much of this experience has been accumulated in recent years by The University of Arizona at the Apache Leap Research Site (ALRS) near Superior, Arizona, and by the U.S. Geological Survey (USGS) near the ALRS (LeCain, 1995) and at Yucca Mountain in Nevada (LeCain, 1996). Earlier work includes air injection tests conducted by Montazer (1982) in unsaturated fractured metamorphic rocks, and injection methods developed for fractured formations containing natural gas of the kind considered by Mishra *et al.* (1987). This report focuses on single-hole and cross-hole pneumatic injection tests conducted by our group at the ALRS under the auspices of the U.S. Nuclear Regulatory Commission (NRC). These tests were part of confirmatory research in support of NRC's role as the licensing agency for a potential high-level nuclear waste repository in unsaturated fractured tuffs at Yucca Mountain. However, unsaturated fractured porous rocks similar to tuffs are found at many locations, including some low-level radioactive waste disposal sites, nuclear decommissioning facilities and sites contaminated with radioactive as well as other hazardous materials. The test

methodologies we have developed, and the understanding we have gained concerning the pneumatic properties of tuffs at the ALRS, are directly relevant to such facilities and sites.

1.2 THE ALRS AND PREVIOUS SITE INVESTIGATIONS

1.2.1 Site Description

The Apache Leap Research Site is situated near Superior in central Arizona, approximately 160 *km* north of Tucson at an elevation of 1,200 *m* above sea level (Figure 1.1). The site is similar in many respects to Yucca Mountain in southern Nevada where the candidate HLW repository site is being characterized. ALRS is located near the extreme western edge of the Pinal Mountains. Lying immediately east of Superior, Arizona, is the Apache Leap, which forms a 600-*m* west-facing escarpment that exposes a volcanic zoned ash-flow tuff sheet and an underlying carbonate stratum. The dacite ash-flow sheet (Peterson, 1961) covers an area of 1,000 *km*^{2} and varies considerably in thickness about an average of 300 *m*. The tuff is a consolidated deposit of volcanic ash with particle diameters of less than 0.4 *mm*, resulting from a turbulent mixture of gas and pyroclastic materials at high temperature about 19 million years ago. The climate is temperate and dry, with a mean annual precipitation of less than 50 *cm*. Most of the precipitation occurs during two periods, from mid-July to late-September and from mid-November to late-March. During periods of high temperature and evapotranspiration demand in the summer, rain is characterized by high intensity, short duration thunderstorms. During cooler periods with much lower evapotranspiration demand in the winter, storms are of longer duration and lower intensity. The regional water table lies at a variable depth of more than 600 *m*. Except for a relatively thin perched zone of saturation at a depth of approximately 150 *m*, the rock above the water table is unsaturated.

The site under investigation consists of a cluster of 22 vertical and inclined (at 45°) boreholes that have been completed to a maximum vertical depth of 30 *m* within a layer of slightly welded unsaturated tuff. A plan view of the boreholes is shown in Figure 1.2 and a three-dimensional perspective in Figure 1.3. Recently surveyed wellhead locations in Figure 1.2, and borehole geometries in Figure 1.3, are given with references to Cartesian coordinates (*x*, *y*, *z*) with origin at the lower lip of the casing in borehole Z3 and a vertical *z*-axis pointing downward. Boreholes having the designations X, Y and Z were drilled during the initial stages of the project, prior to those designated V, W and G. Shortly after the completion of drilling, a surface area of 1500 *m*^{2} that includes all boreholes was covered with a thick plastic sheet to minimize infiltration and evaporation. The V, W, X, Y and Z boreholes span a surface area of approximately 55 *m* by 35 *m* and a volume of rock on the order of 60,000 *m*^{3}. The vertical G boreholes were drilled with conventional rotary equipment using water as cooling fluid; are about 20 *m* deep; and lie to the west of the plastic cover. A total of 270 *m* of oriented core was retrieved from the boreholes and stored at the University of Arizona Core Storage Facility. The upper 1.8 *m* of each borehole was cased. Borehole television images are available for boreholes V1, V2, V3, W1, W2, W2A, W3, X1, X2, X3, Y1, Y2, Y3, Z1, Z2 and Z3.

Figure 1.1: Location map of Apache Leap Research Site, ALRS (adapted from Geddis, 1994).
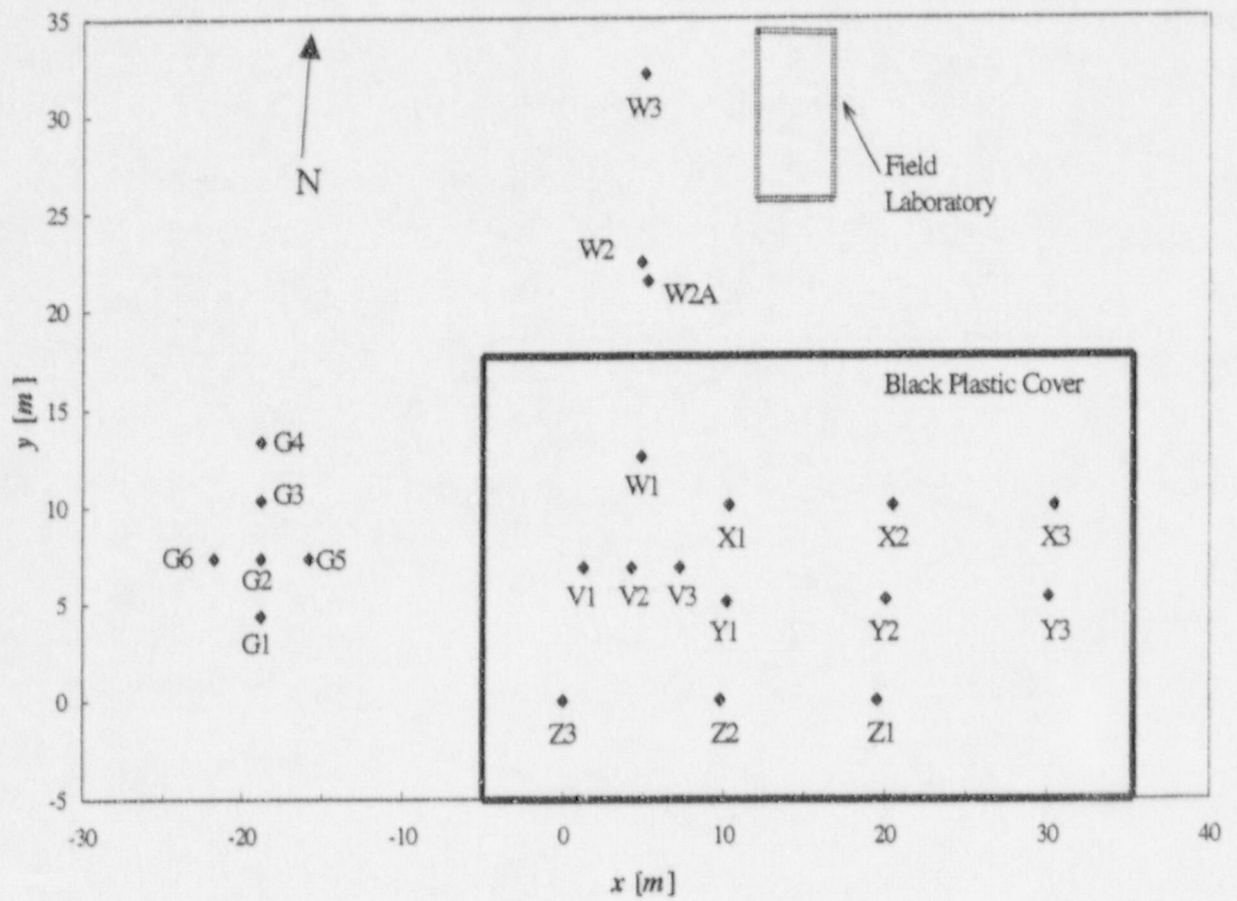
Figure 1.2: Plan view of boreholes, plastic cover, and field laboratory at ALRS.
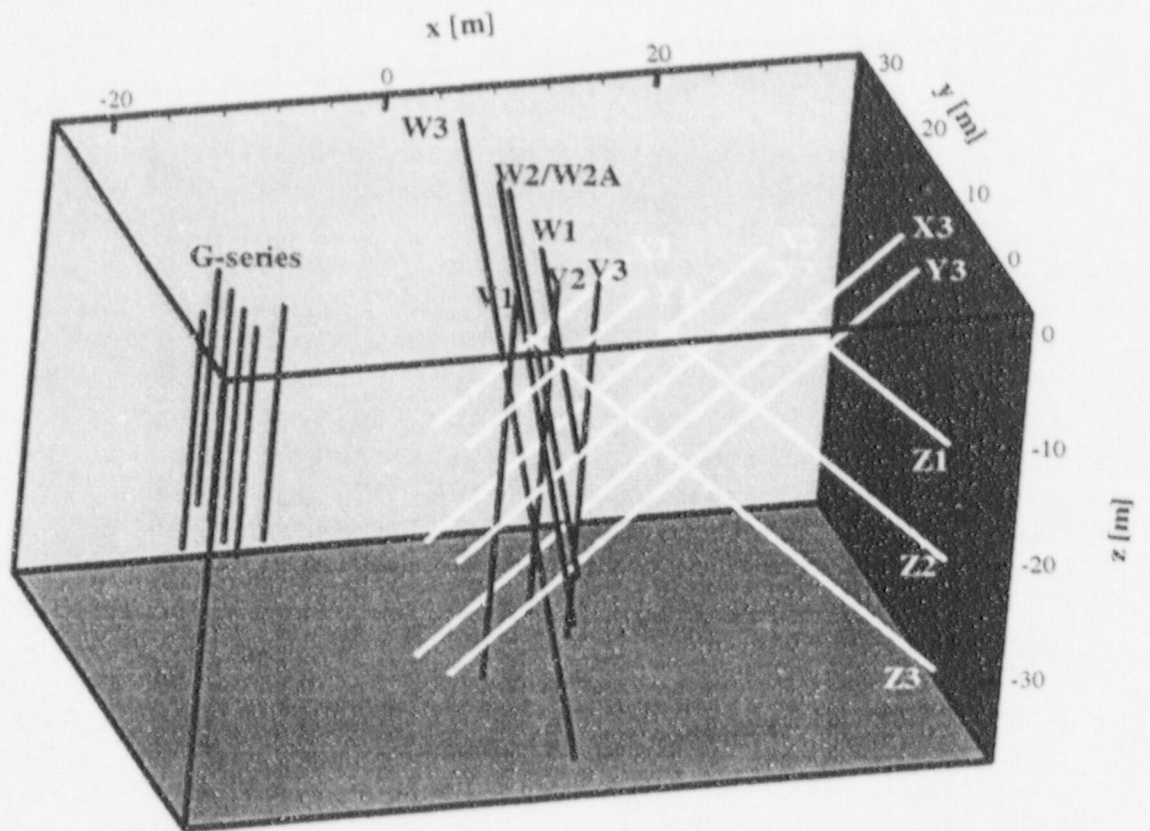
Figure 1.3: Three-dimensional perspective of the boreholes at the site.

1.2.2 Previous Work in Study Area of ALRS

Early work related to our area of study at the ALRS is described by Evans (1983), Schrauf and Evans (1984), Huang and Evans (1984), Green and Evans (1987), Rasmussen and Evans (1987, 1989, 1992), Yeh *et al.* (1988), Weber and Evans (1988), Chuang *et al.* (1990), Rasmussen *et al.* (1990, 1996), Evans and Rasmussen (1991), and Bassett *et al.* (1994). The early work included drilling 15 boreholes (V1, V2, V3, W1, W2, W3, X1, X2, X3, Y1, Y2, Y3, Z1, Z2, and Z3) and conducting numerous field and laboratory investigations. Laboratory measurements of matrix properties were conducted on core segments of various sizes taken from 3-*m* borehole intervals at 105 locations (indicated in Figure 5 of Evans and Rasmussen, 1991) within nine of the boreholes (X1, X2, X3, Y1, Y2, Y3, Z1, Z2, Z3). The measurements include interstitial properties such as bulk density (Table 1 in Rasmussen *et al.*, 1990), effective porosity (Table 1.1), skeletal density (Table 3 in Rasmussen *et al.*, 1990), pore surface area (Table 4 in Rasmussen *et al.*, 1990), and pore size distribution (Table 5 in Rasmussen *et al.*, 1990); hydraulic properties such as saturated and unsaturated hydraulic conductivity (Table 1.2) and moisture retention characteristics (Table 8 in Rasmussen *et al.*, 1990); α-value of the van Genuchten moisture characteristic function (Table 1.3); pneumatic properties such as oven-dry and unsaturated air-phase permeability (Table 1.4); and Klinkenberg slip-flow coefficient (Table 1.5).

The moisture retention properties of the matrix were characterized by the van Genuchten (1976, 1980) parameter α while holding other parameters of the van Genuchten retention model constant: the dimensionless parameter n at 1.6, and the residual water content θ_r at zero (Rasmussen *et al.*, 1990).

Information about the location and geometry of fractures in the study area has been obtained from surface observations, the examination of oriented cores, and borehole televiewer records. A summary of data concerning the orientation, dip and density of fractures in boreholes can be found in Rasmussen *et al.* (1990). A total of 79 fractures have been identified in boreholes at the site. The fractures appear to be exponentially distributed in a manner consistent with a Poisson process of fracture locations. Fracture density, defined by Rasmussen *et al.* (1990) as number of fractures per meter in a 3-*m* borehole interval, ranges from zero to a maximum of 4.3 per meter (Table 1.6). A Schmidt equal-area projection of fracture orientations, with contours indicating number of fractures per unit area of the projection circle, is shown in Figure 1.4. Though the fractures exhibit a wide range of inclinations and trends, most of them are near vertical, strike north-south and dip steeply to the east. The stereonet in Figure 1.4 is based on the data of Rasmussen *et al.* (1990); an earlier stereonet presented by Yeh *et al.* (1988) has the strikes of all fractures rotated by 180° degrees.

Table 1.1: Statistics of effective porosity measurements on ALRS core. Medium size sample measurements obtained using mercury intrusion method which underestimates effective porosity (after Rasmussen *et al.*, 1990).

	Effective Porosity [%]		
	Small	Medium	Large
Mean	17.15	14.62	17.54
Coef. Var.	16%	26%	13%
Minimum	11.02	9.18	14.30
Median	16.52	14.31	17.21
Maximum	24.73	47.58	27.51

Table 1.2: Statistics of hydraulic conductivity values obtained from 105 large core samples at the ALRS (after Rasmussen *et al.*, 1990)

	Hydraulic Conductivity [$*10^{-9}$ m/s]				
	Suction [kPa]				
	0	10	25	50	100
Mean	21.31	3.346	1.475	0.908	0.364
Coef. Var.	301%	105%	156%	115%	112%
Minimum	0.69	0.126	0.110	0.002	0.005
Median	4.24	2.610	0.556	0.498	0.235
Maximum	438.28	25.750	14.588	5.041	2.541

Table 1.3: Statistics for van Genuchten's α (after Rasmussen *et al.*, 1990).

Van Genuchten's Moisture Characteristic Function	
α-value [kPa^{-1}]	
Mean	0.0224
Coef. Var.	37.7%
Minimum	0.0102
Median	0.0203
Maximum	0.0643

Table 1.4: Statistics of laboratory determined air permeabilities for various values of suction and at oven-dried (OD) conditions (after Rasmussen *et al.*, 1990)

	Air Permeability [$m^2 *10^{-16}$]						
	Suction [kPa]						
	10	25	50	100	300	500	OD
Mean	1.54	11.20	16.88	26.67	35.11	38.23	57.12
Coef. Var.	434%	436%	344%	326%	309%	295%	272%
Minimum	<0.01	<0.01	0.02	0.25	1.29	1.91	3.81
Median	0.05	0.10	0.39	2.10	5.09	6.04	12.08
Maximum	41.90	333.10	389.80	678.70	780.50	780.50	1012.60

Table 1.5: Statistics of laboratory determined Klinkenberg slip flow coefficient
(after Rasmussen *et al.*, 1990).

Klinkenberg Coefficient [kPa]	
Mean	322.1
Coef. Var.	82%
Minimum	35
Median	217
Maximum	1277

Table 1.6: Statistics of fracture density and orientation obtained from ALRS cores
(after Rasmussen *et al.*, 1990).

	Fracture	Fracture Orientation	
	Density [m^{-1}]	Strike [deg]	Dip [deg]
Mean	0.77	214.4	64.5
Coef. Var.	108%	56%	37%
Minimum	0.00	3	1
Median	0.67	109	55
Maximum	4.33	359	89

Table 1.7: Statistics of field determined outflow rates and saturated hydraulic
conductivity values at the ALRS (after Rasmussen *et al.*, 1990)

	Outflow	Hydraulic Conductivity [$*10^{-9}$ m/s]		
	[$*10^{-6}$ m^3/s]	Philip	Glover	Dachler
Mean	26.349	59.42	29.10	30.20
Coef. Var.	612%	729%	729%	662%
Minimum	0.016	0.48	0.27	0.41
Median	0.633	11.63	5.64	10.33
Maximum	1232	39224	19126	17900

Table 1.8: Statistics of 3-m scale air permeability data. One interval exceeded capacity of
measurement device, while a second interval was less than the measurement threshold
(after Rasmussen *et al.*, 1990).

Field Air Permeability [$*10^{-16}$ m^2]	
Mean	178.1
Coef. Var.	667%
Minimum	<0.420
Median	4.02
Maximum	>13366

Table 1.9: Field water contents on various days at the ALRS (after Rasmussen *et al.*, 1990).

Borehole Water Content (m^3/m^3)								
Julian Day After 1/1/87	41	236	255	279	372	406	448	505
Mean	13.75	14.12	14.59	14.50	14.36	14.32	14.32	14.26
Coef. Var.	11%	11%	12%	12%	12%	12%	12%	12%
Minimum	10.19	10.85	10.89	10.77	9.99	9.53	9.85	10.14
Median	13.71	14.04	14.46	14.48	14.33	14.35	14.18	14.23
Maximum	17.63	17.29	18.75	18.42	17.74	17.77	17.57	17.51
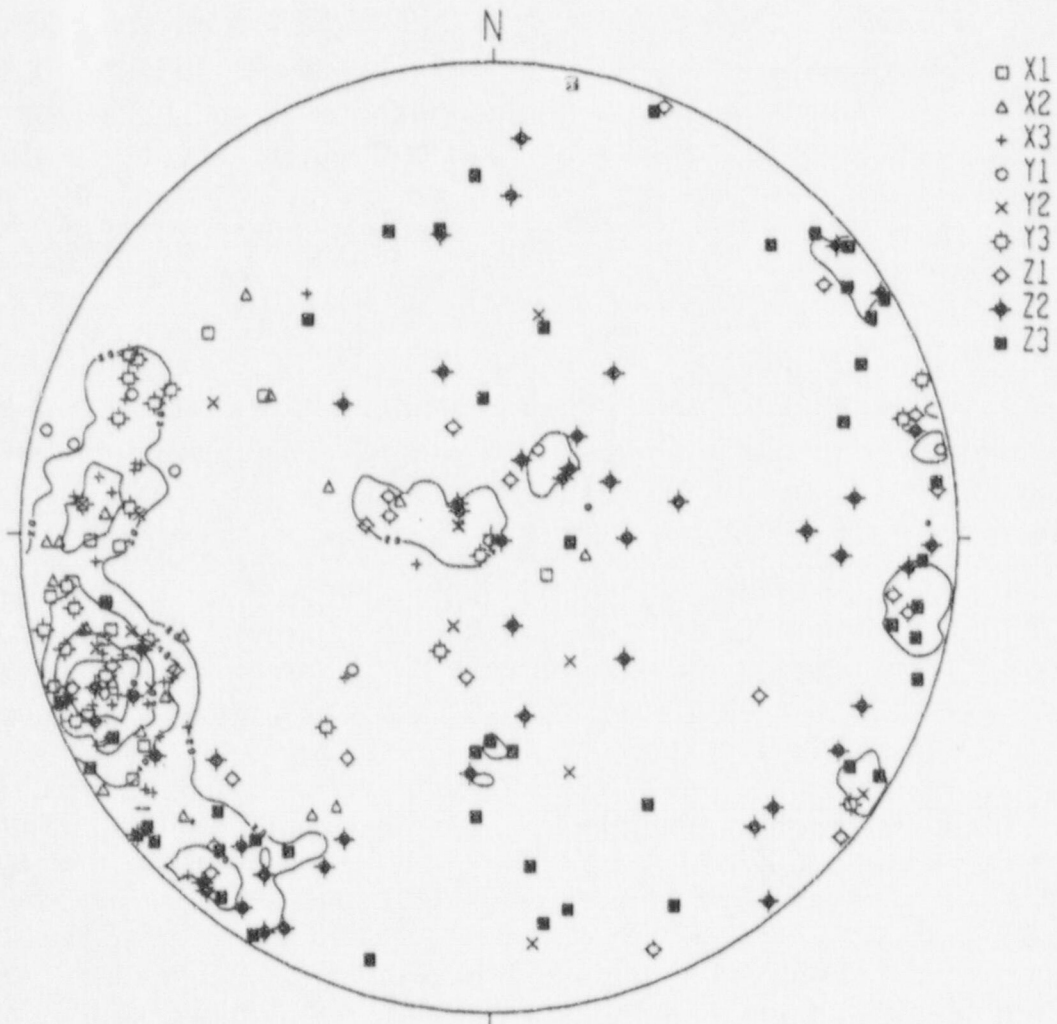
Figure 1.4: Lower hemisphere Schmidt equal-area projection of fractures identified by Rasmussen *et al.*, 1990. Contours indicate number of fractures per unit area of projection circle.

Surface fracture traces include an additional, steeply dipping east-west set. Laboratory experiments have also been conducted on large blocks of fractured tuff, including a study of aperture distribution in a large natural fracture (Vickers et al., 1992).

Single-hole hydraulic injection tests were performed by Tidwell (1988) in 87 out of 105 3-m intervals in boreholes X1, X2, X3, Y1, Y2, Y3, Z1, Z2, and Z3 from which core samples had been taken. The hydraulic tests were conducted by maintaining a constant water level near the top of a borehole until a constant injection rate was established. The injection rate was converted into equivalent hydraulic conductivity using three different formulae for steady state flow. One formula, due to Glover (1953), was modified by Tidwell (1988, p. 65, eq. 4.26) to account for borehole inclination according to

$$K = \frac{Q \sinh^{-1}(L/r) - L/h}{2\pi(2hL - 2Lz_1 - L^2)\sin\beta} \tag{1.1}$$

where K is hydraulic conductivity $[LT^{-1}]$, Q is flow rate $[L^3T^{-1}]$, L is length of injection interval $[L]$, r is borehole radius $[L]$, h is borehole length $[L]$, z_1 is distance from bottom of borehole to lower edge of test interval $[L]$, and β is angle of borehole inclination relative to ground surface (Figure 1.5), and the dimensions of each variable are specified in terms of mass $[M]$, length $[L]$ and time $[T]$ throughout this report. Another formula, due to Philip (1985), was modified in a likewise manner by Tidwell (1988, p. 79, eq. 4.61) to read

$$K = \frac{h^2 Q C_0}{(3/2)^{2/3} r^2 \pi \sin\beta (z_2^2 - z_1^2)} \tag{1.2}$$

where C_0 is a geometric factor related to the eccentricity of an assumed prolate spheroid representing the borehole, and z_2 is distance along the borehole from its bottom to the upper edge of the test interval $[L]$. The third formula, due to Dachler (1936), is written by Rasmussen et al. (1990) as

$$K = \frac{Q \ln(L/r)}{2\pi L h_w} \tag{1.3}$$

where h_w is pressure head in the injection interval $[L]$. Summary statistics are listed in Table 1.7 and show that calculated hydraulic conductivities range over five orders of magnitude. According to Rasmussen et al. (1990), the corresponding hydraulic conductivities are log-normally distributed and strongly skewed toward high values.

Single-hole pneumatic injection tests were conducted in 87 intervals of length 3 m in 9 boreholes (X1, X2, X3, Y1, Y2, Y3, Z1, Z2 and Z3) by Rasmussen et al. (1990, 1991, 1993). According to Rasmussen et al. (1993), the tests were conducted by injecting air at a constant mass rate between two inflated packers while monitoring pressure within the injection interval. Pressure was said to have reached stable values within minutes in most test intervals. Air permeability was calculated using Dachler's (1936) steady state formula, adapted by Rasmussen et al. (1990, 1993) to isothermal airflow,

$$k_a = \frac{Q_a \mu_a p_a \ln(L/r)}{L(p^2 - p_a^2)} \tag{1.4}$$

where k_a is intrinsic permeability to air $[L^2]$, Q_a is volumetric airflow rate at standard temperature and pressure $[L^3 T^{-1}]$, μ_a is air viscosity $[ML^{-1}T^{-1}]$, p_a is atmospheric pressure $[ML^{-1}T^2]$, and p is absolute air pressure $[ML^{-1}T^2]$, in test interval. Summary statistics are listed in Table 1.8. Figure 5b of Rasmussen *et al.* (1993) suggests a good correlation (r = 0.876) between pneumatic and hydraulic permeabilities at the ALRS.
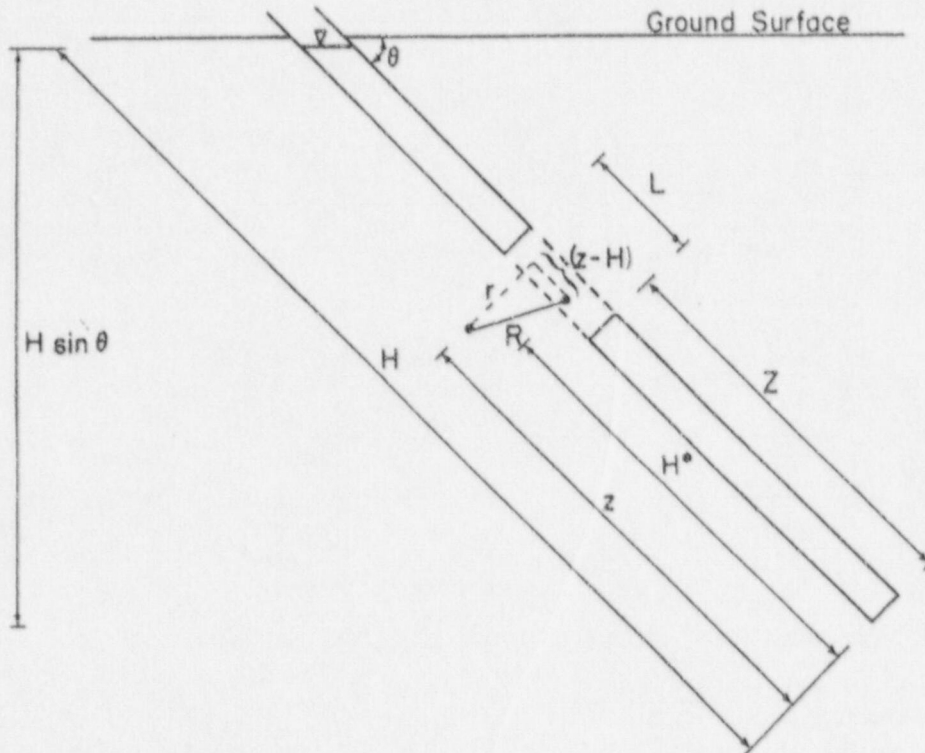
Figure 1.5: Geometric parameters associated with single-hole hydraulic injection test (adapted from Tidwell, 1988)

Figure 1.6 shows a scatter plot of pneumatic permeability versus fracture density for 3-*m* borehole intervals based on the data of Rasmussen *et al.* (1990). It suggests a lack of correlation between fracture density and air permeability
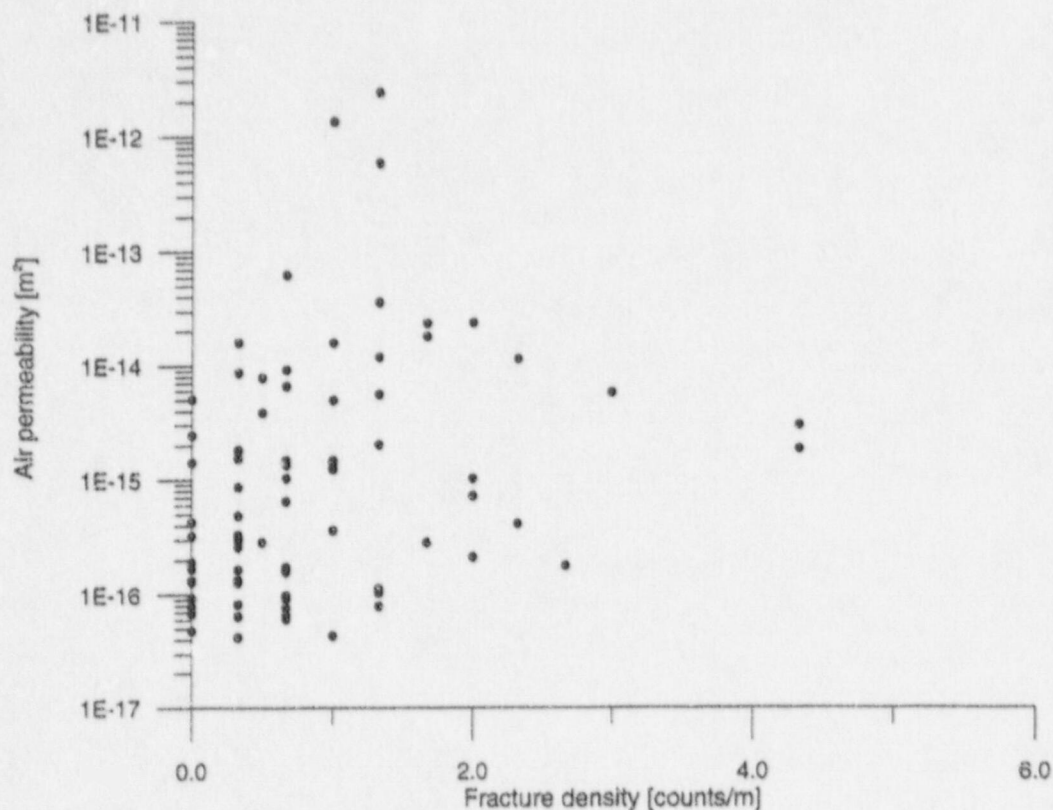
Figure 1.6: Air permeability versus fracture density (data from Rasmussen *et al.*, 1990)

Rasmussen *et al.* (1990) conducted *in situ* determinations of volumetric water content by means of neutron probes at 105 locations within the nine boreholes listed earlier. They took measurements on eight separate occasions 41, 236, 255, 279, 372, 406, 448, and 505 Julian days following 1/1/87 (Table 1.9). Temporal variations in neutron readings were slow during this period. As matrix porosities are much larger than the porosity of fractures, and pore sizes within the matrix are generally much smaller than fracture openings, most of the water resides in the matrix and its water content is much higher than that of the fractures. We therefore attribute the neutron probe measurements, and corresponding water contents, primarily to the matrix.

A gaseous tracer experiment was conducted at the ALRS (Yeh *et al.*, 1988) by injecting helium into one borehole and monitoring its arrival in neighboring boreholes by means of a thermal conductivity meter (utilizing the low thermal conductivity of helium relative to that of standard atmosphere). A test performed by injecting helium into borehole X2, below a packer set at a distance of about 20 *m* from the surface, showed breakthrough of helium into borehole X1 at a distance of 9.5 – 10 *m* from the surface. The breakthrough was attributed by the authors to a fracture that had been encountered in the injection and the detection intervals. No helium was detected in borehole X3 during

the test, but the data collected in borehole X1 are summarized in Figure 10 of Yeh *et al.*, 1988.

1.2.3 Single-Hole Pneumatic Injection Tests

Single-hole pneumatic injection tests conducted at the ALRS by Rasmussen *et al.* (1990, 1991, 1993) were of relatively short duration and involved relatively long test intervals. Guzman *et al.* (1994, 1996) and Guzman and Neuman (1996) conducted a much larger number of single-hole pneumatic injection tests of considerably longer duration over shorter borehole intervals. Their tests were conducted under highly controlled conditions, subject to strict quality assurance, within six boreholes (V2, W2A, X2, Y2, Y3, and Z2) that extend over a horizontal area of 32 *m* by 20 *m*. Five of the boreholes are 30-*m* long (V2, W2A, X2, Y2, Z2) and one has a length of 45 *m* (Y3); five are inclined at 45° (W2A, X2, Y2, Y3, Z2) and one is vertical (V2). A total of 184 borehole segments were tested by setting the packers 1 *m* apart as shown in Figure 1.7. Additional tests were conducted in segments of lengths 0.5, 2.0 and 3.0 *m* in borehole Y2, and 2.0 *m* in borehole X2, bringing the total number of tests to over 270. The tests were conducted by maintaining a constant injection rate until air pressure became relatively stable and remained so for some time. The injection rate was then incremented by a constant value and the procedure repeated. Three or more such incremental steps were conducted in each borehole segment while recording the air injection rate, pressure, temperature and relative humidity. For each relatively stable period of injection rate and pressure, air permeability was estimated by treating the rock around each test interval as a uniform, isotropic continuum within which air flows as a single phase under steady state, in a pressure field exhibiting prolate spheroidal symmetry.

The results of these steady state interpretations of single-hole air injection tests are listed in Guzman *et al.* (1996). The authors found, and noted, that (Guzman *et al.*, 1994, 1996; Guzman and Neuman, 1996)

1. Air permeabilities determined *in situ* from steady state single-hole test data are much higher than those determined on core samples of rock matrix in the laboratory, suggesting that the *in situ* permeabilities represent the properties of fractures at the site.
2. It is generally not possible to distinguish between the permeabilities of individual fractures, and the bulk permeability of the fractured rock in the immediate vicinity of a test interval, by means of steady state single-hole test data.
3. The time required for pressure in the injection interval to stabilize typically ranges from 30 to 60 *min*, increases with flow rate, and may at times exceed 24 *hrs*, suggesting that steady state permeability values published in the literature for this and other sites, based on much shorter air injection tests, may not be entirely valid.
4. Steady state interpretation of single-hole injection tests, based on the assumption of radial flow, is acceptable for intervals of length equal to or greater than 0.5 *m* in boreholes having a radius of 5 *cm*, as is the case at the ALRS.
5. Pressure in the injection interval typically rises to a peak prior to stabilizing at a constant value, due to a two-phase flow effect whereby water in the rock is displaced by air during injection.

6. In most test intervals, pneumatic permeabilities show a systematic increase with applied pressure as air displaces water under two-phase flow.

7. In a few test intervals, intersected by widely open fractures, air permeabilities decrease with applied pressure due to inertial effects.

8. Air permeabilities exhibit a hysteretic variation with applied pressure.

9. The pressure-dependence of air permeability suggests that it is advisable to conduct single-hole air injection tests at several applied flow rates and/or pressures.

10. Enhanced permeability due to slip flow (the Klinkenberg effect) appears to be of little relevance to the interpretation of single-hole air injection tests at the ALRS.

11. Local-scale air permeabilities vary by orders of magnitude between test intervals across the site.

12. Spatial variability is much greater than that due to applied pressure and lends itself to meaningful statistical and geostatistical analysis.

13. Air permeabilities are poorly correlated with fracture densities, as is known to be the case for hydraulic conductivities at many water-saturated fractured rock sites worldwide (Neuman, 1987), providing further support for Neuman's conclusion that the permeability of fractured rocks cannot be reliably predicted from information about fracture geometry (density, trace lengths, orientations, apertures and their roughness) but must be determined directly by means of hydraulic and/or pneumatic tests.

14. Air permeabilities vary systematically with the scale of measurement as represented nominally by the distance between packers in an injection interval.

The work of Guzman *et al.* (1994, 1996) and Guzman and Neuman (1996) strongly suggests that air injection tests yield properties of the fracture system, which are relevant to both unsaturated and saturated conditions. In particular, numerical simulations by these authors show that, whereas the intrinsic permeability one determines from such tests is generally lower than the intrinsic permeability to water of fractures which surround the test interval, it nevertheless approaches the latter as the applied pressure goes up. This is so because capillary forces tend to draw water from fractures into the porous (matrix) blocks of rock between the fractures, thereby leaving the latter saturated primarily with air. Water saturation in the matrix blocks is therefore typically

Locations of 1.0 m Air Permeability Measurements

(Circles do not indicate sphere of influence)
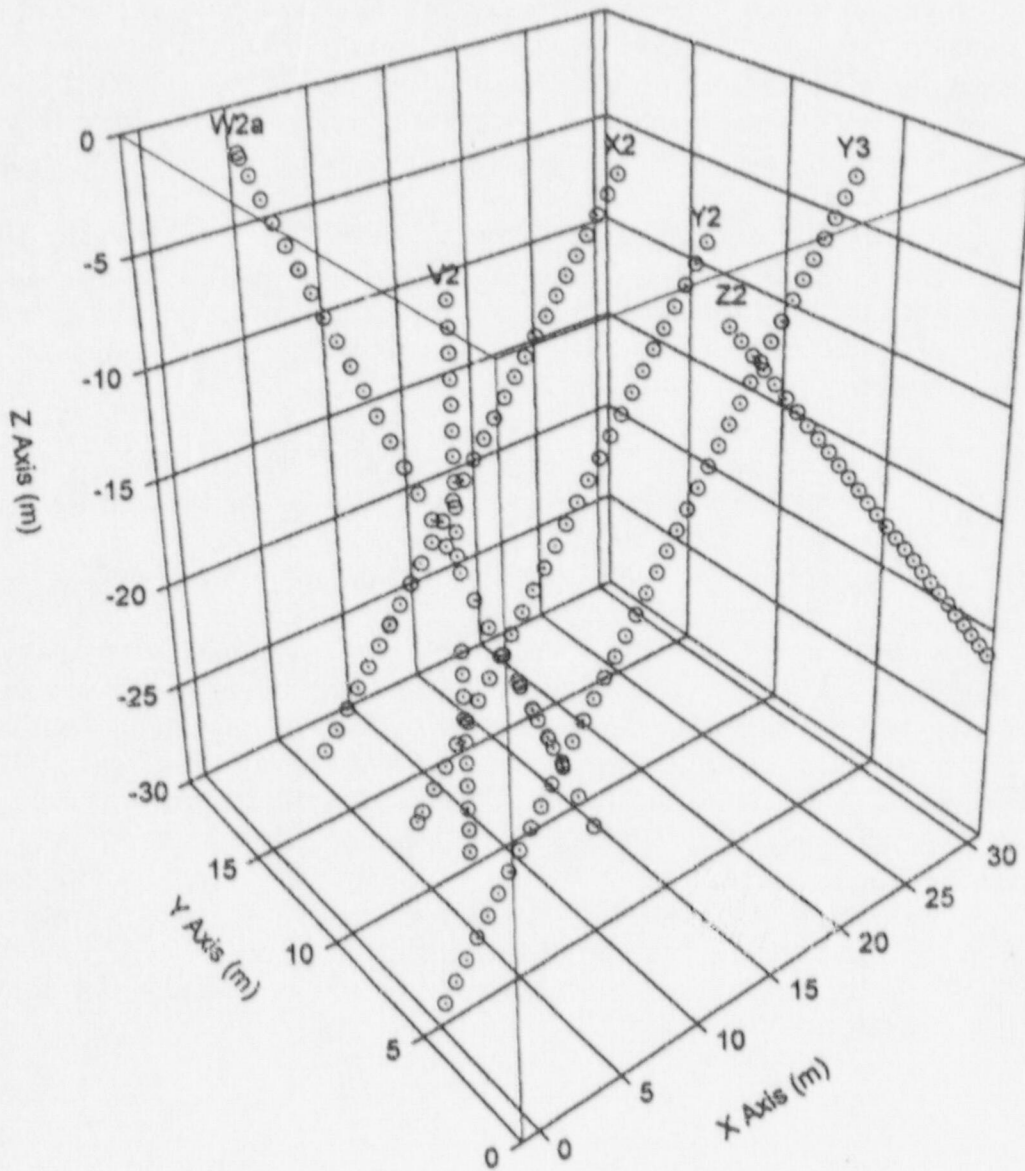
Figure 1.7: Perspective toward the Northeast showing center locations of 1-*m* single-hole pneumatic test intervals; overlapping circles indicate re-tested locations (after Guzman *et al.*, 1996)

much higher than that within the fractures, making it relatively difficult for air to flow through such blocks. It follows that, during a pneumatic injection test, the air moves primarily through fractures (most of which contain relatively little water) and the test therefore yields flow and transport parameters which reflect the intrinsic properties of these largely air-filled fractures.

1.2.4 Geostatistical Analysis of Spatial Variability

Core and single-hole measurements, conducted over short segments of a borehole, provide information only about a small volume of rock in the immediate vicinity of each measurement interval. Available data from the ALRS indicate that rock properties, measured on such small scales, vary erratically in space in a manner which renders the rock randomly heterogeneous and pneumatically anisotropic. A major question is how to describe this spatial and directional dependence of medium properties in untested portions of the rock.

Our analyses to date suggest (Bassett *et al.*, 1994, 1997; Guzman *et al.*, 1996) that it is possible to interpolate some of the core and single-hole measurements at the ALRS between boreholes by means of geostatistical methods, which view the corresponding variables as correlated random fields. This is especially true about air permeability, porosity, fracture density, water content, and the van Genuchten water retention parameter α, for each of which we possess enough measurements to constitute a workable geostatistical sample. Standard geostatistical analysis provides best (minimum variance) linear unbiased estimates of how each such quantity varies in three-dimensional space, together with information about the quality of these estimates.

A geostatistical analysis of the above site variables has been conducted by Chen *et al.* (1997). We repeated and slightly modified some of their calculations. Figure 1.8 shows (among others) an omni-directional sample (semi)variogram of log (to base ten) air permeability data, where k is given in $[m^2]$, obtained from steady state analyses of 1-m scale single-hole pneumatic injection tests at the site. The variogram exhibits statistical inhomogeneity and was analyzed by Chen *et al.* (1997) using two different models (see figure): one which views the data as belonging to a random fractal field that has a power-law variogram and another, more traditional model which views the data as belonging to a statistically homogeneous random field about a linear or quadratic spatial drift. To select the best among these models, they used formal model discrimination criteria based on the Maximum Likelihood Cross Validation (MLCV) approach of Samper and Neuman (1986a,b), coupled with the generalized least squares drift removal approach of Neuman and Jacobson (1984).
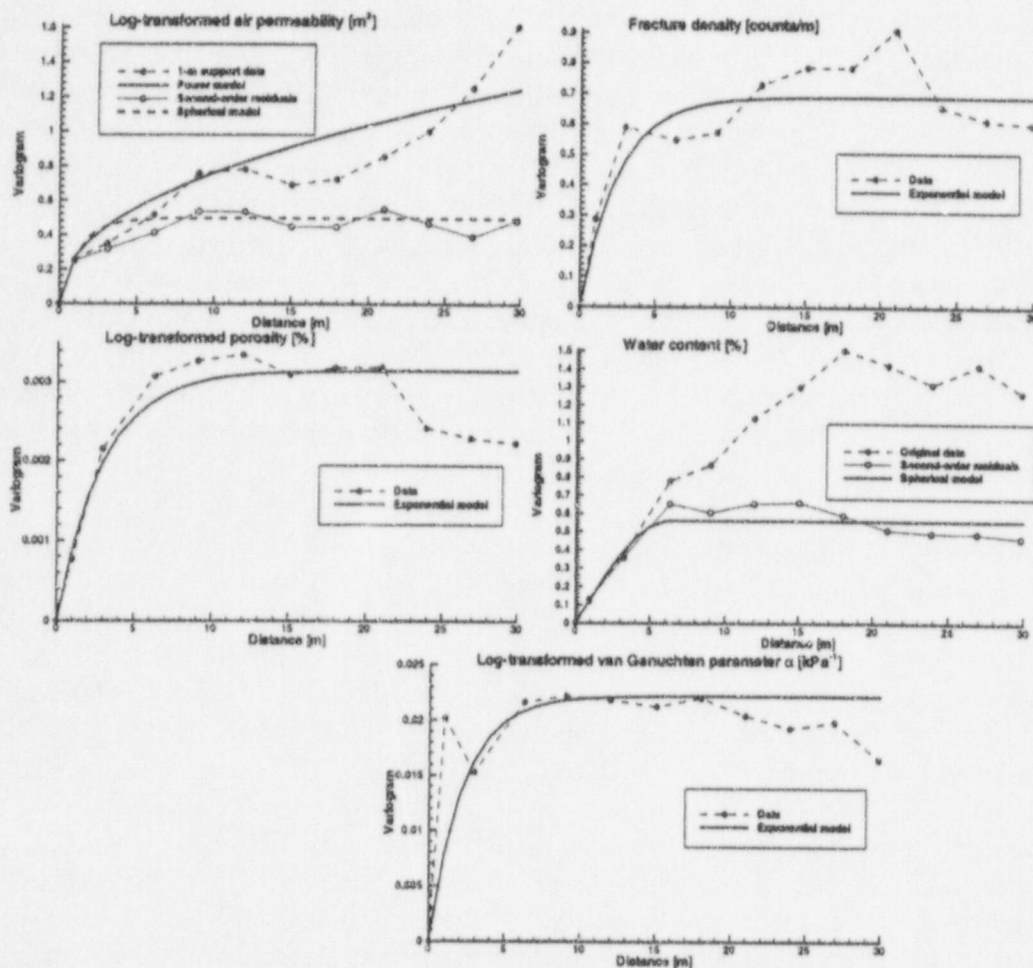
Figure 1.8: Omni-directional sample and model variograms of various parameters at minimum separation distance of 3 m.

MLCV estimates variogram parameters by maximizing the likelihood of kriging (geostatistical interpolation) cross validation errors. As MLCV assumes that the variogram model is known, it leads to optimum parameters for a given model structure without regard to the question how well this model represents the real system. Fortunately, a number of model identification criteria have been developed in the context of maximum likelihood estimation. Earlier work by Carrera and Neuman (1986a, b) and Samper and Neuman (1986a,b) have compared four such criteria, AIC (Akaike, 1974), MAIC (Akaike, 1977), HIC (Hannan, 1980), KIC (Kashyap, 1980), and concluded that the one which comes closest to satisfying these requirement is that due to Kashyap (1982). Kashyap's criterion favors the model which, among all alternatives considered, is least probable (in an average sense) of being incorrect. Stated otherwise, the criterion minimizes the average probability of selecting the wrong model among a set of alternatives. It supports the principle of parsimony in that, everything else being equal, the model with the smallest number of parameters is favored. While this means favoring the simpler model, the criterion nevertheless allows considering models of growing complexity as the database improves in quantity and quality. In other words, the criterion

NUREG/CR-5559

recognizes that when the database is limited and/or of poor quality, one has little justification for selecting an elaborate model with numerous parameters. Instead, one should then prefer a simpler model with fewer parameters, which nevertheless reflects adequately the underlying structure of the rock, and the corresponding flow and transport regime. The cited works by Carrera and Neuman, and Samper and Neuman, clearly indicate that an inadequate model structure is far more detrimental to its predictive ability than is noise in data used to calibrate the model.

Chen *et al.* (1997) extended MLCV so as to render it applicable to statistically nonhomogeneous models such as a random fractal characterized by a power-law variogram (while the random fractal field represented by such a variogram is statistically nonhomogeneous, it does possess statistically homogeneous spatial increments). Figure 1.8 shows the power model fitted to the original sample variogram, and an exponential model fitted to a sample variogram of residuals after removal of a second-order polynomial drift function. The power model represents a nonhomogeneous field that possesses neither a finite variance nor a finite spatial correlation scale. The exponential model represents a homogeneous field with finite variance and spatial correlation scale. Which of these models represents the data more accurately? An answer is found in Table 1.10 which shows that, whereas the exponential variogram model with a quadratic drift (given by $-16.761 + 0.05661x + 0.046311y - 0.23328z + 0.0012554x^2 + 0.0015361y^2 - 0.007176z^2 + 0.000050061xy + 0.0053009xz + 0.0072004yz$) fits the data best (as measured and implied by the smallest negative log likelihood model fit criterion, NLL), all four model discrimination criteria (AIC, MAIC, HIC, KIC) consistently rank the power model as best, and the former model as least acceptable, among the three considered. The reason is that whereas all three models fit the data almost equally well, the power model is most parsimonious with only two parameters, and the exponential variogram model with second-order drift is least parsimonious with twelve parameters. As is shown in Figure 1.9, both models yield very similar kriged (estimated) images of log k, but rather different measures of the associated estimation uncertainty.

Table 1.10: Discrimination Among Log Permeability Geostatistical Models (after Chen *et al.*, 1997).

Drift Model	No Drift	1st Order Polynomial	2nd Order Polynomial
NLL	665.801	665.080	655.849
Variogram model of Residuals	Power	Exponential	Exponential
Number of Parameters	2	6	12
Variance (Scaling Coefficient for Power model)	0.2715	0.5807	0.495
Integral scale (Power for power model)	0.4475	1.665	1.2602
AIC (Rank)	669.801 (1)	677.08 (2)	679.849 (3)
MAIC (Rank)	677.231 (1)	696.37 (2)	718.428 (3)
HIC (Rank)	672.407 (1)	684.898 (2)	695.486 (3)
KIC (Rank)	680.016 (1)	690.088 (2)	700.907 (3)
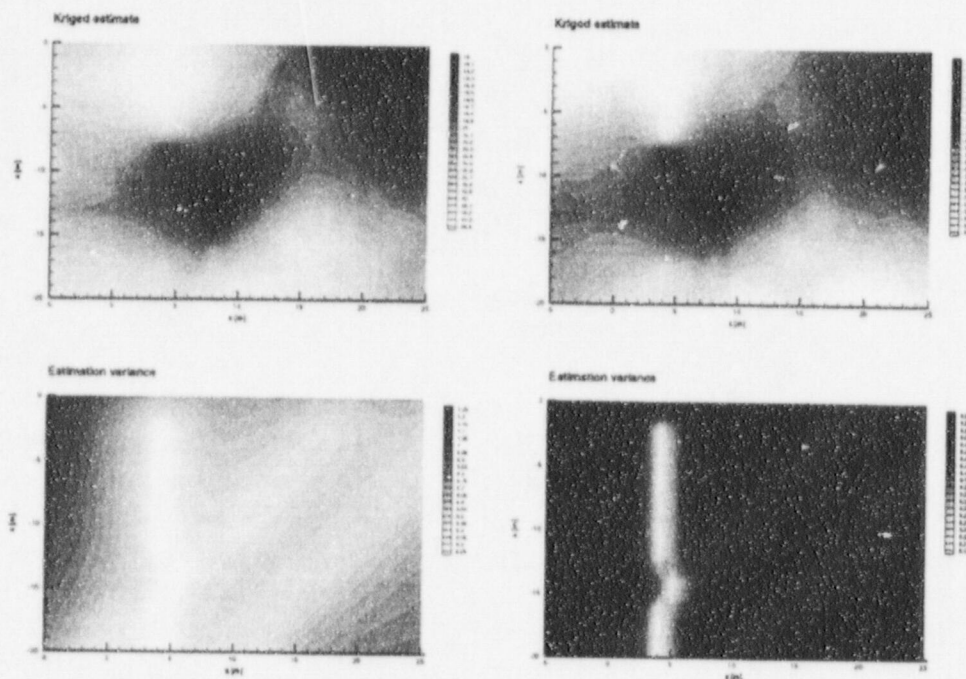
Figure 1.9: Kriged estimates and variance of log k at $y = 7$ m using power model (left) and exponential model with second order de-trending (right).

The geostatistical analysis of 1-m scale air permeabilities, conducted by Chen *et al.* (1997), is based on data from only six boreholes (X2, Y2, Y3, Z2, V2, W2). As these boreholes span only a part of the domain we model for purposes of interpreting our cross-hole tests, it would be good if we could validly augment the 1-m data with air permeabilities obtained from 3-m test intervals in other boreholes (X1, X3, Y1, Z1, Z3). To check whether this is justified, we compare in Figure 1.10 the omni-directional sample variograms of the available 1-m, 3-m, and combined 1-m and 3-m log k data. Though the sample variograms differ somewhat from each other at large separation distances, they are otherwise quite close. Attempts to represent the 3-m data by a variogram model that views them as a sample from a statistically homogeneous random field with a linear or quadratic spatial drift were not successful. We therefore krige the combined set of 227 1-m and 3-m air permeability data jointly, using the same power variogram model as that surmised on the basis of 1-m data by Chen *et al.* (1997). The combined set of 1-m and 3-m scale log-transformed permeability ranges from -17.13 to -11.62 and is characterized by mean, variance, and coefficient of variation equal to -15.2 (corresponding to 6.3×10^{-16} m^2), 8.7×10^{-1}, and -6.1×10^{-2}, respectively.
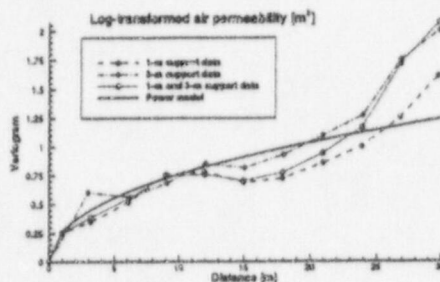
Figure 1.10: Omni-directional sample and power model variograms of log k data with various supports. Power model fitted to 1-m data.

One-meter and three-meter scale single-hole air permeability data are available for boreholes X2, Y2, Y3, and Z2. Figure 1.11 shows how these and 0.5-m data from borehole Y2 vary with depth in each borehole. We see that 3-m scale permeabilities obtained for Y2 by Rasmussen *et al.* (1990) are consistently lower than those obtained by Guzman *et al.* (1996); we attribute this systematic difference to the relatively short duration of tests conducted by Rasmussen *et al.* In general, as support scale increases, the amplitude and frequency of spatial variations in permeability decrease. Figure 1.12 compares kriged images of log air permeability we have generated along four vertical sections at $y = 0, 5, 7,$ and 10 m using 1-m data (left column) and the combined set of 1-m and 3-m data, the latter from boreholes X1, X3, Y1, Z1 and Z3 (right column). The figure shows boreholes intersected by, or located very close to, each cross-section. The two sets of kriged images are considerably different from each other. This is most pronounced at $y = 0$ m, which passes through the Z-series of boreholes: here the inclusion of data from boreholes Z1 and Z3 has caused estimated permeability in the upper right corner of the section to be much higher than it is without these data. The effect extends to all four cross-sections, which exhibit elevated permeabilities near the upper-right corner. Along sections at $y = 5$ m and 7 m, which pass close to the Y and V series, respectively, the addition of data from Y1 affects the shape and size of a prominent high-permeability zone which extends through Y2 (see corresponding peak in Figure 1.11). The addition of data from X3 to the set reveals corresponding high- and low-permeability zones in section $y = 10$ m which correlate well with similar zones, intersected by Y3, in section $y = 5$ m. A three-dimensional representation of kriged log permeability based on the combined set of data is shown in Figure 1.13. Figures 1.14 through 1.16 show corresponding sections in the y-z, z-x, and x-y planes, respectively.
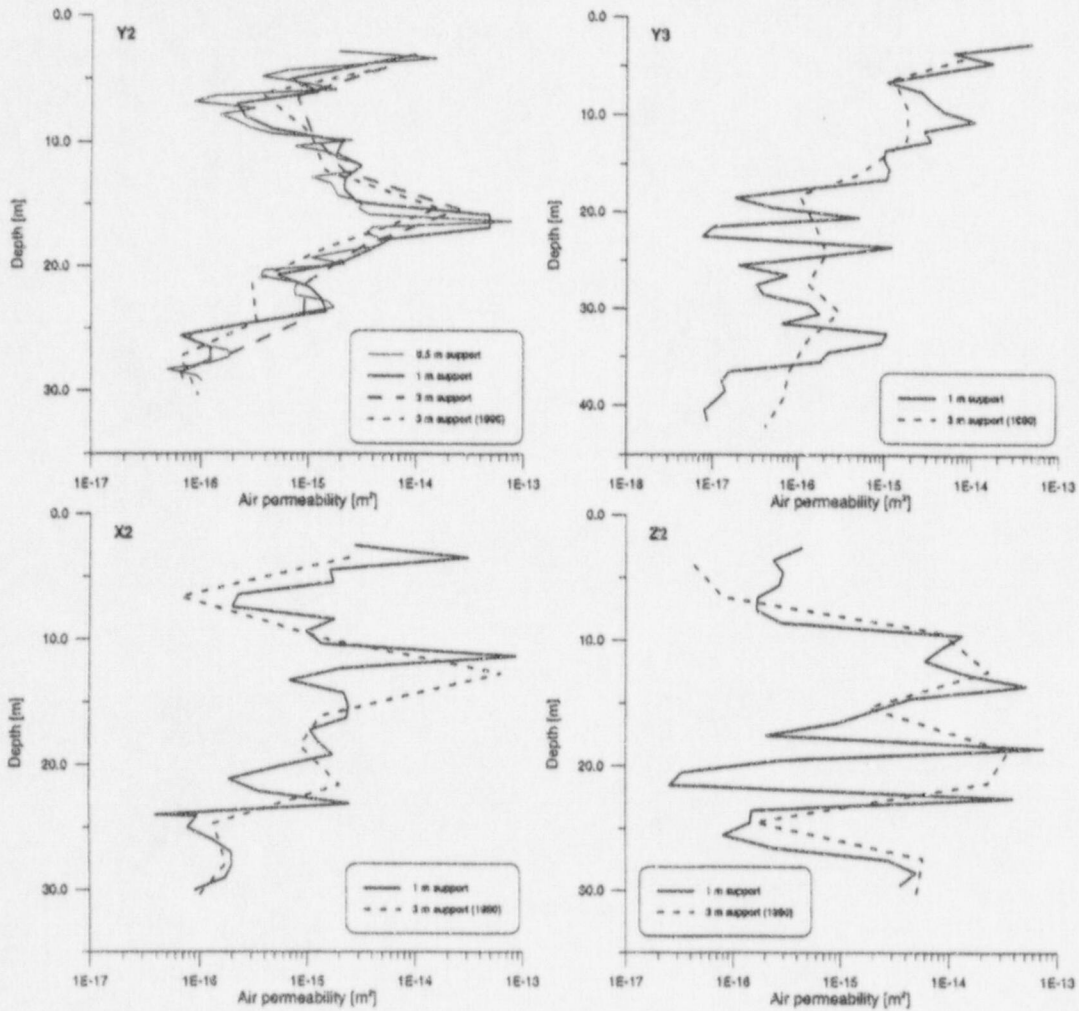
Figure 1.11: Variation of air permeability with depth and support scale (data from Guzman *et al.*, 1996 and Rasmussen *et al.*, 1990)
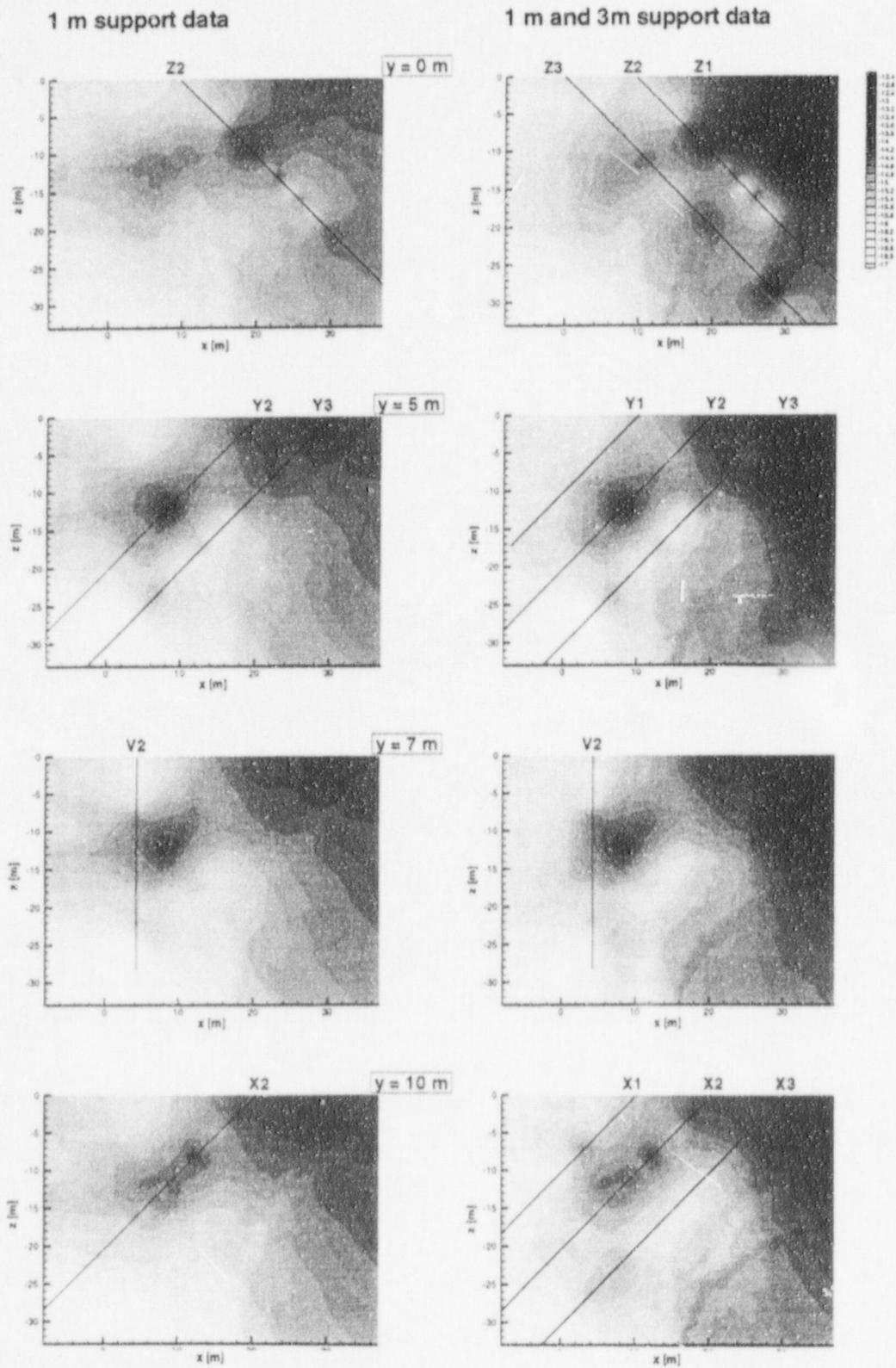
Figure 1.12: Kriged log k estimates obtained using 1-m scale data from boreholes X2, Y2, Y3, Z2, V2, and W2A (left) and same together with 3-m scale data from boreholes X1, X3, Y1, Z1, and Z3 (right).
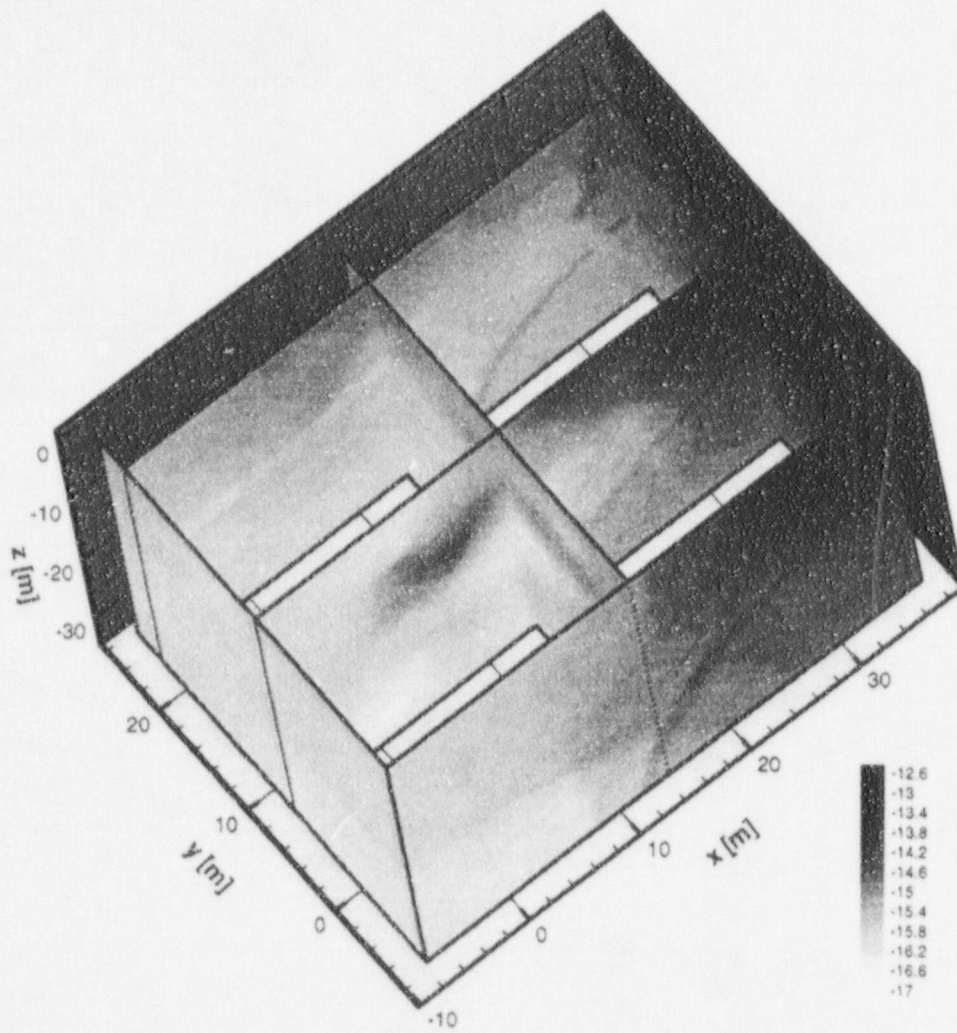
Figure 1.13: Three-dimensional representation of kriged log *k*.
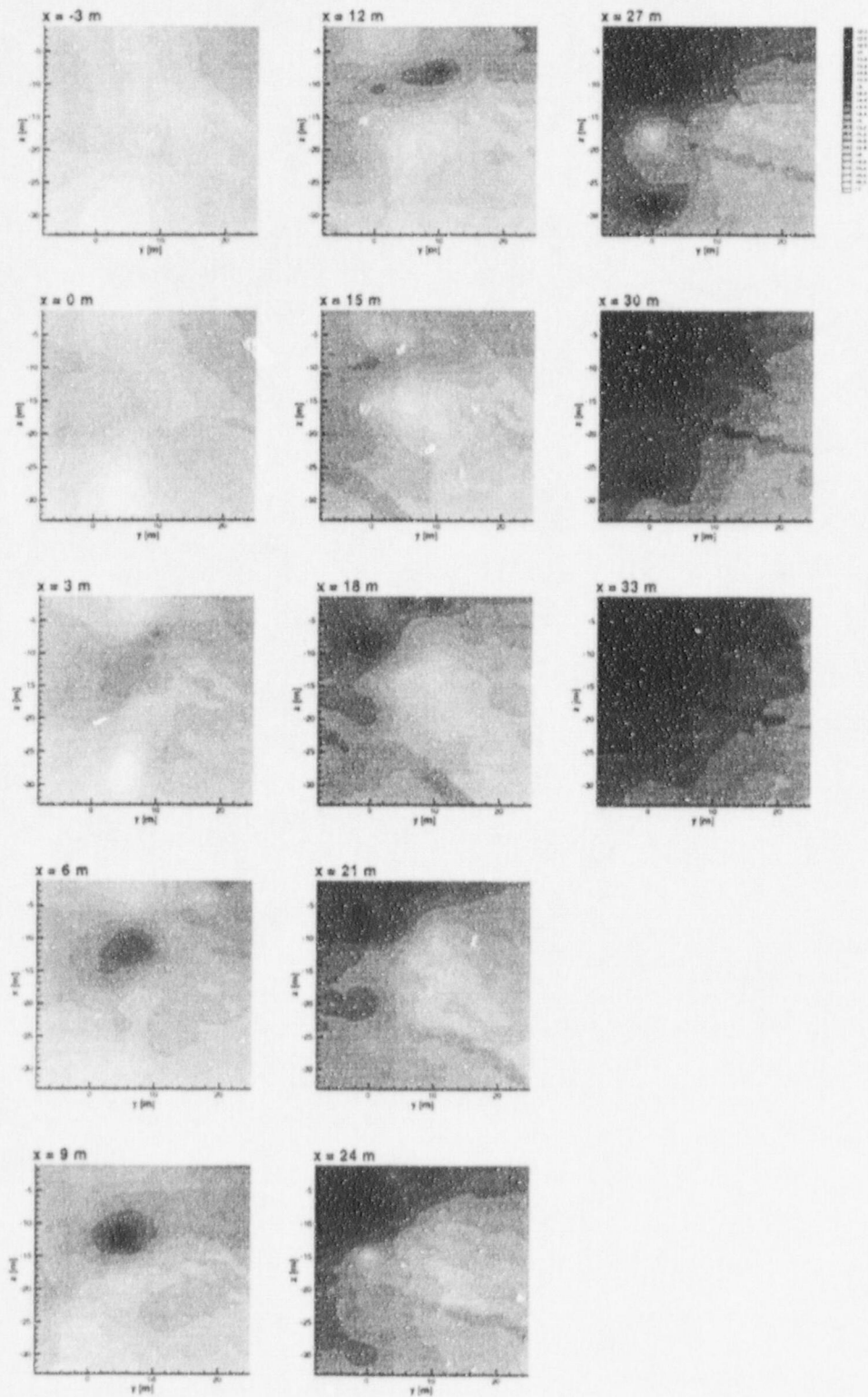
Figure 1.14: Kriged log *k* along various *y-z* planes.
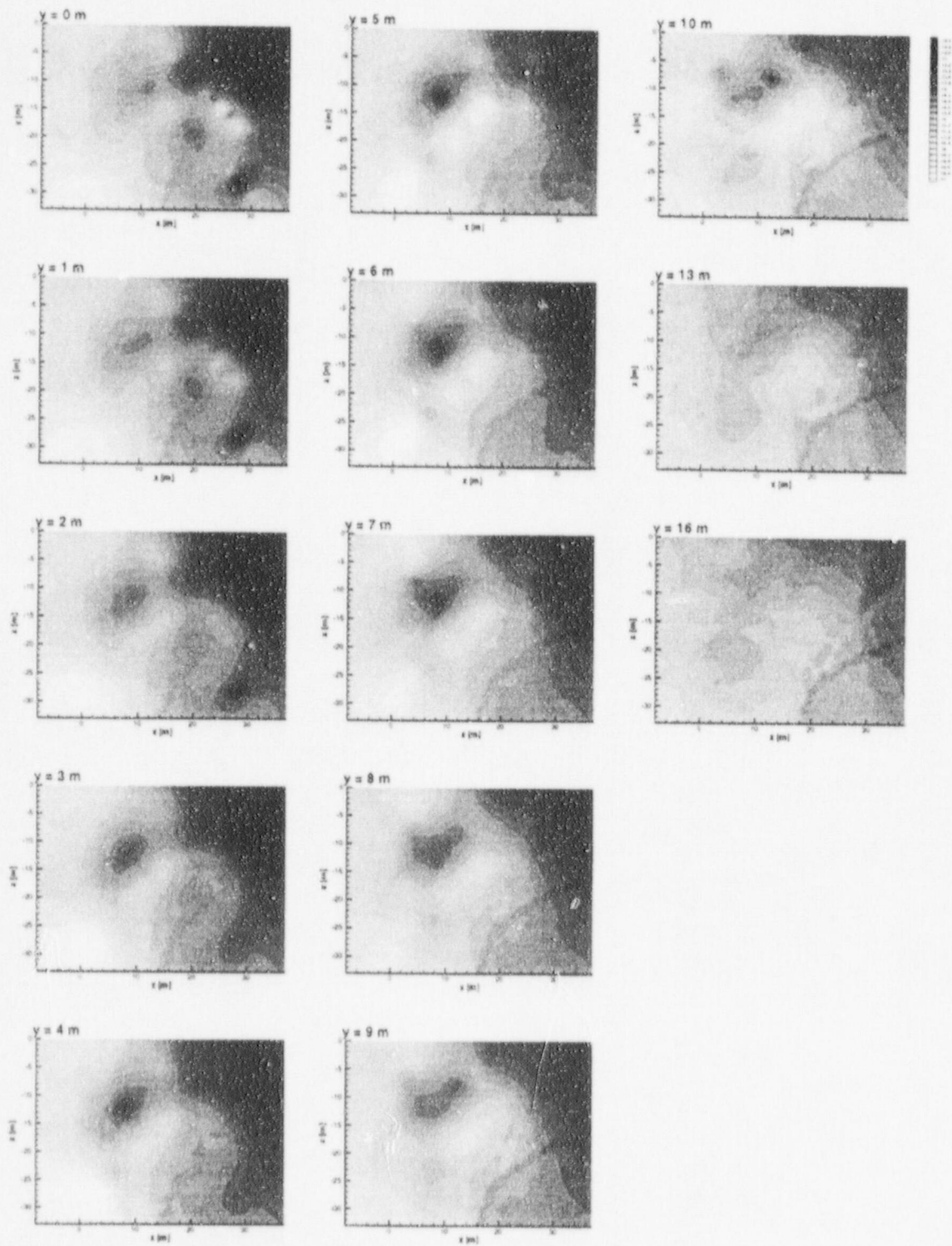
Figure 1.15: Kriged log k along various x-z planes.
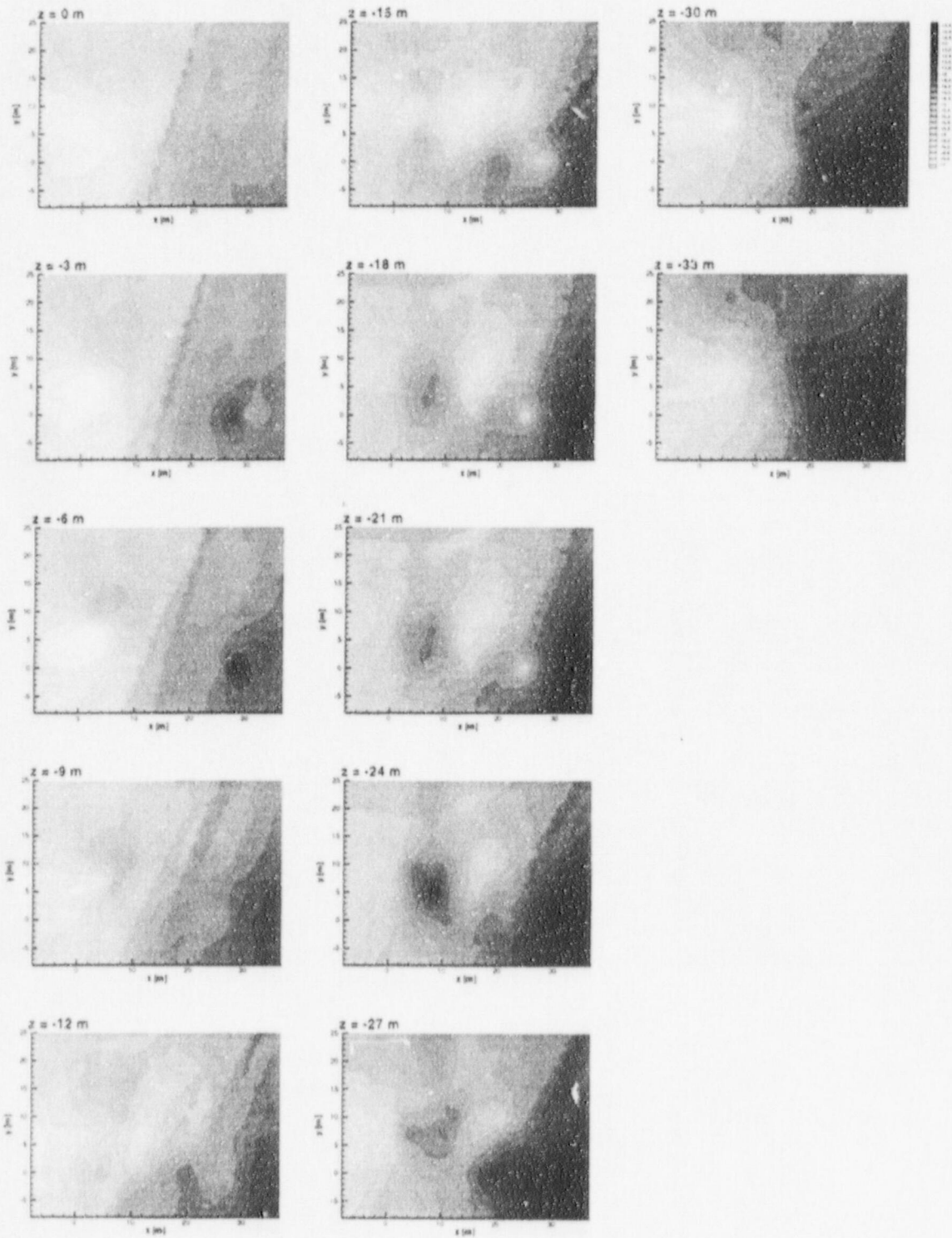
Figure 1.16: Kriged log k along various x-y planes.

A similar analysis has been performed by Chen *et al.* (1997) on *in situ* water content data. Figure 1.8 shows original and residual sample variograms together with the best-fit spherical model (with quadratic polynomial drift) fitted to the latter. A power model does not seem to fit the data well. It is clear from Table 1.11 that all four model discrimination criteria (AIC, MAIC, HIC, KIC) consistently rank the spherical model with quadratic polynomial drift (given by $8.3145 + 0.2234x - 0.05905y + 0.010397z - 0.0049492x^2 + 0.00077045y^2 + 0.0028264z^2 - 0.001986xy + 0.0039864xz - 0.0080923yz$) as better than an exponential model without drift. This is so despite the fact that the chosen spherical model with drift has twelve parameters, and is therefore less parsimonious than the exponential model without drift, which has only two parameters.

Table 1.11: Discrimination Among Geostatistical Models of Water Content (after Chen *et al.*, 1997).

Drift Model	Original Data	2nd Order Polynomial
NLL	398.105	319.18
Variogram model of Residuals	Exponential	Spherical
Number of Parameters	2	12
Variance	1.349	0.5609
Integral scale (Range for Spherical mode)	6.55	6.29
AIC (Rank)	402.105 (2)	343.180 (1)
MAIC (Rank)	397.913 (2)	375.028 (1)
HIC (Rank)	394.307(2)	356.085 (1)
KIC (Rank)	402.116 (2)	364.712 (1)

Figure 1.17 shows kriged images of log-transformed air permeability, fracture density, porosity, water content, and log-transformed van Genuchten α in a vertical plane corresponding to $y = 7.0$ *m* around which many of the available data are clustered. There clearly is no correlation between log permeability and fracture density along this plane (nor anywhere else in our domain of investigation). Porosity is consistently higher than water content, reflecting the fact that the medium is not fully saturated.
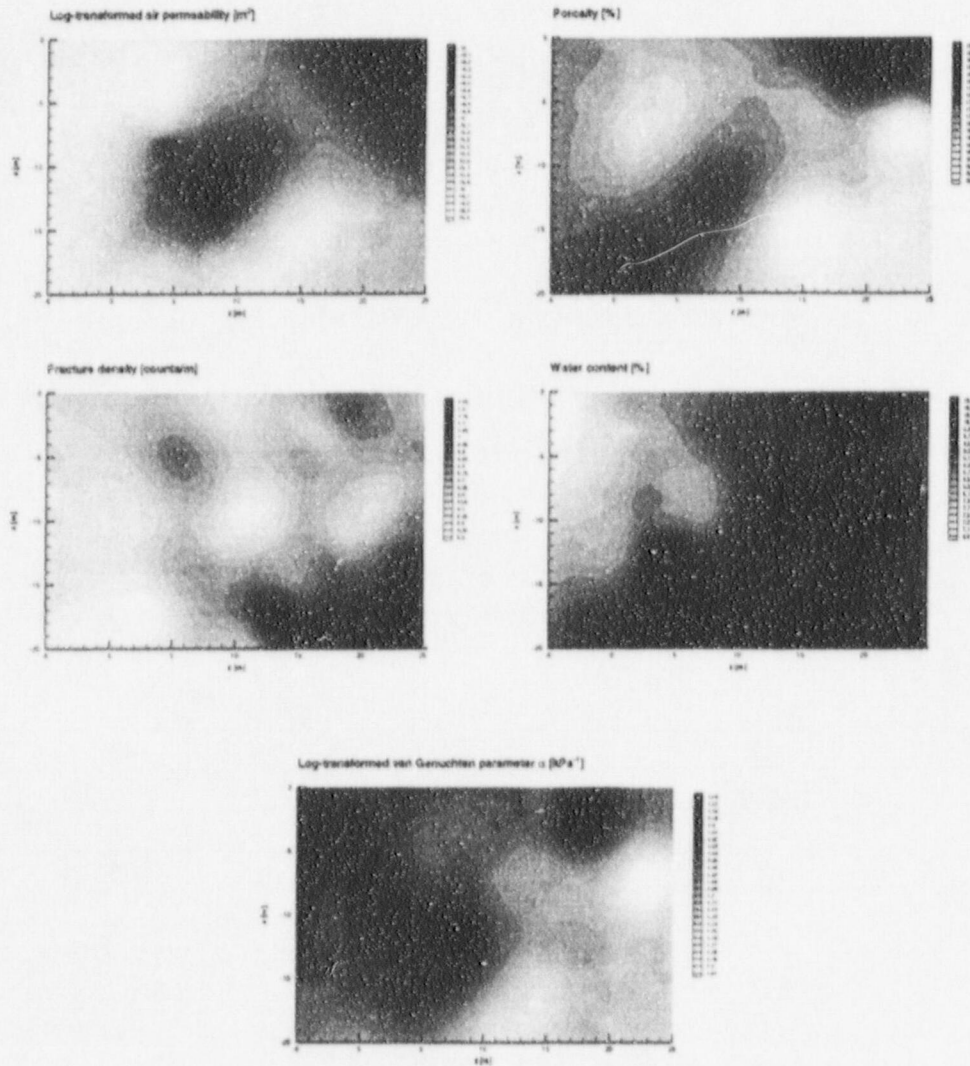
Figure 1.17: Kriged estimates of various parameters at $y = 7\ m$.

Figure 1.8 also shows sample variograms for log porosity and the van Genuchten α parameter, together with their best fit exponential models (without drift). No drift is indicated by the data in either case. The corresponding model parameters are listed in Tables 1.12 and 1.13, respectively. Three models are considered in these tables: exponential, exponential with nugget (white noise at zero lag), and spherical. The second model yields the best fit for both log porosity and log α, yet is not always favored as best by model discrimination criteria. This is due to the fact that it contains three parameters while the other two models contain only two. In general, the exponential model appears to be favored over the spherical model.

Table 1.12: Discrimination Among Geostatistical Models of Log Porosity (after Chen *et al.*, 1997).

Variogram Model	Exponential	Exponential With Nugget	Spherical
NLL	-170.740	-178.84	-175.456
Number of Parameters	2	3	2
Nugget	0.0	1.013×10^{-4}	0.0
Variance	0.00315	0.00294	0.00305
Integral scale (Range for Spherical mode)	3.01	3.011	5.51
AIC (Rank)	-174.740 (1)	-172.849 (2)	-171.456 (3)
MAIC (Rank)	-169.432 (1)	-164.882 (3)	-166.148 (2)
HIC (Rank)	-172.513 (1)	-169.628 (2)	-169.303 (3)
KIC (Rank)	-158.734 (1)	-145.775 (3)	-153.703 (2)

Table 1.13: Discrimination Among Geostatistical Models of Log α (after Chen *et al.*, 1997).

Variogram Model	Exponential	Exponential With Nugget	Spherical
NLL	61.471	56.679	67.965
Number of Parameters	2	3	2
Nugget	0.0	0.0104	0.0
Variance	0.0223	0.0122	0.0235
Integral scale (Range for Spherical mode)	2.253	5.5402	5.133
AIC (Rank)	65.471 (2)	62.679 (1)	71.965 (3)
MAIC (Rank)	70.775 (1)	70.642 (2)	77.265 (3)
HIC (Rank)	67.613 (2)	65.898 (1)	74.111 (3)
KIC (Rank)	77.634 (1)	79.065 (2)	87.050 (3)

Another omni-directional sample variogram in Figure 1.8 concerns fracture density in counts per meter. The corresponding best-fit exponential model (without drift) has a variance 0.69 and an integral scale of 2.5 *m* (Chen *et al.*, 1997).

Kriged estimates of hydrogeologic variables are smooth relative to their random counterparts. To generate less smooth and more realistic images that honor the available data, we have used GCOSIM3D, a sequential Gaussian conditional simulation code developed for three-dimensional data by Gómez-Hernández and Cassiraga (1994). The code is applied to log permeability (conditioned on the combined set of 1-*m* and 3-*m* data), fracture density, log porosity, water content, and log α data on the assumption that each of these variables is Gaussian. Indeed, all but the log porosity data have passed the Kolmogorof-Smirnoff test of Gaussianity at the 95% confidence level. Figure 1.18 shows conditionally simulated images of log air permeability, fracture density, porosity, water content, and log-transformed van Genuchten α in a vertical plane corresponding to $y = 7$ *m*. These images are clearly much less smooth than are their kriged counterparts in Figure 1.17.
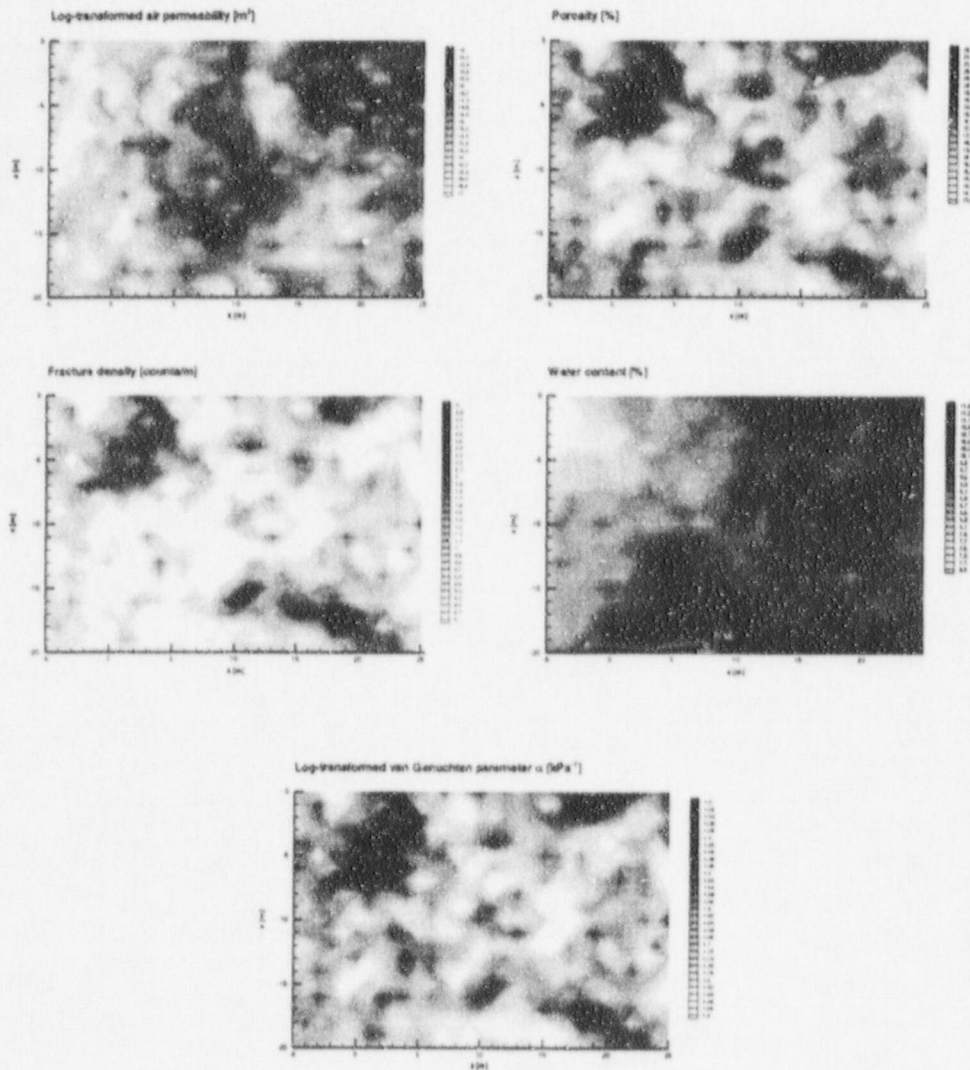
Figure 1.18: Conditional sequential Gaussian simulations of various parameters at $y = 7$ m.

We see clearly that all the above data are amenable to continuum geostatistical analysis and exhibit distinct spatial correlation structures. This suggests that the data can be viewed as samples from a random field, or stochastic continuum, as proposed over a decade ago by Neuman (1987) and affirmed more recently by Tsang *et al.* (1996). This is so despite the fact that the rock is fractured and therefore mechanically discontinuous. Our finding may be contrary to geologic intuition, but it is supported strongly by similar findings in many other fractured rock terrains including crystalline rocks at Oracle, Arizona; Stripa, Sweden; and Fanay-Augeres, France. It strongly supports the application of continuum flow and transport theories and models to fractured porous tuffs on scales of a meter or more.

1.3 TRANSIENT ANALYSIS OF SINGLE-HOLE PNEUMATIC INJECTION TESTS

In this final report to the NRC on pneumatic tests at the ALRS, we present interpretations of transient pressure data from the single-hole air injection tests previously conducted at the site by Guzman et al. (1994, 1996) and Guzman and Neuman (1996). Our interpretations are based on type-curves derived analytically for single-phase gas flow by linearizing the otherwise nonlinear partial differential equations, which govern such flow in uniform, isotropic porous continua. The type-curves correspond to three different flow geometries: three-dimensional flow with spherical symmetry, two-dimensional flow with radial symmetry, and flow in a continuum with an embedded high-permeability planar feature (a major fracture). Included in the type-curves are effects of gas storage in the injection interval (known as borehole storage effect) and reduced or enhanced permeability in the immediate vicinity of this interval (known as positive or negative skin effects). Our test interpretation relies not only on standard type-curves but also on type-curves of pressure derivative versus the logarithm of time. Such pressure derivative curves have become popular in recent years because they accentuate phenomena which might otherwise be missed, help diagnose the prevailing flow regime, and aid in constraining the calculation of corresponding flow parameters. A numerical inverse analysis of some of the single-hole tests is also given.

Our transient analyses of single-hole pneumatic tests yield information about air permeability, air-filled porosity, skin factor and dimensionality of the flow regime on a nominal scale of 1 m in the immediate vicinity of each test interval. We show that transient air permeabilities agree well with previously determined steady state values.

1.4 CROSS-HOLE PNEUMATIC INJECTION TESTS

We also conducted at the ALRS cross-hole air interference tests, which span the entire volume of fractured rock previously subjected to single-hole testing, and beyond. Their purpose was to a) directly characterize the pneumatic properties of the rock on a site-wide scale; b) determine the spatial extent and connectivity of fractures and/or high-permeability flow channels across the site; and c) compare the results with corresponding information that one might deduce from smaller-scale (laboratory and single-hole) tests. A total of forty-four cross-hole tests of diverse types (constant injection rate, step injection rates, instantaneous injection rate) have been conducted between various boreholes and borehole intervals at the site. Several tests were conducted without inflating the packers in monitoring holes in order to ascertain the effect that such open holes may have on pressure response in the injection test interval, i.e., on single-hole pneumatic injection tests. Additional single-hole and cross-hole tests were conducted to investigate the effects of: 1) drierite (calcium sulfate which acts as a drying agent) on humidity in the injection air stream; 2) barometric pressure fluctuations on air pressure in packed-off monitoring intervals under ambient conditions; 3) air injection while measuring changes in neutron counts in the rock surrounding the injection interval; and 4) variations in injection rate on pressure in the injection interval. To design our cross-

hole tests, we relied heavily on information about fracture locations and medium properties derived from core, borehole televiewer, and single-hole air injection test data.

A complete list of all cross-hole tests conducted by us at the ALRS is included in Table 5.1. In most of these tests, air was injected at a constant mass flow rate into a relatively short borehole interval of length $1 - 2$ m while monitoring a) air pressure and temperature in the injection interval; b) barometric pressure, air temperature and relative humidity at the surface; and c) air pressure and temperature in 13 short $(0.5 - 2$ $m)$ and 24 longer $(4 - 20$ $m)$ intervals within the injection and surrounding boreholes. Only one of these tests, labeled PP4, was fully analyzed to date. During this test, which we describe in detail, pressure responses were detected in 12 of the 13 short monitoring intervals and 20 of the 24 longer intervals.

We use two methods to analyze the PP4 cross-hole test results: 1) a graphical matching procedure of data against newly-developed type-curves of dimensionless pressure and pressure squared versus dimensionless time, and of corresponding pressure derivatives with respect to log time, and 2) an automatic parameter estimation method based on a three-dimensional finite volume code (FEHM), coupled with an inverse code (PEST). The type-curve approach treats short and longer borehole intervals as either points or lines, depending on distance between injection and monitoring intervals, while accounting indirectly for storage effects in monitoring intervals due to the compressibility of air. The finite volume code allows representing borehole geometry and storage more realistically, and directly, by treating each borehole as a high-permeability cylinder having finite length and radius. Analyses of pressure data from individual monitoring intervals by the two methods, under the assumption that the rock acts as a uniform and isotropic fractured porous continuum, yield comparable results. These results include information about pneumatic connections between the injection and monitoring intervals, corresponding directional air permeabilities, and air-filled porosities, all of which are found to vary considerably from one monitoring interval to another on a scale of $10 - 20$ m. Together with the results of earlier site investigations, our single- and cross-hole test analyses provide important new insight into the phenomenology of air flow through unsaturated fractured rocks at the ALRS, and about the spatial variability and scale-dependence of corresponding pneumatic parameters such as permeability, connectivity and air-filled porosity.

1.5 SCOPE OF THE REPORT

In Chapter 2 of the report we present a brief introduction to the theory of gasflow in porous media with emphasis on the case where water is relatively immobile. This theory forms the basis for all analytical and numerical methods employed by us to interpret single-hole and cross-hole pneumatic injection tests at the ALRS. Analytical formulae and corresponding type curves for the interpretation of such tests are presented in Chapter 3. Chapter 4 describes our type-curve interpretation of transient single-hole test results and their comparison with corresponding steady state test interpretations. In Chapter 5 we describe our cross-hole pneumatic interference tests at the site and interpret one of them by means of type-curves. The same cross-hole test is interpreted numerically by means of an automated inverse procedure in Chapter 6, which also includes numerical

inverse interpretations of some single-hole tests. The report ends with a comprehensive list of conclusions in Chapter 7.

2. AIRFLOW IN POROUS AND FRACTURED MEI A

2.1 THEORY OF GASFLOW IN POROUS MEDIA

The equations that describe airflow in partially saturated porous media are nonlinear due to the compressible nature of air, its capillary interaction with water, and non-Darcian behavior at high Reynolds numbers. A complete description of air-water interaction requires two systems of coupled partial differential equations, one for each phase. The resulting two-phase flow equations can then be solved by numerical methods of the kind developed by Mendoza and Frind (1990), Pruess (1991) or Zyvoloski *et al.* (1988, 1996, 1997). In special cases it may be possible to solve simplified versions of these equations analytically. We are particularly interested in the use of analytically derived type-curve methods for the interpretation of single-hole and cross-hole pneumatic test results. The development of corresponding analytical formulae requires that two-phase flow is approximated as single-phase gas flow and that water is treated as immobile. The resulting single-phase gas flow equations must additionally be linearized to allow solving them either in terms of pressure, as is customary for liquids, or in terms of pressure-squared or pseudopressure, as is more common for gases. We describe this process of simplification and linearization in the following paragraphs.

2.1.1 Two-Phase and Single-Phase Representations

Consider the flow of two homogenous immiscible fluids, a liquid and a gas, in a rigid porous medium under isothermal conditions. In the absence of mass transfer between the fluid phases, the liquid and gas mass conservation equations take the forms

$$-\nabla \cdot (\rho_l \mathbf{q}_l) = \phi \frac{\partial (S_l \rho_l)}{\partial t}$$

$$-\nabla \cdot (\rho_a \mathbf{q}_a) = \phi \frac{\partial (S_a \rho_a)}{\partial t} \tag{2.1-1}$$

where the subscripts l and g refer to liquid and gas, respectively; ρ is mass density $[ML^{-3}]$; $\mathbf{q}$ is flux $[LT^{-1}]$; ϕ is porosity $[L^0]$; S is fluid saturation $[L^0]$; t is time $[T]$; $\nabla \cdot$ is the divergence operator $[L^{-1}]$; and the dimensions of each variable are specified in terms of mass $[M]$, length $[L]$ and time $[T]$.

It is common to assume in practice that Darcy's law applies to both liquids and gases. In the case of gases, Darcy's law may not apply when Knudsen diffusion or slip flow (the so-called Klinkenberg effect) are important. Both of these phenomena are discussed briefly in Appendix B. Laboratory experiments by Alzaydi *et al.* (1978) have shown that air flux through a column of Ottawa sand is linear in the applied pressure gradient (*i.e.*, Darcian) except at early time following the start of each experiment. They found the same to be true for kaolinite clay, except that here the time required to establish a Darcy regime was longer. As mentioned in Section 1.2.3 of the Introduction, the steady state interpretation of multistep single-hole pneumatic injection tests at the ALRS have revealed inertial (nonlinear, non-Darcian) behavior of airflow in a few test intervals

intersected by highly permeable fractures. In most other test intervals, the flow appeared to be multiphase Darcian. We therefore adopt the following standard forms of Darcy's law for liquid and gas, respectively,

$$\mathbf{q}_l = -\frac{\rho_l g}{\mu_l} k_l \nabla h_l$$

$$\mathbf{q}_a = -\frac{k_a}{\mu_a} \nabla p_a \qquad (2.1\text{-}2)$$

where g is the gravitational constant $[LT^2]$; μ_a is dynamic viscosity $[ML^{-1}T^{-1}]$; k is intrinsic permeability $[L^2]$ for both air and water; ∇ is the gradient operator $[L^{-1}]$; h_l is hydraulic head $[L]$ defined as

$$h_l = \frac{p_l}{\rho_l g} + z \qquad (2.1\text{-}3)$$

p is pressure $[ML^{-1}T^2]$; z is elevation about an arbitrary datum $[L]$; and the effect of gravity on gas flow is neglected. Substituting (2.1-2) into (2.1-1) yields the liquid flow and air-flow equations,

$$\nabla \cdot \left(\rho_l K_l \nabla h_l \right) = \phi \frac{\partial (S_l \rho_l)}{\partial t}$$

$$\nabla \cdot \left(\rho_a \frac{k_a}{\mu_a} \nabla p_a \right) = \phi \frac{\partial (S_a \rho_a)}{\partial t} \qquad (2.1\text{-}4)$$

respectively. The two equations are coupled via the relationships

$$S_l + S_a = 1 \qquad (2.1\text{-}5)$$

$$p_c = p_a - p_l \qquad (2.1\text{-}6)$$

where p_c is capillary pressure. To solve them requires the additional specification of appropriate equations of state (functional relationships between fluid properties and pressure, and between permeability, capillary pressure and saturation, for each phase) and forcing functions (source terms, initial and boundary conditions). As the equations of state are generally nonlinear, so are the above flow equations.

For purposes of analyzing gas flow around wells, it is common to treat the liquid phase as being immobile. Then $S_a = 1$ and the gas flow equation simplifies to

$$\nabla \cdot \left(\rho \frac{k}{\mu} \nabla p \right) = \phi \frac{\partial \rho}{\partial t} \qquad (2.1\text{-}7)$$

where the subscript a has been omitted as all equations now refer to a single gas phase. The corresponding equation of state is commonly written as (Burcik, 1957)

$$pV = Z(p,T)nRT \qquad (2.1\text{-}8)$$

where V is volume $[L^3]$; $Z(p,T)$ is a dimensionless compressibility factor; n is mass in moles $[mol]$; and R is the universal gas constant $[Joules\ ^{o}K^{-1}mol^{-1}]$. Upon rearranging eq. (2.1-8) to read

$$Z(p,T) = \frac{pV}{nRT} = \frac{pV_s}{RT} \qquad (2.1\text{-}9)$$

where $V_s = V/n$ is specific volume $[L^3M^{-1}]$, the dependence of Z on p and T is made explicit. One can thus readily calculate Z for any pressure, temperature and specific

volume. A sample calculation of Z for conditions typically found at the ALRS $\left(p = 200\,kPa, T = 300^\circ\,K\right)$ is included in Appendix A. Figure 2.1 shows corresponding variations of Z with pressure and temperature. The value of Z is seen to be 1 for a large range of pressures $\left(10^2 - 10^4\,kPa\right)$ and temperatures $\left(270 - 400\,^\circ K\right)$. During single-hole tests at the ALRS, pressures within the injection interval ranged between 80 kPa and 360 kPa (Table A.2) and temperatures between 288.10° K and 302.74° K (Table A.3). This allows us to treat air, for purposes of test analysis at the ALRS, as an ideal gas with $Z \cong 1$.
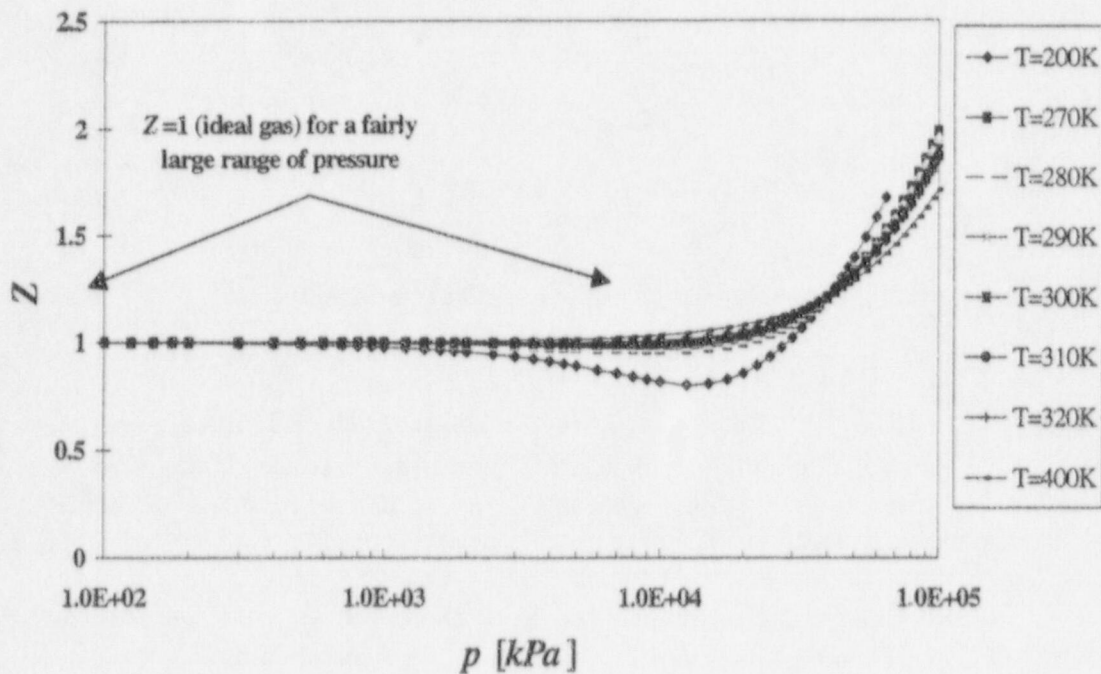
Figure 2.1: Variation of compressibility factor Z with pressure and temperature.
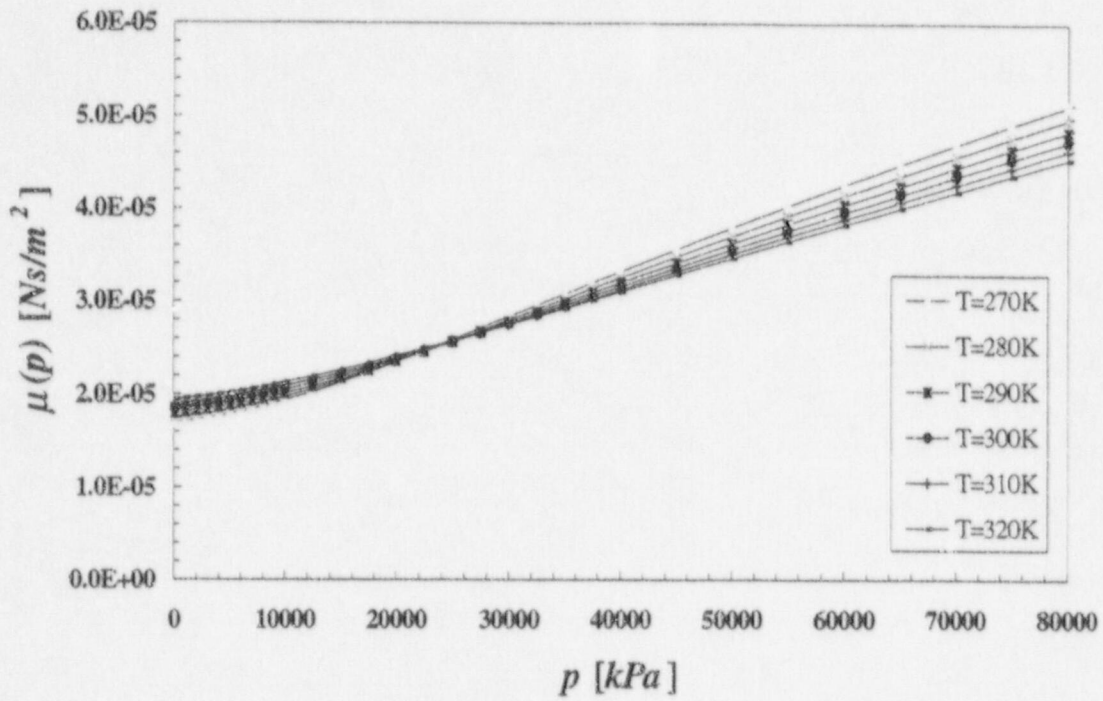
Figure 2.2: Variation of air viscosity μ with pressure and temperature.
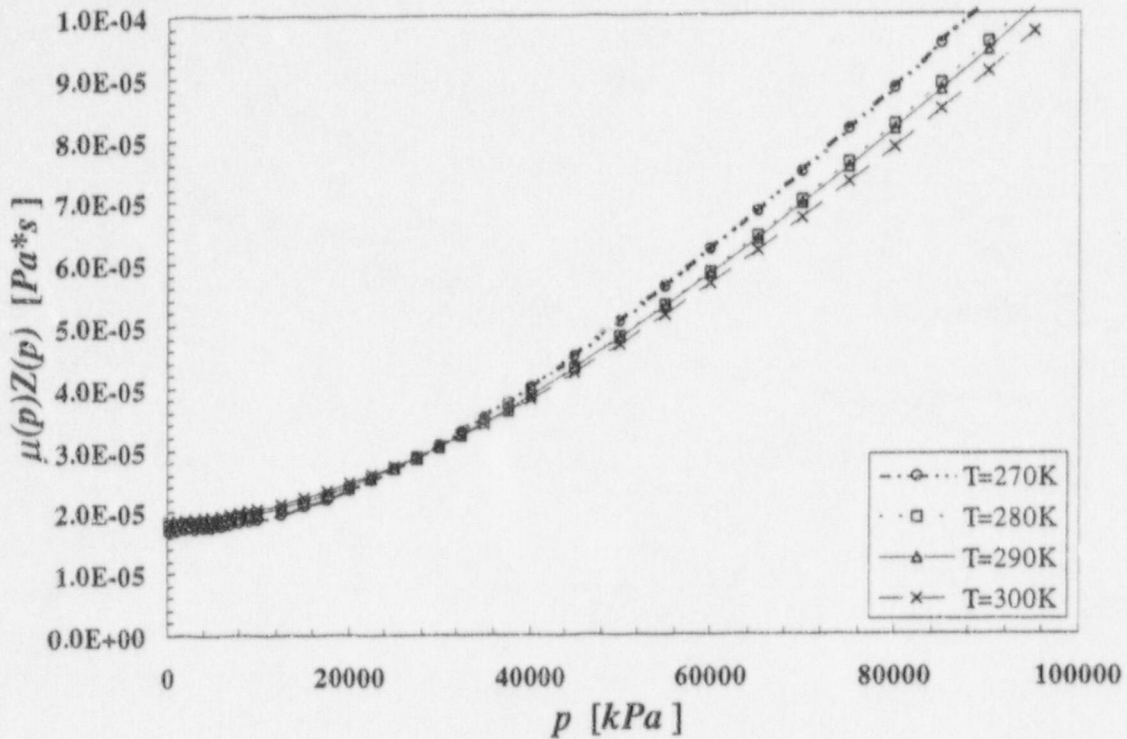
Figure 2.3: Variation of μZ with pressure and temperature.

Figure 2.2 shows the variation of air viscosity μ with pressure and temperature. Air viscosity is seen to increase slowly with pressure, and to increase with temperature at low pressures but decrease at higher pressures. Figure 2.3 has been included to show how the corresponding product μZ varies with pressure for a range of temperatures. The product is seen to remain constant (equal to $1.81 \times 10^{-5} Pa \cdot s$) for the range of pressures and temperatures encountered under field-testing conditions at the ALRS. Since Z is virtually constant under these conditions, so is μ (equal to $1.81 \times 10^{-5} Pa \cdot s$).

Upon considering isothermal conditions, and treating Z and μ as constants, one finds from eq. (2.1-8) that mass density is proportional to pressure. For purposes of solving the gas flow equation analytically, it is additionally common to treat k as a constant. This allows rewriting (2.1-7) as

$$\nabla \cdot (p \nabla p) = \frac{\phi \mu}{k} \frac{\partial p}{\partial t} \tag{2.1-10}$$

which can be rewritten as

$$\nabla^2 p^2 = \frac{2 \phi \mu}{k} \frac{\partial p}{\partial t} \tag{2.1-11}$$

or, alternatively, as

$$\nabla^2 p^2 = \frac{\phi \mu c}{k} \frac{\partial p^2}{\partial t} \tag{2.1-12}$$

where c is gas compressibility, defined as

$$c \equiv \frac{1}{\rho}\frac{\partial \rho}{\partial p} \cong \frac{1}{p} \tag{2.1-13}$$

In the more general case where μZ is not a constant, the equation in terms of p^2 includes an additional logarithmic term (Al-Hussainy et al., 1966; Raghavan, 1993; see derivation in Appendix C),

$$\nabla^2 p^2 - \frac{d \ln(\mu Z)}{dp^2}\nabla p^2 \cdot \nabla p^2 = \frac{\phi \mu c}{k}\frac{\partial p^2}{\partial t} \tag{2.1-14}$$

Yet another form of the gas flow equation can be obtained upon introducing the pseudopressure $w(p)$, defined as (Al-Hussainy et al., 1966; Raghavan, 1993)

$$w(p) = 2\int_{p_o}^{p}\frac{p}{\mu(p)Z(p)}dp \tag{2.1-15}$$

where $w(p)$ has dimensions $[ML^{-1}T^{-3}]$. This is akin to the well-known Kirchhoff transformation (Kirchhoff, 1894) and has, according to Raghavan, been used earlier by Carter (1962) in a slightly different form. For our purposes, the lower limit of zero on p represents barometric pressure. In the case where μZ is constant,

$$w(p) = \frac{2}{\mu Z}\int_{p_0}^{p}pdp = \frac{p^2 - p_0^2}{\mu Z} \tag{2.1-16}$$

where p_b is the barometric pressure. Figure 2-3 shows that, at high pressures, μZ varies more-or-less linearly with p. It then follows that (Gradshteyn and Ryzhik, 1994, p. 79, eq. 2.152),

$$w(p) = \int_0^p \frac{p}{a+bp}dp = \frac{p}{b} - \frac{a}{b^2}\left[\ln\left(\frac{a+bp}{a}\right)\right] \tag{2.1-17}$$

In general,

$$\frac{\partial w(p)}{\partial t} = \frac{dw(p)}{dp}\frac{\partial p}{\partial t} = \frac{2p}{\mu Z}\frac{\partial p}{\partial t}$$

$$\nabla w(p) = \frac{dw(p)}{dp}\nabla p = \frac{2p}{\mu Z}\nabla p \tag{2.1-18}$$

and so the gas flow equation in terms of pseudopressure takes on a quasilinear form,

$$\nabla^2 w = \frac{\phi \mu c}{k}\frac{\partial w}{\partial t} \tag{2.1-19}$$

2.1.2 Linearization of the Gas flow Equation

Under steady state, equations (2.1-10) and (2.1-11) are linear in p^2, and equation (2.1-19) is linear in w. Linearization of the transient p-based equation (2.1-10) requires that the leftmost p be set equal to a constant, $\overline{p}$ (typically some average pressure). The equation can then be rewritten as

$$\nabla^2 p \approx \frac{\phi\mu\bar{c}}{k}\frac{\partial p}{\partial t} \tag{2.1-20}$$

where, by virtue of (2.1-13), $\bar{c} = 1/\bar{p}$. This equation is similar to that typically used for liquids in the absence of gravity. Setting c in (2.1-10) or (2.1-19) to a constant, say $\bar{c} = 1/\bar{p}$, renders these equations linear in p^2 or w, respectively,

$$\nabla^2 p^2 \approx \frac{1}{\alpha}\frac{\partial p^2}{\partial t} \tag{2.1-21}$$

$$\nabla^2 w \approx \frac{1}{\alpha}\frac{\partial w}{\partial t} \tag{2.1-22}$$

where $\alpha = k/\mu S_G$ is pneumatic diffusivity in terms of a gas storage factor

$$S_G = \phi\bar{c} \approx \frac{\phi}{\bar{p}} \tag{2.1-23}$$

The latter differs from the specific storage factor commonly used in hydrology which, in our case, would be defined as $S_s = \rho g S_G$.

In Chapter 3 we modify a number of analytical type-curve expressions, derived by various authors for liquid flow under conditions similar in principle to those we encounter during single-hole and cross-hole pneumatic injection tests at the ALRS, in a manner which renders them applicable to gasflow. Among others, we recast these expressions in terms of pseudo-pressure, which by virtue of (2.1-16) is analogous to rewriting them in terms of p^2 when μZ is constant, as is the case at the ALRS. Our type-curve analyses of single-hole pneumatic air injection tests at the ALRS, described in Chapter 4, are conducted using both the p-based equation (2.1-20), and the p^2-based equation (2.1-22) with pseudopressure defined according to (2.1-16). As the two sets of results are consistent, we conduct our type-curve analysis of cross-hole tests, described in Chapter 5, using only the simpler p-based form.

3. TYPE CURVE MODELS FOR THE INTERPRETATION OF SINGLE-HOLE AND CROSS-HOLE TEST DATA

3.0 CONCEPTUALIZATION OF FLOW THROUGH FRACTURED ROCKS

For purposes of analyzing fluid flow and solute transport through fractured rocks on the field scale, it has become common to think of matrix blocks as forming a continuum, and of fractures as forming another, overlapping continuum (Barenblatt *et al.*, 1960; Warren and Root, 1963). If one of these overlapping entities dominates all relevant aspects of flow and transport, one treats the rock as a single matrix- or fracture-dominated continuum. Otherwise, one must allow for the possibility that fluids and solutes could migrate from one entity to the other under a pressure and/or concentration differential between the two. If such fluid and mass transfer *between* matrix and fractures is fast in comparison to flow and transport *through* the rock, one considers the two entities to be at equilibrium and treat the rock as an equivalent or effective (single) matrix-fracture continuum (Dykhuizen, 1990; Peters and Klavetter, 1988; Pruess *et al.*, 1990). In the absence of such equilibrium, it is common to adopt the dual porosity model (Bibby, 1981; Moench, 1984; Zimmerman *et al.*, 1993) in which the matrix acts as a nonconducting storage reservoir; the fractures form a conducting medium with negligible storage capacity; and the transfer of fluids (or solutes) between these two overlapping continua is proportional to the pressure (or concentration) differential between them at each point in space-time. A more general version of the latter is the dual permeability model (Duguid and Lee, 1977; Gerke and van Genuchten, 1993a,b) in which both the matrix and fracture continua conduct fluids and solutes; still another version is one that accounts for internal gradients of pressure (or concentration) within matrix blocks, referred to as interacting multiple continua by Pruess and Narasimhan (1985; see also Kazemi, 1969; Berkowitz *et al.*, 1988; and Birkhölzer *et al.*, 1993). Carrera *et al.* (1990) were able to successfully reproduce pumping tests in a fractured block of monzonitic gneiss by treating discrete fracture zones, and the rest of the fractured rock mass, as juxtaposed (nonoverlapping) fracture-dominated (single) continua.

The extent to which continuum (single, equivalent, dual, multiple, juxtaposed, deterministic or stochastic) concepts may or may not apply to fractured rocks has been the subject of intense research and debate for over two decades. In such rocks, flow and transport often take place preferentially through discrete fractures and channels. Some of these discontinuities can usually be identified and mapped in surface outcrops, boreholes, and subsurface openings. This has led to the belief on the part of some that it should be possible to delineate the geometry of the subsurface "plumbing system" through which most flow and advective transport take place. Several hydrologists consider it especially feasible to construct realistic models of fracture networks deterministically or stochastically. Typically, such networks consist of discrete polygonal or oval-shaped planes of finite size, embedded in an impermeable, or at times permeable, rock matrix. Each plane is assigned effective flow and transport properties, usually at random; in some single fracture studies, these properties are further treated as random fields defined at each point in the fracture plane. Fracture network models containing thousands of planes have been used to simulate flow and tracer migration at several experimental sites, most notably in crystalline rocks of the Site Characterization and Validation (SCV) complex at

the Stripa mine in Sweden (Dershowitz *et al.*, 1991; National Research Council, 1996) and the Fanay-Augeres mine in France (Cacas *et al.*, 1990).

The conceptual-theoretical framework behind the discrete fracture modeling approach was seen by Neuman (1987, 1988) as lacking firm experimental support. Neuman also questioned the practicality of the approach on the grounds that existing field techniques make it extremely difficult, if not impossible, to reconstruct with any reasonable degree of fidelity either the geometry of the subsurface plumbing system (which consists of porous blocks, fractures, and channels that are known to evolve dynamically along fracture planes and fracture intersections) or the flow and transport properties of its individual components. Indeed, Tsang and Neuman (1995) recently reached a similar conclusion based on extensive experience gained during the six-year international INTRAVAL project. The authors pointed out that several INTRAVAL field hydraulic and tracer experiments have proven equally amenable to analysis by discrete and continuum models, rendering the validation of either approach difficult. The best models appeared to be those that were neither too simplistic nor too complex. A recent summary of the international Stripa project (SKB, 1993) has concluded that while it has been possible to construct working fracture network models with thousands of discrete planes for the SCV site by calibrating them against observed hydraulic and tracer data, these models have not necessarily performed better than much simpler and more parsimonious continuum models (only very elementary continuum models were considered in this comparison; more sophisticated stochastic continuum models were not considered and could potentially perform much better). The idea of representing fractured rocks as stochastic continua, originally proposed by Neuman (1987), has been adopted by Tsang *et al.* (1996) in their recent analysis of flow and transport at the Aspo Island SKB Hard Rock laboratory in Sweden.

Most single-hole and cross-hole pneumatic test data at the ALRS have proven amenable to analysis by means of a single fracture-dominated continuum representation of the fractured-porous tuff at the site. This is in line with the more general conclusion by Neuman (1987, 1988) that flow and transport in many fractured rock environments is amenable to analysis by continuum models which account in sufficient detail for medium heterogeneity and anisotropy. Only when one can distinguish clearly between distinct hydrogeologic units or features such as layers, faults, fracture zones, or major individual fractures of low or high permeability, on scales not much smaller than the domain of interest, should one in our view attempt to model them discretely (delineate their geometry deterministically); one should then still consider treating the internal properties of each such discrete unit as random fields. Recent evidence that the latter idea often works can be found in the University of Arizona theses of Kostner (1993) and Ando (1995), and in the work of Guzman and Neuman (1996). The two theses demonstrate that hydraulic and tracer tests in saturated fractured granites at the Fanay-Augeres mine in France can be reproduced by means of continuum indicator geostatistics (Journel, 1989), and fracture-dominated single-continuum stochastic flow and transport models, with better accuracy than has been achieved previously with discrete fracture network models. Our Introduction demonstrates that small-scale, single-hole, steady state pneumatic permeability data from unsaturated fractured tuffs at the ALRS are likewise amenable to continuum geostatistical analysis, exhibiting both anisotropic and random fractal behaviors.

Most type-curve models currently available for the interpretation of single-hole and cross-hole fluid injection (or withdrawal) tests in fractured rocks fall into three broad categories: 1) those that treat the rock as a single porous continuum representing the fracture network; 2) those that treat the rock as two overlapping continua of the dual porosity type; and 3) those that allow an additional major fracture to intersect the injection (or withdrawal) test interval at various angles. The prevailing interpretation of dual continua is that one represents the fracture network and the other embedded blocks of rock matrix. We take the broader view that multiple (including dual) continua may represent fractures on a multiplicity of scales, not necessarily fractures and matrix. When a dominant fracture is present in a type-curve model, it is usually pictured as a high-permeability slab of finite or infinitesimal thickness. To allow developing analytical solutions in support of type-curve models, the continua are taken to be uniform and either isotropic or anisotropic. The test interval is taken to intersect a dominant fracture at its center. Either flow across the walls of such a fracture, or incremental pressure within the fracture, are taken to be uniform in most models. Flow is usually taken to be transient with radial or spherical symmetry, which may transition into near-uniform flow as one approaches a major fracture that intersects the test interval. Some models account for borehole storage and skin effects in the injection (or withdrawal) interval.

In this report, we interpret transient data from single-hole pneumatic injection tests at the ALRS by means of modified single-continuum type-curve models developed for spherical flow by Joseph and Koederitz (1985); for radial flow by Agarwal et al. (1970); for a single horizontal fracture by Gringarten and Ramey (1974); and for a single vertical fracture by Gringarten *et al.* (1974). We interpret cross-hole injection tests by means of a type-curve model developed for spherical flow in an anisotropic continuum by Hsieh and Neuman (1985a). Our modifications consist of recasting the first three models in terms of pseudopressure; developing corresponding expressions and type-curves in terms of (pseudo)pressure-derivatives; and adding compressible storage in monitoring wells to the model of Hsieh and Neuman. A brief description of these modified models is given in the following sections.

3.1 SPHERICAL GAS FLOW MODEL

Single-hole pneumatic pressure data tend to stabilize with time in most injection intervals at the ALRS. As recharge boundaries are not likely to be a major cause of such stabilization at the site, we consider instead a model in which air is injected at a constant mass rate $Q\,[L^3 T^{-1}]$ from a spherical source of (equivalent or pseudo) radius $r_{sw}\,[L]$ into a uniform, isotropic continuum of infinite extent. This results in a spherically symmetric flow regime governed by (2.1-22) and subject to the following initial and boundary conditions (Appendix D)

$$w(r,0) = 0; \qquad r \geq r_{sw} \qquad (3.1\text{-}1)$$

$$\lim_{r \to \infty} w(r,t) = 0; \qquad t > 0 \qquad (3.1\text{-}2)$$

$$C_w \frac{\mu T_{sc}}{2 Q_{sc} T p_{sc}} \frac{p_{in}}{p_w} \frac{dw_w}{dt} - 2\pi k \frac{T_{sc}}{Q_{sc} T p_{sc}} \left(r^2 \frac{\partial w}{\partial r} \right)_{r_{sw}} = 1 \qquad (3.1\text{-}3)$$

$$w_{wf} = w_w + \frac{Q_{sc}}{2\pi k r_{sw}} \left(\frac{T p_{sc}}{T_{sc}} \right) s \qquad (3.1\text{-}4)$$

where most variables have been defined in Chapter 2; p_{in} is pressure in the injection line; C_w is storage coefficient $[L^4 T^2 M^{-1}]$ of the injection interval w; w_{wf} is pseudopressure in the rock just outside the skin; s is a dimensionless skin factor; the subscript sc denotes standard conditions; and (Guzman and Neuman, 1994, eq. (C.7), p. C-2)

$$Q = \frac{Q_{sc} T p_{sc} Z}{T_{sc} p} \qquad (3.1\text{-}5)$$

Eq. (3.1-3) represents mass balance in the injection interval under the assumption that gas density within it is the same as in the injection system and the rock. Eq. (3.1-4) relates pressure in the injection interval to that in the rock by means of an additive skin factor. The latter represents an infinitesimal skin or membrane that resists flow but does not store fluid so that flow across it takes place at a steady rate. Reduced permeability around the injection interval is represented by a positive skin factor, enhanced permeability by a negative skin. The above formulation is analogous to that of Joseph and Koederitz (1985) who additionally write

$$r_{sw} = \frac{b}{2 \ln \left(b/r_w \right)} \qquad (3.1\text{-}6)$$

where b is the length of the actual cylindrical injection interval; this follows from equating the spherical source volume to that of a prolate-spheroid that fits snugly into the cylindrical interval. Upon defining dimensionless pseudopressure, time, radius and borehole storage coefficient as

$$w_D = \frac{2\pi k r_{sw}}{Q_{sc}} \left(\frac{T_{sc}}{T p_{sc}} \right) w \qquad (3.1\text{-}7)$$

$$t_D = \frac{k r_{sw}^2 \bar{p} t}{\phi \mu r^4}; \qquad r \geq r_{sw} \qquad (3.1\text{-}8)$$

$$r_D = 1 - \frac{r_{sw}}{r}; \qquad r \geq r_{sw} \qquad (3.1\text{-}9)$$

$$C_D = \frac{C_w \bar{p}}{4\pi \phi r_{sw}^3} = \frac{1}{3\phi} \qquad (3.1\text{-}10)$$

respectively, it is possible to recast the problem in dimensionless form. Here, we have defined the storage coefficient of the injection interval to be $C_w = \frac{4}{3} \pi r_{sw}^3 \bar{p}$. The corresponding solution has the same form as that given by Joseph and Koederitz (1985),

$$w_{wD} = L^{-1} \left\{ \frac{\left(1 - e^{-2\sqrt{\lambda}}\right) + s\left(1 + e^{-2\sqrt{\lambda}}\right)\sqrt{\lambda}}{\lambda^{3/2} \left\{ \sqrt{\lambda} C_D \left[\left(1 - e^{-2\sqrt{\lambda}}\right) + s\sqrt{\lambda}\left(1 + e^{-2\sqrt{\lambda}}\right) \right] + \left(1 + e^{-2\sqrt{\lambda}}\right) \right\}} \right\} \qquad (3.1\text{-}11)$$

where w_{wD} is dimensionless pseudopressure in the well, L^{-1} is inverse Laplace transform and λ is the corresponding transform parameter. We invert the Laplace transform numerically using an algorithm due to DeHoog et al. (1982).

Figure 3.1 is a logarithmic plot of w_{wD} versus t_D/C_D for various values of C_D when s = 0. The early unit slope of the type curve is a diagnostic feature of borehole storage. The stabilization of w_{wD} at late time is diagnostic of three-dimensional (in our case spherical) flow. Type curves corresponding to $C_D \geq 2.5 \times 10^2$ are difficult to distinguish from each other. Under test conditions at the ALRS, this means that one cannot use type-curves based on the spherical model to determine porosity from single-hole test data.

The dimensionless time derivative of pseudo-pressure is obtained directly from (3.1-11) in the form

$$\frac{\partial w_{wD}}{\partial \ln t_D} = L^{-1}\left\{ \frac{\left(1-e^{-2\sqrt{\lambda}}\right)+s\left(1+e^{-2\sqrt{\lambda}}\right)\sqrt{\lambda}}{\lambda^{\frac{1}{2}}\left\{\sqrt{\lambda}C_D\left[\left(1-e^{-2\sqrt{\lambda}}\right)+s\sqrt{\lambda}\left(1+e^{-2\sqrt{\lambda}}\right)\right]+\left(1+e^{-2\sqrt{\lambda}}\right)\right\}} \right\} \tag{3.1-12}$$

Figure 3.2 shows type curves of w_{wD} (solid) and $\partial w_{wD}/\partial \ln t_D$ (dashed) versus t_D for various values of C_D and s. The derivative is seen to climb to a peak and then to diminish asymptotically toward zero at a rapid rate.

3.2 RADIAL GAS FLOW MODEL

Some single-hole pneumatic test data from the ALRS appear to fit a radial flow model during part or the entire test. The model we use has been modified after Agarwal et al. (1970; see also Raghavan, 1993, p. 68, eq. 4.105) in the manner mentioned earlier. Their model is in turn a modification of an earlier solution due to Papadopulos and Cooper (1967) by adding to it the effect of a skin. Airflow is governed by eq. (2.1-22) subject to

$$w(r,0) = 0 \tag{3.2-1}$$

$$\lim_{r \to \infty} w(r,t) = 0 \tag{3.2-2}$$

$$C_{wf}\frac{\mu T_{sc}}{2Q_{sc}Tp_{sc}}\left(\frac{p}{p_{wf}}\right)\left[\frac{dw_{wf}}{dt}\right] - \pi k b \frac{T_{sc}}{Q_{sc}Tp_{sc}}\left(r\frac{\partial w}{\partial r}\right)_{r_w} = 1 \tag{3.2-3}$$

$$w_{wf} = w_w + \frac{Q_{sc}}{\pi k b r_w}\left(\frac{Tp_{sc}}{T_{sc}}\right)s \tag{3.2-4}$$

The dimensionless pseudo-pressure and its derivative are given by

$$w_{wD} = L^{-1}\left\langle \frac{K_0(\lambda)+s\sqrt{\lambda}K_1\left(\sqrt{\lambda}\right)}{\lambda\left\{\sqrt{\lambda}K_1\left(\sqrt{\lambda}\right)+\lambda C_D\left[K_0\left(\sqrt{\lambda}\right)+s\sqrt{\lambda}K_1\left(\sqrt{\lambda}\right)\right]\right\}} \right\rangle \tag{3.2-5}$$

$$\frac{\partial w_{wD}}{\partial \ln t_D} = L^{-1}\left\langle \frac{K_0(\lambda) + s\sqrt{\lambda}\,K_1\!\left(\sqrt{\lambda}\right)}{\left\{\sqrt{\lambda}\,K_1\!\left(\sqrt{\lambda}\right) + \lambda C_D\!\left[K_0\!\left(\sqrt{\lambda}\right) + s\sqrt{\lambda}\,K_1\!\left(\sqrt{\lambda}\right)\right]\right\}}\right\rangle \tag{3.2-6}$$

which, in this case, can be inverted analytically to read

$$w_{wD} = \frac{4}{\pi^2}\int_0^\infty \frac{1 - \exp\!\left(-v^2 t_D\right)}{v^3\left\{\left[vC_D J_0(v) - \left(1 - C_D s v^2\right)J_1(v)\right]^2 + \left[vC_D Y_0(v) - \left(1 - C_D s v^2\right)Y_1(v)\right]^2\right\}}\,dv \tag{3.2-7}$$

$$\frac{\partial w_{wD}}{\partial \ln t_D} = \frac{4}{\pi^2}\int_0^\infty \frac{t_D\left(1 - \exp\!\left(-v^2 t_D\right)\right)}{v^3\left\{\left[vC_D J_0(v) - \left(1 - C_D s v^2\right)J_1(v)\right]^2 + \left[vC_D Y_0(v) - \left(1 - C_D s v^2\right)Y_1(v)\right]^2\right\}}\,dv \tag{3.2-8}$$

where now

$$w_{wD} = \frac{\pi k b}{Q_{sc}}\left(\frac{T_{sc}}{Tp_{sc}}\right)w \tag{3.2-9}$$

$$t_D = \frac{kt\bar{p}}{\phi\mu r_w^2} \tag{3.2-10}$$

$$r_D = \frac{r}{r_w}; \qquad r \geq r_w \tag{3.2-11}$$

$$C_D = \frac{C_w \bar{p}}{2\pi b r_w^2 \phi} = \frac{1}{2\phi} \tag{3.2-12}$$

where $C_w = \pi b r_w^2 \bar{p}$. The solution is plotted on logarithmic paper versus t_D/C_D for $s = 0$ in Figure 3.3. At early time, w_{wD} (solid) exhibits a unit slope due to borehole storage. Asymptotically, w_{wD} becomes proportional to $\ln t_D$, and its derivative (dashed) with respect to $\ln t_D$ becomes a constant. This makes radial flow easy to distinguish from spherical flow. Both the pseudo-pressure and derivative type curves are sufficiently sensitive to C_D to allow extracting porosity values from time-pressure data that match the radial type curves.
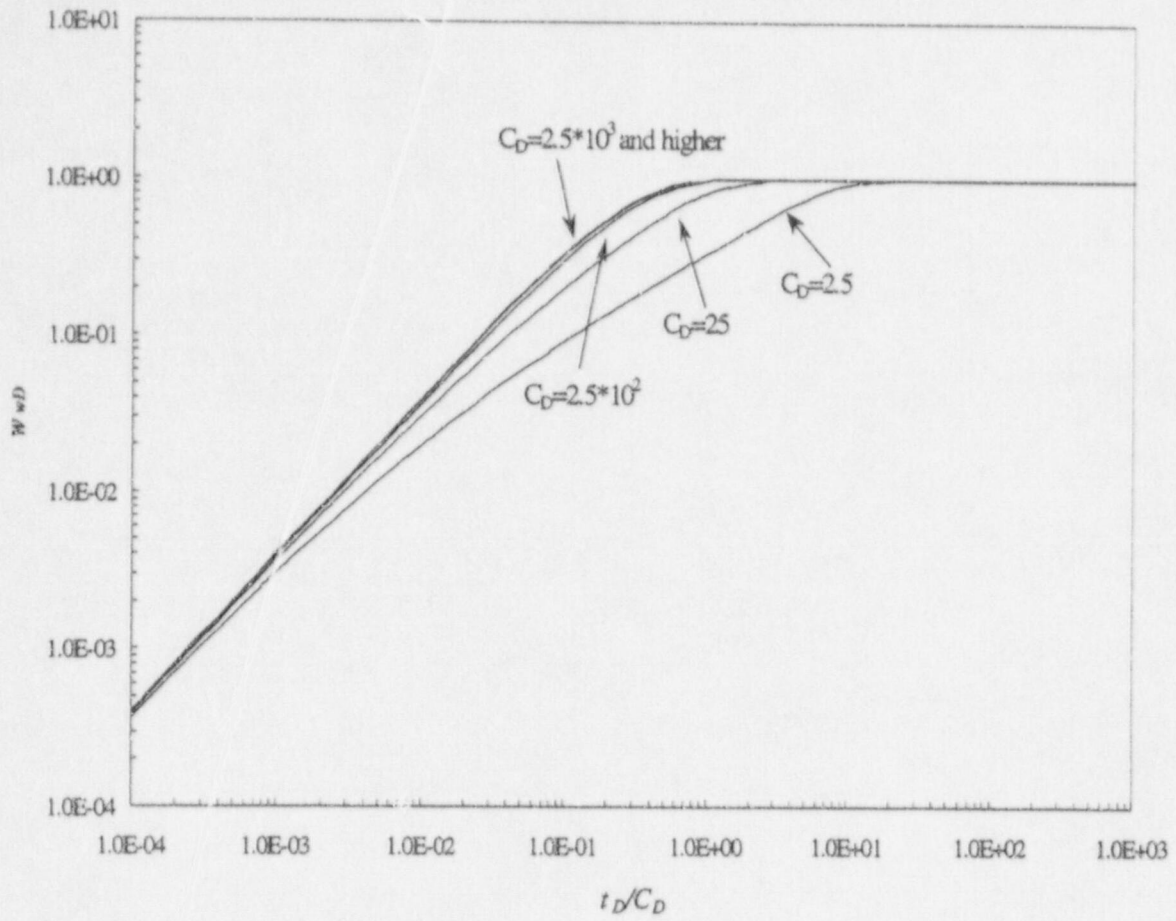
Figure 3.1: Type curves of dimensionless pseudopressure in injection interval versus normalized dimensionless time for various C_D and $s = 0$ under spherical flow.
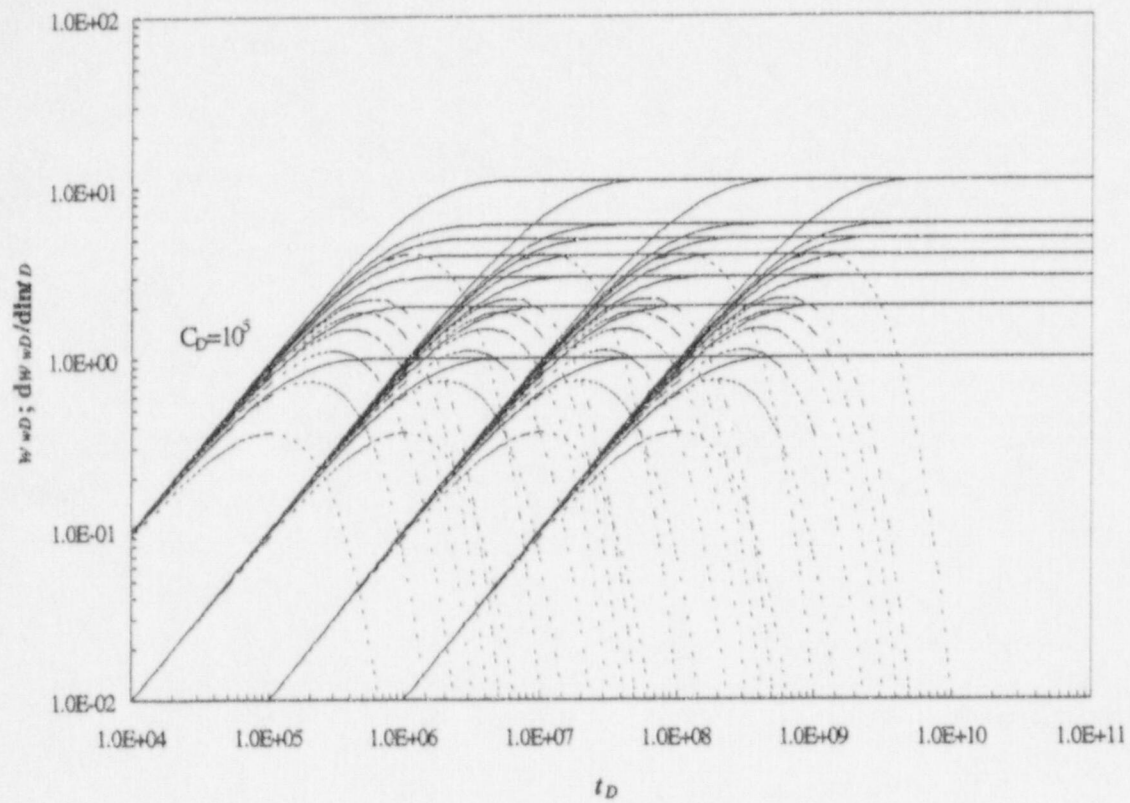
Figure 3.2: Type curves of dimensionless pseudopressure and its derivative in injection interval versus dimensionless time for various C_D and s under spherical flow.
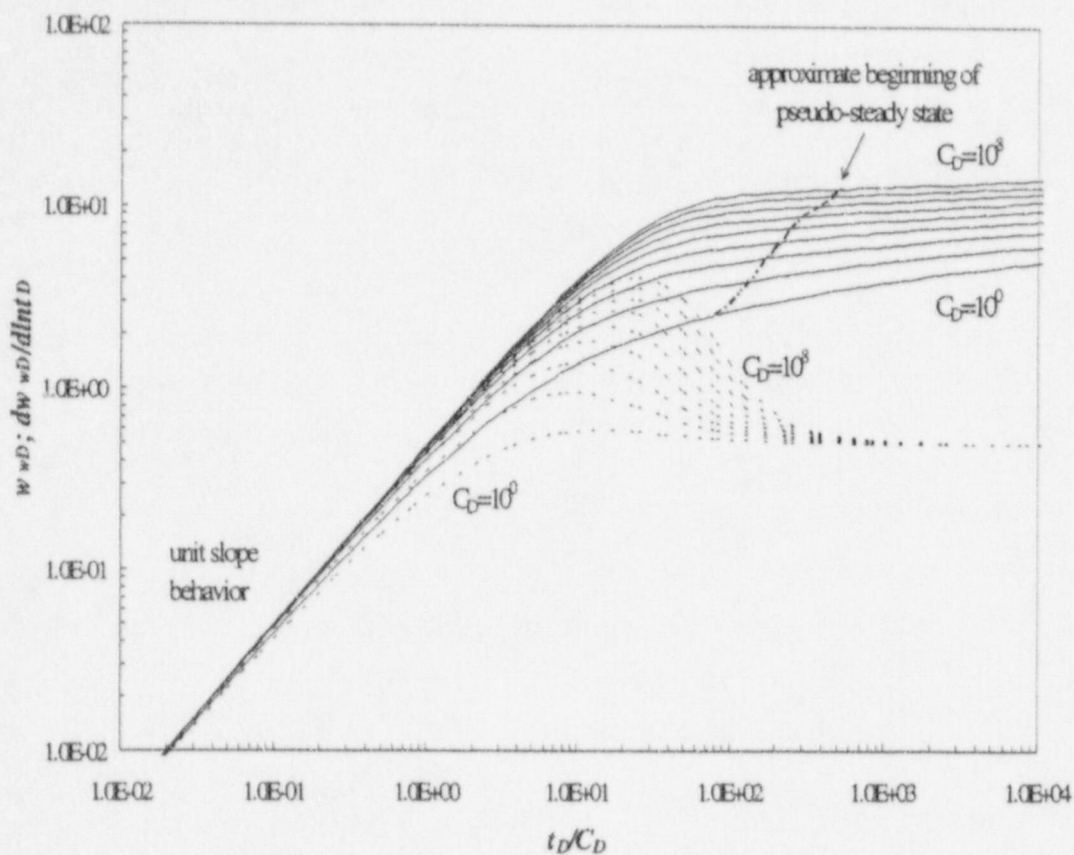
Figure 3.3: Type curves of dimensionless pseudopressure and its derivative in injection interval versus dimensionless time for various C_D under radial flow.

3.3 UNIFORM FLUX HORIZONTAL AND VERTICAL FRACTURES

Some of the early single-hole pneumatic time-pressure data from the ALRS delineate a half-slope on logarithmic paper. Such behavior is typically observed in boreholes that are intersected by a high-permeability planar feature like a major fracture.

Gringarten and Ramey (1974) developed a uniform flux model for a horizontal fracture in an infinite, uniform confined aquifer. In this model, flow rate across the fracture is uniform and equal to the rate of injection or withdrawal. The fracture has finite thickness h_f, is disk-shaped with radius r_f, centered about the well, and lies at an elevation z_f above the bottom of the aquifer (Figure 3.4). The presence of the fracture

NUREG/CR-5559

renders the aquifer anisotropic with horizontal permeability k_r greater than the vertical permeability k_z. Our modified version of this solution is

$$w_D = \int_0^{t_D} \frac{1}{\tau_D} \cdot \exp\left(-\frac{r_D^2}{4\tau_D}\right) \int_0^1 \exp\left(-\frac{r_D'^2}{4\tau_D}\right) I_0\left(\frac{r_D r_D'}{2\tau_D}\right) r_D' dr_D' \cdot$$

$$\left\{1 + \frac{4h}{\pi h_f} \sum_{n=1}^{\infty} \left(\frac{1}{n}\right) \exp\left(-\frac{n^2\pi^2\tau_D}{h_D}\right) \cdot \cos\left(\frac{n\pi z}{h}\right) \cdot \cos\left(\frac{n\pi z_f}{h}\right) \cdot \sin\left(\frac{n\pi h_f}{2h}\right)\right\} d\tau \quad (3.3\text{-}1)$$

where the dimensionless variables are now defined as

$$w_D = \frac{\pi k_r b}{Q_{sc}} \left(\frac{T_{sc}}{T p_{sc}}\right) w \quad (3.3\text{-}2)$$

$$r_{D_f} = \frac{r}{r_f} \quad (3.3\text{-}3)$$

$$h_D = \frac{h}{r_f} \sqrt{\frac{k_r}{k_z}} \quad (3.3\text{-}4)$$

$$t_D = \frac{k_r \bar{p}}{\phi \mu r_f^2} \quad (3.3\text{-}5)$$

The derivative with respect to $\ln t_D$ is (Gradshteyn and Ryzhik, 1965, p. 23, eq. 0.410)

$$\frac{dw_D}{d\ln t_D} = \exp\left(-\frac{r_D^2}{4\tau_D}\right) \int_0^1 \exp\left(-\frac{r_D'^2}{4\tau_D}\right) I_0\left(\frac{r_D r_D'}{2\tau_D}\right) r_D' dr_D'$$

$$\left\{1 + \frac{4h}{\pi h_f} \sum_{n=1}^{\infty} \left(\frac{1}{n}\right) \exp\left(-\frac{n^2\pi^2\tau_D}{h_D}\right) \cdot \cos\left(\frac{n\pi z}{h}\right) \cdot \cos\left(\frac{n\pi z_f}{h}\right) \cdot \sin\left(\frac{n\pi h_f}{2h}\right)\right\} \quad (3.3\text{-}6)$$

Figure 3.5 shows type curves of w_D (solid) versus t_D for various values of h_D.

Another model by Gringarten et al. (1974) considers a pumping well intersected by a vertical fracture of zero thickness that completely penetrates a confined, uniform and isotropic aquifer. Under the assumption that flux is distributed uniformly across the fracture, whose edges are at equal distances x_f from the well, their solution at the center of the fracture where it intersects the active well reads, in modified form,

$$w_{wD} = \sqrt{\pi t_{D_{xf}}} \, erf\left(\frac{1}{2\sqrt{t_{D_{xf}}}}\right) + \frac{1}{2} Ei\left(\frac{1}{4t_{D_{xf}}}\right) \quad (3.3\text{-}7)$$
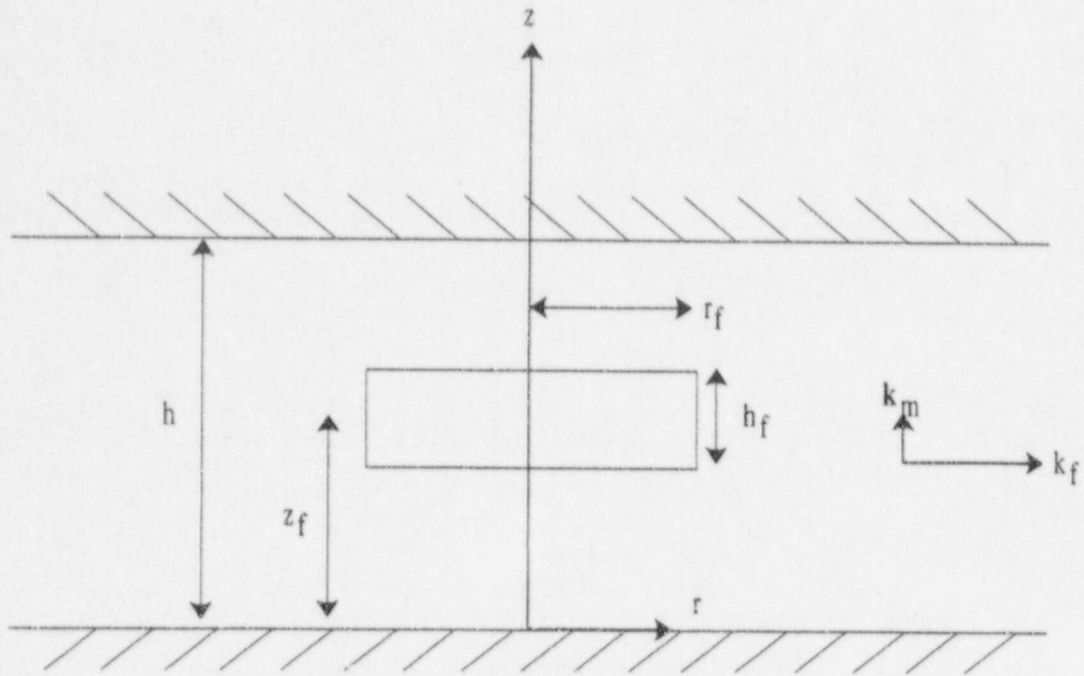
Figure 3.4: Geometry of idealized horizontal fracture in an infinite flow domain.
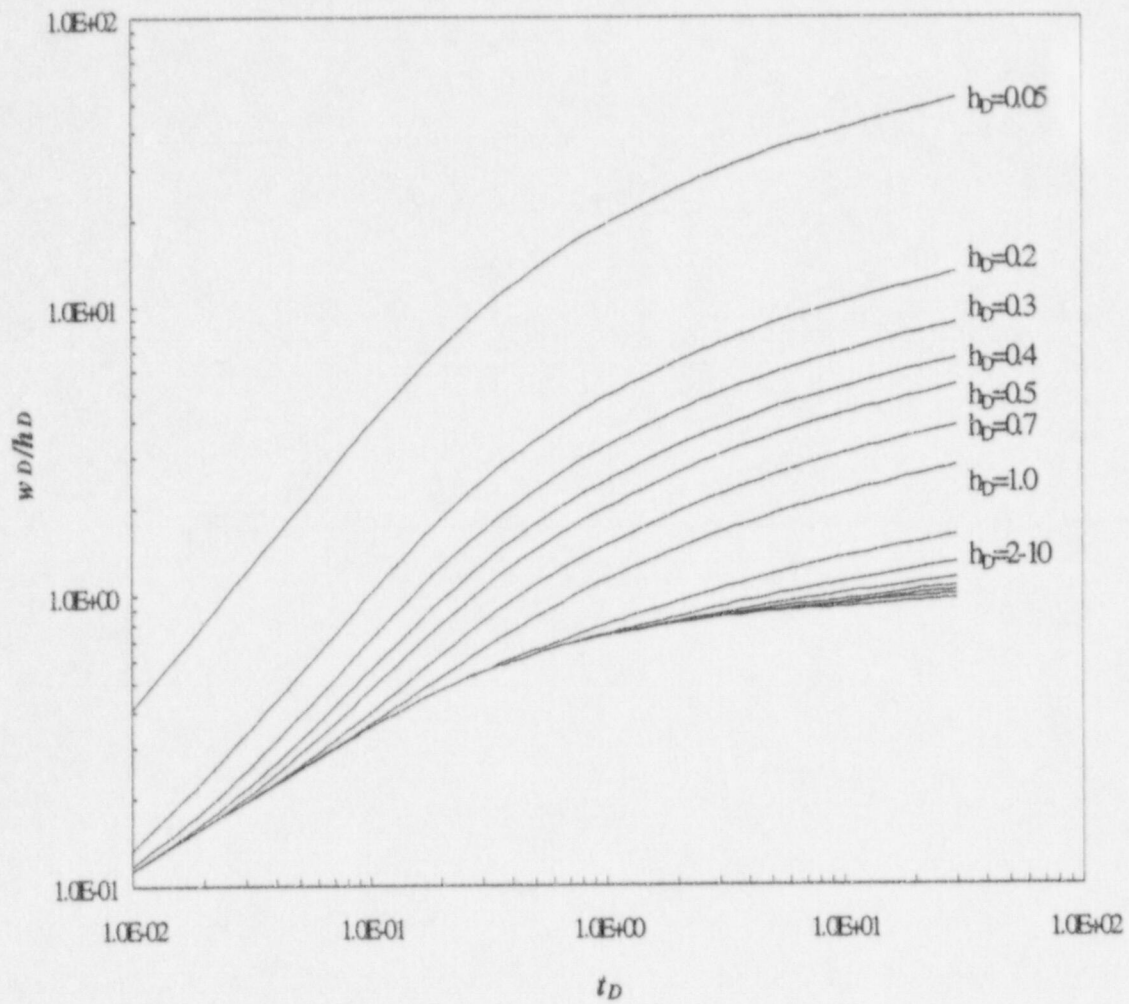
Figure 3.5: Type curves of dimensionless pseudopressure in injection interval, normalized by dimensionless height, versus dimensionless time for various h_D in uniform flux horizontal fracture model.
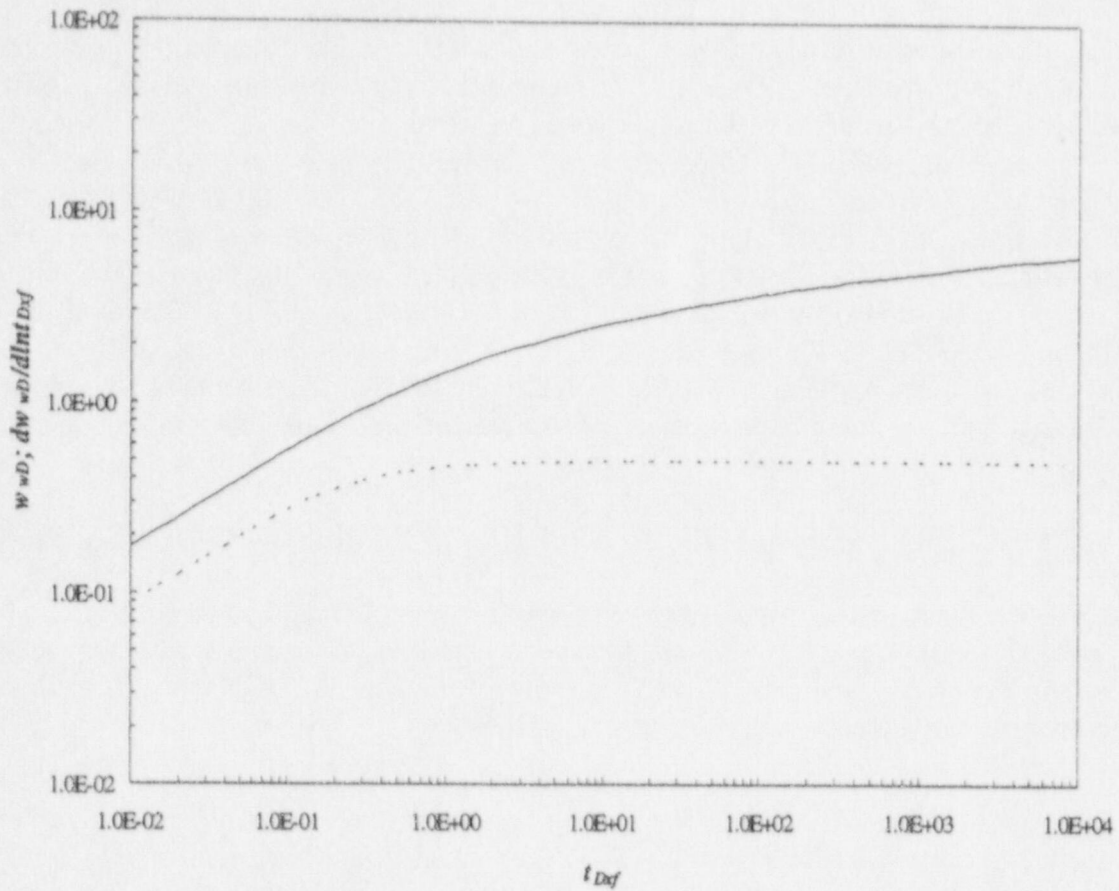
Figure 3.6: Type curves of dimensionless pseudopressure and its derivative in injection interval versus dimensionless time in uniform flux vertical fracture model at center of fracture ($x_D = y_D = 0$).

where

$$w_{wD} = \frac{\pi k b}{Q_{sc}} \left(\frac{T_{sc}}{T p_{sc}} \right) w \qquad (3.3\text{-}8)$$

$$t_{D\,xf} = \frac{k t \overline{p}}{\phi \mu x_f^{\,2}} \qquad (3.3\text{-}9)$$

erf is error function, *Ei* is exponential integral, and Q_{sc} is volumetric withdrawal/injection rate written in terms of standard conditions, from/into the fracture which, in turn, is equal to that from/into the well. The time derivative is given by Mathematica™ as

$$\frac{d w_{wD}}{d \ln t_{D_{xf}}} = \frac{\sqrt{\pi t_{D_{xf}}}}{2} \, erf \left(\frac{1}{2\sqrt{t_{D_{xf}}}} \right) \qquad (3.3\text{-}10)$$

Figure 3.6 shows type curves of w_{wD} (solid) and $dw_{wD}/d\ln t_{D_q}$ (dashed) versus t_{D_q} for a pumping well at the center of the fracture. Half-slope behavior is evident during early time when uniform flow into the fracture dominates. At late time, the flow pattern is predominantly radial. The derivative of pseudopressure (dashed line) reaches a constant value of ½ as in the radial flow case without a fracture.

Solutions have also been developed for partially penetrating (Raghavan *et al.*, 1978) and finite conductivity (Cinco-Ley *et al.*, 1978) vertical as well as inclined (Cinco-Ley *et al.*, 1975) fractures. These models are more complex than the ones already presented and include a larger number of parameters. They do not necessarily provide a more realistic representation of pneumatic test conditions at the ALRS than do the simpler models we just described, and many of their parameters are difficult to either define or measure at the site. We are therefore guided by the principle of parsimony in working with the simplest models that nevertheless help us interpret the available pneumatic test data in a satisfactory manner.

3.4 TYPE CURVES USED FOR INTERPRETATION OF CROSS-HOLE TESTS

For purposes of cross-hole test analysis by means of type-curves we represent the fractured rock by an infinite three-dimensional uniform, anisotropic continuum as was done by Hsieh and Neuman (1985a). In terms of pressure, single-phase airflow is then governed approximately (due to linearization) by

$$\nabla \cdot \mathbf{k} \nabla p = \frac{1}{\alpha} \frac{\partial p}{\partial t} \tag{3.4-1}$$

where the permeability $\mathbf{k}$ is now a second-rank symmetric, positive-definite tensor. As in the single-hole case, pressure is zero at initial time and at infinity. Hsieh and Neuman treat injection and observation intervals as points or lines. In this report we consider the special case where injection takes place at a point, and observation along a line. However, we modify their solution to account for the effects of storage and skin on pressure, and its derivative (not considered by these authors), in the observation interval. The corresponding dimensionless pressure is given by Hsieh and Neuman (1985a; eq. 27, p. 1658) as

$$p_D = \frac{\beta_1}{4} \int_{u=1/4t_D}^{u=\infty} \frac{1}{u} \exp\left[-\left(1-\beta_2^2\right)u\right] \cdot \left\{ erf\left[u^{1/2}(\beta_2 + 1/\beta_1)\right] - erf\left[u^{1/2}(\beta_2 - 1/\beta_1)\right]\right\} du$$

$$\tag{3.4-2}$$

$$\frac{dp_D}{d\ln t_D} = \frac{\beta_1}{4} \exp\left[-\left(1-\beta_2^2\right)u\right] \cdot \left\{ erf\left[u^{1/2}(\beta_2 + 1/\beta_1)\right] - erf\left[u^{1/2}(\beta_2 - 1/\beta_1)\right]\right\} \tag{3.4-3}$$

where, for an isotropic medium, dimensionless pressure and time are defined respectively, as

$$p_D = 4\pi p k R / Q \mu \tag{3.4-4}$$

$$t_D = k\bar{p}t/\phi\mu R^2 \tag{3.4-5}$$

while β_1 and β_2 are geometric parameters defined as

$$\beta_1 = (2R/B)\left[\left(\mathbf{e}^T \mathbf{A} \mathbf{e}\right)/\left(\mathbf{e}_b^T \mathbf{A} \mathbf{e}_b\right)\right]^{1/2} \tag{3.4-6}$$

$$\beta_2 = \left(\mathbf{e}^T \mathbf{A} \mathbf{e}_b\right) \Big/ \left[\left(\mathbf{e}^T \mathbf{A} \mathbf{e}\right)\left(\mathbf{e}_b{}^T \mathbf{A} \mathbf{e}_b\right)\right]^{1/2} \tag{3.4-7}$$

Here R is radial distance between the centroids of any two injection and monitoring intervals, B is length of the observation interval, $\mathbf{e}$ is a unit vector pointing from the centroid of the injection interval toward the centroid of the monitoring interval, $\mathbf{A}$ is the adjoint of $\mathbf{k}$, and $\mathbf{e}_b$ is a unit vector parallel to the monitoring interval (see Hsieh and Neuman, 1985a, for further details). For an isotropic medium, the above reduce to $\beta_1 = 2R/B$ and $\beta_2 = \cos\theta$ where the θ is an angle between $\mathbf{e}$ and $\mathbf{e}_b$ which is given in radians.

Tongpenyai and Raghavan (1981) present a solution for radial flow, which considers storage and skin effects in both the pumping and the observation wells. We follow a much simpler approach due to Black and Kipp (1977) that is based on a concept introduced by Hvorslev (1951). According to their approach (see also Neuman and Gardner, 1989), the pressure p in the rock is related to observed pressure p_{ow}

$$p = p_{ow} + t_B \frac{dp_{ow}}{dt} \tag{3.4-8}$$

where $t_B = C_{ow}\mu/Fk_s$ is the characteristic response time of the instrument, known as basic time lag; $C_{ow} = V/p_{ow}$ is storage coefficient $[L^4 T^2 M^{-1}]$ associated with an interval of volume V; k_s is permeability (which we attribute to skin); and F is a geometric shape factor $[L]$. The basic time lag can be determined by means of a pressurized slug test so that there is no need to know either k_s or F. Once t_B has been determined, one can correct p_{ow} for the effects of storage and skin by means of (3.4-8).

The general solution of (3.4-8), in dimensionless form, is (Appendix E)

$$p_{ow} = \frac{1}{\Omega}\left(\frac{Q\mu\sigma}{k}\right)\exp\left(-\frac{1}{\Omega u}\right)\int_u^\infty \exp\left(\frac{1}{\Omega\xi}\right)p_D(\xi)\frac{d\xi}{\xi^2} \tag{3.4-9}$$

where $\Omega = 4k_s t_B/S_G\mu R^2$ is a dimensionless well response time, σ is a constant related to the geometry of the observation well intake (for example, $\sigma = 1/2\pi b$ for radial flow in which b is the length of the injection interval), and S_G is the gas storage factor $[M^{-1}LT^2]$ defined in Chapter 2 (eq. 2.1-23). Substituting (3.4-2) into (3.4-9) yields for dimensionless pressure, and its derivative,

$$p_D(u,\Omega) = \frac{\beta_1}{4}\int_{u=1/4t_D}^{u=\infty}\frac{1}{\xi}\exp\left[-\left(1-\beta_2^2\right)\xi\right]\cdot\left\{erf\left[\xi^{1/2}\left(\beta_2+1/\beta_1\right)\right] - erf\left[\xi^{1/2}\left(\beta_2-1/\beta_1\right)\right]\right\}$$

$$\cdot\left\{1 - \exp\left[-1/\Omega\left(1/u - 1/\xi\right)\right]\right\}d\xi$$

$$\tag{3.4-10}$$

$$\frac{\partial p_D(u,\Omega)}{\partial \ln t_D} = \frac{\beta_1}{4\Omega u}\int_{u=1/4t_D}^{u=\infty}\frac{1}{\xi}\exp\left[-\left(1-\beta_2^2\right)\xi\right]\cdot\left\{erf\left[\xi^{1/2}\left(\beta_2+1/\beta_1\right)\right] - erf\left[\xi^{1/2}\left(\beta_2-1/\beta_1\right)\right]\right\}$$

$$\cdot\left\{\exp\left[-1/\Omega\left(1/u - 1/\xi\right)\right]\right\}d\xi$$

$$\tag{3.4-11}$$

Figures 3.7 through 3.9 depict corresponding type-curves for various values of Ω, $\beta_2 = 0.01$, and $\beta_1 = 5.0$, 0.1 and 0.01, respectively where p_D is represented by solid

curves and $dp_D/d \ln t_D$ by dashed curves. There clearly is a delay in response as Ω increases. The original solution (circles, eq. 3.4-2) of Hsieh and Neuman (1985a) and its derivative (triangles, eq. 3.4-3) are included for comparison.

In the case of Figure 3.7 where $\beta_l = 5.0$, radial distance between the centroids of the injection and observation intervals is large compared to the length of the observation interval. Here the pressure derivative decays towards zero as is typical of three-dimensional flow which develops around the point injection interval. As β_l diminishes, so does the response which is additionally delayed in time. In Figure 3.9 where $\beta_l=0.01$, so that the monitoring interval is long relative to its distance from the injection interval, the pressure derivative corresponding to $\Omega = 1.0$ and 10.0 is constant during intermediate time as is typical of radial flow. We use these type curves to interpret cross-hole test data from the ALRS in Chapter 5.
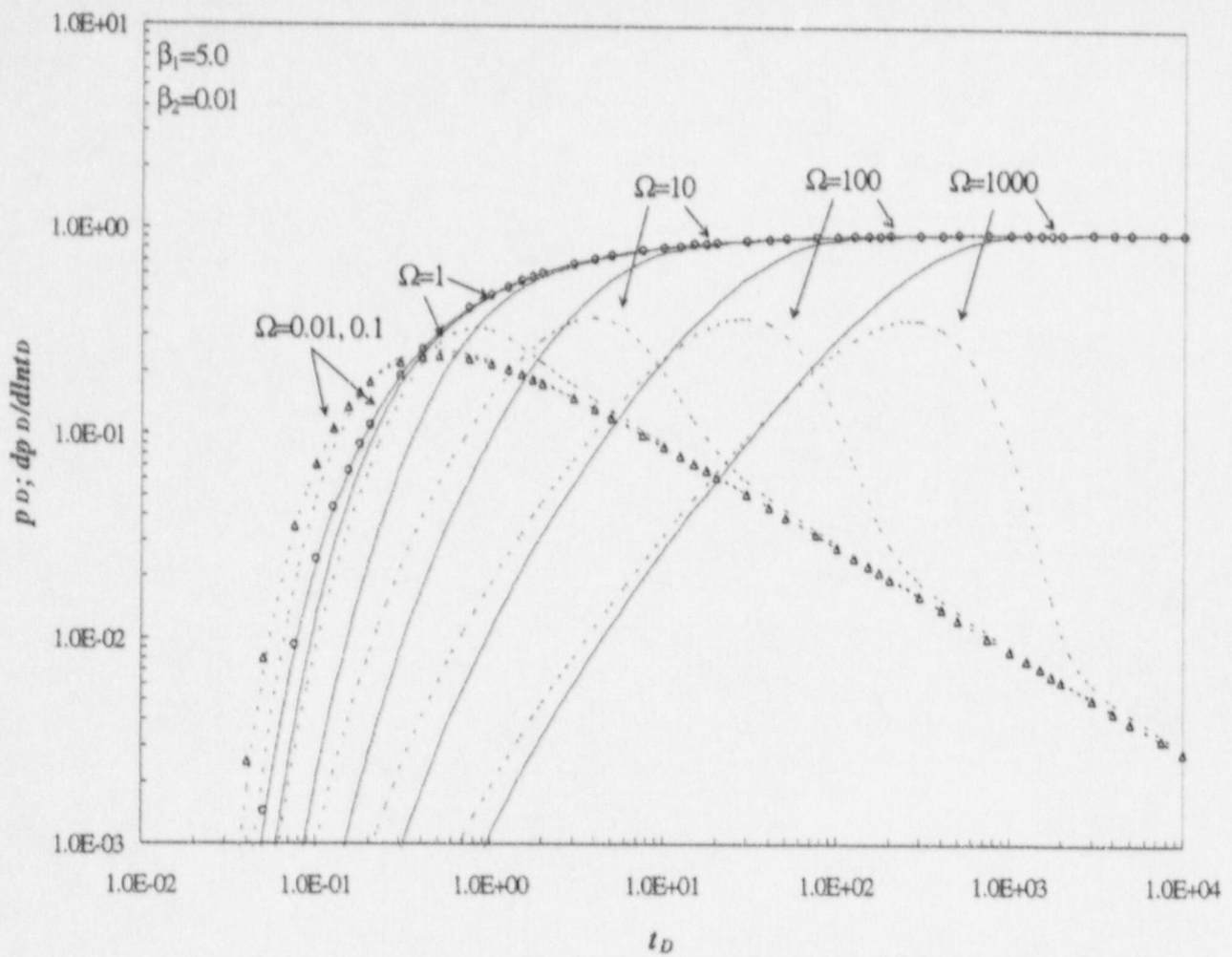
Figure 3.7: Type curves of dimensionless pressure in observation interval (solid) and its derivative (dashed) versus dimensionless time for various Ω and $\beta_1 = 5.0$, $\beta_2 = 0.01$. Circles represent dimensionless pressure in the solution of Hsieh and Neuman (1985a) and triangles their derivatives.
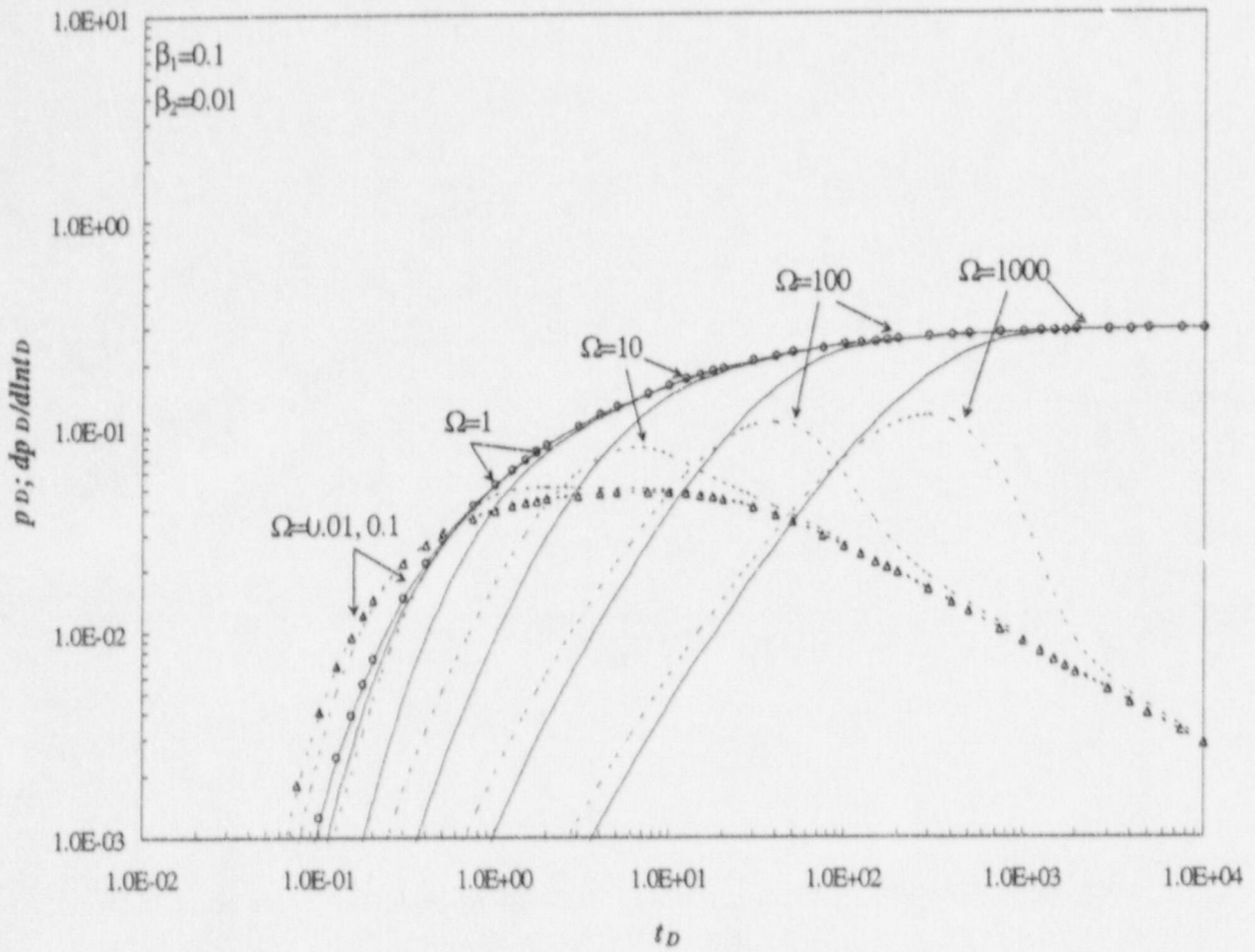
Figure 3.8: Type curves of dimensionless pressure in observation interval (solid) and its derivative (dashed) versus dimensionless time for various Ω and $\beta_1 = 0.2$, $\beta_2 = 0.01$. Circles represent dimensionless pressure in the solution of Hsieh and Neuman (1985a) and triangles their derivatives.
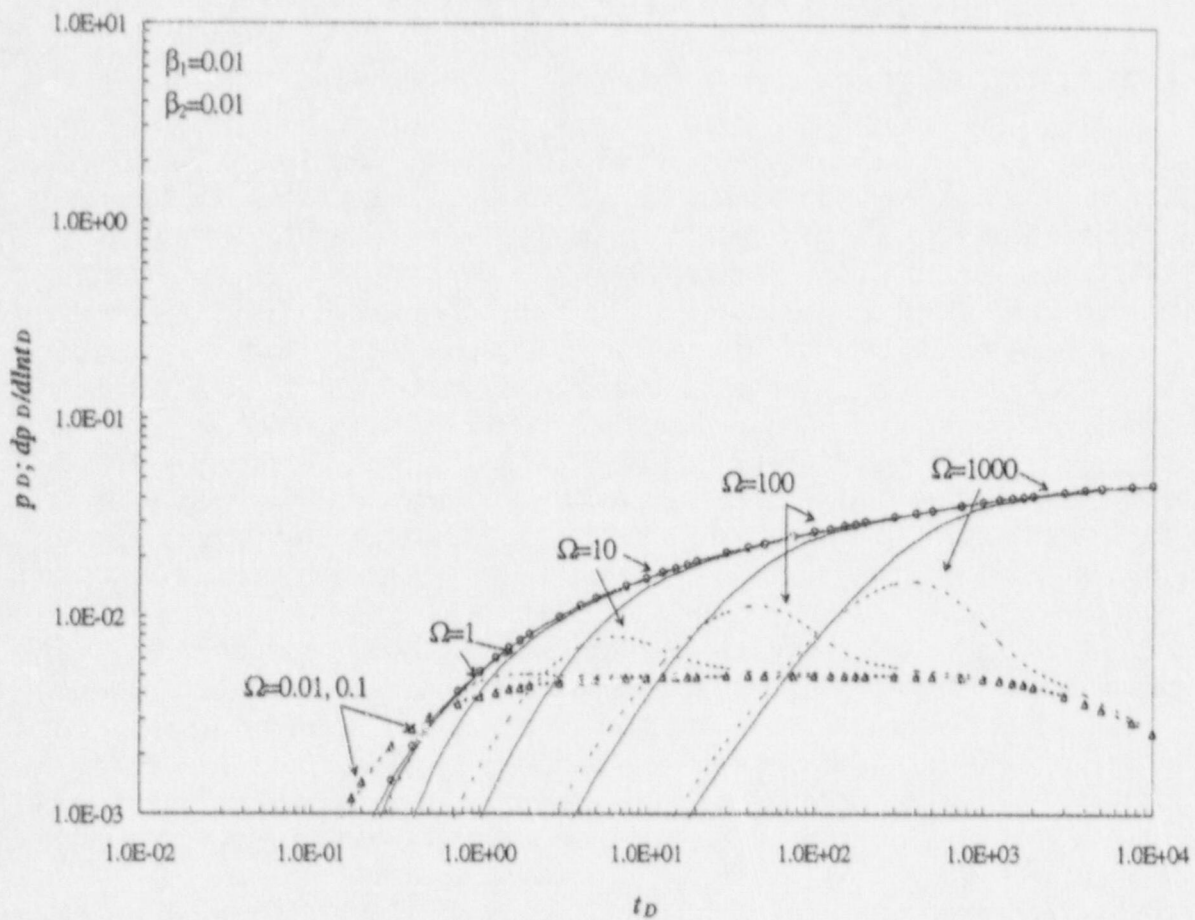
Figure 3.9: Type curves of dimensionless pressure in observation interval (solid) and its derivative (dashed) versus dimensionless time for various Ω and $\beta_1 = 0.01$, $\beta_2 = 0.01$. Circles represent dimensionless pressure in the solution of Hsieh and Neuman (1985a) and triangles their derivatives.

4. TYPE-CURVE INTERPRETATION OF SINGLE-HOLE PNEUMATIC INJECTION TEST DATA

4.1 SINGLE-HOLE TEST METHODOLOGY

Single-hole pneumatic tests were conducted to help characterize unsaturated fractured rocks at the ALRS on nominal scales of 0.5, 1.0, 2.0 and 3.0 m. The tests, and their analyses by means of steady state formulae, were conducted by Guzman *et al.* (1994, 1996) and Guzman and Neuman (1996). Each test involved the injection of air into a section of a borehole isolated by means of inflatable packers. The corresponding air injection system is depicted schematically in Figure 4.1. The system included a straddle packer assembly consisting of two inflatable rubber bladders (each 3 m in length), a set of flow meters and flow controllers, pressure valves and regulators, and an electronic monitoring system to automatically record field data. The distance between bladders was adjustable. Air pressure, temperature and relative humidity were recorded in the test interval. Mass flow meters and controllers were used to cover two ranges of equivalent volumetric rate, 0 - 0.1 *slpm* (standard liters per minute) and 0 – 20 *slpm*. Flow rotameters served as visual backup to help maintain a constant volume rate between 0.01 *slpm* and 20 *slpm*. Measurements were recorded using a data logger connected to an optically isolated interface, which allowed periodic downloading onto an on-site personal computer. Recording was done at small intervals during early times when changes in pressures were expected to be largest and at successively longer intervals thereafter.

Table 4.1 lists the coordinates of six boreholes subjected to single-hole air permeability testing at the ALRS. The coordinate system is shown in Figure 1.2 and its origin coincides with the lower lip of the near-surface casing in borehole Z3. The table also lists the approximate length and dip of each borehole. A three-dimensional perspective of all 1-m scale air permeability test locations, viewed from the Southwest toward the Northeast, is shown in Figure 1.5. Each point in the perspective represents the center of a borehole test interval between packers. Each test interval is identified by borehole and the distance along the borehole from its center to the L.L. point listed in Table 4.1. There were neither gaps nor significant overlaps between test intervals in a borehole.

Prior to each air injection test, the packers were inflated to isolate the test interval, and the resulting pressure was allowed to dissipate. The test commenced by injecting air into the packed off interval at a constant mass flow rate. This continued until the pressure stabilized so as to vary by not more than the equivalent of 1 mm of mercury in 30 *min*. The test continued by incrementing the mass flow rate and monitoring pressure until it attained a new stable value. Most tests included three or more such incremental steps of mass flow rate. Injection was then discontinued and the pressure allowed to recover back to atmospheric.

Table 4.1: Coordinates of boreholes subjected to air permeability testing (adapted from
Guzman *et al.*, 1996)

Bore -hole	L.L. x [m]	L.L. y [m]	L.L. z [m]	Borehole length [m]	B.B. x [m]	B.B. y [m]	B.B. z [m]	General dip direction
V2	4.24	6.84	0.01	30	4.2	6.8	-30.0	Vertical
W2a	5.42	21.46	-0.03	30	5.4	0.2	-21.2	SSE
X2	20.44	10.03	-0.02	30	-0.8	10.0	-21.2	WSW
Y2	20.04	5.20	-0.31	30	-1.2	5.2	-21.5	WSW
Y3	30.07	5.35	-0.27	45	-1.8	5.3	-32.0	WSW
Z2	9.80	0.03	-0.20	30	31.0	0.0	-21.4	ENE

Coordinates are shown in Figure 1.2 and their origin is at lower lip of Z3 casing.
Borehole length is approximate. L.L. marks lower lip of near-surface casing in each
borehole; B.B. marks borehole bottom (approximate).

Table 4.2: Nominal Scale and Number of Single-Hole Pneumatic Injection Tests at the
ALRS.

Borehole	Nominal Scale (Length of Test Interval)	Number of Intervals Tested
V2	1.0 m	21
W2A	1.0 m	37
X2	1.0 m	30
X2	2.0 m	10
Y2	0.5 m	54
Y2	1.0 m	28
Y2	2.0 m	14
Y2	3.0 m	9
Y3	1.0 m	39
Z2	1.0 m	28
	Total	270

The packers were deflated, the instrument was repositioned in the borehole, and
testing resumed until the entire uncased length of a borehole has been tested. The method
has proved reliable in that repeated tests of selected intervals, over several years, have
given highly reproducible permeability estimates. This was due in part to a strict quality
assurance and quality control protocol at each stage of testing.

Tests were conducted along borehole intervals of lengths 0.5, 1.0, 2.0 and 3.0 *m* in
borehole Y2; 1.0 and 2.0 *m* in borehole X2; and 1.0 *m* in boreholes V2, W2A, Y3 and Z2.
A total of more than 270 single-hole injection tests have been completed, of which 180
were conducted along 1-*m* sections in six boreholes (Figure 1.5 and Table 4.2) that span
20,000 *m³* of unsaturated porous fractured tuff. Guzman *et al.* (1996) relied on a steady

state analysis of late data during each step to obtain a corresponding pneumatic permeability value. They used a modified formula originally developed by Hvorslev (1951; see also Hsieh et al., 1983) which assumes that, during each relatively stable period of injection rate and pressure, air is the only mobile phase within the rock near the test interval and its steady-state pressure field has prolate-spheroidal symmetry. This implies that the rock forms a uniform, isotropic porous continuum. The formula reads

$$k = Q_{sc} \frac{\mu \ln(b/r_w)}{\pi b (p^2 - p_o^2)} \frac{T p_{sc} Z}{T_{sc}} \tag{4-1}$$

where k is permeability $[L^2]$, Q_{sc} is volumetric flow rate at standard conditions $[L^3 T^{-1}]$, μ is dynamic viscosity of air at standard conditions $(1.81 \times 10^{-5} \, Ns/m^2)$, b is length of the test interval $[L]$, r_w is borehole radius $(0.05 \, m)$, T is air temperature in degrees Kelvin, p_{sc} is pressure at standard conditions $(101.3 \, kPa)$, Z is dimensionless compressibility factor, p is pressure in the injection interval, p_o is ambient air pressure, and T_{sc} is temperature at standard conditions $(293.16 \, ^\circ K)$.

During single-hole tests, air injection was conducted at a number of incremental mass flow rates. The type-curve analyses of transient single-hole test data that we present below concern only the first of any such multistep sequence.

4.2 PHENOMENOLOGY OF SINGLE-HOLE TESTS

Figure 4.2 shows how air pressure and temperature varied during a typical multistep single-hole pneumatic injection test, labeled VCC1001, conducted within a 1-m interval whose center was located 10.37 m below the LL marker (Table 4.1) in borehole V2 at the ALRS (our designation of single-hole tests follows that established by Guzman et al., 1994, 1996). Whereas temperature was nearly constant throughout the test, pressure first rose to a peak and then declined toward a stable value. The same pressure phenomenon is seen more clearly in a plot of pressure versus time during the first step of test CGA1120 (Figure 4.3), conducted within a 1-m interval whose center was located 20.15-m below the LL marker (Table 4.1) in borehole X2. Simulations of two-phase flow in a porous medium by Guzman et al. (1996) have confirmed that this phenomenon is due to displacement of water by air in the immediate vicinity of the injection interval. When air is injected into a rock that contains water at partial saturation, the latter acts to block its movement. Hence the permeability one computes for air is lower than what one would compute in the absence of a water phase. It follows that the computed air permeability is less than the intrinsic permeability of the rock. Indeed, Guzman et al. (1996) were able to demonstrate computationally that the higher is the applied pressure during a test, the closer is the computed air permeability to its intrinsic value. They also found that, in most test intervals, pneumatic permeabilities show a systematic increase with applied pressure as air displaces water under two-phase flow. Only in a few test intervals, which were intersected by high-permeability fractures, did air permeability decrease with applied pressure due to inertial effects. In many cases, air permeability exhibited a hysteretic variation with applied pressure.

The observed stabilization of pressure at late time during each step recurs in more than 90 percent of single-hole tests at the ALRS. This could, in principle, be due either to

the establishment of three-dimensional flow around the test interval or the presence of an atmospheric pressure boundary in its vicinity. As pressure and pressure derivative data from most test intervals fit type-curves based on a spherical flow model in an infinite domain, we attribute the observed pressure stabilization to three-dimensional flow.

Figure 4.4 shows the same data as those in Figure 4.3 re-plotted on logarithmic paper. It reveals that, at early time, the pressure increases linearly with a unit slope that is diagnostic of borehole storage due to gas compressibility (van Everdingen and Hurst 1949; Papadopulos and Cooper, 1967, Agarwal et al., 1970, Joseph and Koederitz, 1985). Only when this straight line starts curving does air start penetrating into the rock in a measurable way. The ensuing period of transitional flow, prior to pressure stabilization, is seen to be extremely short and dominated by two-phase flow effects. As such, it cannot be analyzed to yield reliable values of fracture porosity or borehole skin factor. A similar difficulty is encountered in the majority of single-hole tests at the ALRS in which the pressure stabilizes in a manner typical to three-dimensional flow. The two-phase flow effect is more pronounced on an arithmetic than on a logarithmic plot of pneumatic pressure versus time.

Figure 4.5 shows a relatively rare example of a single-hole test (JJA0616 in a 1-m interval with center located 17.77 m from the LL mark along borehole) at the ALRS in which the pressure does not stabilize but continues to increase in a manner that is characteristic of radial flow (on semi-logarithmic paper, the late pressure data would delineate a straight line). Here the transient period, following that dominated by borehole storage, is sufficiently long to allow extracting from the corresponding data information about air-filled porosity and skin factor. Our attempts to do so, for this and other data that appear to fit radial type-curves, led to air-filled porosity values that are much smaller than those we obtain later by a numerical inverse analysis of similar data and from cross-hole tests; we therefore suspect the reliability of porosity values obtained from radial type-curve fits at the ALRS and do not quote them in this report. In a still smaller number of tests, such as that illustrated in Figure 4.6 (JHB0612 in a 1-m interval with center located 15.81 m from the LL mark along borehole), pneumatic pressure data delineate a straight line with a half-slope at early time on logarithmic paper. Such behavior is diagnostic of a highly conductive planar feature such as a wide fracture. Indeed, a televiewer image of the test interval in Figure 4.7 reveals the presence of a wide-open fracture or cavity within it. At late time, the pressure in Figure 4.6 continues to climb as is typical of radial flow. We analyze this test in this chapter with the aid of various analytical continuum (radial, spherical) and fracture (horizontal, vertical) flow type-curve models, and in Chapter 6 by means of a numerical inverse procedure. In contrast, Figure 4.8 shows an example of a test (ZDC0826 in a 1-m interval with center located 13.56-m from the LL mark along borehole Z2 in which an early half-slope indicates the presence of a conductive planar feature, and the stable late pressure data are indicative of a three-dimensional flow regime or possibly a recharge boundary.

Some single-hole tests, during which the pressure eventually stabilizes, contain a sufficiently long transition period that is amenable to analysis by type-curves based on a radial flow model. This is true about numerous 1-m test data from boreholes W2A and Y2. It suggests to us that flow around such test intervals evolves from radial to three-dimensional with time. Though it seems to allow extracting from these tests information about air-filled porosity and skin factor, we consider the results of such analyses

unreliable, for reasons mentioned earlier, and do not quote the corresponding parameter values in this report.

The fact that transient pressure behavior is not entirely consistent across the site, but varies from one test interval to another, provides a qualitative indication that the site is pneumatically nonuniform and the local rock is heterogeneous.
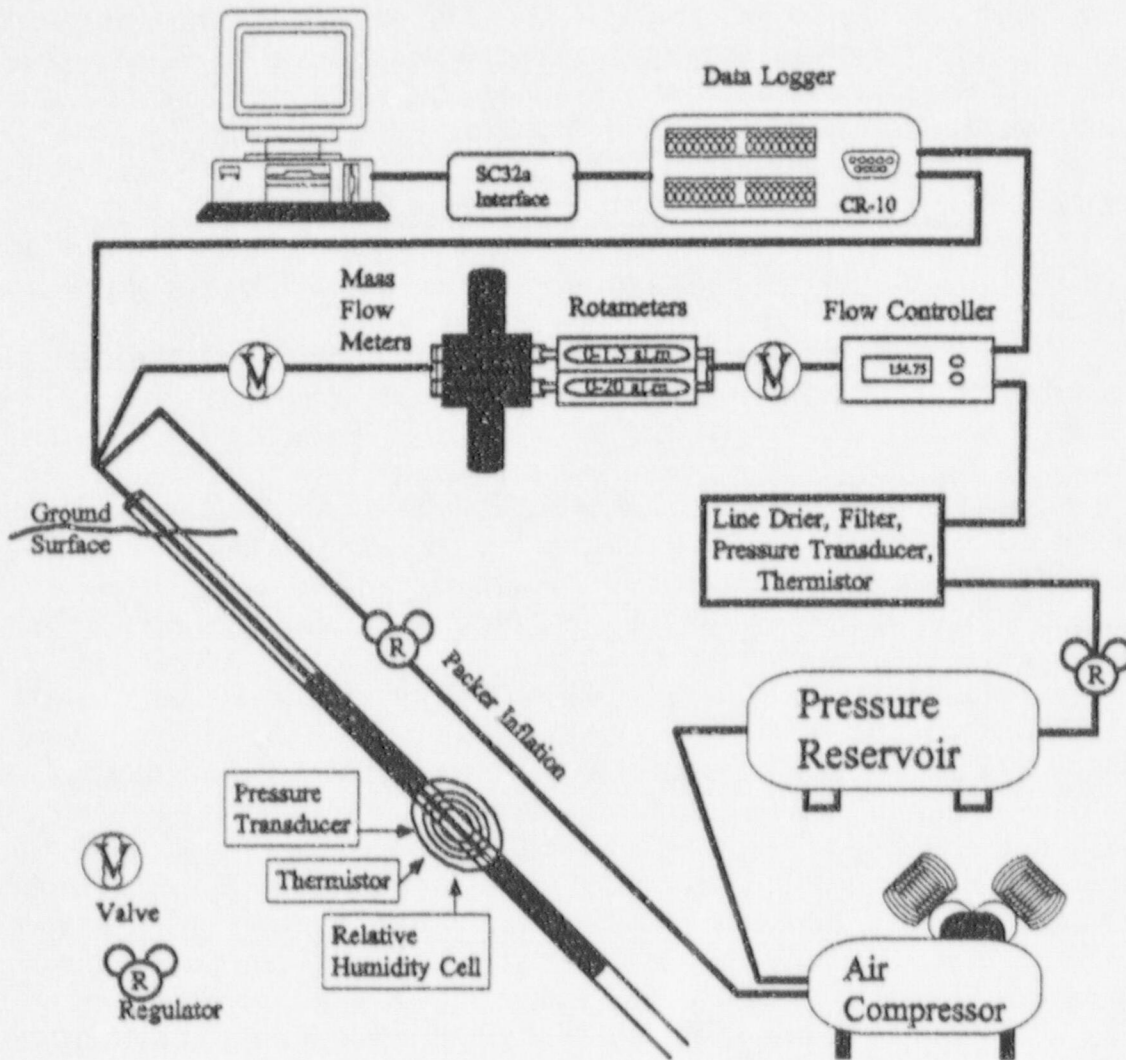
Figure 4.1: Schematic diagram of the air injection system (adapted from Guzman *et al.*, 1996)
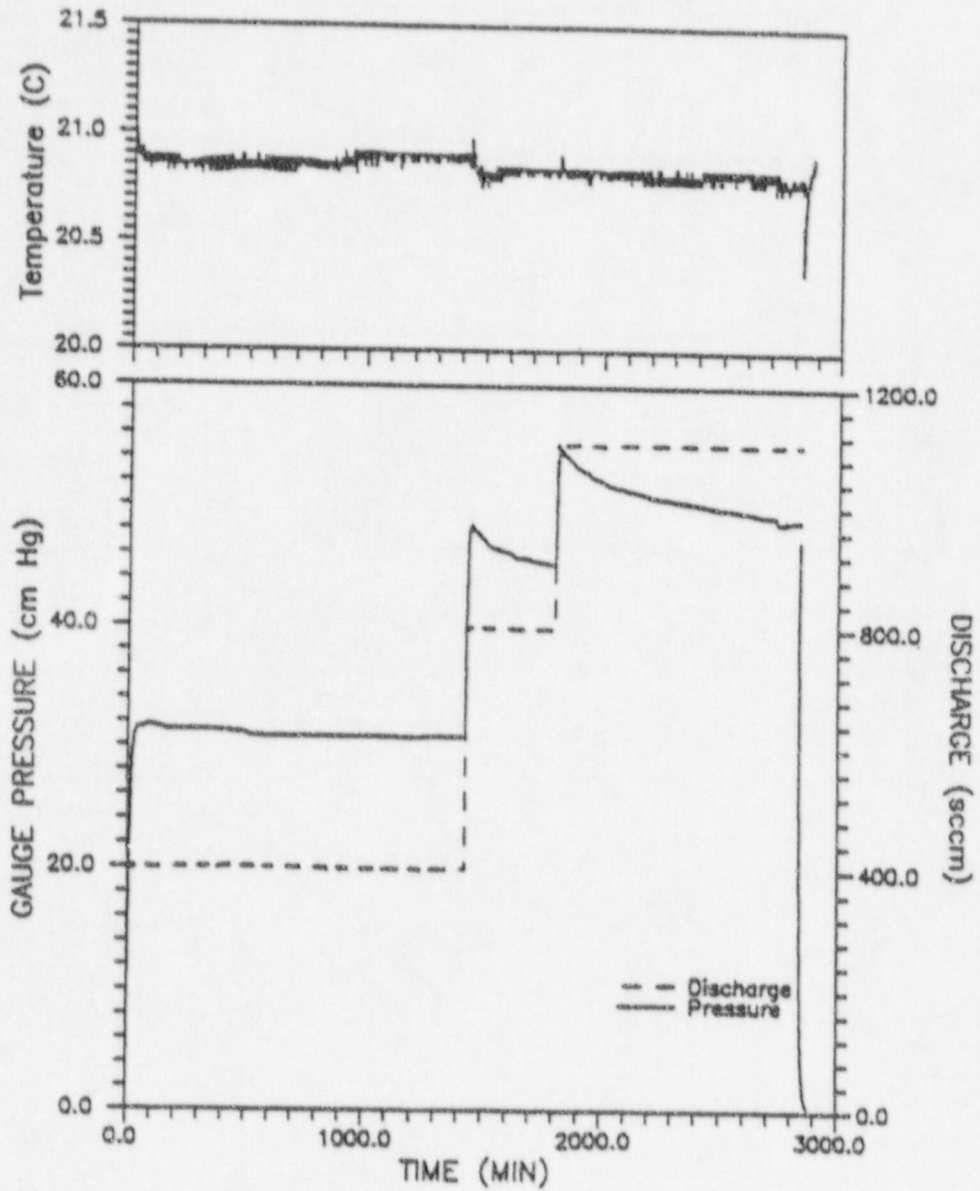
Figure 4.2: Example of multi-rate single-hole test (VCC1001 in borehole V2 at 10.37 *m* from LL marker)
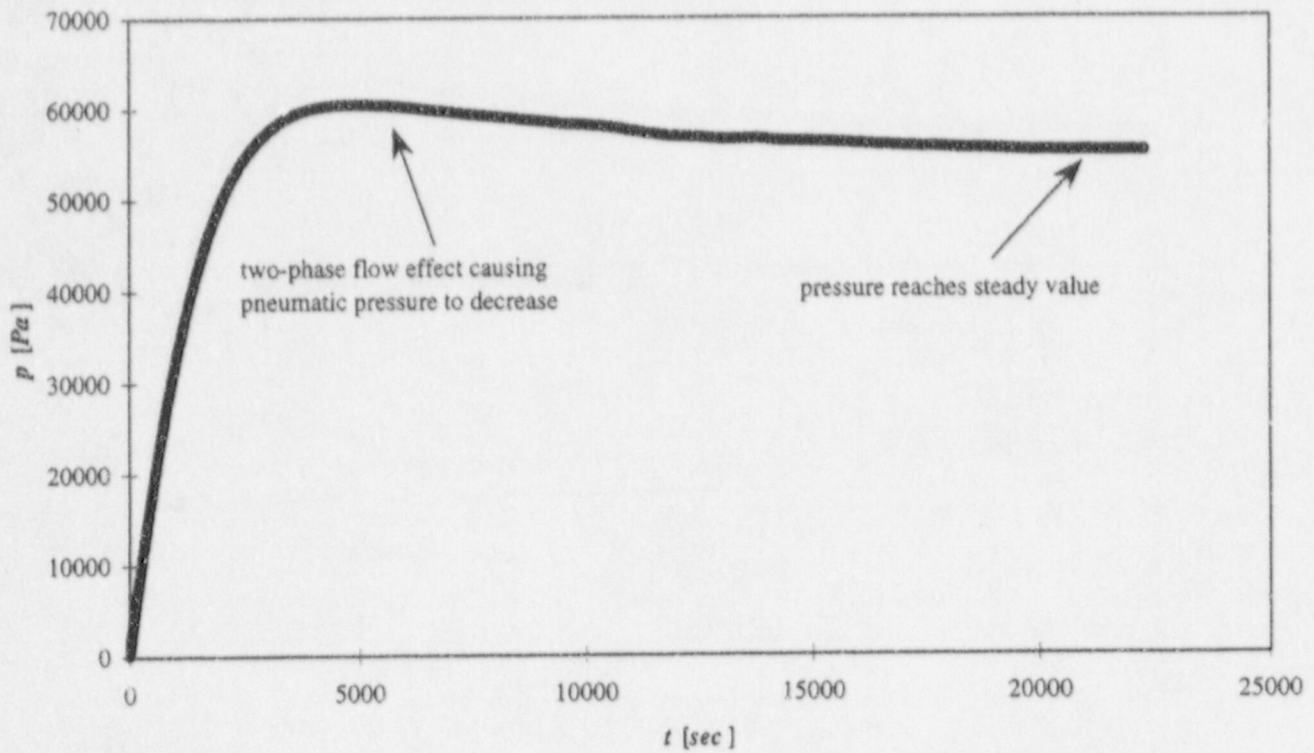
Figure 4.3: Arithmetic plot of pressure data from test CGA1120
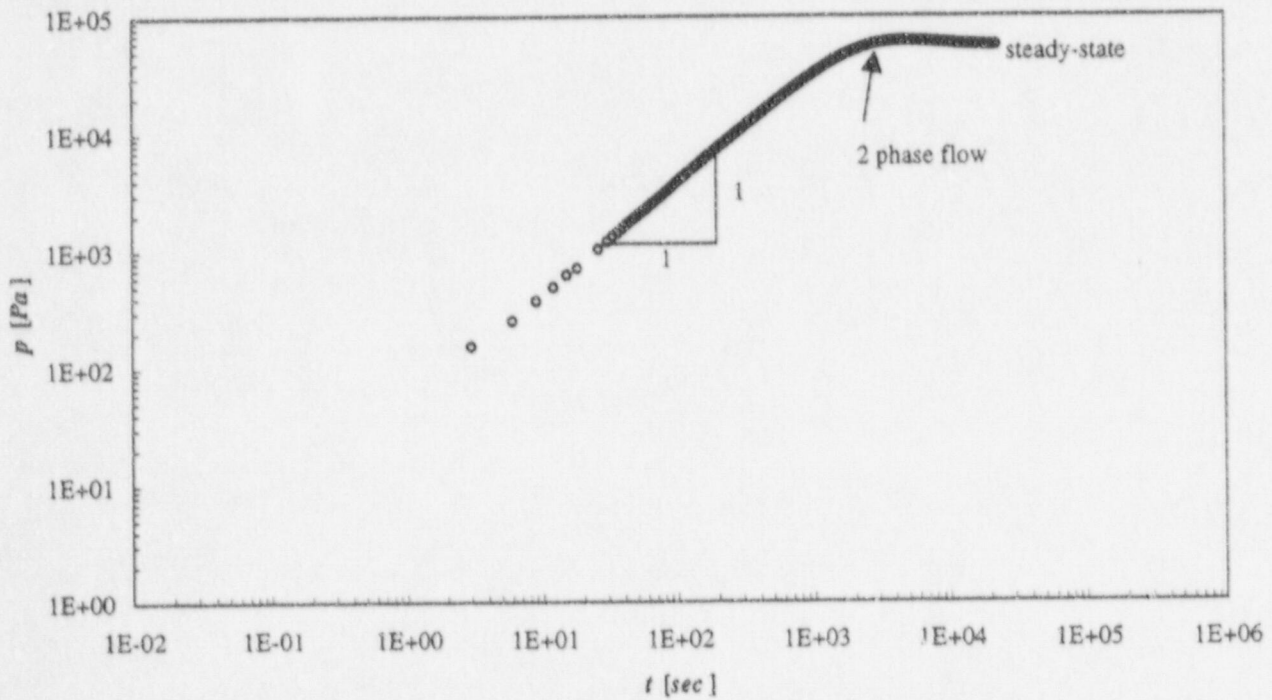
Figure 4.4: Logarithmic plot of pressure data from test CGA1120
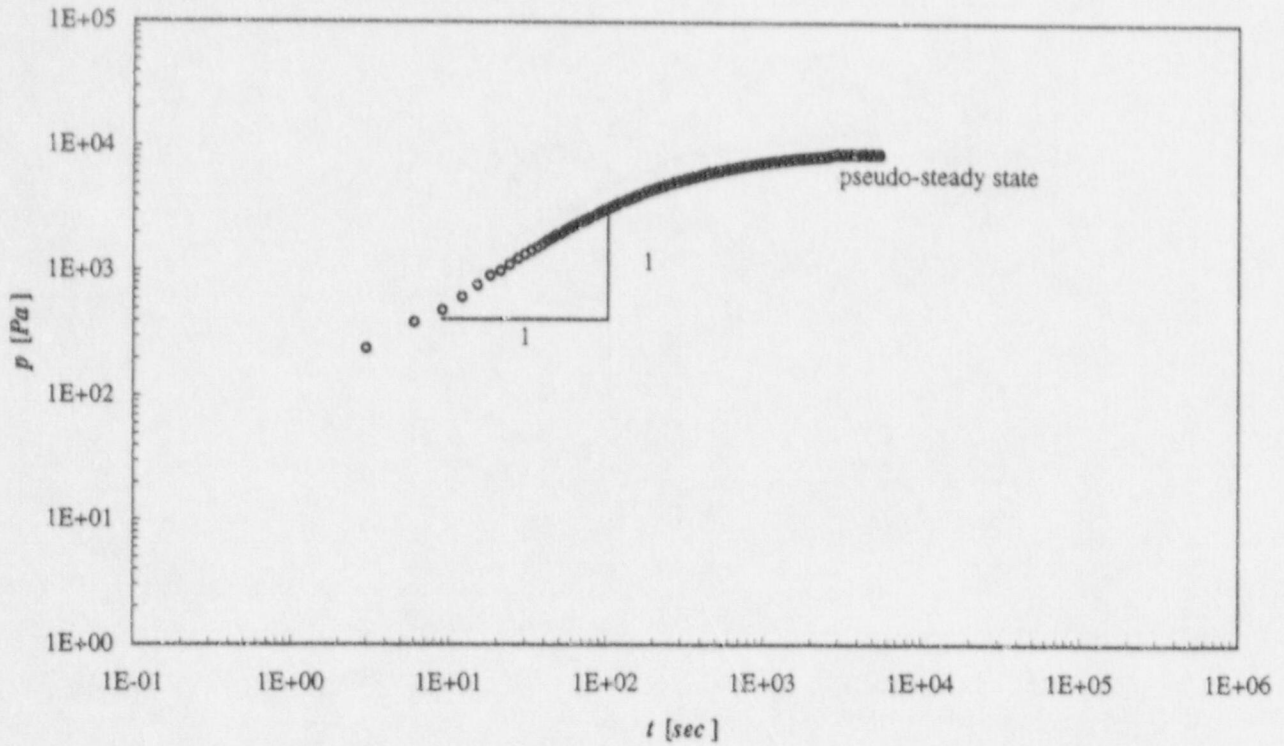
Figure 4.5: Logarithmic plot of pressure data from test JGA0616
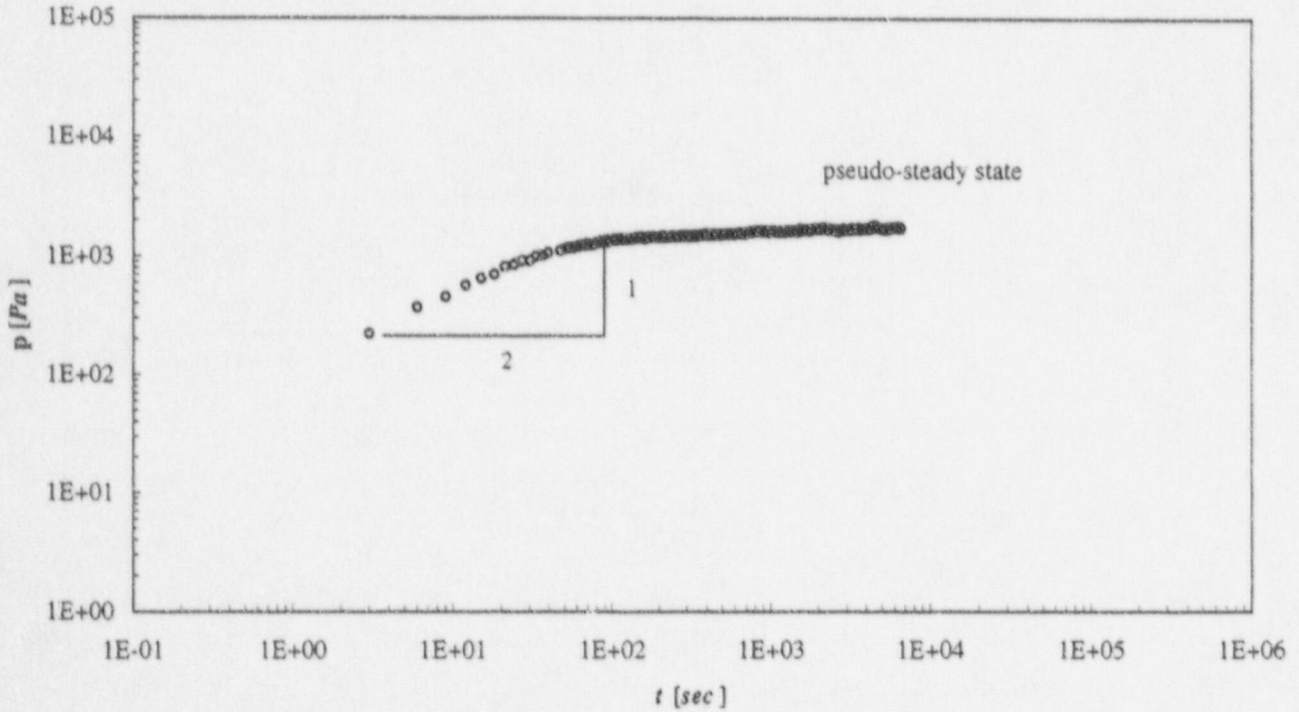
Figure 4.6: Logarithmic plot of pressure data from test JHB0612
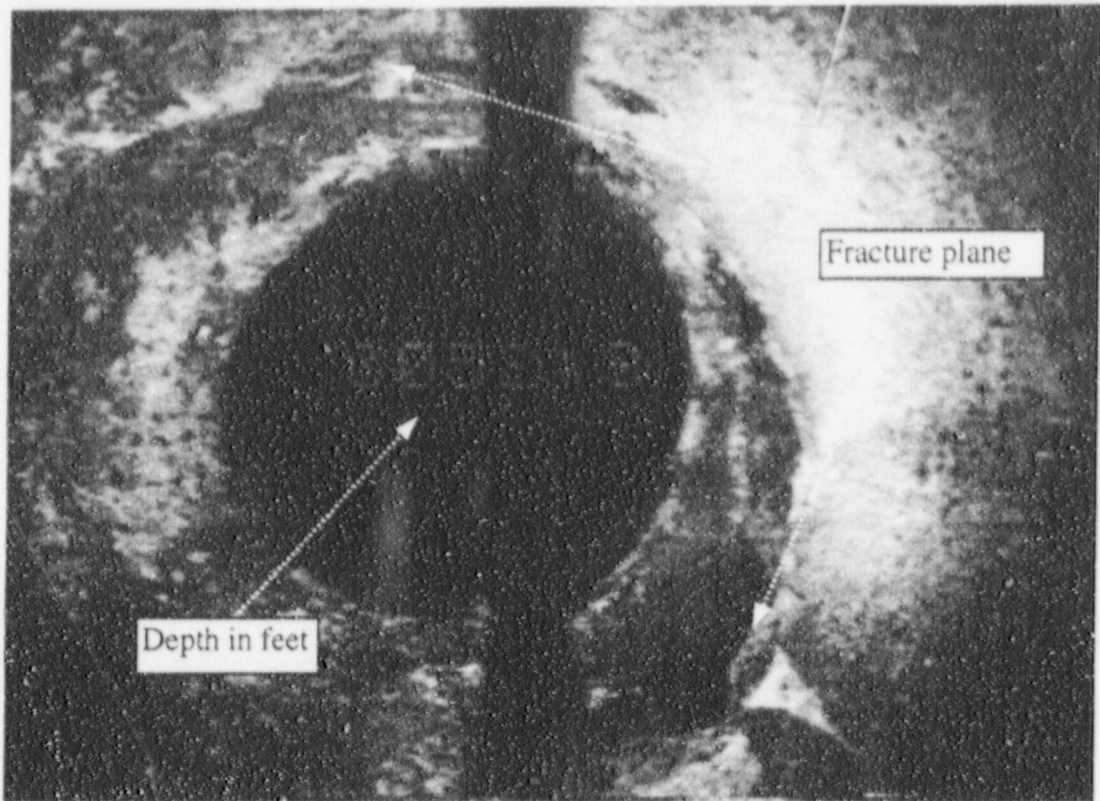
Figure 4.7: BHTV image taken in borehole Y2 (high permeability zone)
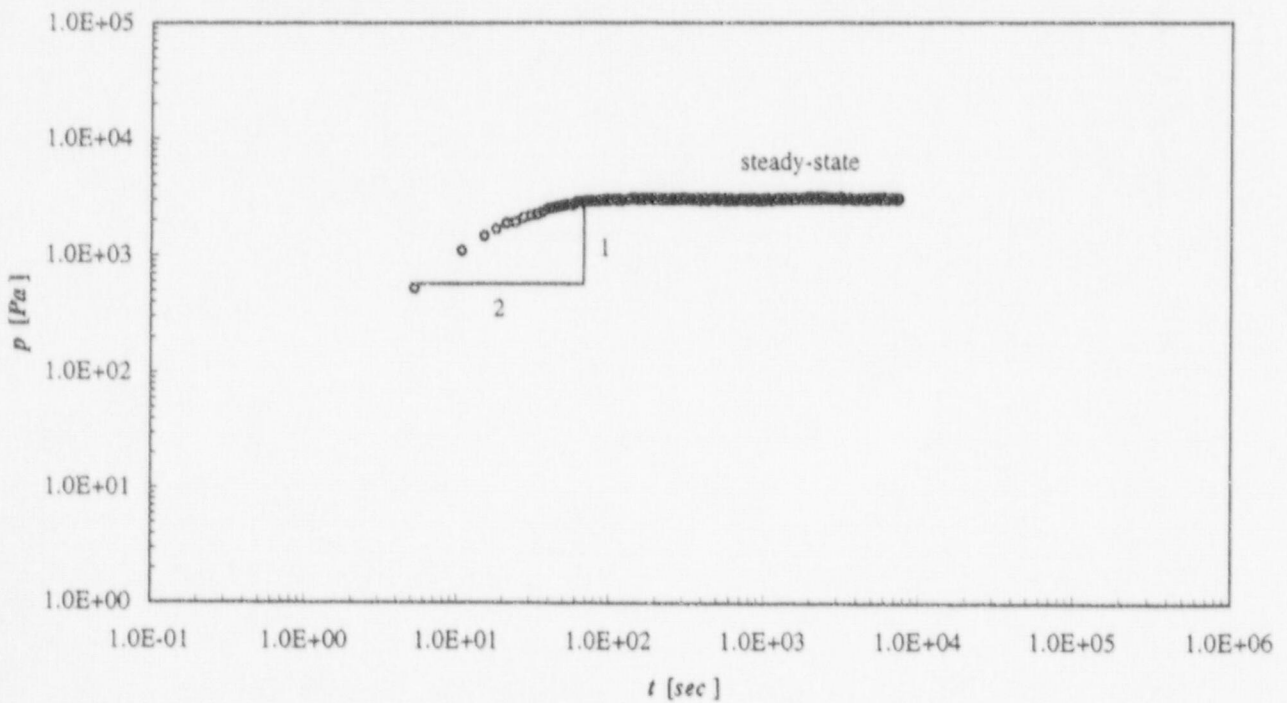
Figure 4.8: Logarithmic plot of pressure data from single-hole test ZDC0826

4.3 TYPE CURVE INTERPRETATION OF SINGLE-HOLE TESTS

We have interpreted over 40 sets of 1-m scale single-hole pneumatic injection test data by means of the spherical, radial, vertical and horizontal fracture flow models described in Chapter 3. Some of the data were interpreted using both p-based and p^2-based formulae in order to check the extent to which the method of linearizing the gas flow equations affects test result. As will be illustrated below, the single-hole test data we looked at show little sensitivity to the method of linearization. As was already mentioned, the majority of our data conform to the spherical flow model regardless of number or orientation of fractures in a test interval. We interpret this to mean that flow around most test intervals is controlled by a single continuum, representative of a three-dimensional network of interconnected fractures, rather than by discrete planar features. Only in a small number of test intervals, known to be intersected by widely open fractures, have the latter dominated flow as evidenced by the development of an early half-slope on logarithmic plots of pressure versus time; unfortunately, the corresponding data do not fully conform to available type-curve models of fracture flow. Some pressure records conform to the radial flow model during early and intermediate times but none do so fully at late time.

Figure 4.9a shows visual fits between pressure (circles) and pressure derivative (triangles) data from test CAC0813 (in a 1-m interval with center located 4.47 m from the LL mark along borehole X2), and p-based type-curves corresponding to the spherical flow model. Figure 4.9b shows similar fits between incremental squared pressure (circles) and derivative (triangles) data, and type-curves corresponding to a spherical flow model expressed in terms of dimensionless pseudo pressure w_D and its derivative $\partial w_D / \partial \ln t_D$; we recall from (2.1-16) that pseudopressure, w, is proportional to incremental squared pressure, Δp^2, when μZ is constant as we take it to be at the ALRS. Both the p-based and p^2-based sets of data exhibit a good match with type curves that correspond to zero skin ($s = 0$); indeed, most test data from the ALRS show little evidence of a skin effect. The two sets of data yield similar values of air permeability, 1.29 x 10^{-15} m^2 based on p and 1.56 x 10^{-15} m^2 based on p^2. Each set of early-time data falls on a straight line with unit slope, indicative of compressible air storage within the test interval. A pressure peak due to two-phase flow is not discernible on the logarithmic scale of Figures 4.9a,b.

Figures 4.10a,b show similar type curve matches for test CHB0617 (in a 1-m interval with center located 24.1-m from the LL mark along borehole X2). Both the p- and p^2-based sets of data exhibit a fair match with type curves that correspond to zero skin for early to intermediate data. The two matches yield comparable permeabilities, 6.11 x 10^{-17} m^2 based on p and 6.01 x 10^{-17} m^2 based on p^2. Late data do not match the type curves due to apparent displacement of water by air, which manifests itself as a gradually increasing skin effect; this two-phase flow effect is most clearly discernible when derivative data are plotted in terms of pressure squared. Each set of early-time data is strongly affected by compressible air storage within the test interval. A pressure peak due to two-phase flow is now discernible on the logarithmic scale of Figures 4.10a,b.

A complete list of air permeability values and skin obtained by means of p-based and p^2-based spherical type curve analyses is given in Table 4.3. Skin factors that appear to evolve with time due to two-phase flow are not included in the table. Figures 4.11

compares permeabilities obtained by steady-state and p-based transient analyses; Figure 4.12 compares those obtained by steady-state and p^2-based transient analyses; and Figure 4.13 does so for permeabilities obtained by p^2-based and p-based analyses. Overall, all three data sets agree reasonably well with each other. The good agreement between p^2-based and p-based results suggests that the method of linearization has little influence on our interpretation of 1-m single-hole pneumatic air injection tests at the ALRS.

Figures 4.14 a,b show p- and p^2-based type curve matches for single-hole test JGA0605 in a 1-m interval with center located 11.89 m from the LL mark along borehole Y2. In this case, the early and intermediate data appear to fit the radial flow model but the late pressure data stabilize, and the late pressure derivative data drop, in manners characteristic of three-dimensional flow. The same is seen to happen when we consider in Figures 4.15a and b data from single-hole test JJA0616 in a 1-m interval with center located 17.77-m from the LL mark along borehole Y2. We take this to indicate that the flow regime evolves from radial to spherical with time. Matching the early and intermediate data to the radial flow model yields estimates of both air permeability and air-filled porosity. We performed such analyses on data from eight 1-m test intervals in borehole Y2 but do not list them for reasons mentioned earlier.

The 1-m test interval JHB0612, with center located 15.81-m from the LL mark along borehole Y2, intersects a fracture which on televiewer (Figure 4.7) appears to be widely open. Figure 4.16 depicts an attempt on our part to match the corresponding incremental squared pressure data to type curves of pseudopressure based on the horizontal fracture flow model described in Chapter 3. Only the early time data appear to match one of these curves. We suspect that deviation of the late data from the type curves is due to the fact that whereas in reality the flow evolves with time to become three-dimensional, in the model it evolves to become radial. Upon ignoring the late data and considering only the early match, we obtain an air permeability of 1.32×10^{-13} m^2. This is about four times the value of 4.8×10^{-14} m^2 obtained by Guzman *et al.* (1996) on the basis of a steady state analysis of the late data.

An unsuccessful attempt to match the same data with a type-curve corresponding to the vertical fracture flow model, described in Chapter 3, is depicted in Figure 4.17.

Pressure and, to a much greater extent, pressure derivative data from several single-hole pneumatic injection tests, some of which are illustrated in Figures 4.18 through 4.21, exhibit inflections that are suggestive of dual or multiple continuum behaviors. We ascribe such behavior not to fractures and rock matrix as is common in the literature (Warren and Root, 1963; Odeh, 1965; Gringarten, 1979, 1984), but to fractures associated with two or more distinct length scales.

Table 4.3: Air permeabilities obtained using p- and p^2-based spherical flow models.

Test	borehole	location [m]	p-based k [m^2]	p²-based k [m^2]	k_{ss} [m^2]	skin	
CAC0813	X2	4.5	1.3E-15	1.6E-15	1.4E-15	0	
CBA0902	X2	5.5	7.7E-16	8.2E-16	1.1E-15	negative	
CDB1007	X2	12.3	1.1E-14	1.3E-14	1.8E-15	3 and increasing	
CGA1204	X2	20.2	3.1E-16	3.4E-16	3.6E-16	negative	
CHA0121	X2	23.1	1.4E-15	1.5E-15	1.6E-15	0	
CHB0617	X2	24.1	6.1E-17	6.0E-17	7.8E-17	negative	
CIA0621	X2	26.0	5.8E-17	6.4E-17	5.9E-17	0	
JFC0604	Y2	10.9	1.8E-15	1.9E-15	1.6E-15	0	
JGA0605	Y2	11.9	4.3E-15	4.6E-15	3.0E-15	0 and increasing	
JGB0608	Y2	12.9	9.2E-15	1.2E-14	2.1E-15	3 and increasing	
JGC0609	Y2	13.9	2.2E-15	2.9E-15	2.0E-15	0 and increasing	
JHA0611	Y2	14.8	3.6E-15	4.0E-15	2.7E-15	0 and increasing	
JHB0612	Y2	15.8	5.1E-14	6.5E-14	4.8E-14	0 and increasing	
JJA0616	Y2	17.8	6.5E-15	8.0E-15	5.6E-15	0 and increasing	
JJB0618	Y2	18.8	3.9E-15	4.5E-15	3.4E-15	0 and increasing	
JKB0623	Y2	21.7		9.1E-16	8.7E-16	0	
JKC0625	Y2	22.7	2.9E-15	4.3E-15	1.2E-15	2 and increasing	
JNA0713	Y2	26.6	1.2E-16	1.7E-16	9.1E-17	0 and increasing	
Y2JG0921	Y2	16.1		2.6E-14	2.8E-14	0	
VCB0924	V2	9.4	3.1E-16	3.2E-16	4.5E-16	neagtive	
VCC1001	V2	10.4	1.3E-15	1.4E-15	1.3E-15	0 and decreasing	
VFB0318	V2	18.4	1.5E-16	8.3E-17	1.1E-16	0 and increasing	
VHA0422	V2	23.4	3.1E-17	1.6E-17	2.7E-17	?	
VHB0429	V2	24.4	2.5E-17		2.0E-17	?	
WFC1014	W2A	19.6	9.0E-16	9.1E-16	8.0E-16	0	
YAA0301	Y3	2.6	4.9E-14		5.2E-14		
YDA0426	Y3	11.6	5.0E-16	5.0E-16	5.6E-16	0 and decreasing	
YFB0621	Y3	18.6	1.2E-17	1.1E-17	1.0E-17	?	
YGB0705	Y3	21.6	1.3E-17		1.0E-17	0	
YGC0709	Y3	22.6		1.3E-17	7.5E-18	?	
YIC1002	Y3	28.6	4.4E-17	3.5E-17	3.9E-17	?	
YLB1108	Y3	36.6	2.1E-17		1.6E-17		
ZCB0819	Z2	9.6	1.1E-14	1.2E-14	1.3E-14	0	
ZDB0825	Z2	12.6	1.2E-14		1.3E-14	0	
ZDC0826	Z2	13.6	4.6E-14	5.9E-14	5.3E-14	0	
ZFC0918	Z2	19.5	7.2E-17	1.6E-16	1.4E-16	negative	
ZHA1006	Z2	23.5	7.4E-17		8.2E-17		
ZIB1109	Z2	27.5	1.1E-15	1.2E-15	1.3E-15	0	
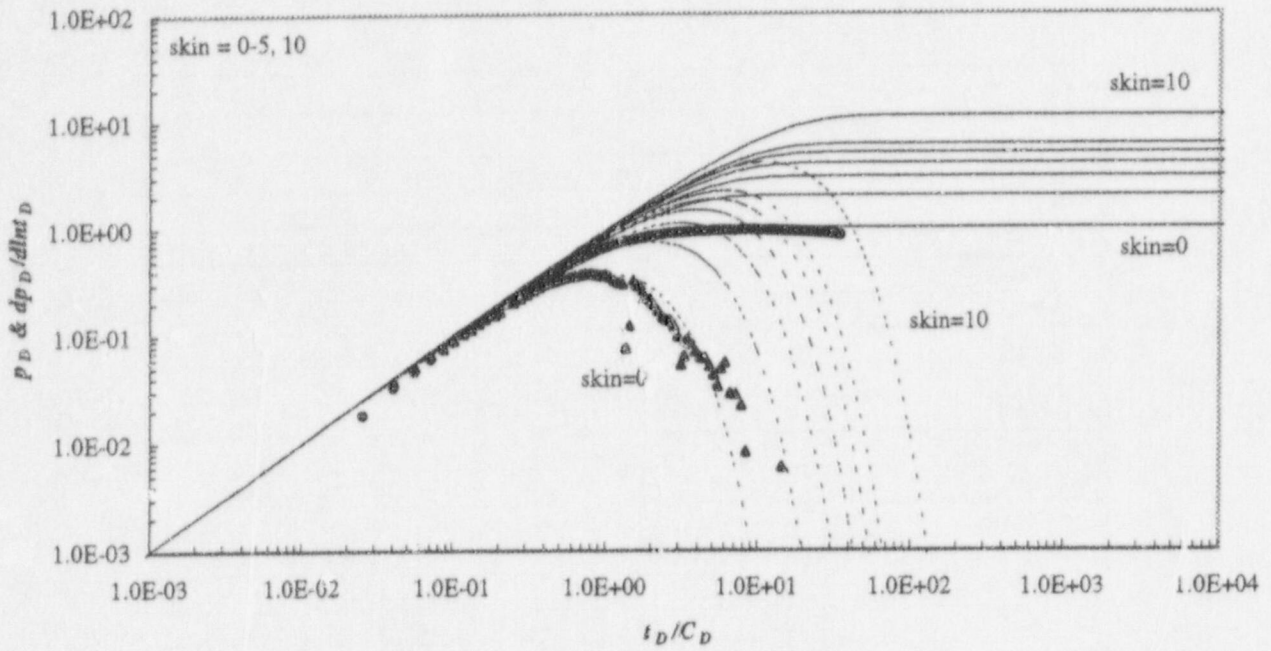
Figure 4.9a: Type curve match of data from single-hole pneumatic test CAC0813 to the liquid, spherical flow model.
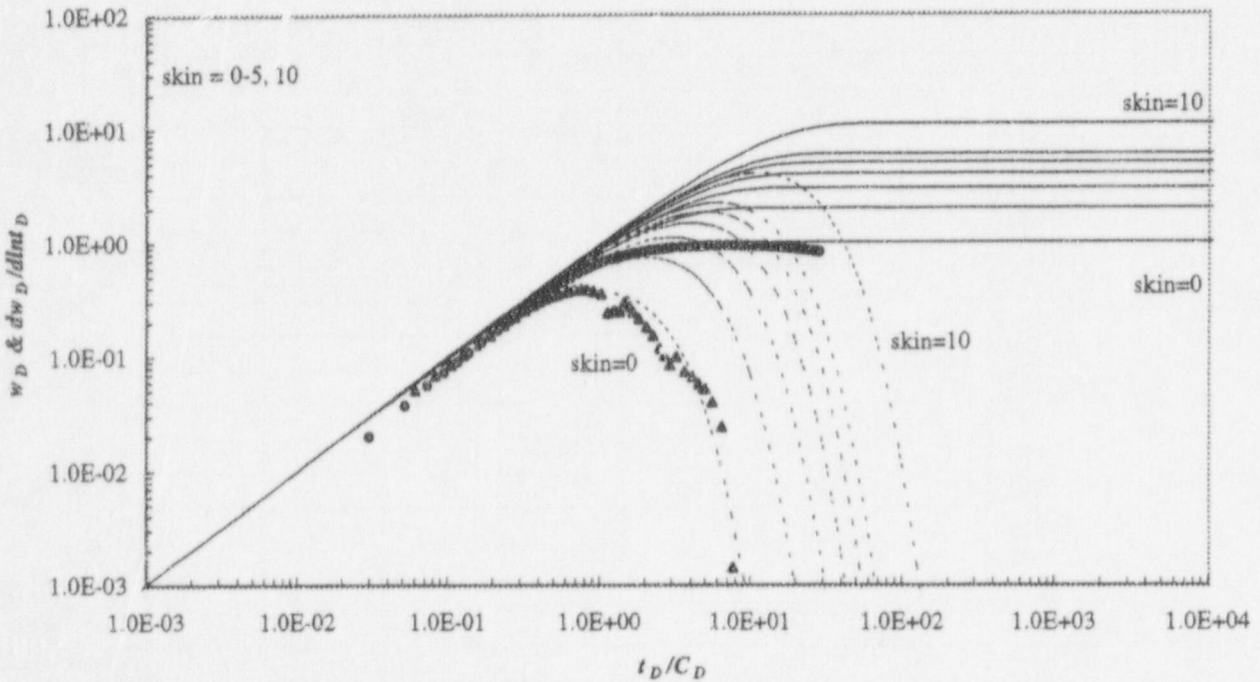
Figure 4.9b: Type curve match of data from single-hole pneumatic test CAC0813 to the gas, spherical flow model.
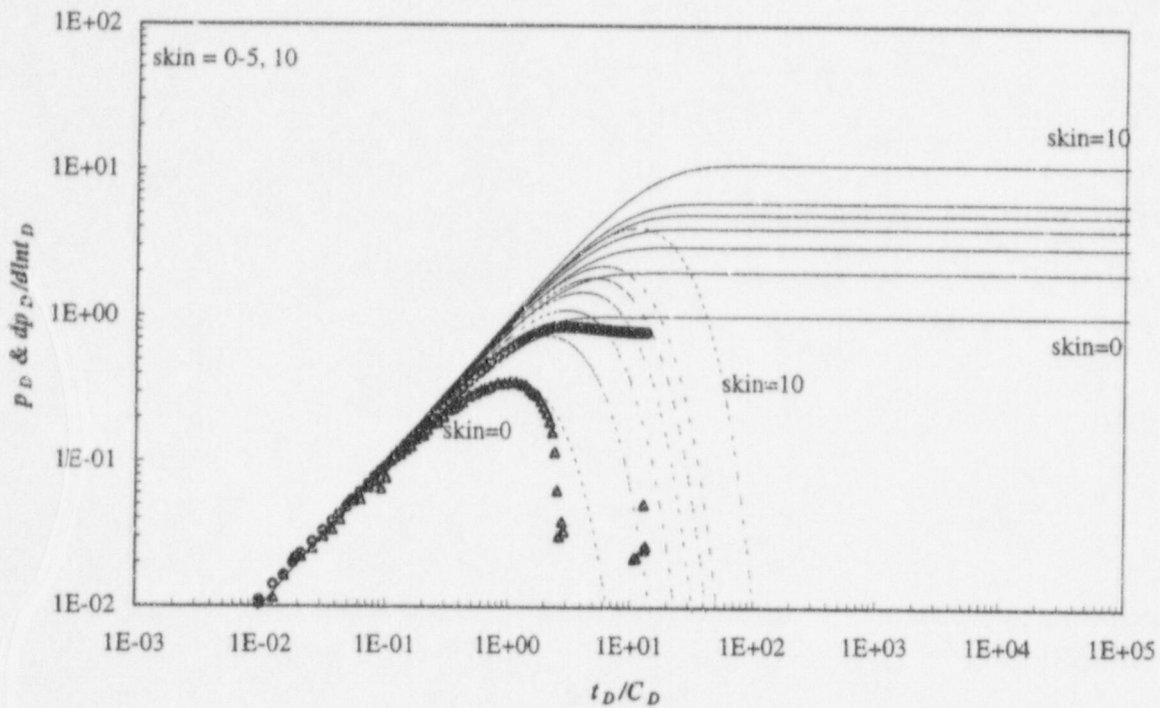
Figure 4.10a: Type curve match of data from single-hole pneumatic test CHB0617 with liquid, spherical flow model.
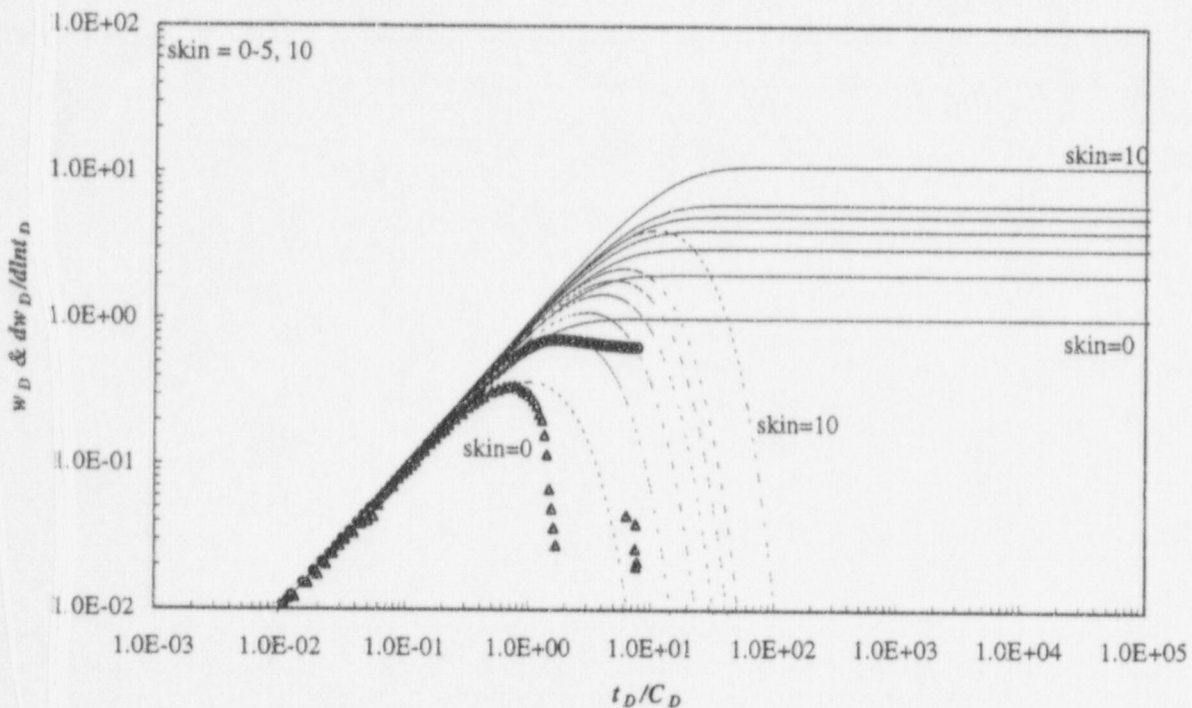
Figure 4.10b: Type curve match of data from single-hole pneumatic test CHB0617 with gas, spherical flow model.
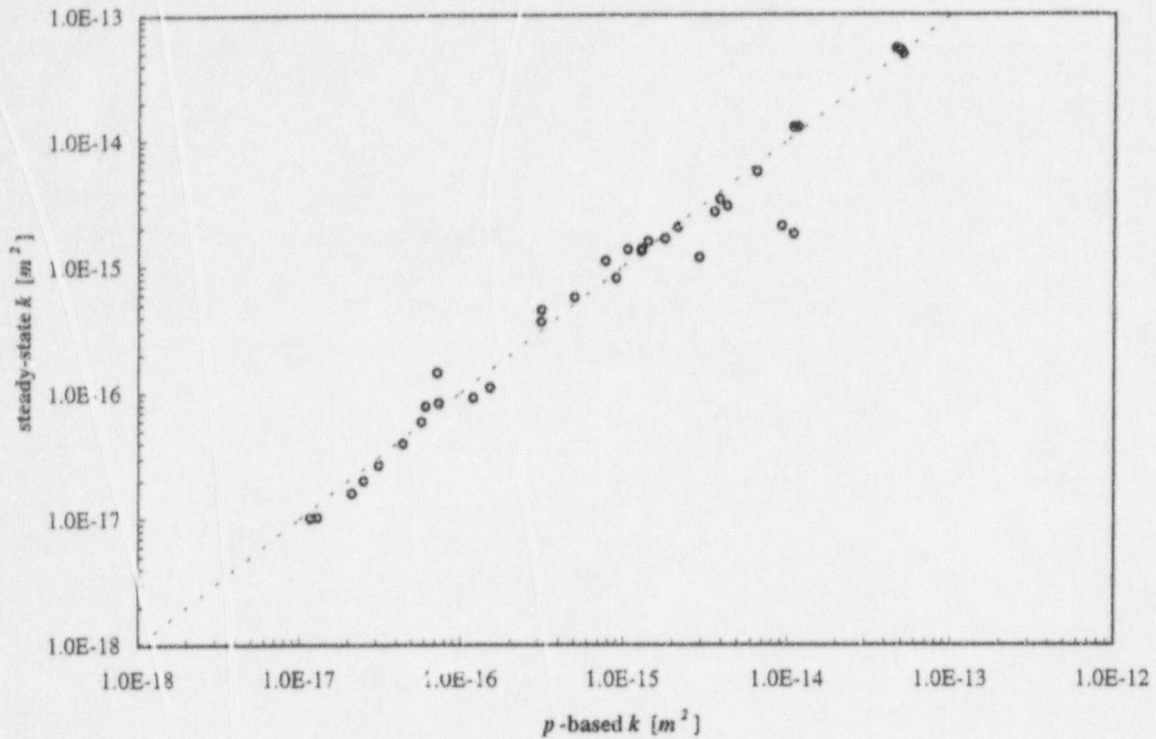
Figure 4.11: Scatter diagram of results of permeability obtained from steady-state and p-based spherical models.
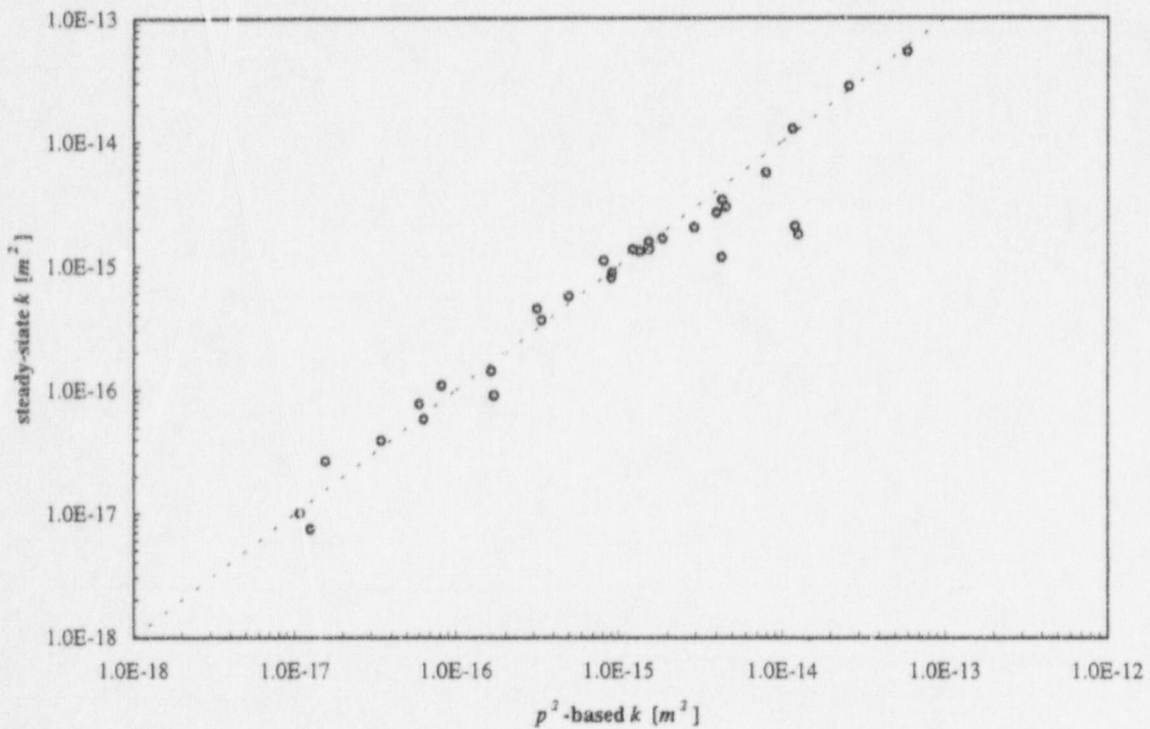
Figure 4.12: Scatter diagram of results of permeability obtained from steady-state and p^2-based spherical models
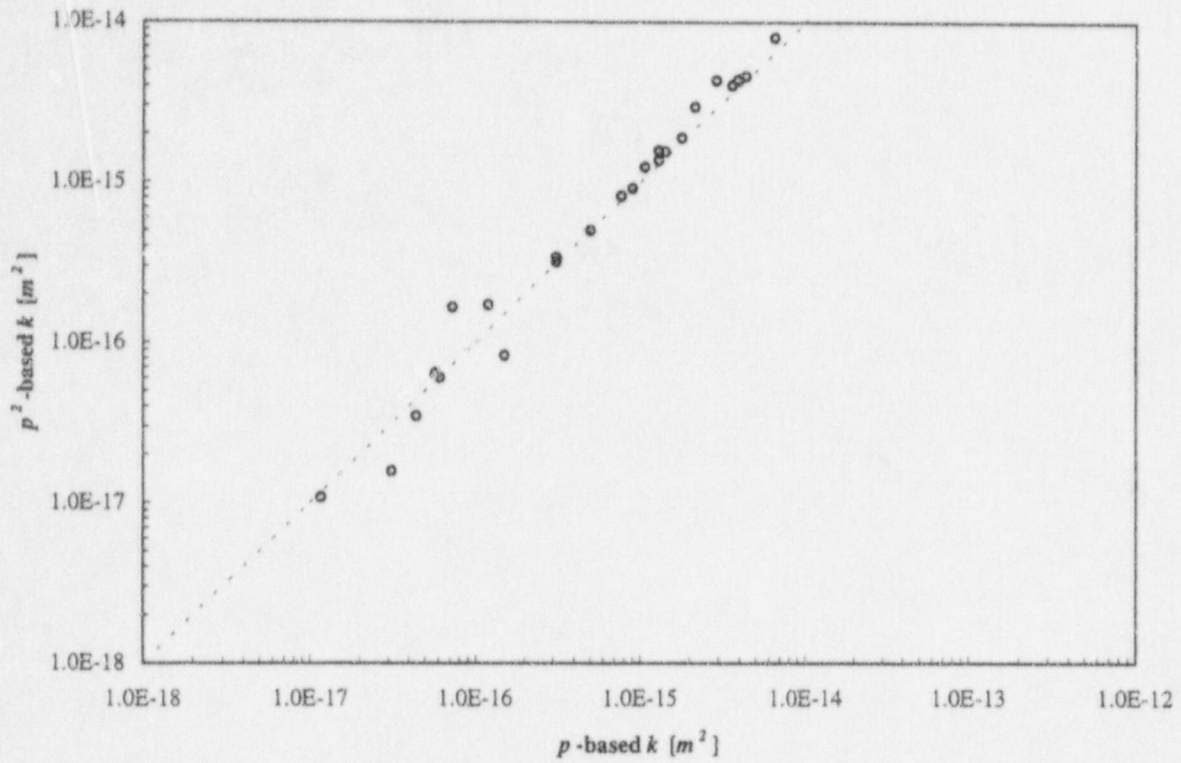
Figure 4.13: Scatter diagram of results of permeability obtained from p - and p^2-based spherical models.
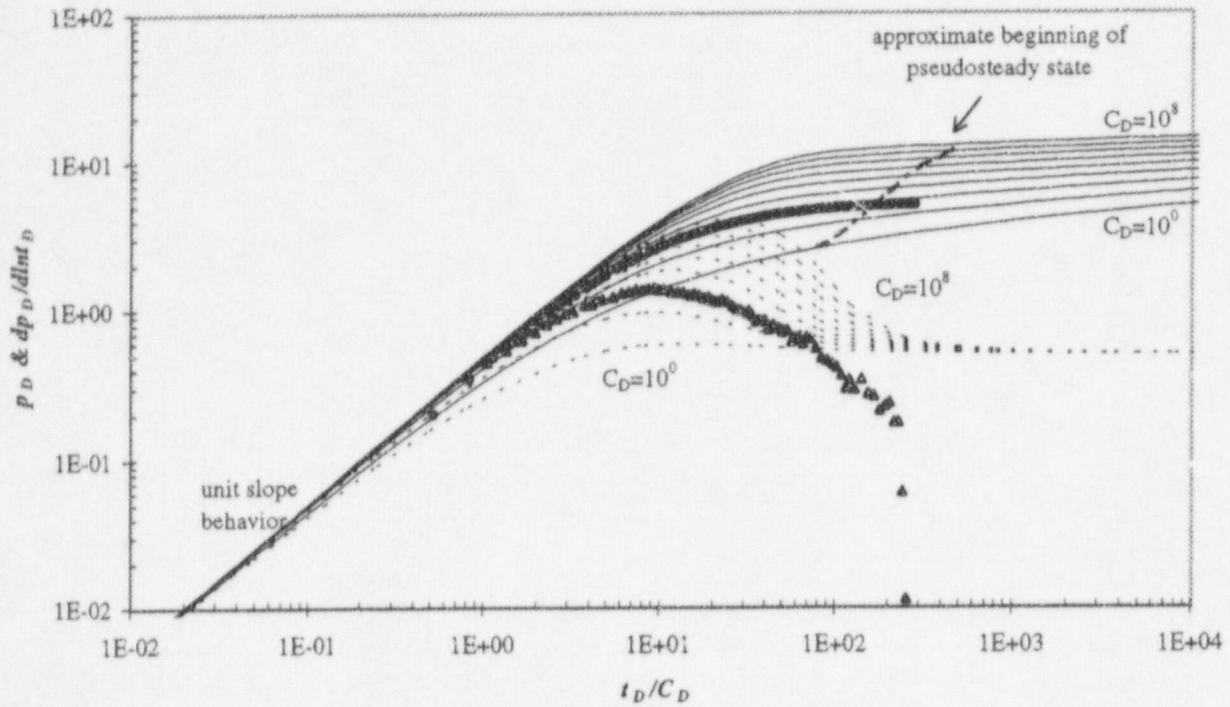
Figure 4.14a: Type curve match of data from single-hole pneumatic test JGA0605 with liquid, radial flow model.
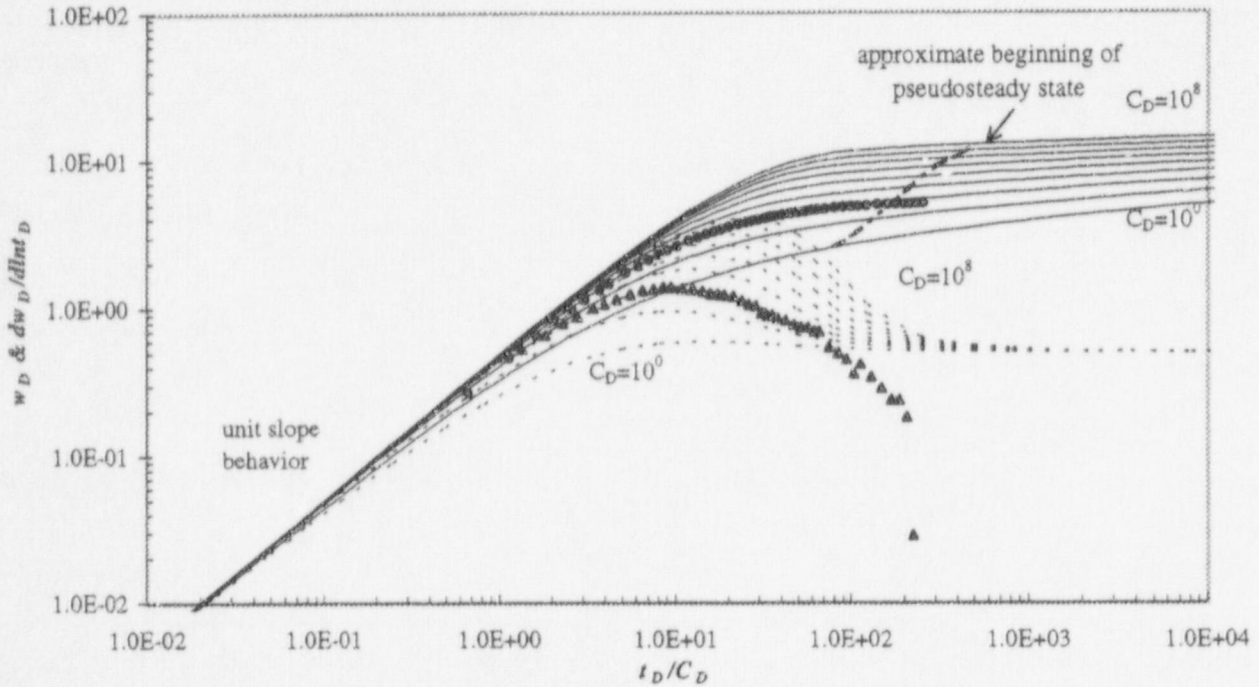
Figure 4.14b: Type curve match of data from single-hole pneumatic test JGA0605 with gas, radial flow model.
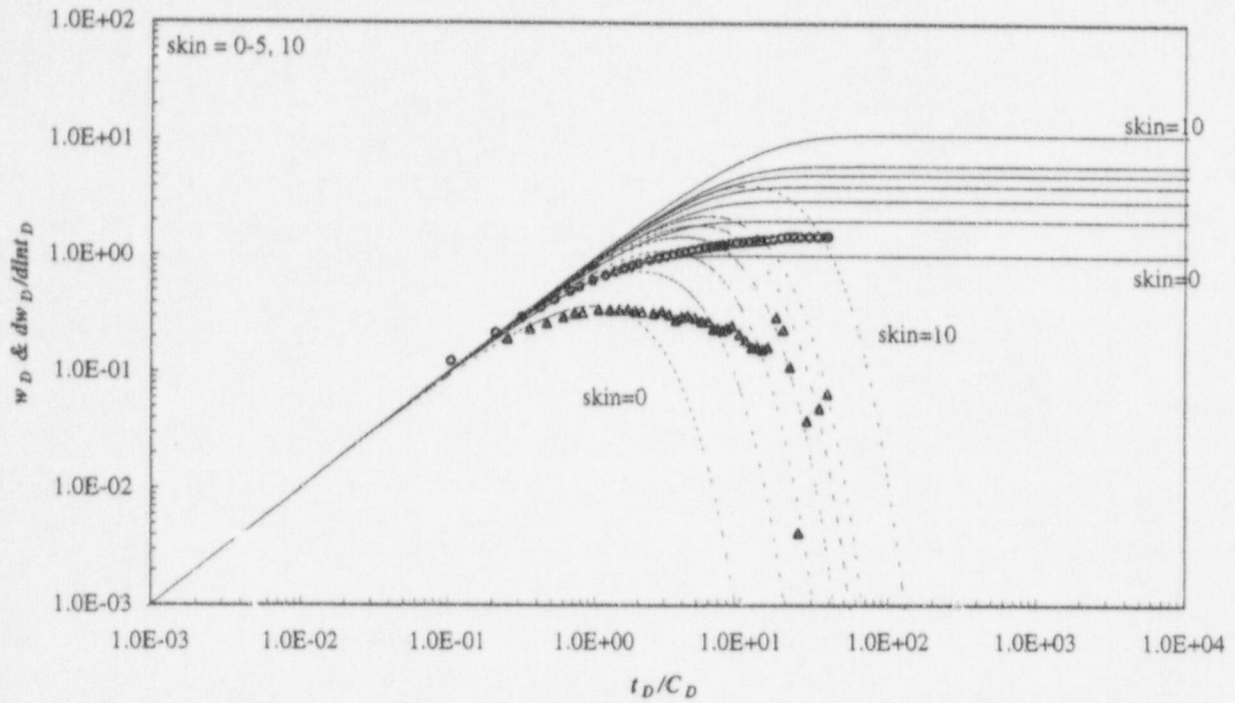
Figure 4.15a: Type curve match of data from single-hole pneumatic test JJA0616 to the gas, spherical flow model.
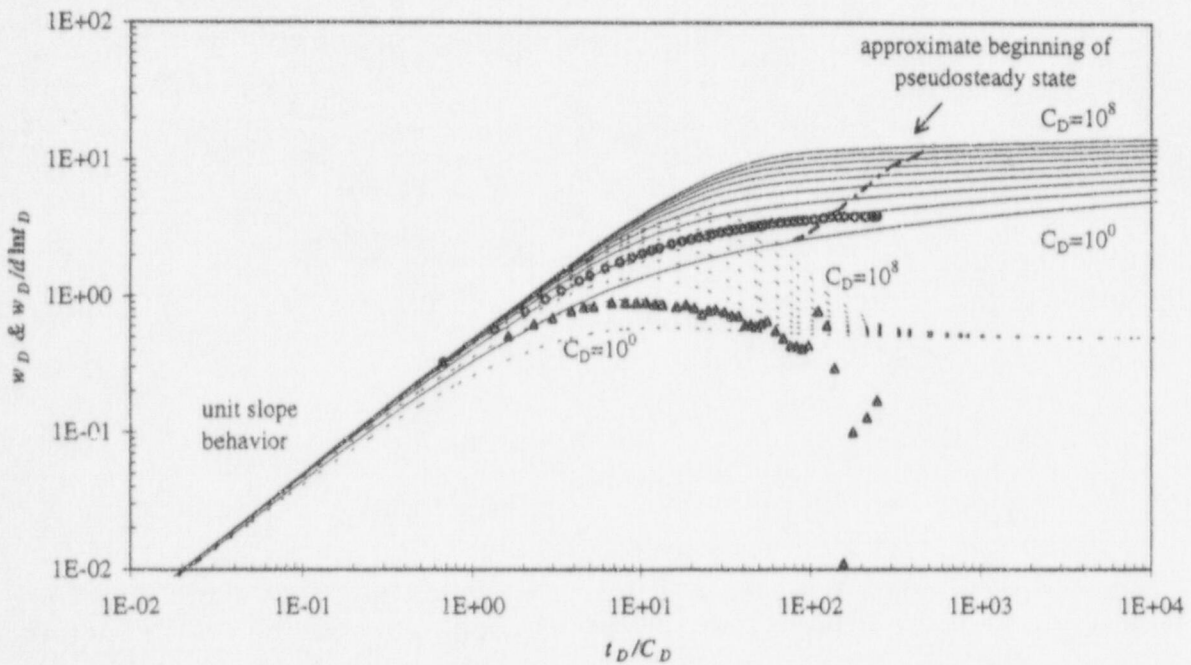
Figure 4.15b: Type curve match of data from single-hole pneumatic test JJA0616 to the gas, radial flow model.
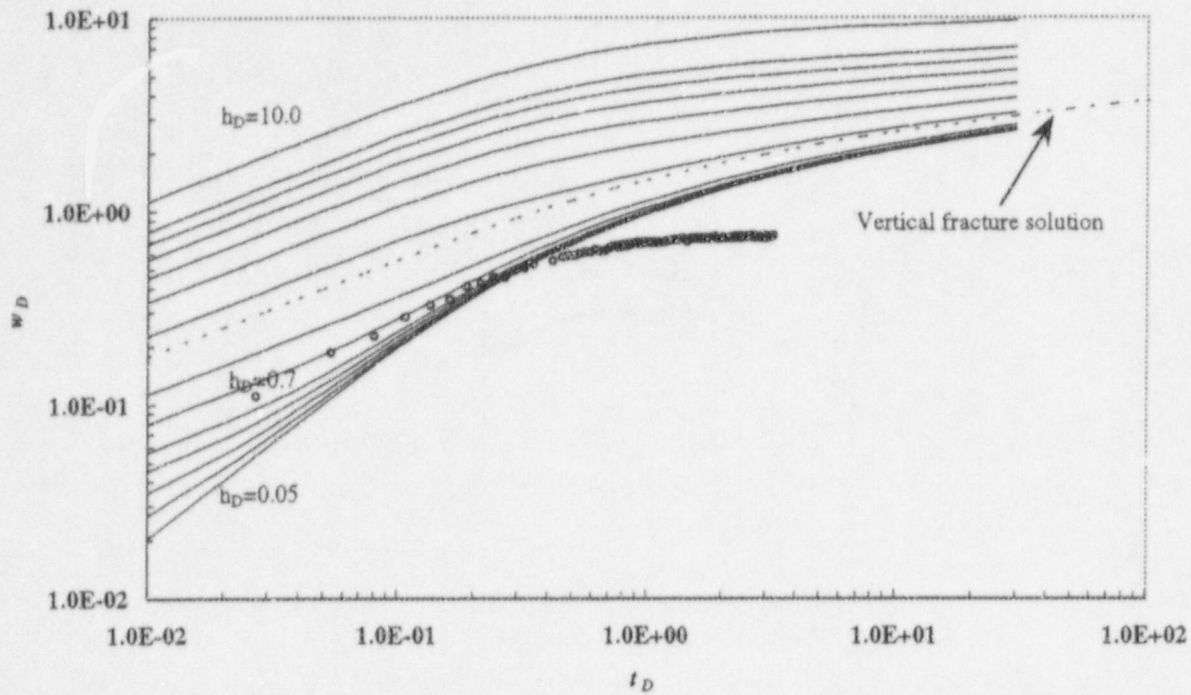
Figure 4.16: Type curve match of data from single-hole pneumatic test JHB0612 to the horizontal fracture model.
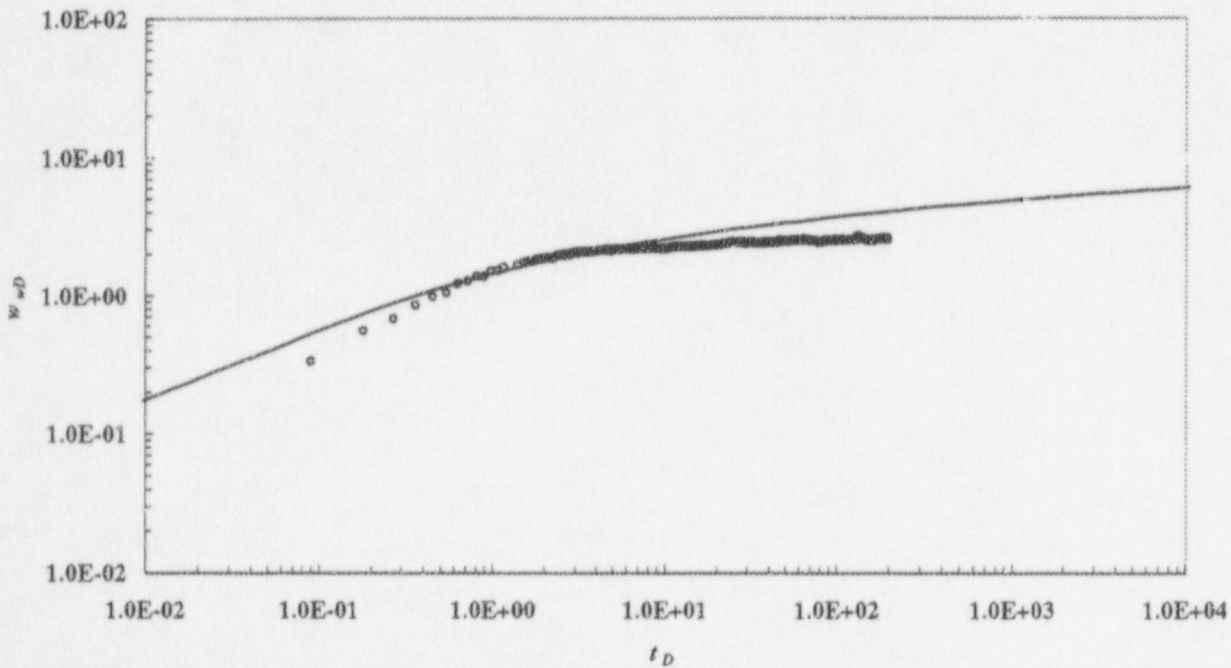
Figure 4.17: Type curve match of data from single-hole pneumatic test JHB0612 to the vertical fracture model.
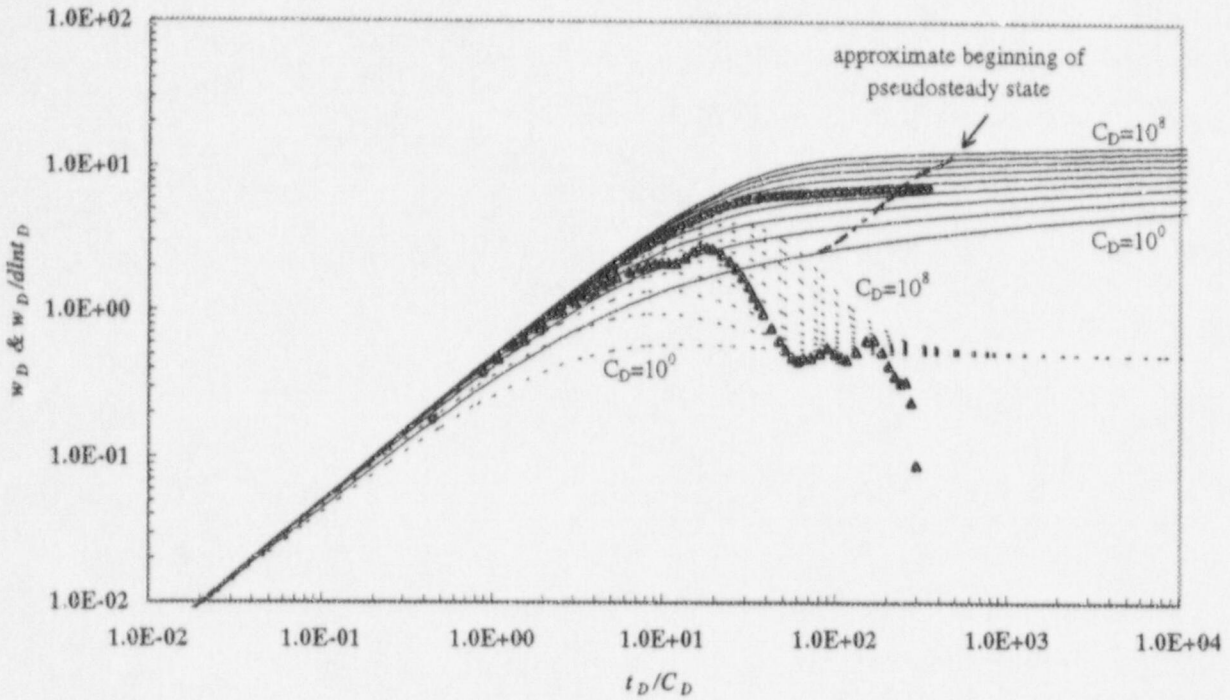
Figure 4.18: Type curve match of data from single-hole pneumatic test CDB1007 to the gas, radial flow model.
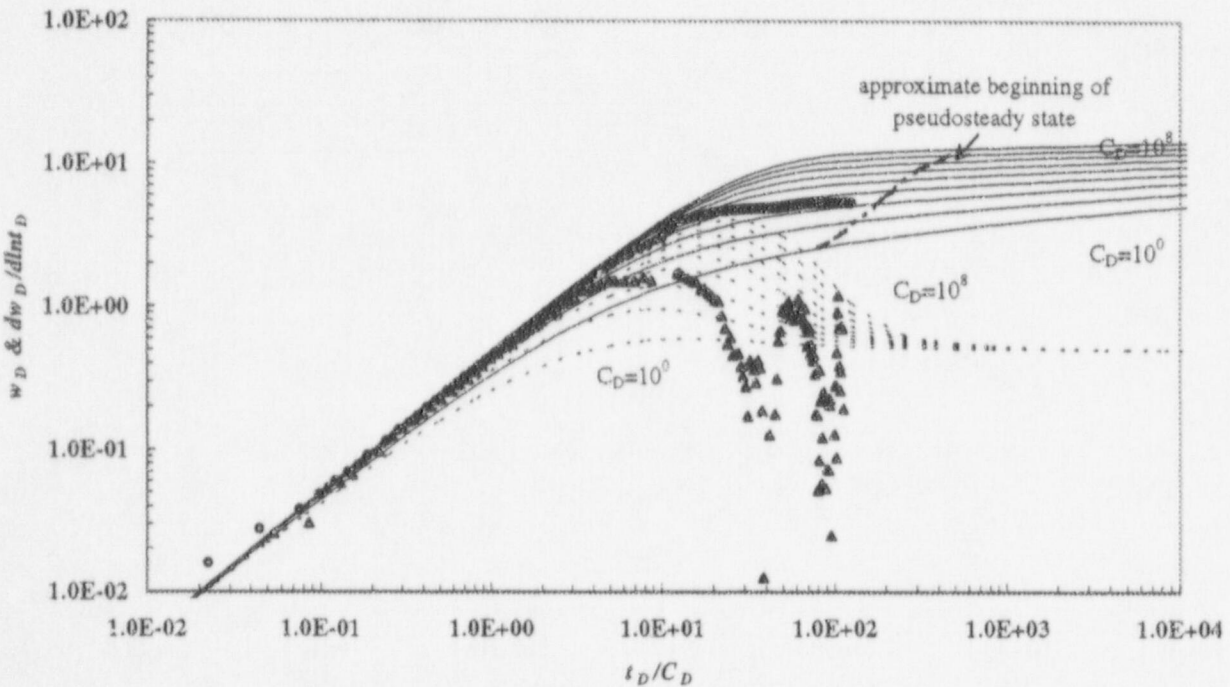
Figure 4.19: Type curve match of data from single-hole pneumatic test JNA0713 to the gas, radial flow model.
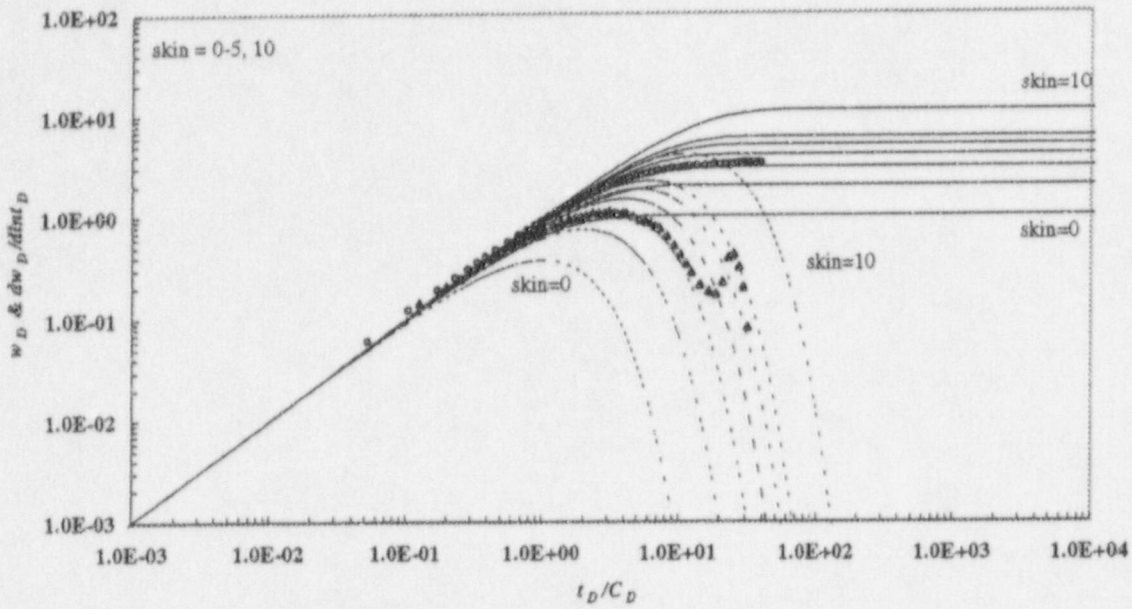
Figure 4.20: Type curve match of data from single-hole pneumatic test JKC0625 to the gas, spherical flow model.
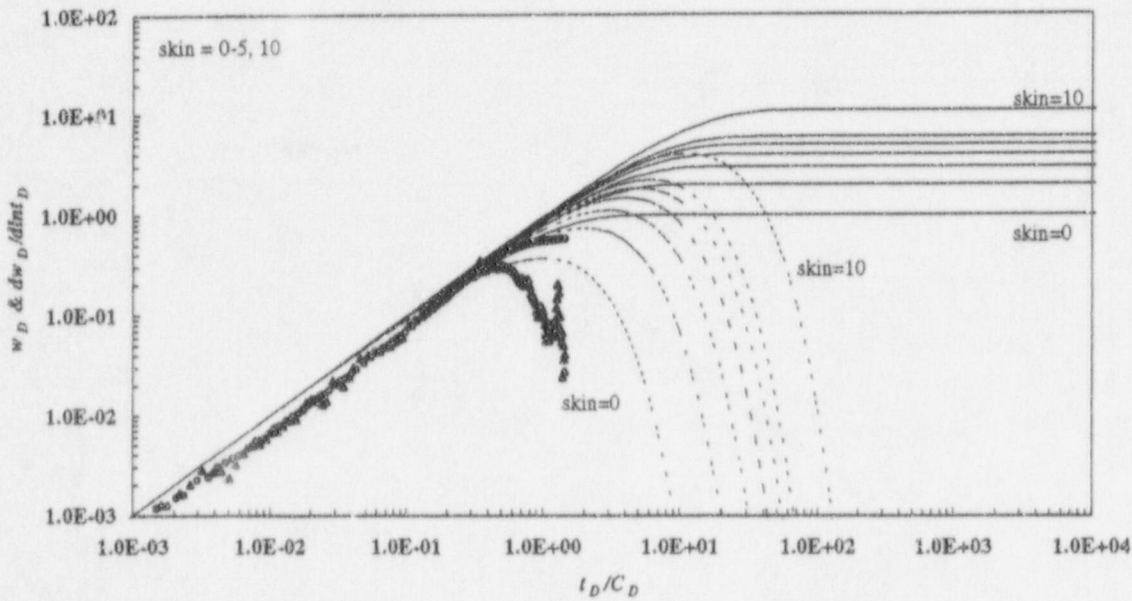
Figure 4.21: Type curve match of pressure data from test YFB0621 to the gas, spherical flow model.

5. TYPE-CURVE INTERPRETATION OF CROSS-HOLE PNEUMATIC INJECTION TEST DATA

5.1 CROSS-HOLE TEST METHODOLOGY

Single-hole air injection tests provide information only about a small volume of rock in the close vicinity of the injection interval. Our data indicate (see sections 1.2.4 and 4.2) that rock properties, measured on such small scales, vary rapidly and erratically in space so as to render the rock strongly and randomly heterogeneous. To determine the properties of the rock on a larger scale, we conducted cross-hole interference tests by injecting air into an isolated interval within one borehole, while monitoring pressure responses in isolated intervals within this and other boreholes. Of the 16 boreholes we used for cross-hole testing, 6 were previously subjected to single-hole testing. The results of the single-hole tests (primarily spatial distribution of air permeabilities and local flow geometry) together with other site information (primarily borehole televiewer images) served as a guide in our design of the cross-hole tests.

As there is little prior experience with pneumatic cross-hole tests in unsaturated fractured rocks, we conducted our tests at the ALRS in three phases. Phase 1 included line-injection/line-monitoring (LL) tests in which injection and monitoring took place along the entire length of a borehole that had been isolated from the atmosphere by means of shallow packers. Phase 2 consisted of point-injection/line-monitoring (PL) tests in which air was injected into a 2-m section in one borehole while pressure was recorded along the entire length of each monitoring borehole. During Phase 3, we conducted point-injection/point-monitoring (PP) tests in which both the injection and the monitoring intervals were short enough to be regarded, for purposes of type-curve analysis, as points. A total of 44 cross-hole pneumatic interference tests of various types (constant injection rate, multiple step injection rates, instantaneous injection) have been conducted during the years 1995 - 1997 using various configurations of injection and monitoring intervals (LL, PL and PP). The type of cross-hole test; injection borehole, interval and rate; monitoring borehole and intervals; as well as brief comments on each test are listed in Table 5.1. A test was considered to be successful when all equipment functioned reliably throughout the entire period; injection rate was adequately controlled; and all data were recorded properly.

Table 5.1: Cross-hole tests completed at ALRS

Test	Flow	Inj. Hole	Inj. Int. [m]	Q [slpm]	Comments
LL1	CR	Y2	10.0-30.0	50.0	Pressure increase appears to
LL2	CR	Y2	10.0-30.0	100.0	be proportional to Q
PL1	CR	Y2	15.0-17.0	8.5-10.0	Could not maintain constant Q
PL2	CR	Y2	15.0-17.0	10.0	Rupturing of packer lines
PL3	CR	Y2	15.0-17.0	20.0	First successful test
PL4	CR	Y2	21.0-23.0	1.0	Responses in W2A and V2
PL5	CR	Y2	18.0-20.0	1.0	Generator problems
PL6	CR	Y2	18.0-20.0	1.0	Generator problems
PL7	CR	Y2	18.0-20.0	1.0	Generator problems
PL8	CR	Y2	18.0-20.0	1.0	
PL9	CR	Y2	26.0-28.0	1.0	
PL10	CR	Y2	23.0-25.0	1.0	Response in V1
PL11	CR	Y2	21.0-23.0	1.0	Inadvertent lack of proper data recording
PL12	CR	Y2	21.0-23.0	1.0	
PL13	Barometric	Y2	21.0-23.0	0.0	No air injection
PL14	CR	Y2	21.0-23.0	1.0	First point-to-point connection
PL15	CR	Y2	21.0-23.0	1.0	Same as PL14 but without drierite
PL16	CR	Y2	21.0-23.0	1.5	Same with larger Q
PL17	Slug	Y2	21.0-23.0	2.0	First cross-hole slug test
PL18	Slug	Y2	21.0-23.0	2.0	Repeat of PL17 with more data points
PL19	CR	Y2	21.0-23.0	1.0	
PL20	CR	Y2	21.0-23.0	1.0	
PL21	Slug	Y2	21.0-23.0	0.0	Packer inflation slug test
PL22	Barometric	Y2	21.0-23.0	0.0	
PL23	Barometric	Y2	21.0-23.0	0.0	
PL24	CR	Y2	21.0-23.0	?	Data lost?
PL25	CR	Y2	21.0-23.0	1.0	Added 3-packer monitoring system in V2
PL26	Step	Y2	21.0-23.0	0.5, 1.0, 1.5, 2.0	Isolated V2-W2 intersection
PL27	SH-neutron	W3	14.7-16.9	0.5	No change in neutron counts
PL28	SH-neutron	W3	16.9-19.1	0.5	No change in neutron counts
PP1	CR	Y2	15.0-17.0	1.5	Unknown flow rate
PP2	CR	Y2	15.0-17.0	18.0	Y3 and X2 surface guard packers kept uninflated
PP3	CR	Y2	15.0-17.0	15.0	All packers inflated
PP4	CR	Y2	15.0-17.0	50.0	All packers inflated
PP5	Step	X2	18.5-20.7	5.0 and 10.0	All packers inflated
PP6	Step	Z3	15.9-17.9	5.0 and 10.0	All packers inflated
PP7	Step	W3	19.2-20.4	5.0 and 10.0	All packers inflated
PP8	CR	Y2	15.0-17.0	50.0	Flow rate changes towards end of test
PP9	Step	Y2	15.0-17.0	75.0 and	Flow rate changes towards

				50.0	end of test
PP10	CR	Y2	15.0-17.0	25.0	All packers deflated except Y2 injection string
PP11	Slug	Y2	15.0-17.0	100.0	Monitored Y2M, Y1M, W2AM, V3M and X2M at fastest possible rate
PP12	CR	Y2	15.0-17.0	25.0	All packers inflated
PP13	CR	Y2	15.0-17.0	0.5	
PP14	SH-neutron; Step	W3	25.7-26.9	0.5, 1.0, 1.3, 1.9	Slight decrease in neutron counts

CR = constant rate

SH-neutron = single-hole test with neutron probe installed in the injection interval

Slug = slug injection of air

Barometric = barometric test in which all packers were inflated, pressure in the intervals were monitored while there was no air injection at the injection interval

5.1.1 Instrumentation Used in Cross-Hole Tests

Cross-hole tests were conducted using modular straddle packer systems that were easily adapted to various test configurations and allowed rapid replacement of failed components, modification of the number of packers, and adjustment of distances between them in both the injection and monitoring boreholes. For their construction we relied on relatively inexpensive PVC pipes, which can be worked on in the field using hand tools and are sufficiently flexible to slide with relative ease up and down an uneven borehole. Figure 5.1 is a schematic diagram of the main cross-hole injection string of packers. The air-filled volume of the injection interval was made smaller than it had been during single-hole testing so as to minimize borehole storage effects.

The main injection string installed in borehole Y2 consisted of three packers, one near the soil surface to isolate the borehole from the atmosphere, and two to enclose the injection interval. Pressure transducers were used to monitor absolute pressure and temperature in each of the three borehole sections that had been isolated from each other in this manner. In general, the most sensitive transducers (GEOKON-4500H-0010) were placed close to the injection interval were we expected to see relatively pronounced pressure responses. Sensitive transducers were also placed furthest away from the injection interval, and in monitoring intervals Y1M, Y3M, Y3B, Z2M, Z2L, Z3M and Z3B, where we expected to see pronounced barometric pressure effects.

Two types of borehole monitoring systems were employed, one with a single packer near the soil surface to monitor pressure along the entire length of a borehole (6 units) and another, modular system with three or four packers to monitor pressure in several isolated segments of a borehole (9 units). Monitoring intervals with a single packer near the soil surface are identified by borehole designation; for example V1, X1 and W1. Where a modular system separates a borehole into three isolated intervals, we append to the borehole designation a suffix U, M or B to identify the upper, middle or bottom interval, respectively; for example V3U, V3M and V3B. Where a modular system separates a borehole into four isolated intervals, we append to the borehole designation a suffix U, M, L or B to identify the upper, lower or bottom interval, respectively; for example Z2U, Z2M, Z2L, and Z2B. Of the 9 modular monitoring

systems, 7 were equipped with two tracer-sampling ports each, which we had use for air injection.
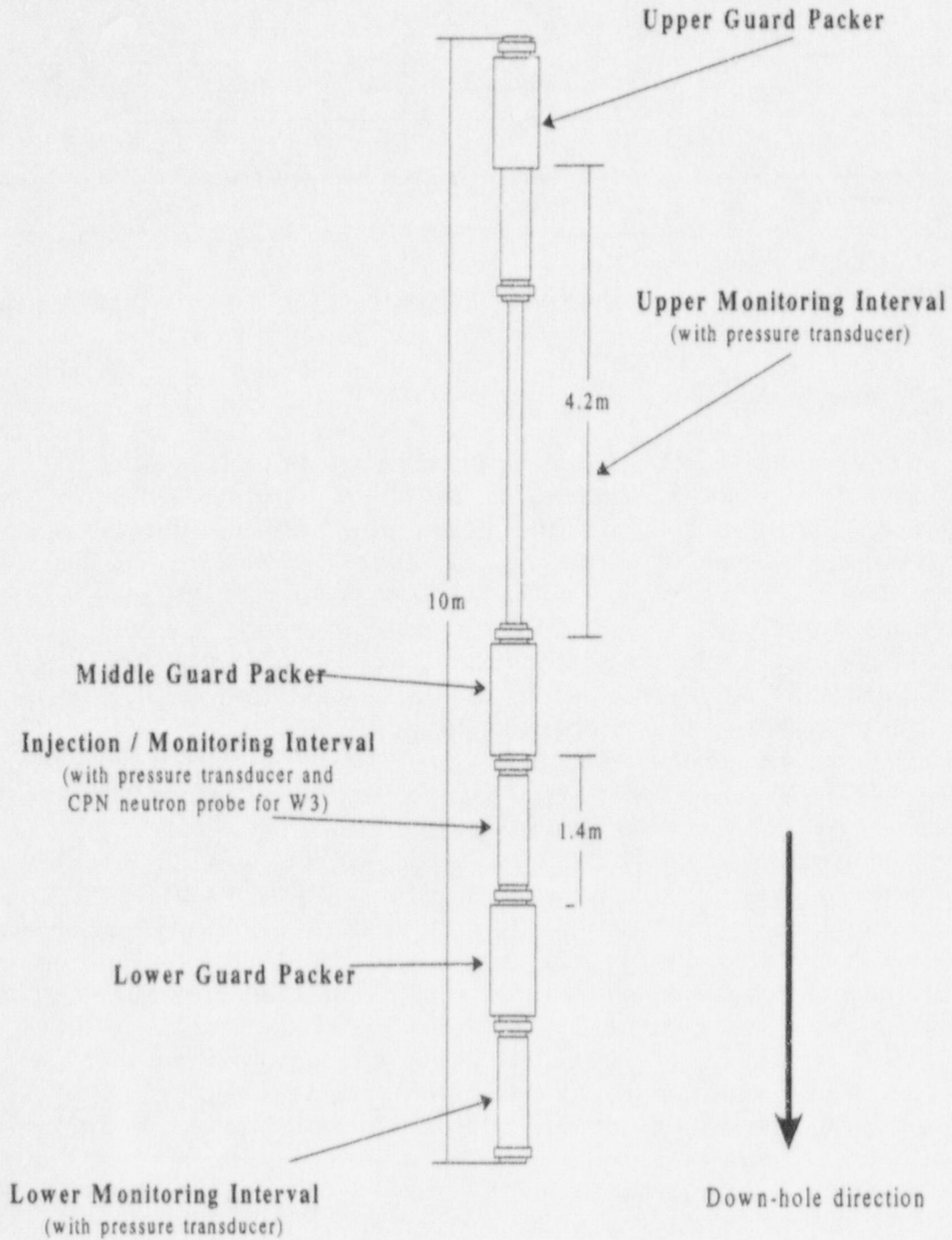
Figure 5.1: Injection and monitoring systems used for cross-hole tests

Table 5.2: Information on injection and monitoring intervals with pressure transducer types during phase 3 cross-hole tests

Interval	Interval type	PT manufacturer	Model	PT Range [Psi]	PT Resolution	Tracer sampling ports (injection port)
Pressure transducer installed in injection and monitoring intervals						
V1	Line	Geokon	4500AL-25	0-25	High	No
V2U	Line	Honeywell	Microswitch	0-15	Medium	No
V2M	Point	Geokon	4500AL-25	0-25	High	Yes
V2B	Line	Honeywell	Microswitch	0-15	Medium	No
V3U	Line	Druck	PDCR	0-15	Medium	No
V3M	Point	Geokon	4500AL-25	0-25	High	No
V3B	Line	Druck	PDCR	0-15	Medium	No
W1	Line	Geokon	4500AL-25	0-25	High	No
W2	Line	Honeywell	Microswitch	0-15	Medium	No
W2AU	Line	Honeywell	Microswitch	0-15	Medium	No
W2AM	Point	Geokon	4500AL-25	0-25	High	No
W2AL	Point	Geokon	4500AL-25	0-25	High	No
W2AB	Line	Honeywell	Microswitch	0-15	Medium	No
W3U	Line	Honeywell	Microswitch	0-15	Medium	No
W3M	Point	Geokon	4500AL-25	0-25	High	No
W3B	Line	Honeywell	Microswitch	0-15	Medium	No
X1	Line	Geokon	4500AL-25	0-25	High	No
X2U	Line	Geokon	4500AL-25	0-25	High	No
X2M	Point	Geokon	4500AL-25	0-25	High	Yes
X2B	Line	Geokon	4500AL-25	0-25	High	No
X3	Line	Geokon	4500AL-25	0-25	High	No
Y1U	Point	Druck	PDCR	0-15	Medium	No
Y1M	Point	Geokon	4500H-0010	0-10	Very High	Yes
Y1B	Line	Geokon	4500AL-25	0-25	High	No
Y2U	Line	Honeywell	Microswitch	0-15	Medium	No
Y2M	Point	Geokon	4500AL-25	0-25	High	Yes
Y2B	Line	Honeywell	Microswitch	0-15	Medium	No
Y3U	Line	Geokon	4500AL-25	0-25	High	No
Y3M	Point	Geokon	4500H-0010	0-10	Very High	Yes
Y3B	Line	Geokon	4500H-0010	0-10	Very High	No
Z1	Line	Geokon	4500AL-25	0-25	High	No
Z2U	Line	Geokon	4500AL-25	0-25	High	No
Z2M	Point	Geokon	4500H-0010	0-10	Very High	No
Z2L	Point	Geokon	4500H-0010	0-10	Very High	Yes
Z2B	Line	Geokon	4500AL-25	0-25	High	No
Z3U	Line	Geokon	4500AL-25	0-25	High	No
Z3M	Point	Geokon	4500H-0010	0-10	Very High	Yes
Z3B	Line	Geokon	4500H-0010	0-10	Very High	No
Pressure transducers installed within injection system in field laboratory						
Injection system		Geokon	4500AL-25	0-25	High	
Packer line		Honeywell	MS	0-60	Medium	
Barometer		Geokon	4580-1-2.5	0-2.5	Very High	

In total, thirty-eight packers were used in each cross-hole test. The packers were approximately 1-*m* long in all PP tests performed during phase 3 of the project except in monitoring system V3 where shorter packers, 50-*cm* in length, had been employed. An air manifold was constructed to distribute air pressure evenly and efficiently through the system. A pressure gauge was placed in the manifold to allow visual check of packer inflation. The system allowed inflating packers individually and, in this way, monitoring and recording their pressure as well as varying the lengths and configurations of monitoring intervals without necessarily moving the down-hole equipment. Packer inflation pressure was maintained at 60 *Psi* throughout each cross-hole test. Temperature readings were taken by downhole and surface pressure transducers that are temperature compensated as noted in Table 5.2.

The equipment included twenty-seven Geokon™ 4500 pressure transducers which compensate pressure for fluctuations in temperature, one Geokon™ 4580 barometric transducer which provides temperature compensation, three Druck PDCR™ pressure transducers without such compensation, and ten Honeywell-MICROSWITCH™ pressure transducers without temperature compensation. The type of pressure transducers, their locations, range and relative resolutions are listed in Table 5.2.

To monitor relative changes in water content around the injection interval, we installed a BOART LONGYEAR CPN® model 503 neutron probe in the injection interval toward the end of our project. As the probe was sensitive to PVC, the latter was replaced by galvanized steel.

The air injection system is illustrated schematically in Figure 5.2. It included a mass flow meter, several pressure valves and regulators, an oil and a water filter, a 7-μm particle filter, a pressure transducer, a relative humidity sensor, drierite (anhydrous calcium sulfate) and electronic equipment to automatically collect field data. Pressure and temperature in the injection air stream were measured using a Geokon™ 4500 pressure transducer compensated for temperature. Relative humidity (RH) in the air stream was measured using a VAISALA™ 50Y probe. Various Sierra Instruments Sidetrack™ 830/840 mass flow controllers and meters operated over ranges of 0-0.1 *slpm* (standard liters per minute), 0-20 *slpm*, and 0-100 *slpm*, supplying a constant injection flow rate that could be adjusted to between 0.1 to 100 *slpm*. For simplicity of test interpretation, we tried to maintain a constant mass injection flow rate during each test. As the mass flow controller was sensitive to variations in moisture content in the air stream, we used dry air for injection to help maintain the rate constant. This, we believe, had little if any effect on pressure variations in the monitoring intervals. Not shown in Figure 5.2 are a 0-2 *Psi* barometric transducer, two 10-*kW* generators, four compressors, and solar panels that made up the rest of the system.

Data were recorded at 1- to 10-*sec* intervals throughout the duration of each cross-hole test using three Campbell Scientific™ CR10 dataloggers connected to a Campbell Scientific™ SC32a optically isolated interface, which allowed periodic downloading of data onto an on-site personal computer with a removable, large capacity disk drive. Three Campbell Scientific™ AM416 multiplexers were concatenated to allow simultaneous recording of downhole pressure and temperature data, packer pressure, battery voltage, mass flow rate, air temperature, air relative humidity and barometric pressure throughout the duration of each test. The electronic system was tested

thoroughly for defects. The computer program which controls each datalogger was optimized for maximum efficiency.

5.2 CROSS-HOLE TESTING PROCEDURE WITH EMPHASIS ON TEST PP4

A typical cross-hole test consisted of packer inflation, a period of pressure recovery, air injection and another period of pressure recovery. Our system allowed rapid release of packer inflation pressure when the corresponding recovery was slow, but this feature was never activated even though recovery had sometimes taken several hours. Once packer inflation pressure had dissipated in all (monitoring and injection) intervals, air injection at a constant mass flow rate began. It generally continued for several days until pressure in most monitoring intervals appeared to have stabilized. In some tests, injection pressure was allowed to dissipate until ambient conditions have been recovered. In other tests, air injection continued at incremental flow rates, each lasting until the corresponding pressure had stabilized, before the system was allowed to recover.

In this report we focus on the analysis of test PP4 conducted during the third phase of our program. This test was selected because it involved 1) injection into a high-permeability zone in borehole Y2 which helped pressure to propagate rapidly across much of the site; 2) injection at a relatively high flow rate which led to unambiguous pressure responses in a relatively large number of monitoring intervals; 3) the largest number of pressure and temperature monitoring intervals among all tests; 4) a complete record of relative humidity, battery voltage, atmospheric pressure, packer pressure, and injection pressure; 5) the least number of equipment failures among all tests; 6) flow conditions (such as injection rate, fluctuations in barometric pressure, battery voltage, and relative humidity) that were better controlled, and more stable, than in all other tests; 7) minimum boundary effects due to injection into the central part of the tested rock mass; 8) a relatively long injection period; 9) rapid recovery; and 10) a test configuration that allowed direct comparison of test results with those obtained from two line-injection/line-monitoring tests (LL1 and LL2), and a point-injection/line-monitoring test (PL3), at the same location (see Table 5.1 for a list of cross-hole tests). Stable flow rate and barometric pressure made type-curve analysis of test PP4 results relatively straightforward.

Test PP4 was conducted by injecting air at a rate of 50 *slpm* into a 2-*m* interval located 15 – 17 *m* below the LL marker (Table 4.1) in borehole Y2 as indicated by a large solid circle in Figure 5.3. The figure also shows a system of Cartesian coordinates x, y, z with origin at the center of the injection interval which we use to identify the placement of monitoring intervals relative to this center. Responses were monitored in 13 relatively short intervals (0.5 - 2 *m*) whose centers are indicated in the figure by small white circles, and 24 relatively long intervals (4 - 42.6 *m*) whose centers are indicated by small solid circles, located in 16 boreholes. Several of the short monitoring intervals (V2M, V3M, W2AM, W2AL, W3M, X2M, Z2M, Z2L and Z3M) were designed to intersect a high permeability region (Figures 1.12 and 1.13) that extends across much of the site at a depth comparable to that of the injection interval. Table 5.3 lists coordinates of the centers of all monitoring intervals, their lengths B, radial distances R from the center of the injection interval, geometric parameters β_1 and β_2 defined in (3.4-4) and (3.4-5), and maximum pressure during the test.

Data recorded at the surface during the test included barometric pressure (Figure 5.4), mass flow rate (Figure 5.5), packer pressure (Figure 5.6), battery voltage (Figure 5.7) and relative humidity in the injection air stream (Figure 5.8). Fluctuations in barometric pressure are seen to have been quite regular with an amplitude of about 0.25 kPa during the first 250,000 sec of the test. It later dropped by about 1 kPa and stayed nearly constant until the end of the test. Mass flow rate remained constant except for a slight drop of 1 to 2 $slpm$ at about 175,000 sec. Packer pressure remained constant at 60 Psi throughout the first part of the test but dropped approximately 275,000 sec into the test in apparent response to a concurrent drop in barometric pressure. Battery voltage, supplied by solar panels, increased during the day and decreased at night to form a square wave. Relative humidity in the injection stream varied diurnally.
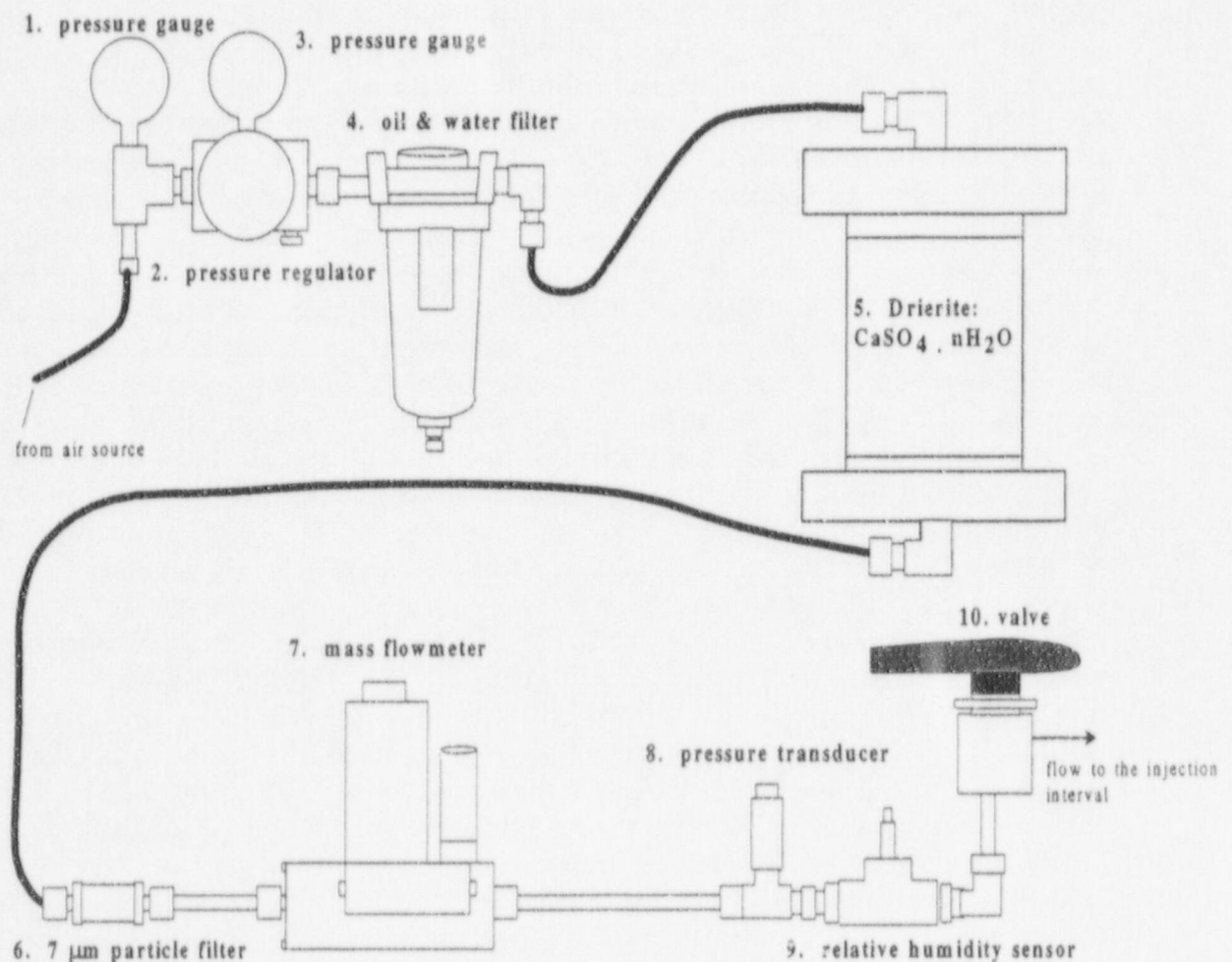
Figure 5.2: Air injection system installed in the field laboratory.
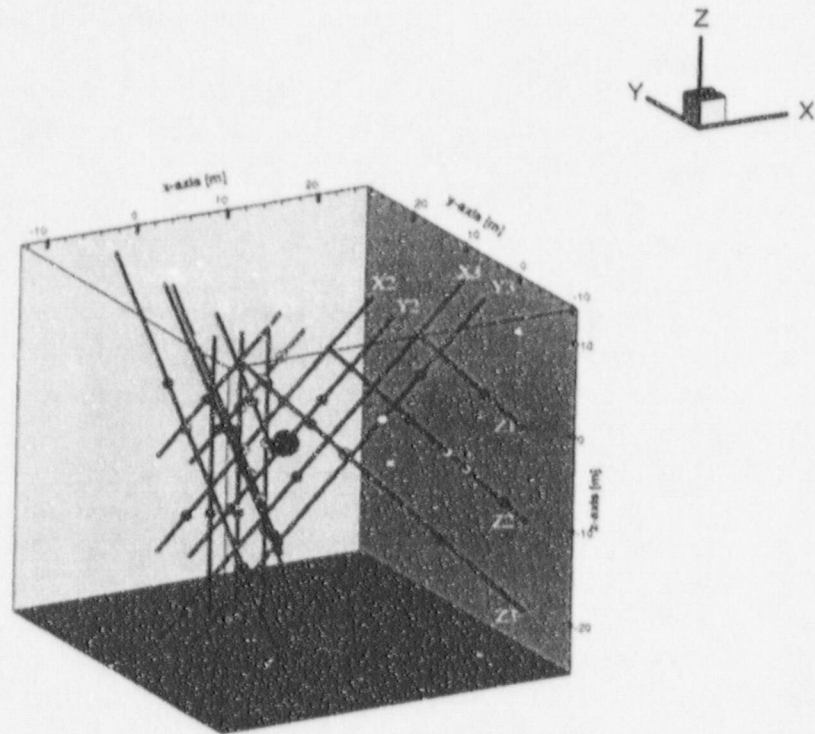
Figure 5.3: Locations of centers of injection and monitoring intervals. Large solid circle represents injection interval, small solid circles represent short monitoring intervals, and open circles represent long monitoring intervals.

Arithmetic plots of pressure responses in all monitoring intervals as well as in the injection interval are presented in Figures 5.9 - 5.24. Pressure responses in the 2.0-m injection interval Y2M, 7.1-m monitoring interval Y2U above it, and 12.9-m monitoring interval Y2B below it are depicted in Figure 5.9. The figure also shows back pressure at the surface, recorded behind the mass flow controller (Figure 5.2), which is seen to be about twice as high as pressure in the injection interval. Fluctuations in back pressure could be due to variations in relative humidity and air temperature within the injection line at the surface. As injection mass flow rate is constant, these fluctuations have no adverse effect on pressure in the injection interval.

Pressure in the injection interval (Figure 5.9) is seen to reach a stable value almost immediately after the start of injection and then to decline slowly with time. A similar pressure behavior was observed in many single-hole tests by Guzman *et al.* (1994, 1996) and attributed by them to a two-phase flow effect, as discussed in section 4.2. No such effect is seen in any of the monitoring intervals, not even in those situated immediately above and below the injection interval in borehole Y2. On the other hand, the Y2M

injection interval shows an inflection (175,000-200,000 sec) that we consider characteristic of dual continuum behavior.

Barometric pressure fluctuations are included when they are deemed to have had a potential impact on downhole pressure. There was no measurable pressure response in monitoring interval Y1B, and pressure transducers in monitoring intervals V2U, V2B, W3B and Y1U appeared to have malfunctioned during cross-hole test PP4. In general, pressure responses tended to be largest in monitoring intervals with lengths ranging from 0.5-m to 2-m and to diminish with distance from the injection interval.

Pressure in monitoring interval V1 (Figure 5.10) shows an inflection at about 150,000 sec which may be an indication of dual continuum behavior; a similar inflection occurs in monitoring intervals V2M (Figure 5.11), V3M (Figure 5.12), W1 (Figure 5.13), W2AM (Figure 5.15), W3M (Figure 5.16), X1 (Figure 5.17), X2U (Figure 5.18), X2M (Figure 5.18), X2B (Figure 5.18), Y2M (Figure 5.9), Y3B (Figure 5.21), and Z3M (Figure 5.24). At late time, the pressure in V1 declines in apparent response to a concurrent decline in barometric pressure; this too is seen in several intervals including V2M (Figure 5.11), W1 (Figure 5.13), W2AM (Figure 5.15), W2AL (5.15), W3M (Figure 5.16), X1 (Figure 5.17), X2U (Figure 5.18), X2M (Figure 5.18), X2B (Figure 5.18), X3 (Figure 5.19), Y1M (Figure 5.20), Y1B (Figure 5.20), Y3U (Figure 5.21), Y3M (Figure 5.21), Y3B (Figure 5.21), Z1 (Figure 5.22), Z2U (Figure 5.23), Z2M (Figure 5.23), Z2L (Figure 5.23), Z2B (Figure 5.23), Z3U (Figure 5.24), Z3M (Figure 5.24) and Z3B (Figure 5.24). Otherwise, barometric pressure fluctuations seem to have only a small effect on pressure in V1 as well as in V2M (Figure 5.11), V3U (Figure 5.12), V3M (Figure 5.12), V3B (Figure 5.12), W1 (Figure 5.13), W2AM (Figure 5.15), W2AL (Figure 5.15), X2U (Figure 5.18), X2M (Figure 5.18), X2B (Figure 5.18), Y2U (Figure 5.9), Y2M (Figure 5.9), Y2B (Figure 5.9), Z3U (Figure 5.24) and Z3M (Figure 5.24). On the other hand, such fluctuations seem to have a measurable impact on pressure in W3M (Figure 5.15), Y1M (Figure 5.19), Y3B (Figure 5.21), Z3U (Figure 5.24) and Z3M (Figure 5.24), and to dominate pressure variations in X3 (Figure 5.19), Y3U (Figure 5.21), Y3M (Figure 5.21), Z1 (Figure 5.22), Z2U (Figure 5.23), Z2M (Figure 5.23), Z2L (Figure 5.23), Z2B (Figure 5.23) and Z3B (Figure 5.24). These intervals must have excellent pneumatic communication with the atmosphere through high-permeability fractures.

We do not have a complete record of pressure recovery for cross-hole test PP4. We did observe, however, that the rate of recovery was much faster in intervals V2M, V3M, W1, W2AM, W2AL, W3M, X1, Y2M, Y3M, Y3B and Z3M than in V1, V2B, V3U, V3B, W2AU, W2AB, W3U, Y1U, Y2U, Y2B, Y3U, Z2U, Z2M and Z3U; was nearly identical in intervals X2U, X2M and X2B; and was imperceptible in interval Y1U.

Table 5.3: Coordinates of centers of monitoring intervals relative to origin at center of injection interval, interval lengths, radial distances between centers of injection and monitoring intervals, geometric parameters β_1 and β_2 and maximum recorded pressure change.

Interval	x [m]	y [m]	z [m]	B [m]	R [m]	β_1	β_2	max Δp [kPa]
V1	-7.2	1.6	-6.8	29.5	10.0	0.7	0.7	8.3
V2U	-4.2	1.6	8.4	5.0	9.6	3.9	0.9	Broken PT
V2M	-4.2	1.6	3.9	2.0	6.0	5.9	0.7	9.8
V2B	-4.2	1.6	-7.2	18.2	8.5	0.9	0.8	Broken PT
V3U	-1.2	1.6	6.1	9.6	6.4	1.3	0.9	6.3
V3M	-1.2	1.6	-0.3	0.5	2.0	8.2	0.2	49.2
V3B	-1.2	1.6	-9.5	18.1	9.7	1.1	1.0	23.5
W1	-3.6	0.3	4.9	11.9	6.1	1.0	0.6	9.2
W2AU	-3.2	4.8	0.4	6.7	5.7	1.7	0.6	2.9
W2AM	-3.2	1.2	-3.2	1.5	4.7	6.1	0.3	13.8
W2AL	-3.2	-0.8	-5.2	2.1	6.1	5.9	0.7	7.5
W2AB	-3.2	-3.7	-8.0	4.0	9.4	4.7	0.9	6.9
W3U	-3.4	16.5	1.5	6.8	16.9	5.0	0.8	4.5
W3M	-3.4	12.9	-2.1	1.2	13.5	22.0	0.6	4.8
W3B	-3.4	1.8	-13.3	28.6	13.8	1.0	0.6	Broken PT
X1	-6.0	4.8	4.0	14.4	8.7	1.2	0.2	7.0
X2U	2.6	4.8	2.4	8.2	6.0	1.5	0.6	9.2
X2M	-1.8	4.8	-1.9	2.2	5.5	5.0	0.5	17.9
X2B	-7.9	4.8	-8.0	12.9	12.2	1.9	0.9	7.3
X3	4.2	4.8	-5.9	42.6	8.7	0.4	0.1	0.2
Y1U	-0.7	-0.1	9.4	2.1	9.4	8.9	0.7	broken PT
Y1M	-2.8	-0.1	7.3	1.8	7.8	8.5	0.4	7.2
Y1B	-7.3	-0.1	2.8	8.8	7.8	1.8	0.4	0.0
Y2U	4.0	0.0	4.0	7.1	5.6	1.6	0.0	16.9
Y2M	0.0	0.0	0.0	2.0	0.0			116.6
Y2B	-6.0	0.0	-6.0	12.9	8.5	1.3	0.0	21.5
Y3U	14.8	0.1	4.8	7.5	15.6	4.2	0.9	0.6
Y3M	10.7	0.1	0.7	2.0	10.8	10.6	0.8	0.7
Y3B	-0.5	0.1	-10.5	27.8	10.5	0.8	0.7	3.0
Z1	18.9	-5.2	3.8	13.0	19.9	3.1	0.5	0.2
Z2U	10.5	-5.2	2.6	8.1	12.0	3.0	0.5	0.7
Z2M	14.8	-5.2	-1.7	2.0	15.8	15.8	0.7	0.3
Z2L	16.9	-5.2	-3.8	2.0	18.1	18.0	0.8	0.1
Z2B	21.1	-5.2	-8.0	7.7	23.2	6.0	0.9	0.1
Z3U	-0.3	-5.2	3.8	6.8	6.4	1.9	0.4	6.5
Z3M	3.5	-5.2	0.0	2.0	6.3	6.3	0.4	6.9
Z3B	14.4	-5.2	-10.9	26.0	18.8	1.4	1.0	0.2

PT = Pressure Transducer
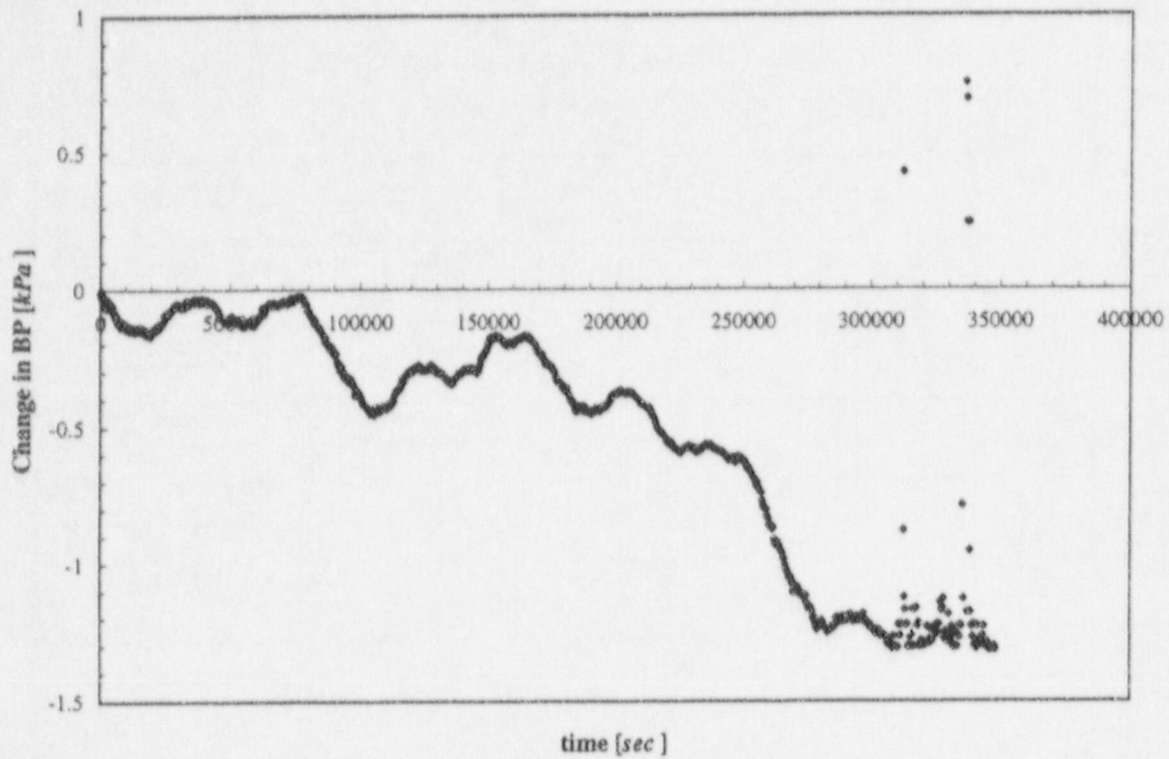
Figure 5.4: Barometric pressure during cross-hole test PP4
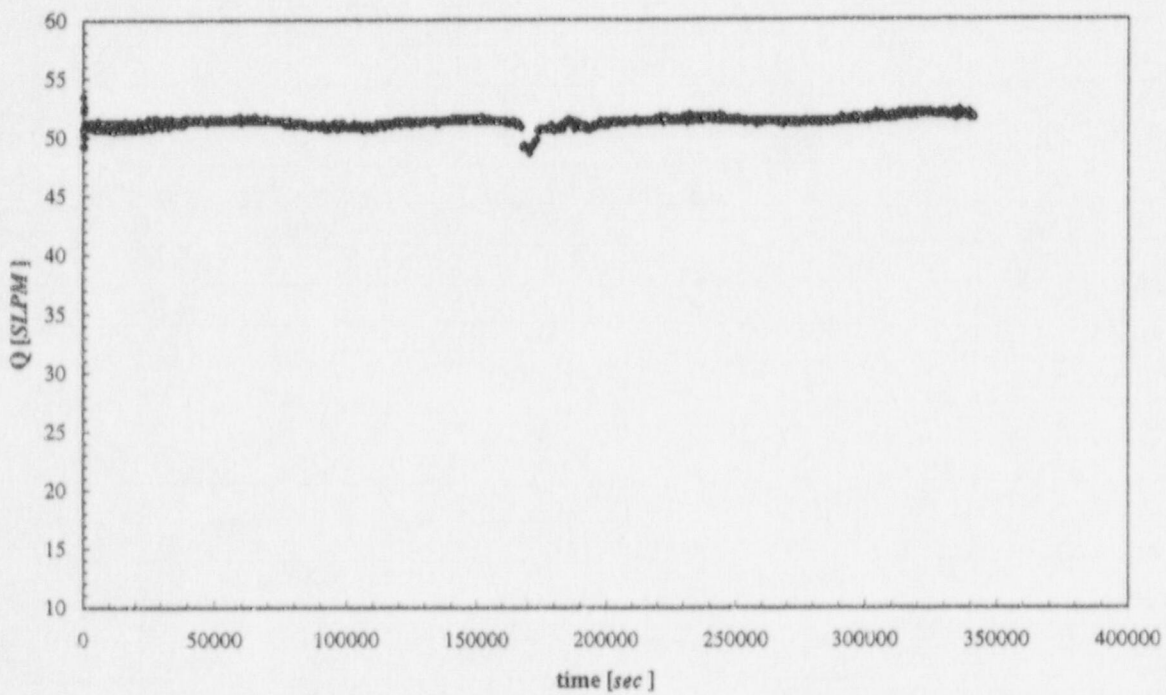
Figure 5.5: Flow rate during cross-hole test PP4
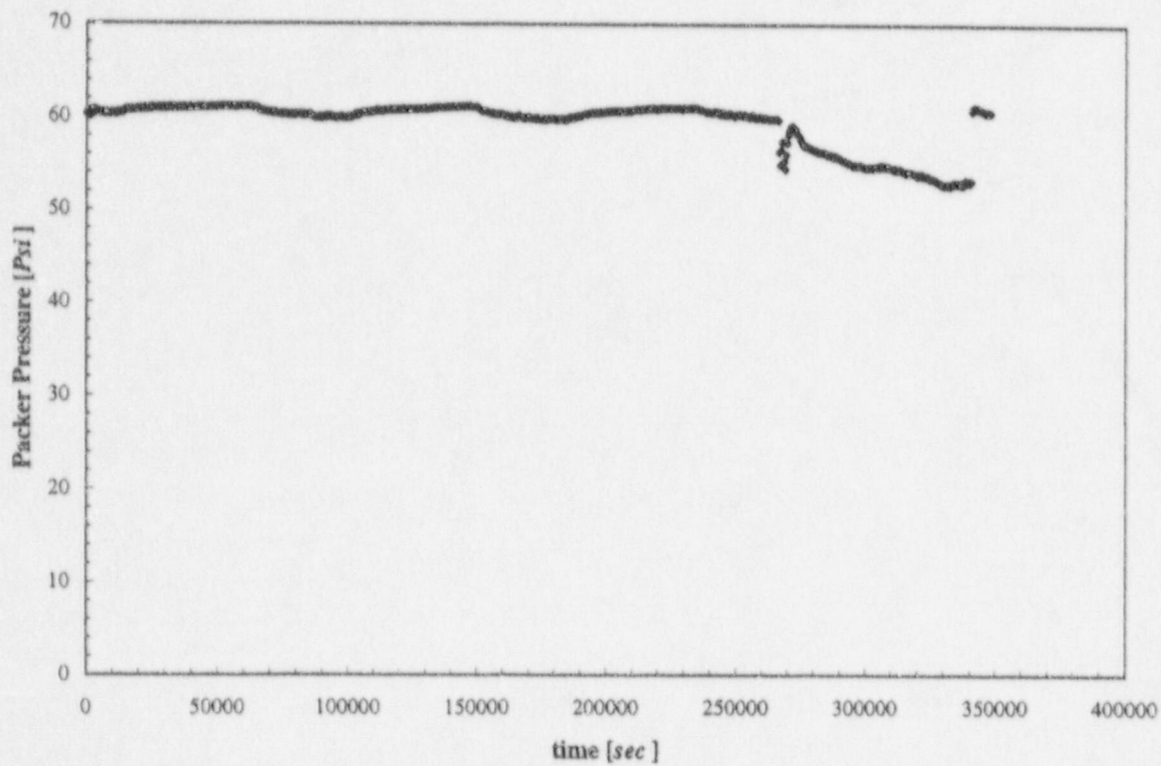
Figure 5.6: Packer pressure during cross-hole test PP4
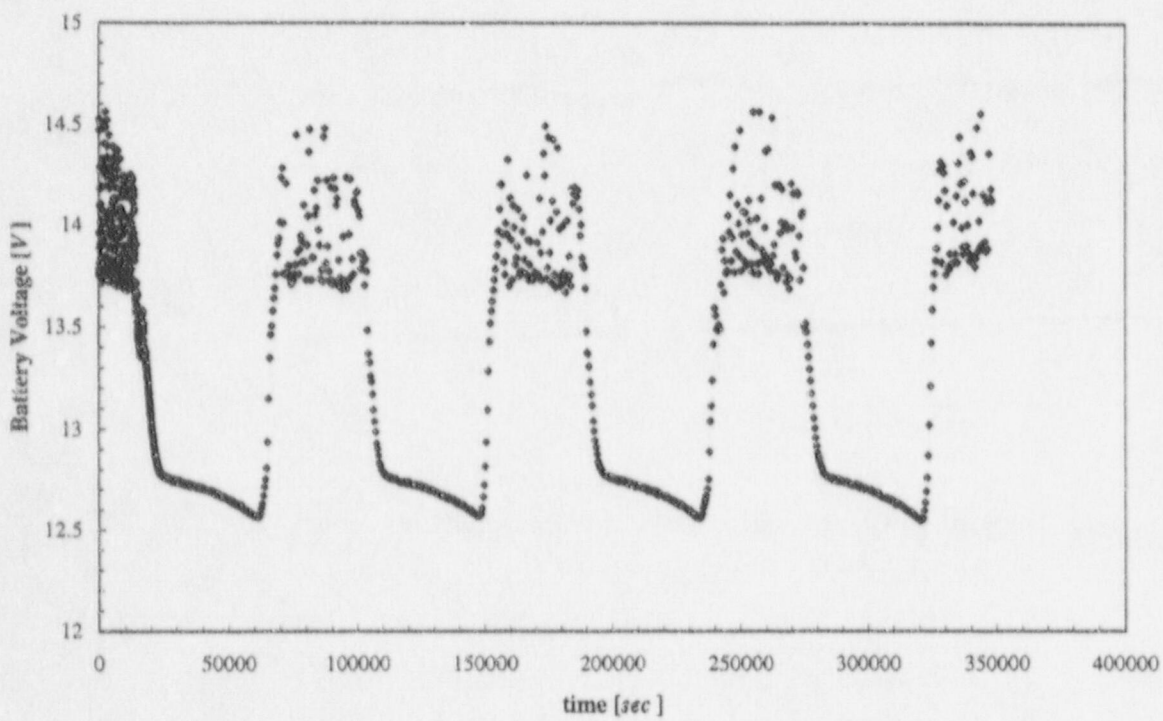
Figure 5.7: Battery voltage during cross-hole test PP4
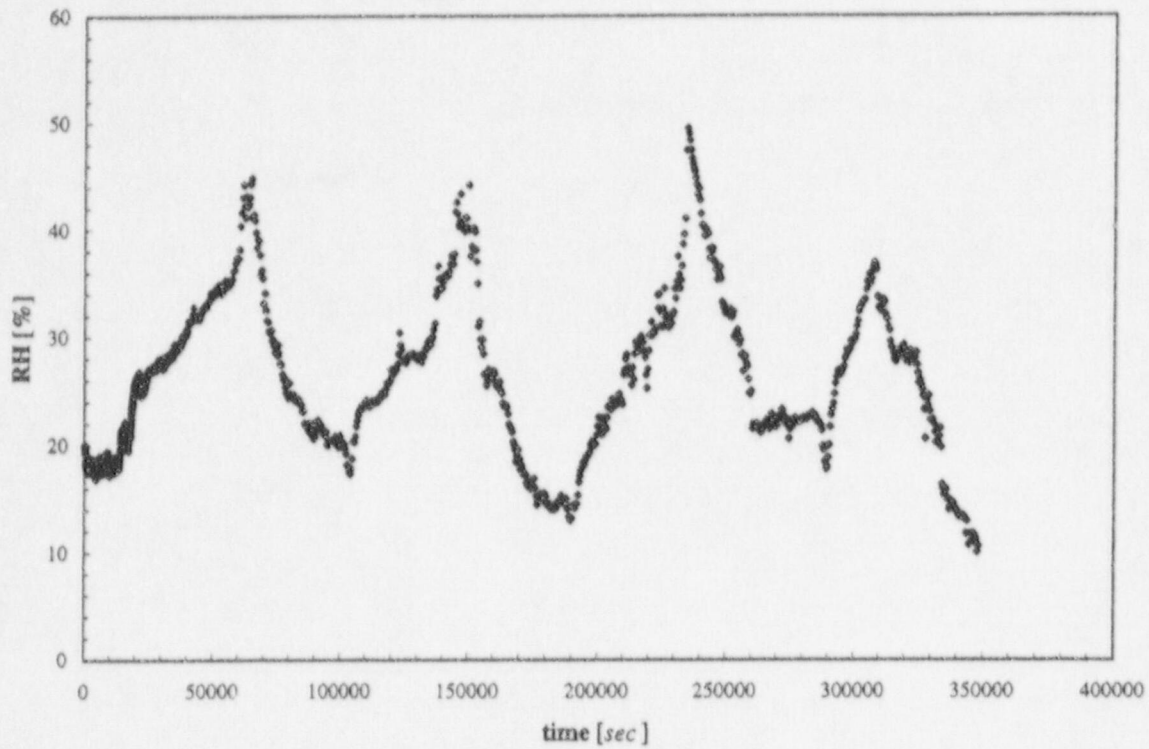
Figure 5.8: Fluctuations in relative humidity during cross-hole test PP4
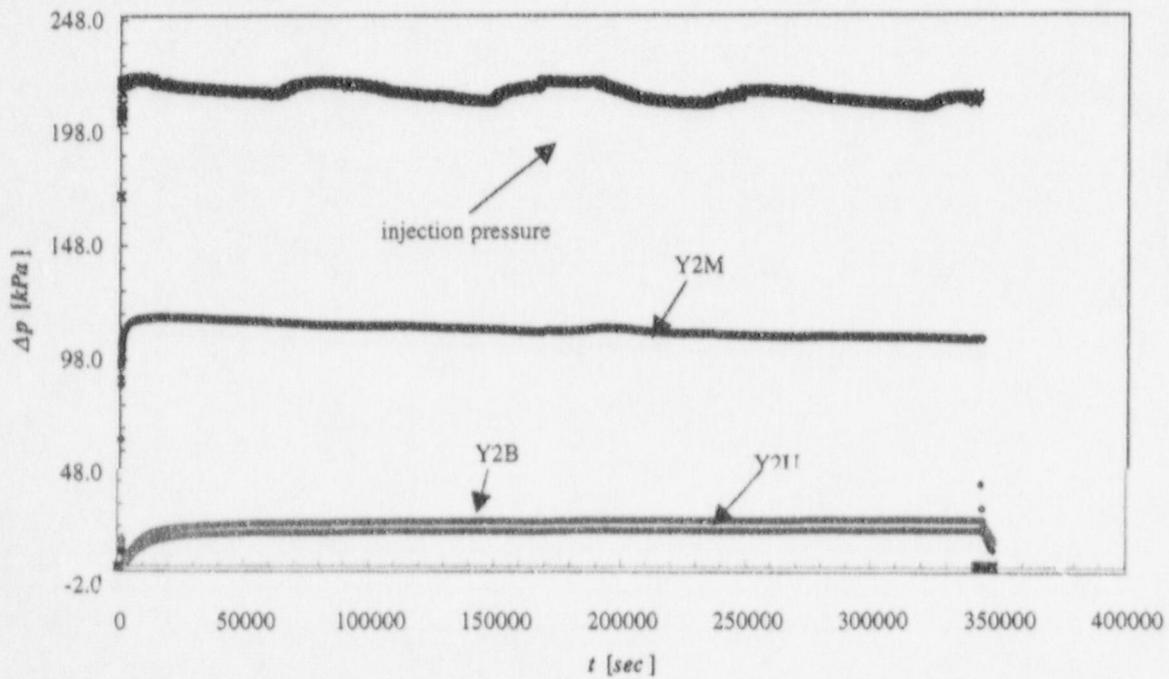
Figure 5.9: Surface injection pressure and pressure in injection (Y2M) and monitoring (Y2U, Y2B) intervals within borehole Y2 during cross-hole test PP4.
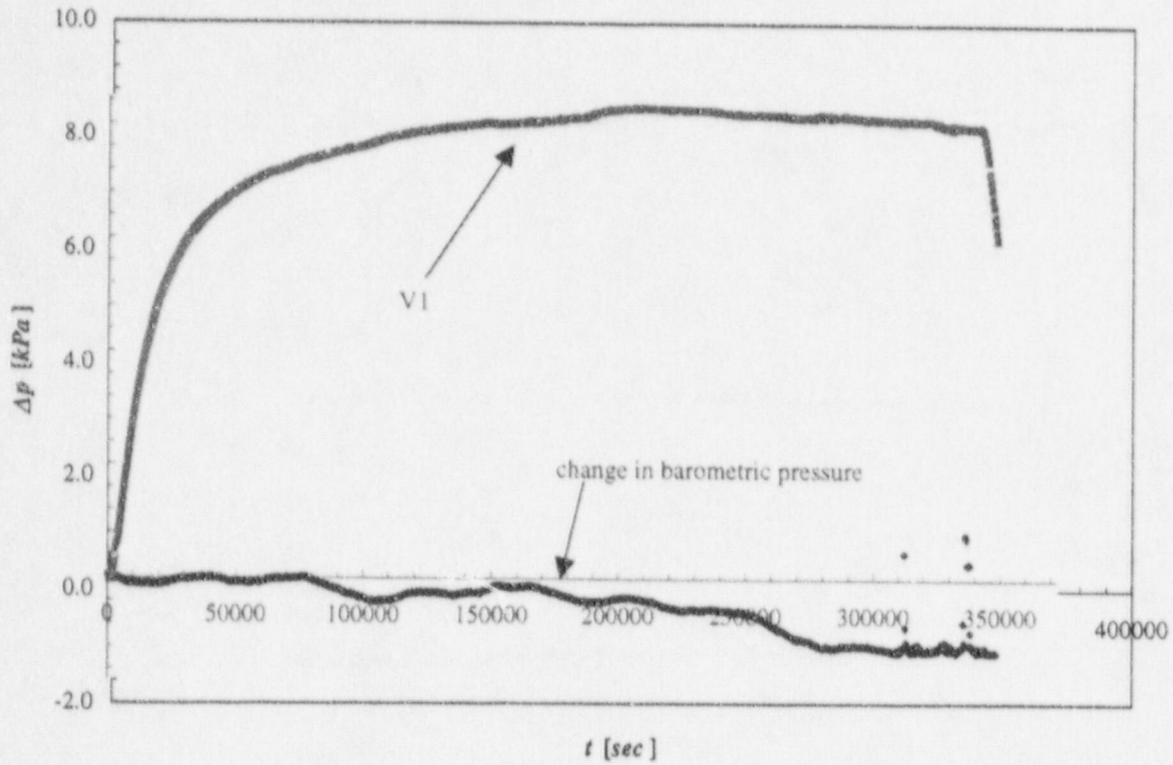
Figure 5.10: Pressure in monitoring interval V1 during cross-hole test PP4
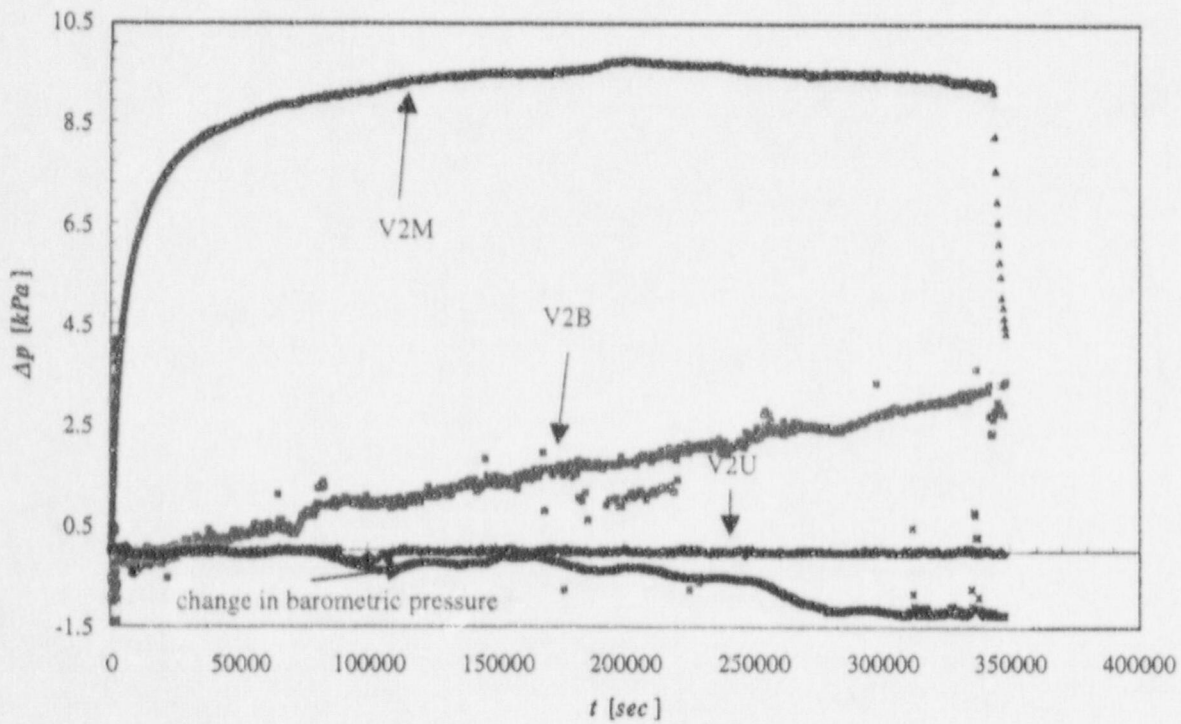
Figure 5.11: Pressure in monitoring intervals V2U, V2M, and V2B during cross-hole test PP4.

NUREG/CR-5559
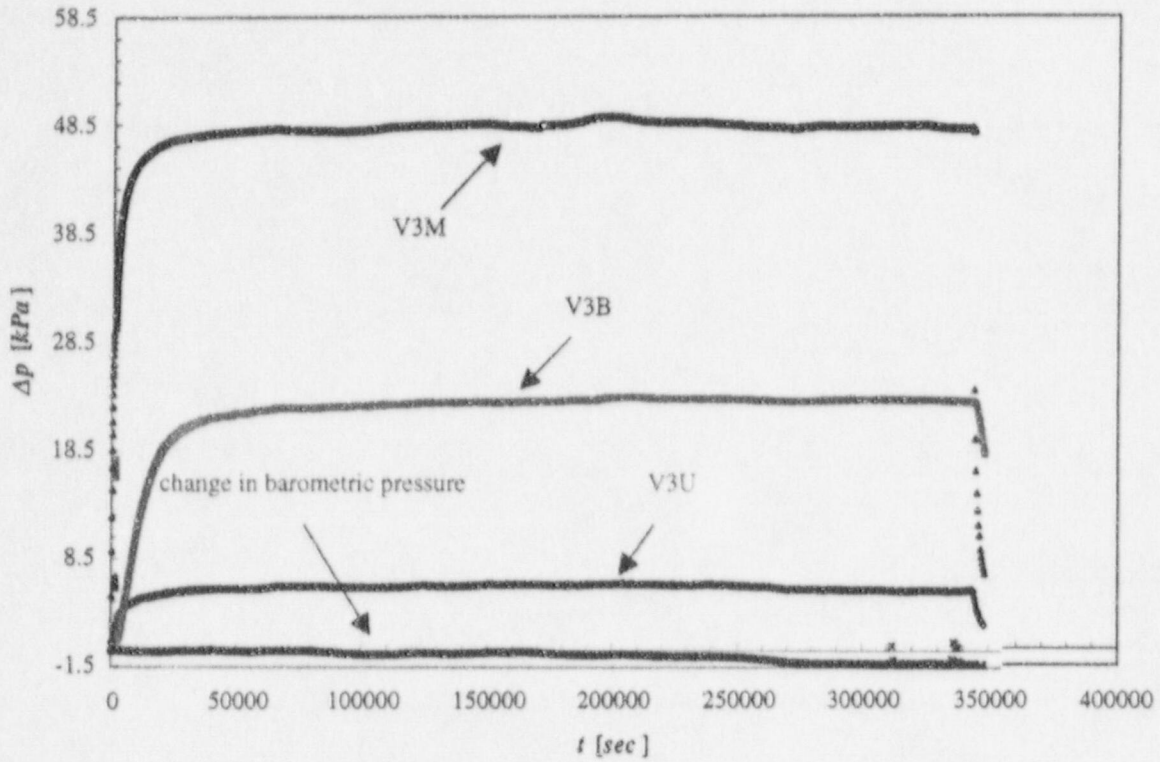
Figure 5.12: Pressure in monitoring intervals V3U, V3M, and V3B during cross-hole test PP4.
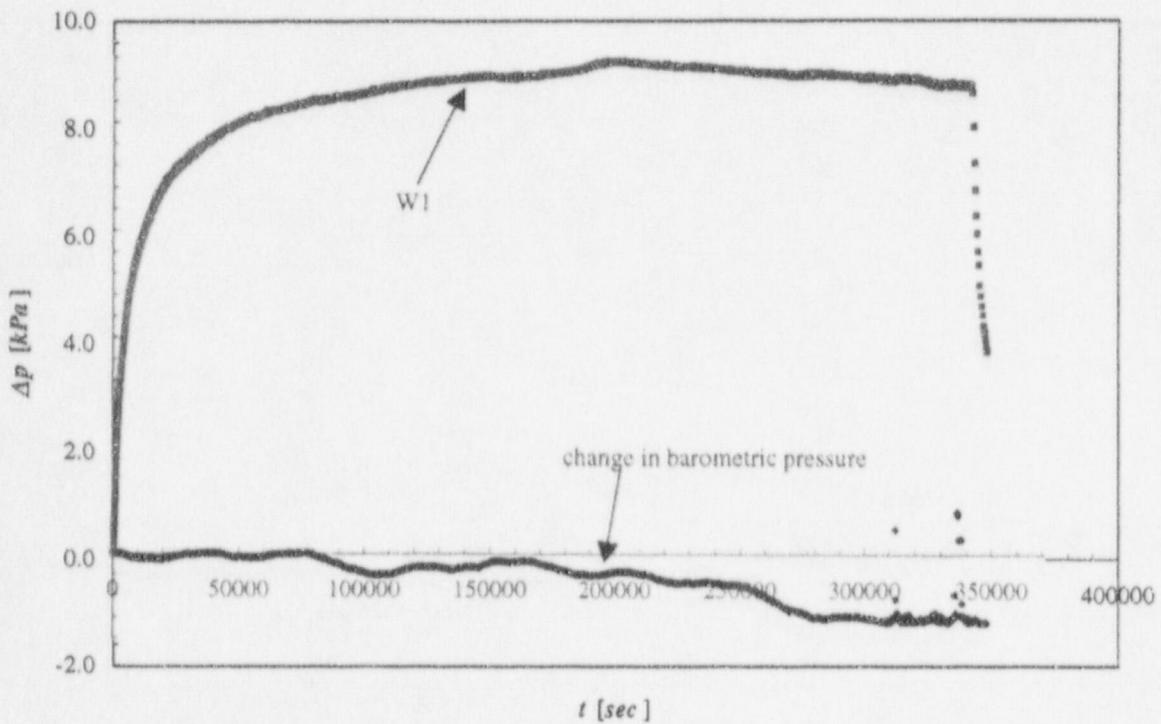
Figure 5.13: Pressure in monitoring interval W1 during cross-hole test PP4.
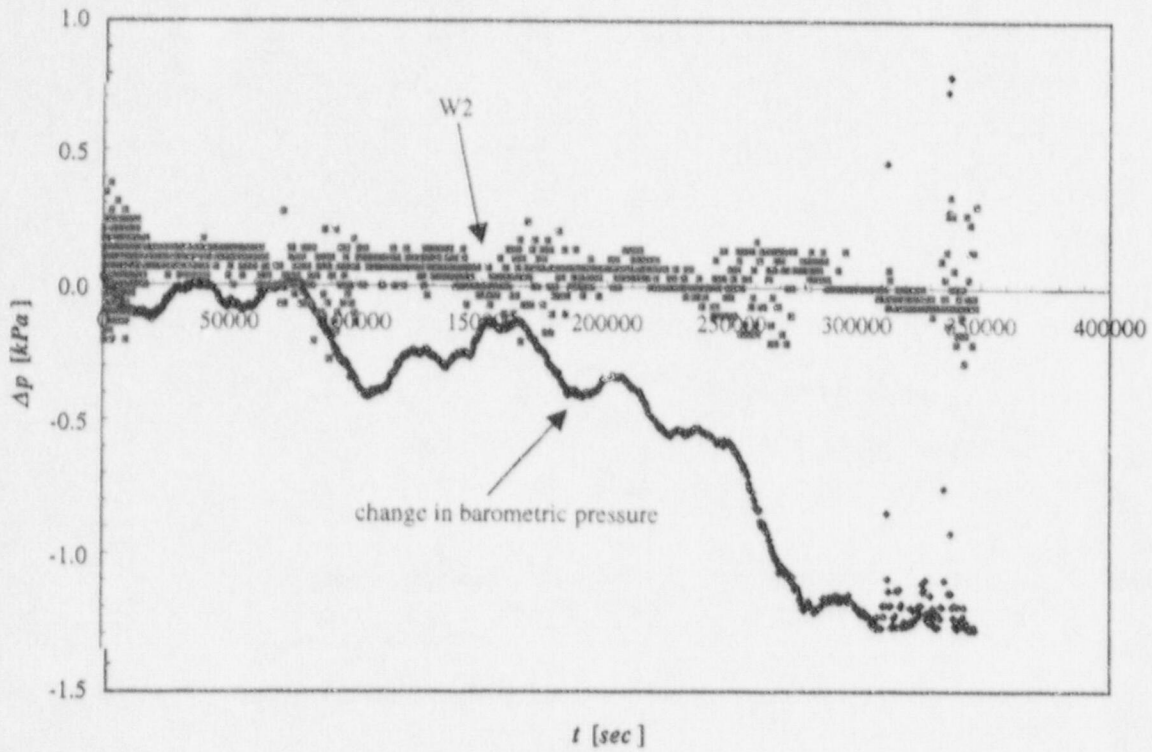
Figure 5.14: Pressure in monitoring interval W2 during cross-hole test PP4.
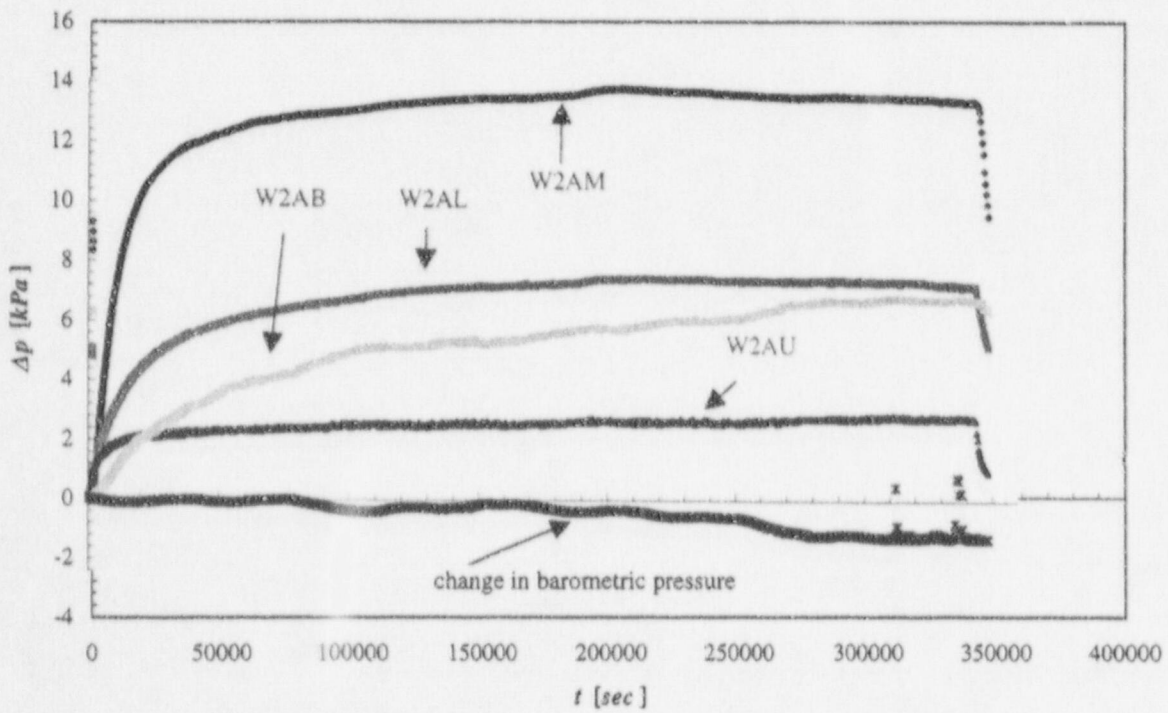
Figure 5.15: Pressure in monitoring intervals W2AU, W2AM, W2AL, and W2AB during cross-hole test PP4.
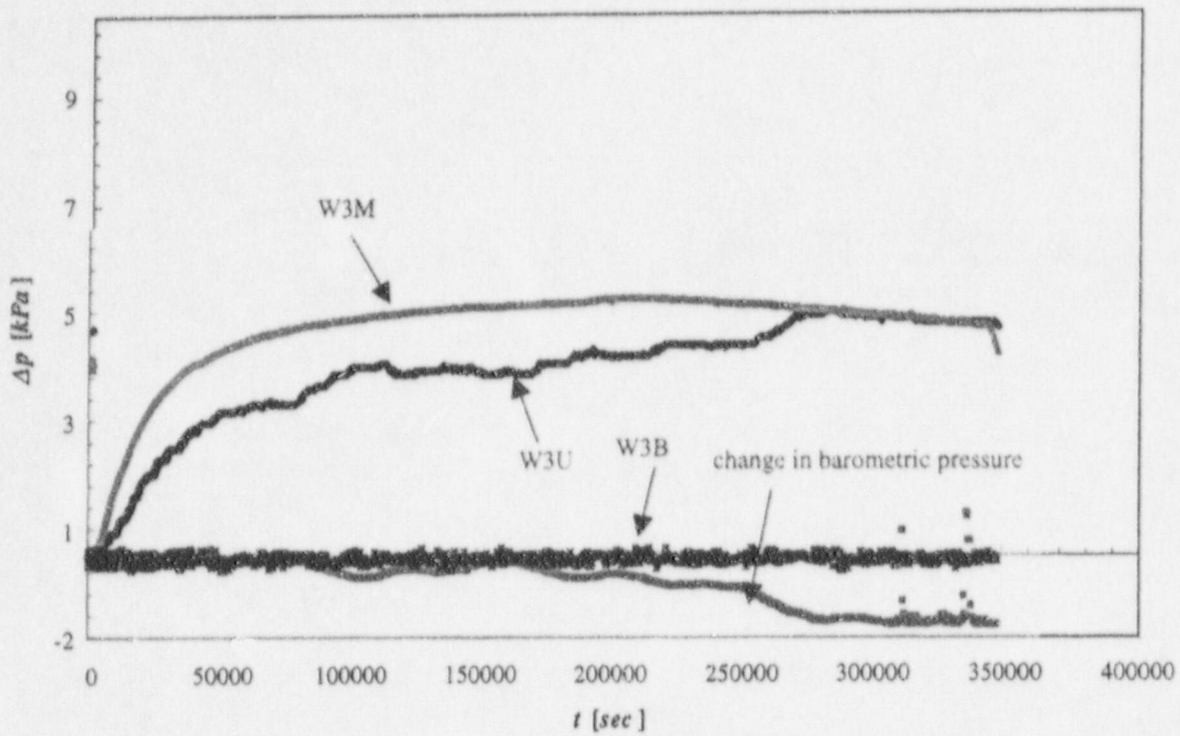
Figure 5.16: Pressure in monitoring intervals W3U, W3M, and W3B during cross-hole test PP4.
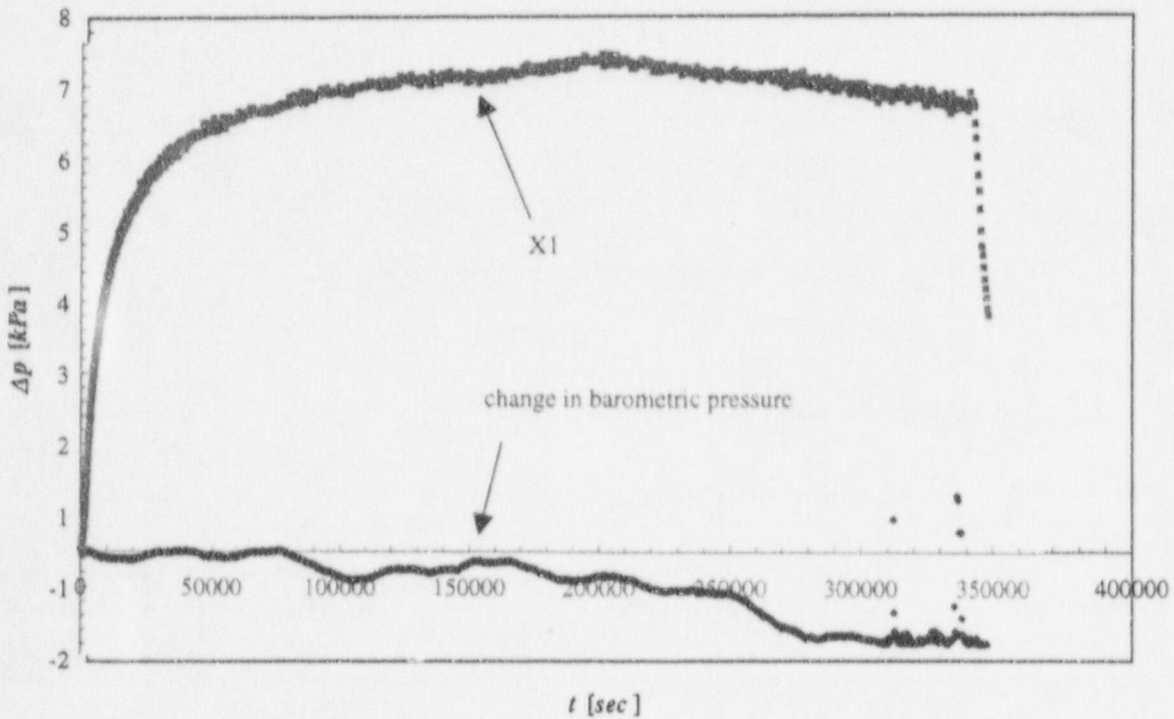
Figure 5.17: Pressure in monitoring interval X1 during cross-hole test PP4.
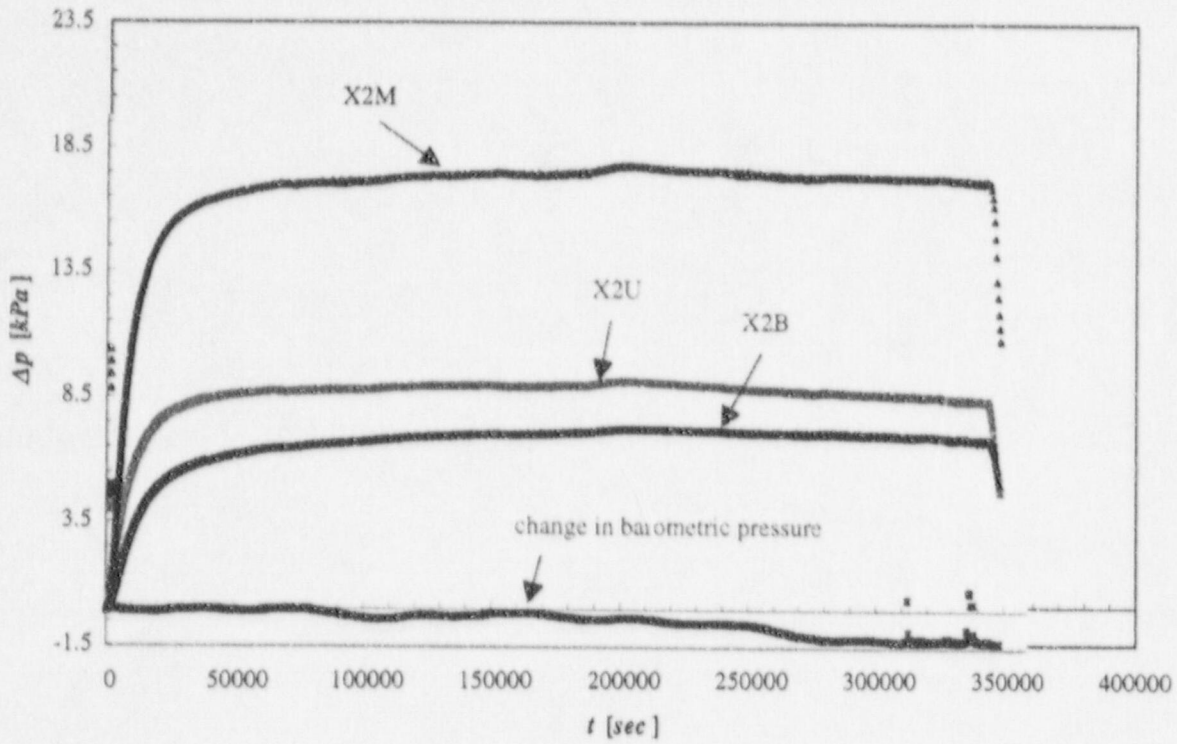
Figure 5.18: Pressure in monitoring intervals X2U, X2M, and X2B during cross-hole test PP4.
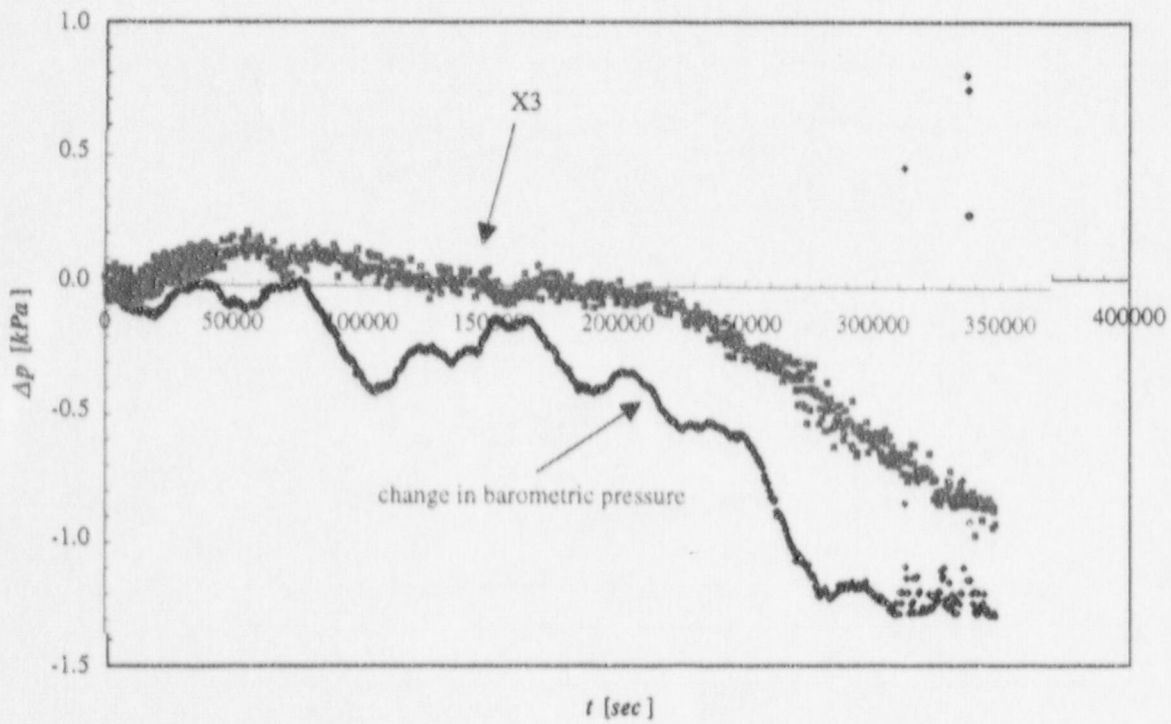
Figure 5.19: Pressure in monitoring interval X3 during cross-hole test PP4.

NUREG/CR-5559
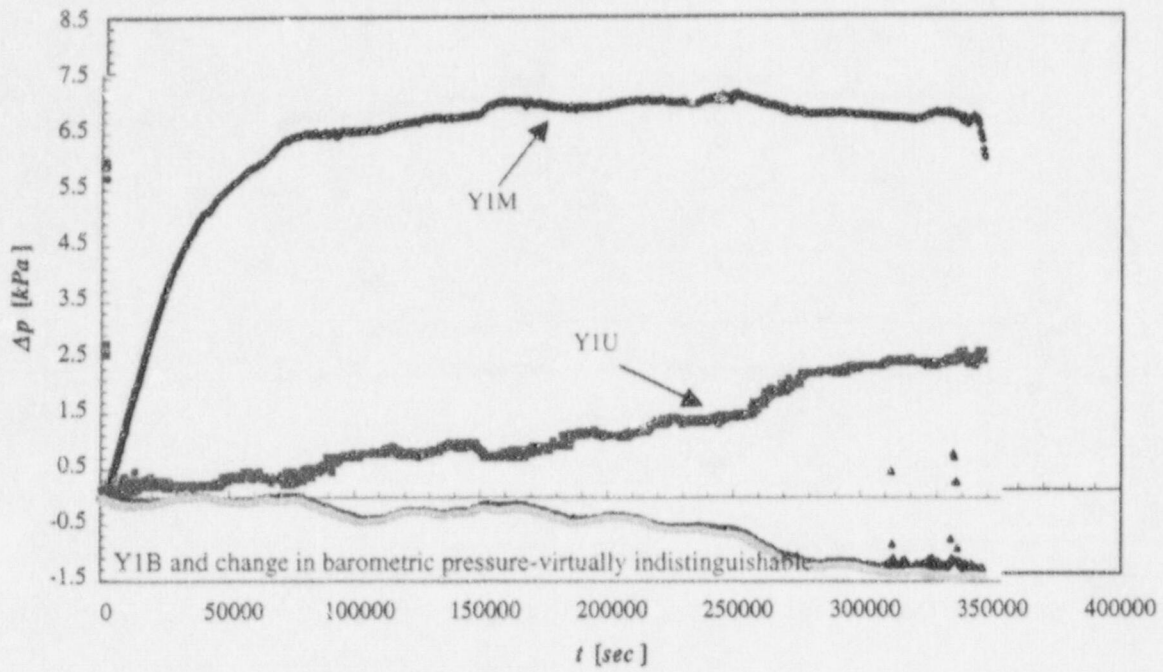
Figure 5.20: Pressure in monitoring intervals Y1U, Y1M, and Y1B during cross-hole test PP4.
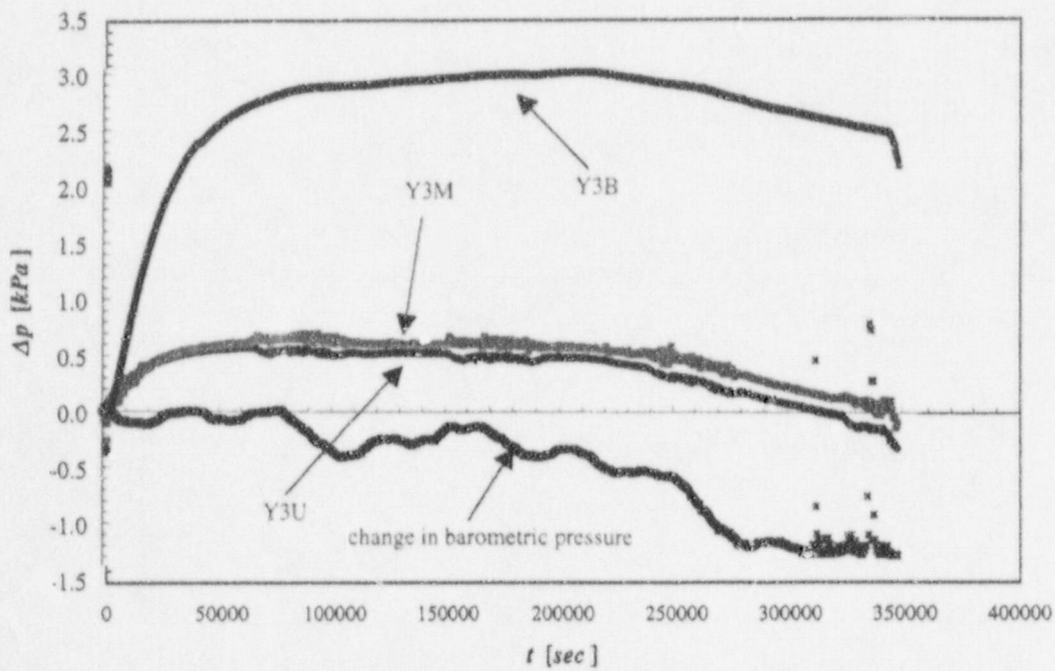
Figure 5.21: Pressure in monitoring intervals Y3U, Y3M, and Y3B during cross-hole test PP4.
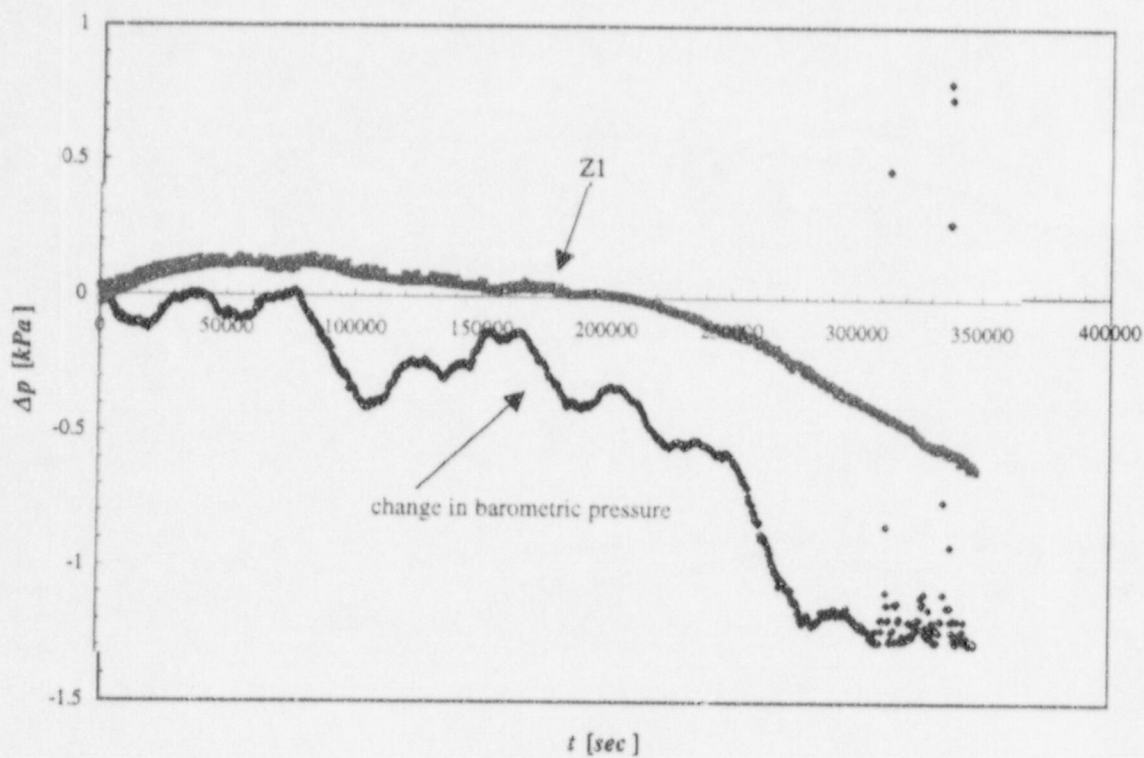
Figure 5.22: Pressure in monitoring interval Z1 during cross-hole test PP4.
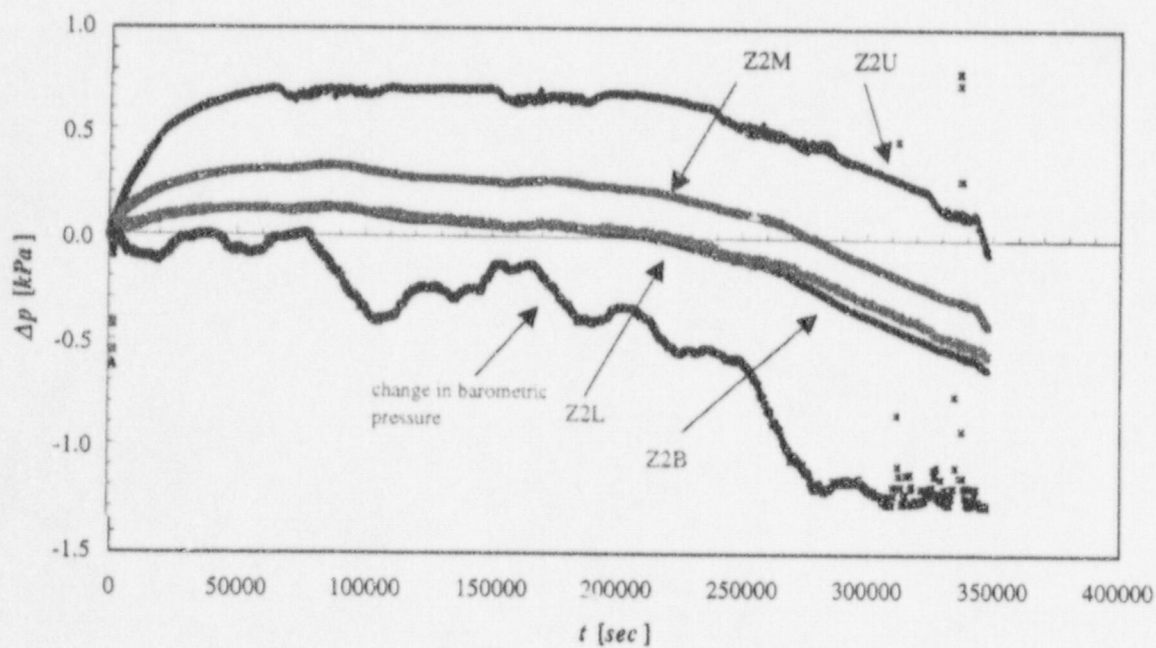
Figure 5.23: Pressure in monitoring intervals Z2U, Z2M, Z2L, and Z2B during cross-hole test PP4.

101
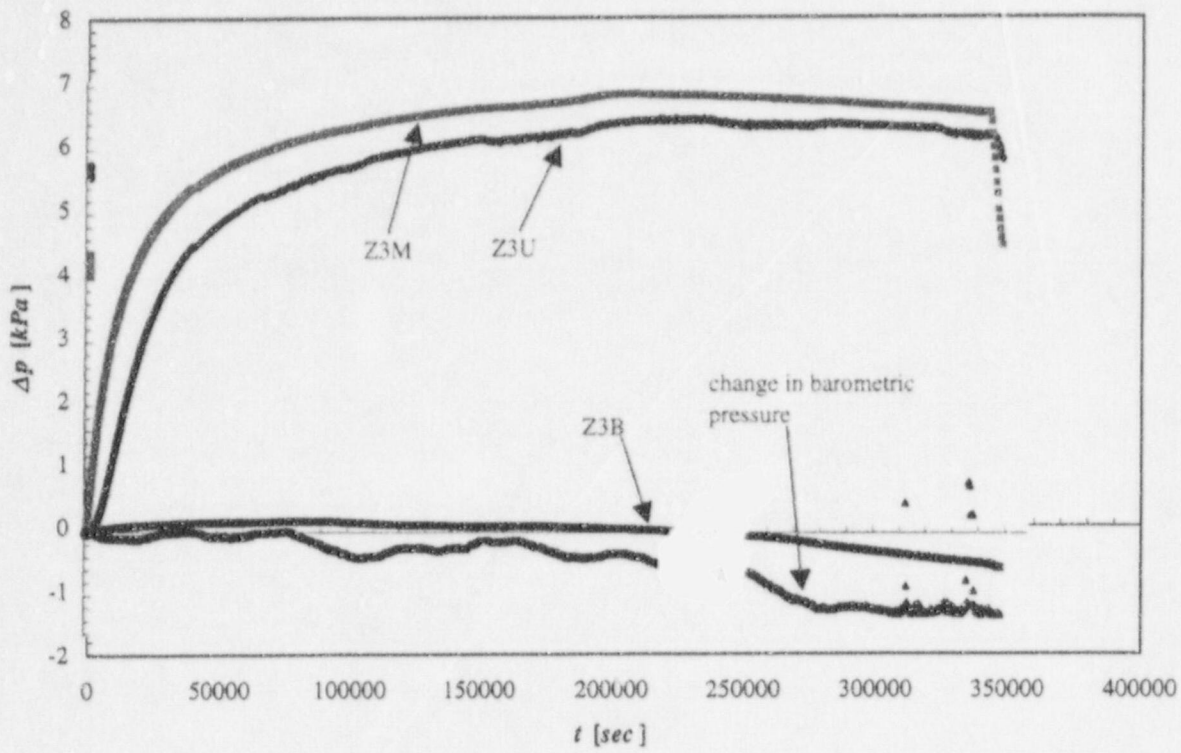
Figure 5.24: Pressure in monitoring intervals Z3U, Z3M, and Z3B during cross-hole test PP4.

5.3 TYPE CURVE INTERPRETATION OF CROSS-HOLE TEST PP4

Type-curve interpretation of pressure data from cross-hole test PP4 included intervals V1, V2M, V3U, V3M, V3B, W1, W2AU, W2AM, W2AL, W2AB, W3U, W3M, X1, X2U, X2M, X2B, Y1U, Y1M, Y2U, Y2B, Y3U, Y3M, Y3B, Z1, Z2U, Z2M, Z2L, Z2B, Z3U, Z3M and Z3B. Pressure data from intervals V2U, V2B, W2, W3B and Y1B were not amenable for type-curve interpretation and have therefore been excluded. A special set of type-curves was developed for each pressure monitoring interval based on the point-injection/line-monitoring solution, modified for storage and skin in the monitoring interval, given by equations (3.4-8) and (3.4-9) in Chapter 3. Evaluation of the corresponding integrals was done by Rhomberg integration. The geometric parameters β_1 and β_2 were calculated according to

$$\beta_1 = 2R/B \qquad (5.6\text{-}1)$$
$$\beta_2 = \cos\theta \qquad (5.6\text{-}2)$$

where R is radial distance between the centroids of the injection and monitoring intervals, B is the length of the monitoring interval, and θ is the angle between the corresponding radius vectors. Equations (5.6-1) and (5.6-2) are obtained from (3.4-4) and (3.4-5), respectively, upon treating the medium as if it was pneumatically isotropic. Indeed, our type-curve analysis additionally treats the rock as if it was pneumatically uniform. However, since the analysis of pressure data from different monitoring intervals yield different values of pneumatic parameters, our analysis ultimately yields information about the spatial and directional dependence of these parameters.

Figures 5.25 - 5.55 show how we matched each record of pressure buildup from cross-hole injection test PP4 to corresponding type-curves on logarithmic paper. Though the figures include type-curves of pressure derivatives, many of the pressure derivative data are noisy and we show only some that are not excessively so. The match between pressure data and type-curves in Figures 5.25, 5.28, 5.32, 5.36, 5.38, 5.40, 5.42, 5.43, 5.44, and 5.53 are excellent over the entire length of the buildup record; those in Figures 5.27, 5.31, 5.37, 5.43, 5.44, 5.47 and 5.54 are good except for intermediate time where the data exhibit an inflection, which suggests dual continuum behavior; in Figures 5.26, 5.33, 5.50, and 5.54 intermediate time and late pressure data match the type-curves well, but early data lie above the type-curves; in Figures 5.29, intermediate time and late pressure data match the type-curves well but early data lie below the type-curves; in Figures 5.47, 5.50, 5.51, 5.52 and 5.55, early and intermediate time data fit the type-curves well, but late data fall below the type curves; and in Figures 5.41, 5.48, and 5.52 the matches are poor.

Fluctuations in barometric pressure (Figure 5.4) affect some of the late pressure buildup data as seen in Figures 5.36, 5.37, 5.38, 5.40, 5.42, 5.45, 5.46, 5.47, 5.48, 5.49, 5.50, 5.51, 5.52, and 5.55. The timing and magnitude of this barometric effect varies between intervals; it tends to be most pronounced in monitoring intervals that show a weak response to air injection into Y2M (Figures 5.41, 5.45, 5.48, 5.49, 5.50, 5.51, 5.52, and 5.55), in intervals close to the soil surface (Figures 5.41 and 5.45), and within the Z holes (Figure 5.48, 5.49, 5.50, 5.51, 5.52, and 5.55).

Our finding that most pressure buildup data match the type-curves well is a clear indication that the majority of cross-hole test PP4 results are amenable to interpretation by means of a continuum model, which treats the rock as being pneumatically uniform

and isotropic while describing airflow by means of linearized, pressure-based equations. The fact that some of our data do not fit this model shows that the latter does not provide a complete description of pneumatic pressure behavior at the site. That the site is not pneumatically uniform or isotropic on the scale of cross-hole test PP4 is made evident by pneumatic parameters derived from our type-curve matches. Table 5.4 lists values of the dimensionless well response time Ω defined in section 3.4, pneumatic permeability, and air-filled porosity derived from these matches. The latter two parameters represent bulk properties of the rock between the corresponding monitoring interval and the injection interval. The permeabilities additionally represent directional values along lines that connect the centers of these intervals. Corresponding statistics are listed in Table 5.5, which compares them with similar statistics of 1-m scale permeabilities, obtained from steady sate interpretations of single-hole test data. The directional permeabilities range from $5.4 \times 10^{-15} m^2$ to $4.6 \times 10^{-13} m^2$ with a mean of -13.1 for $\log_{10}$-based k while a corresponding (anti-log) value is $3.5 \times 10^{-14} m^2$. The corresponding variance and coefficient of variation (CV) are 3.2×10^{-1} and -4.2×10^{-1}, respectively. Corresponding air-filled porosities range from 7.6×10^{-4} to 2.2×10^{-1} with a geometric mean of 6.7×10^{-3} while the variance and coefficient of variation are 3.0×10^{-1} and -2.5×10^{-1}, respectively. Permeabilities derived from cross-hole tests are seen to have a much higher mean, and lower variance, than those from the smaller-scale single-hole tests.

Table 5.4: Pneumatic parameters obtained from type curve analysis of pressure buildup data collected during cross-hole test PP4

Interval	Ω	$k\,[m^2]$	ϕ
V1	1.0	1.1E-14	4.5E-03
V2M	1.0	2.0E-14	5.7E-03
V3U	1.0	3.4E-14	8.2E-03
V3M	0.0	1.2E-14	5.4E-03
V3B	1.0	6.2E-15	3.8E-03
W1	10.0	2.1E-14	1.4E-03
W2AU	1.0	7.6E-14	1.2E-02
W2AM	1.0	1.5E-14	2.0E-02
W2AL	1.0	2.4E-14	2.1E-02
W2AB	10.0	1.9E-14	5.4E-03
W3U	1.0	1.6E-14	4.6E-03
W3M	1.0	1.5E-14	4.1E-03
X1	10.0	1.8E-14	1.1E-03
X2U	10.0	2.0E-14	3.4E-03
X2M	1.0	1.1E-14	6.3E-03
X2B	1.0	1.2E-14	3.2E-03
Y1U	1.0	3.2E-14	2.2E-01
Y1M	10.0	2.0E-14	6.6E-03
Y2U	1.0	1.1E-14	7.4E-03
Y2B	1.0	5.4E-15	1.5E-03
Y3U	100.0	1.3E-13	7.6E-04
Y3M	1.0	1.4E-13	4.2E-02
Y3B	1.0	2.6E-14	1.5E-02
Z1	10.0	4.2E-13	1.8E-02
Z2U	100.0	1.4E-13	1.4E-03
Z2M	1.0	1.9E-13	2.2E-02
Z2L	100.0	4.6E-13	2.3E-03
Z2B	100.0	3.6E-13	1.3E-03
Z3U	1.0	2.4E-14	3.7E-02
Z3M	1.0	2.5E-14	2.3E-02
Z3B	10.0	4.0E-13	1.3E-02

Table 5.5 Sample statistics of directional air permeabilities and air-filled porosities obtained from type curve interpretation of cross-hole test PP4, and of air permeabilities from steady state interpretations of 1-m scale single-hole tests. Numbers in parentheses represent corresponding actual values.

Statistic	Cross-hole values		Single-hole values
	$Log_{10} k \ [m^2]$	$Log_{10} \phi$	$Log_{10} k \ [m^2]$
Minimum	-14.3 (5.4 x 10^{-15})	-3.1 (7.6 x 10^{-4})	-17.1
Maximum	-12.3 (4.6 x 10^{-13})	-0.7 (2.2 x 10^{-1})	-13.1
Mean (Log_{10})	-13.0	-2.2	-15.3
Mean	3.5 x 10^{-14}	6.7 x 10^{-3}	5.6 x 10^{-16}
Variance	3.2 x 10^{-1}	3.0 x 10^{-1}	7.6 x 10^{-1}
CV	-4.2 x 10^{-2}	-2.5 x 10^{-1}	-5.8 x 10^{-2}
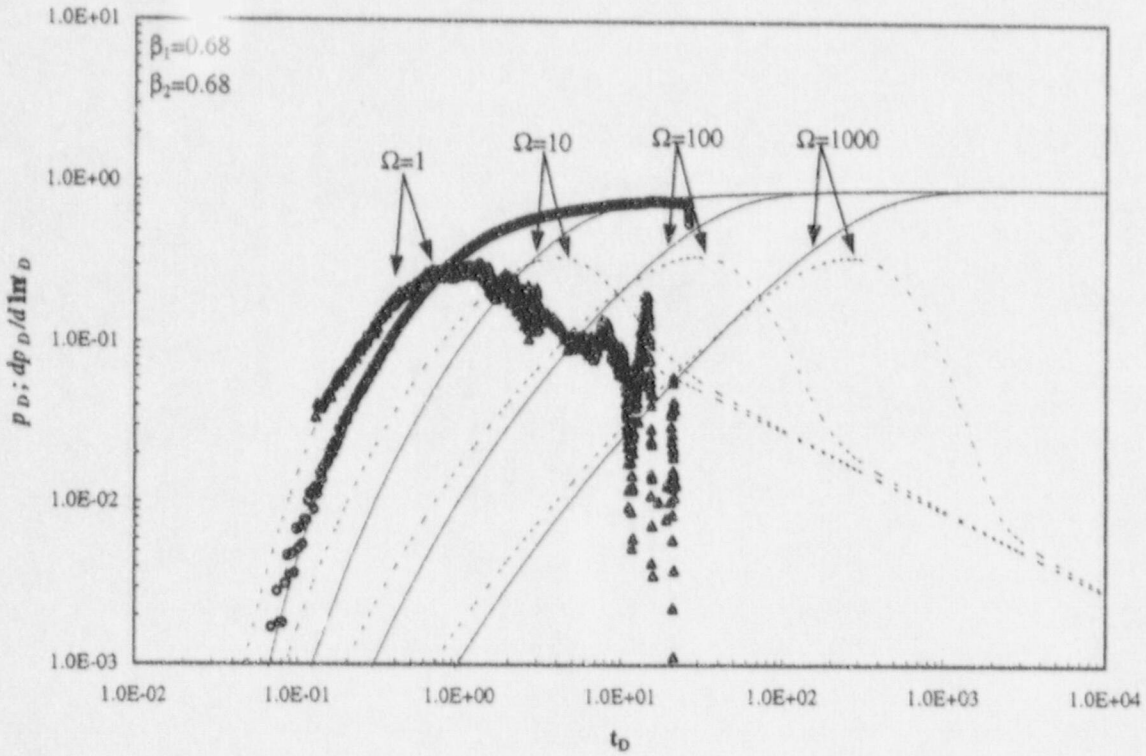
Figure 5.25: Type curve match of pressure data from monitoring interval V1
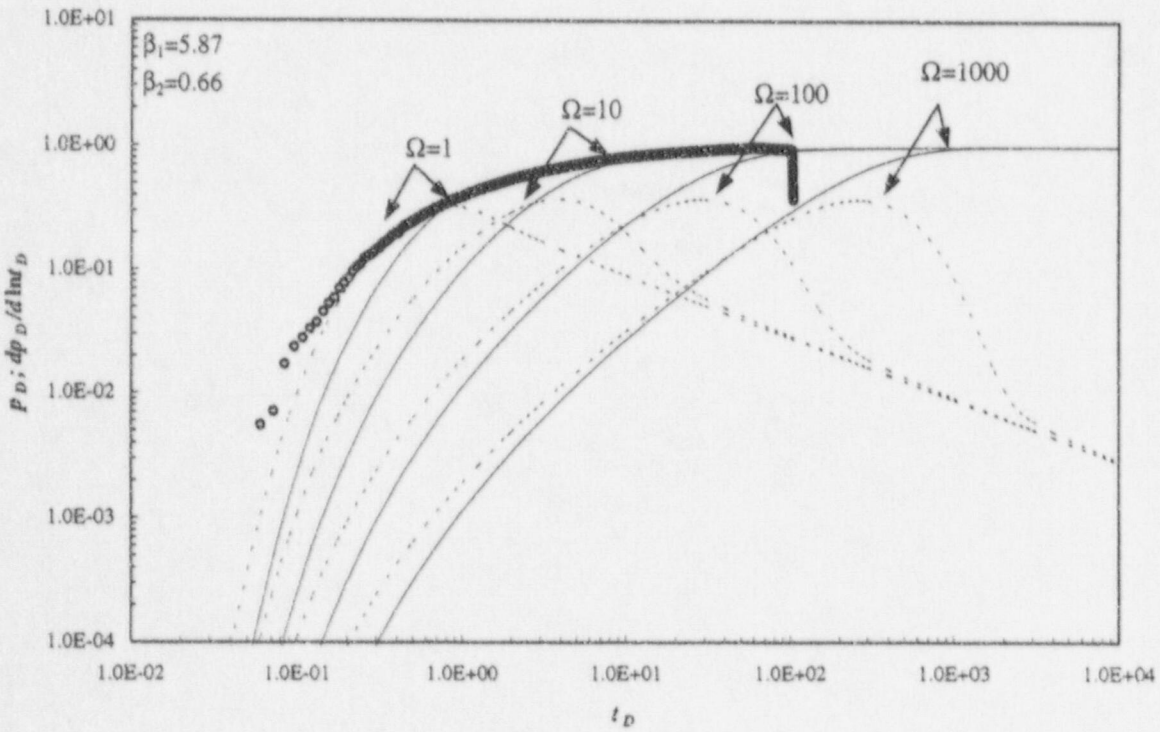
Figure 5.26: Type curve match of pressure data from monitoring interval V2M
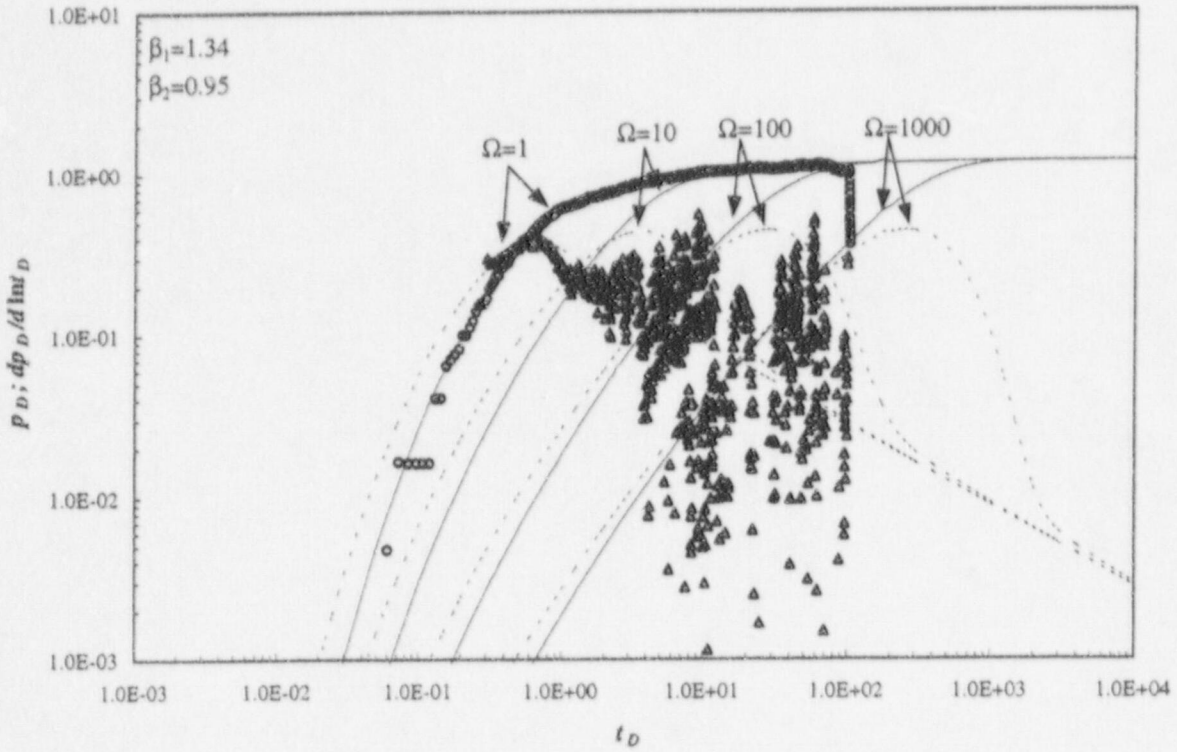
Figure 5.27: Type curve match of pressure data from monitoring interval V3U
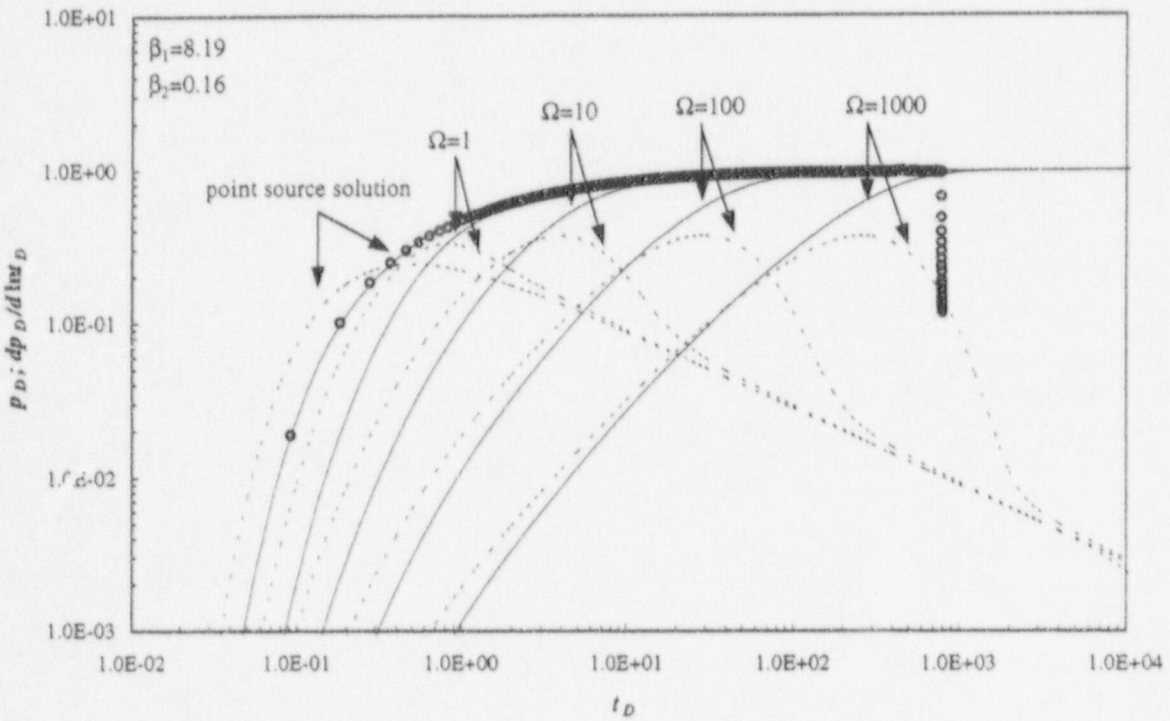
Figure 5.28: Type curve match of pressure data from monitoring interval V3M
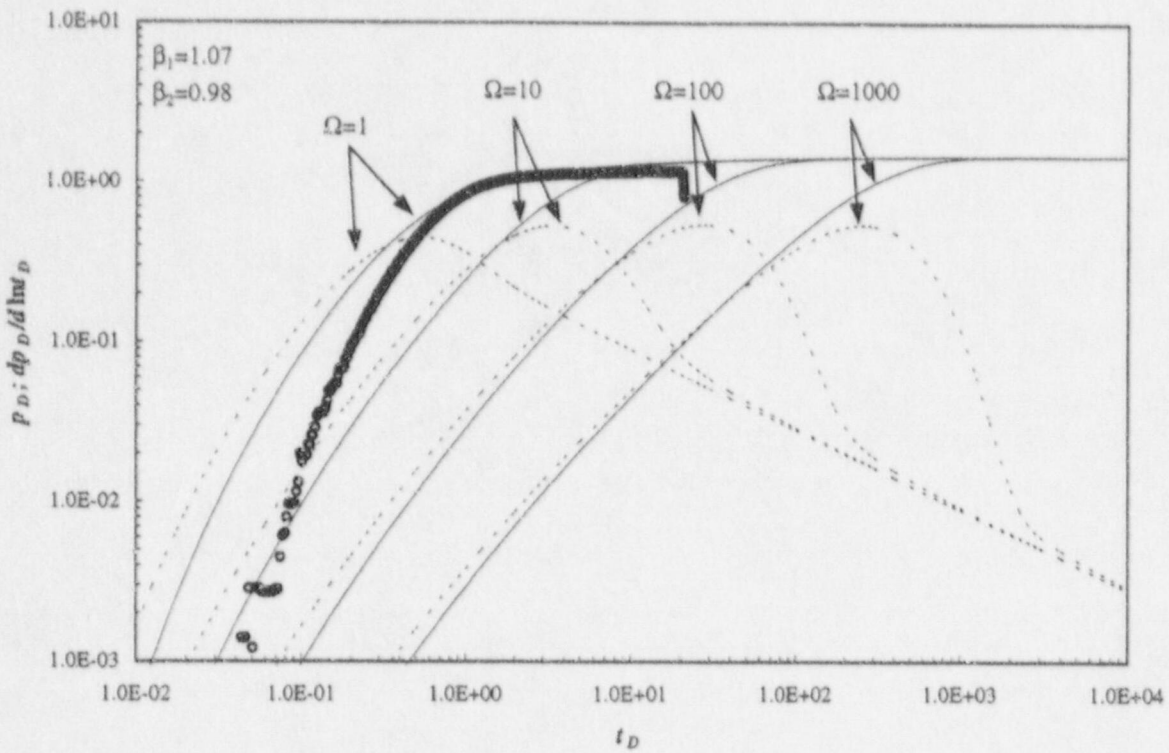
Figure 5.29: Type curve match of pressure data from monitoring interval V3B
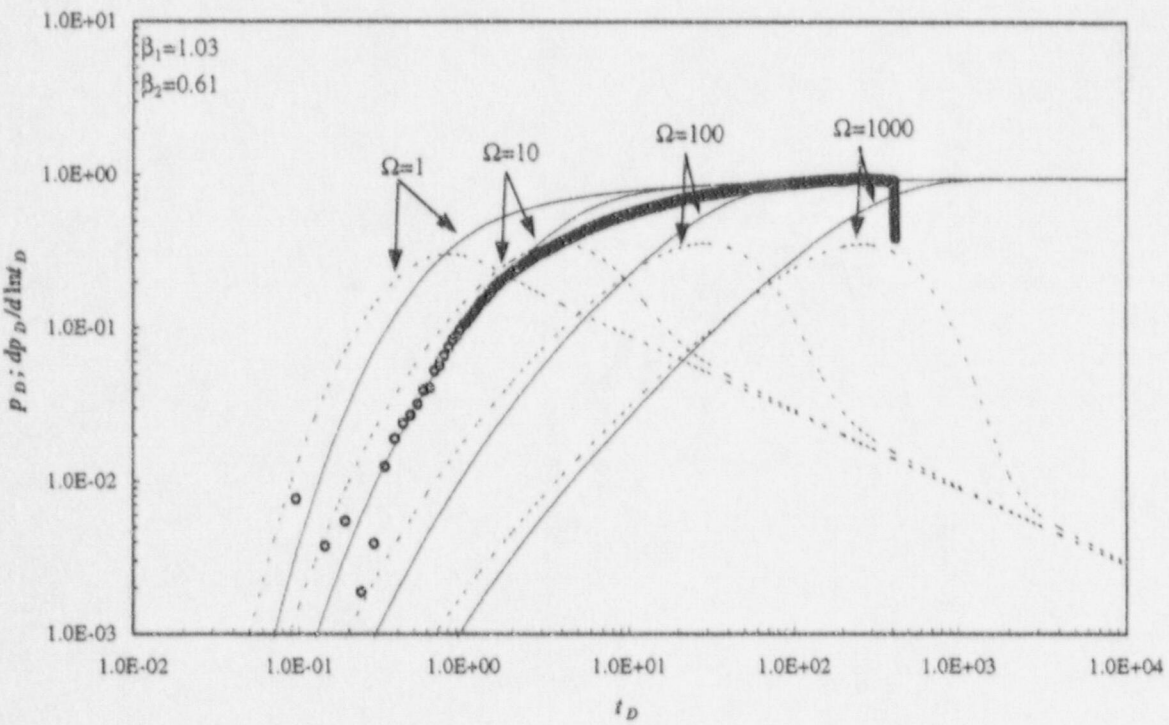
Figure 5.30: Type curve match of pressure data from monitoring interval W1
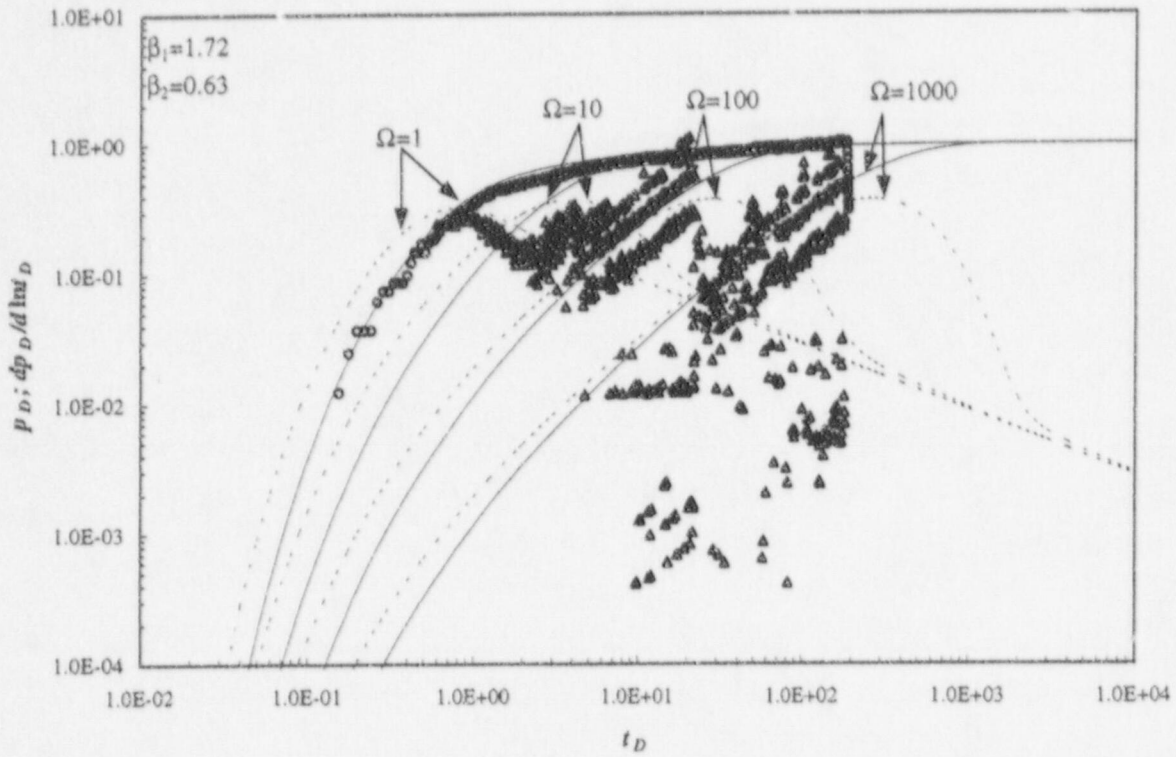
Figure 5.31: Type curve match of pressure data from monitoring interval W2AU
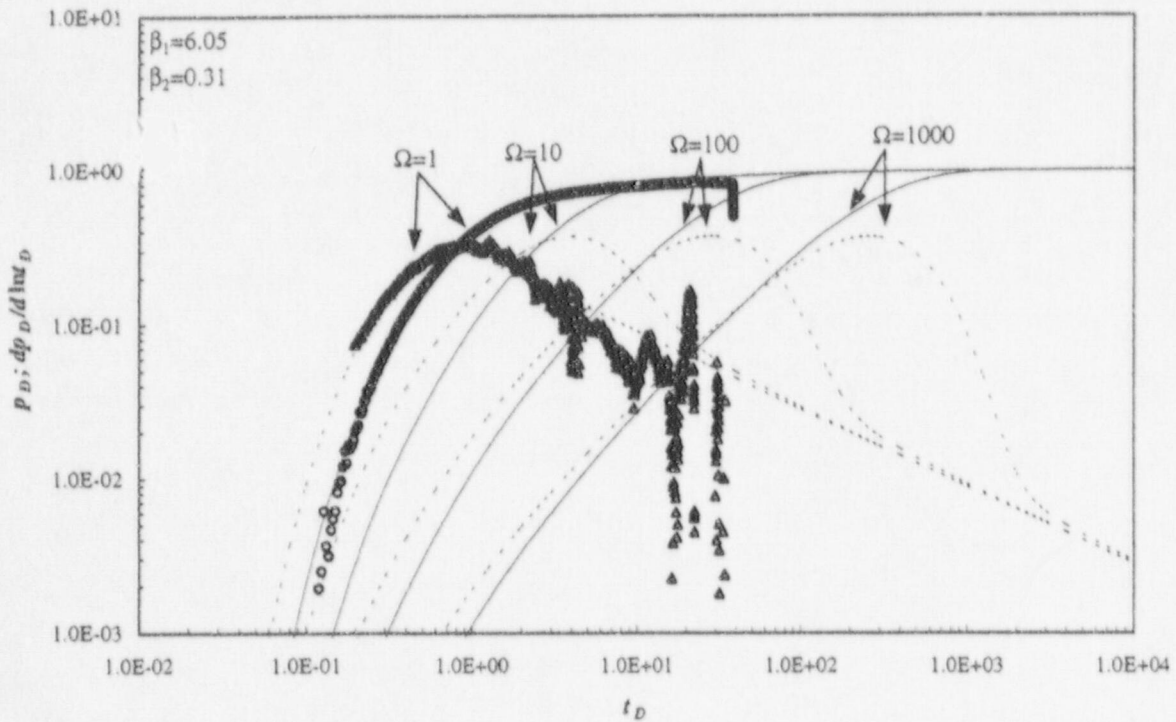
Figure 5.32: Type curve match of pressure data from monitoring interval W2AM
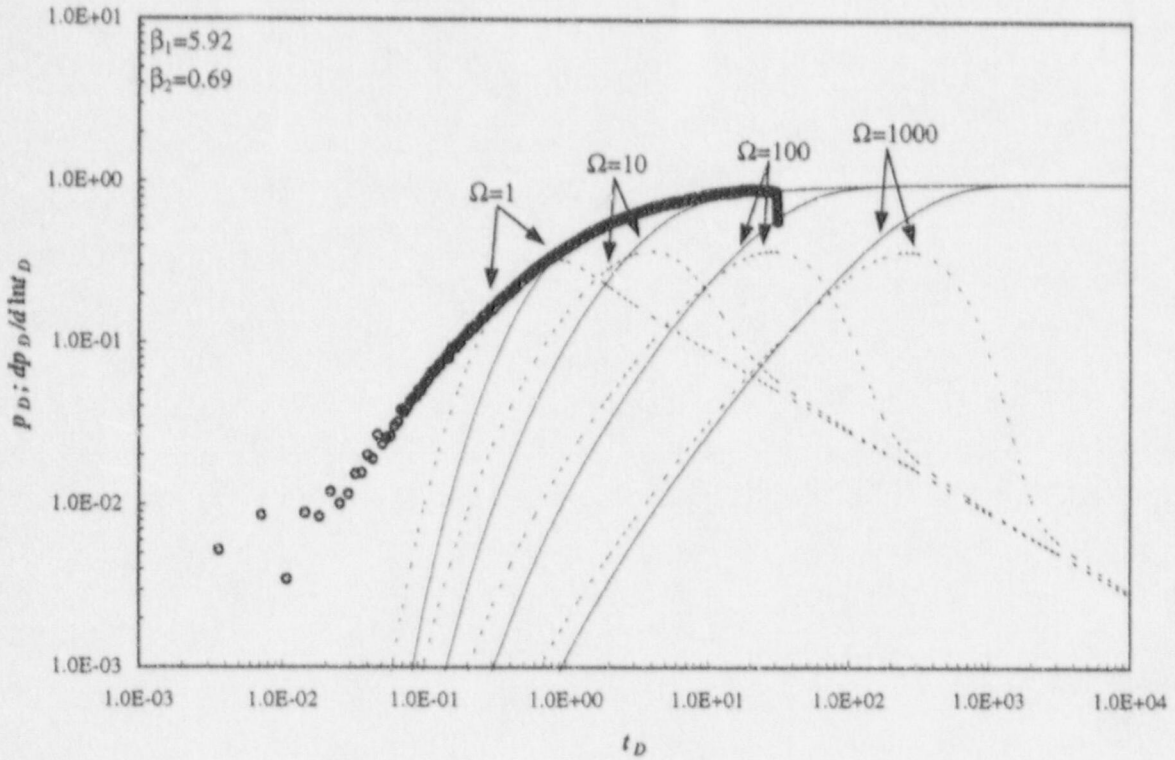
Figure 5.33: Type curve match of pressure data from monitoring interval W2AL
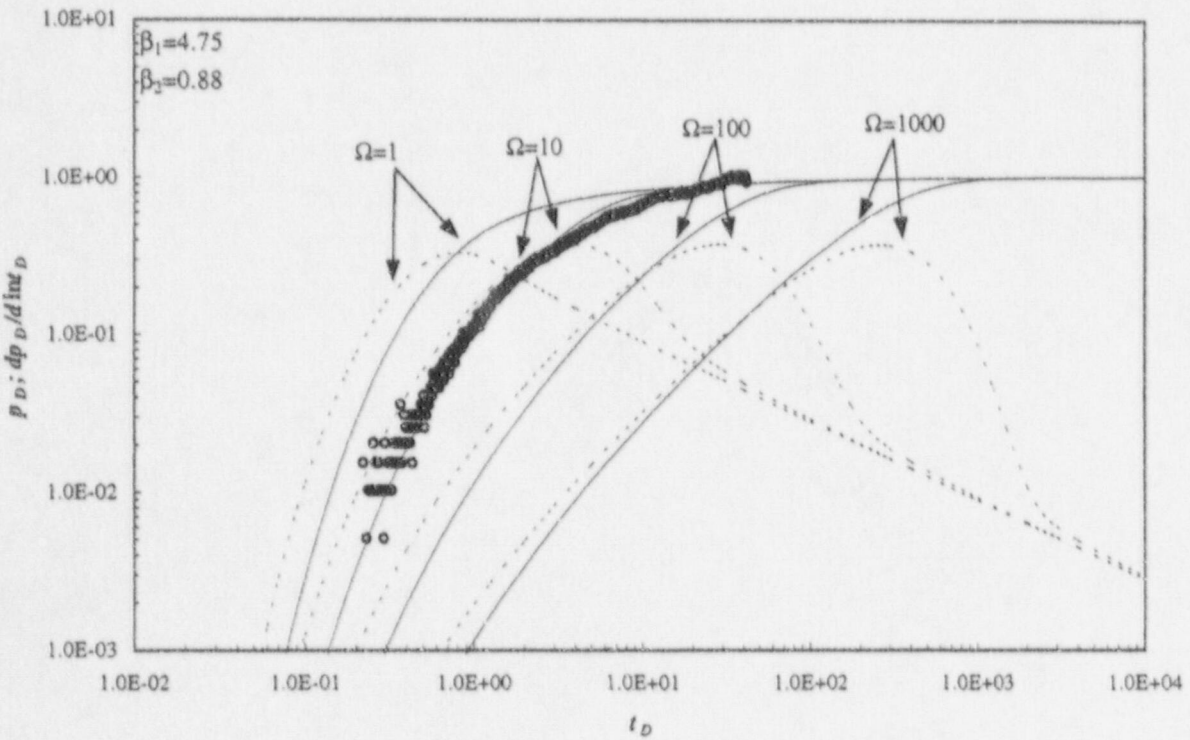
Figure 5.34: Type curve match of pressure data from monitoring interval W2AB
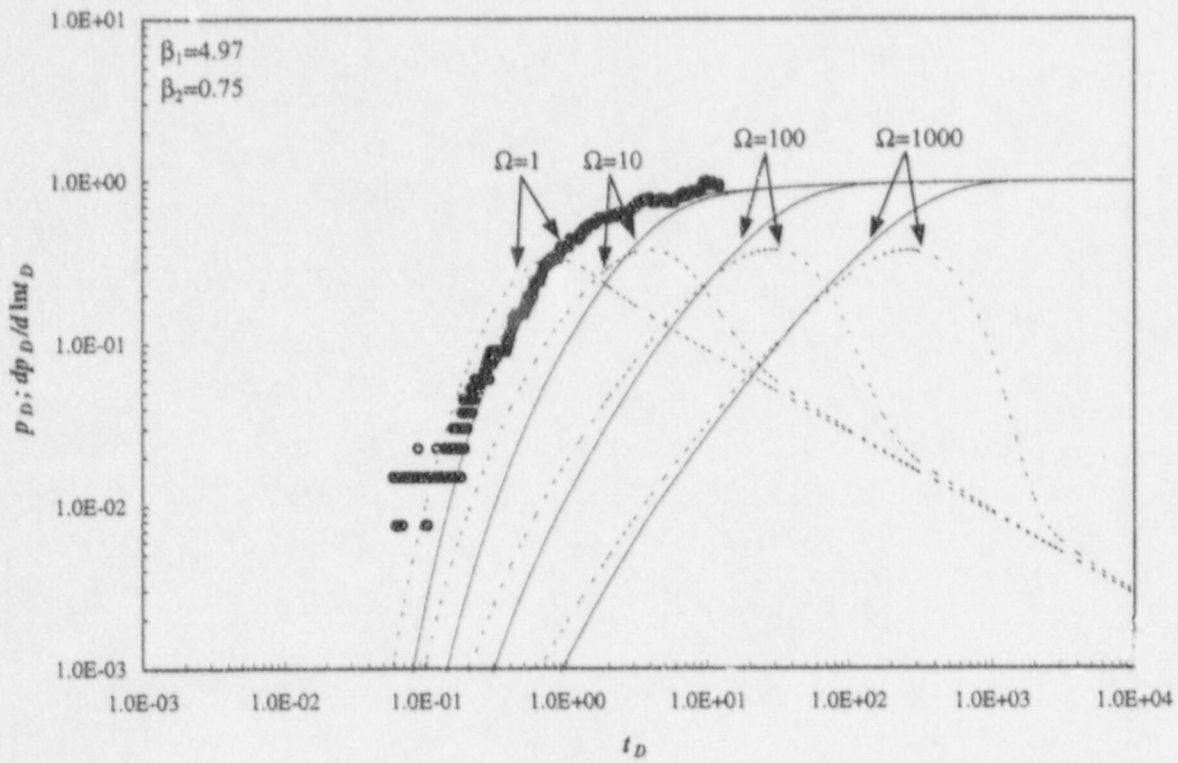
Figure 5.35: Type curve match of pressure data from monitoring interval W3U
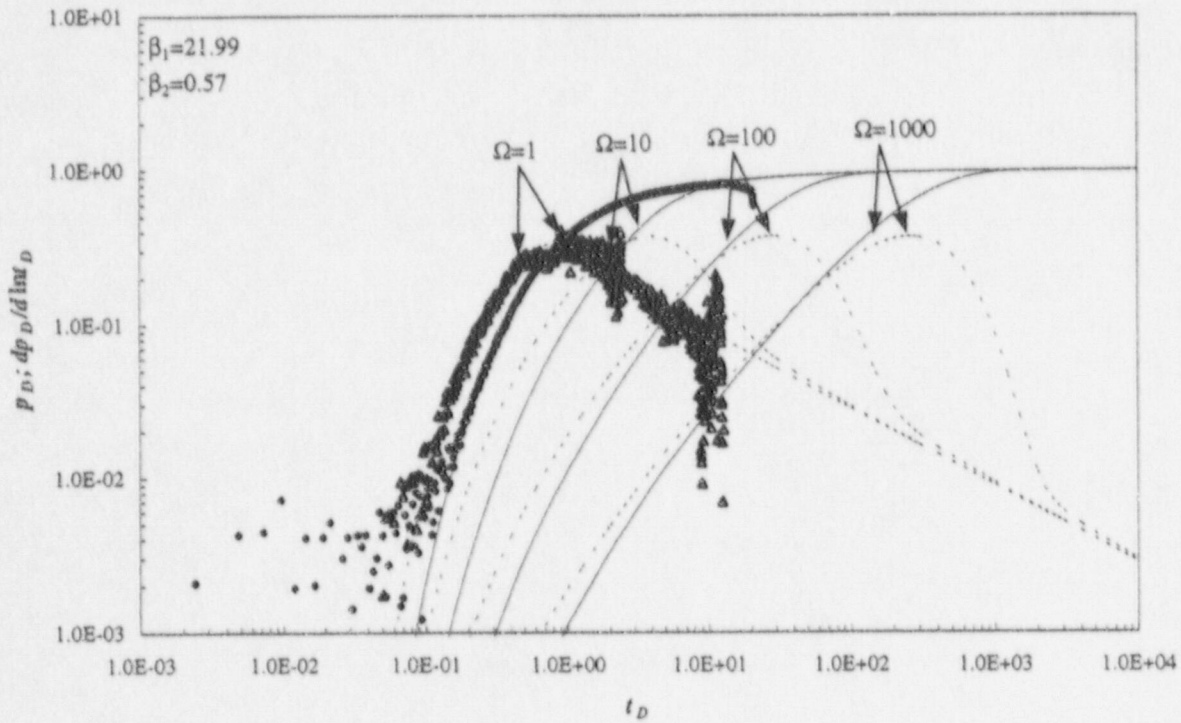
Figure 5.36: Type curve match of pressure data from monitoring interval W3M
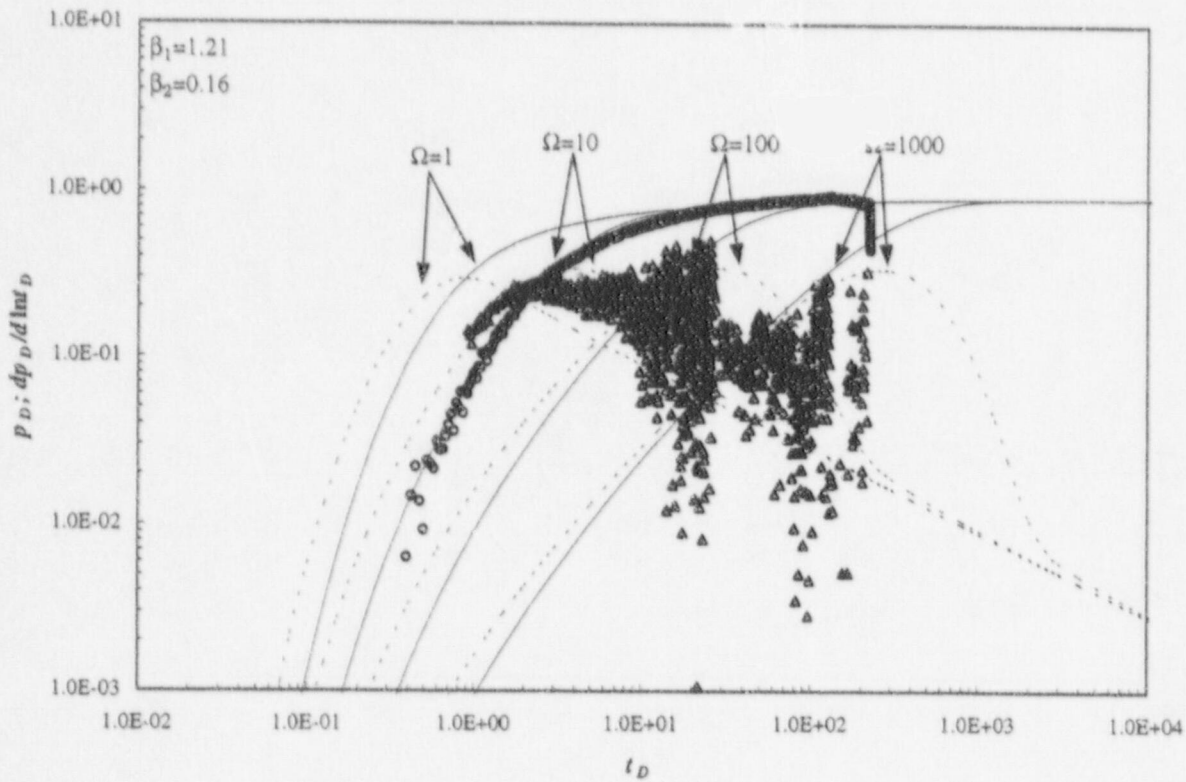
Figure 5.37: Type curve match of pressure data from monitoring interval X1
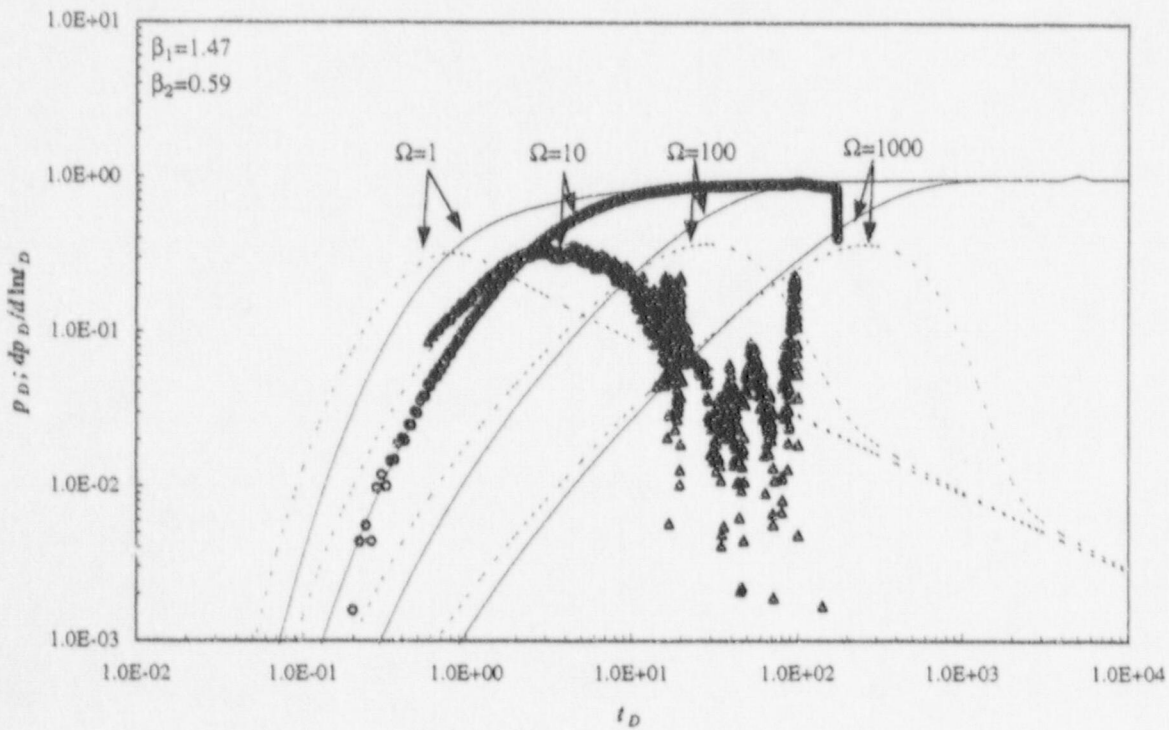
Figure 5.38: Type curve match of pressure data from monitoring interval X2U
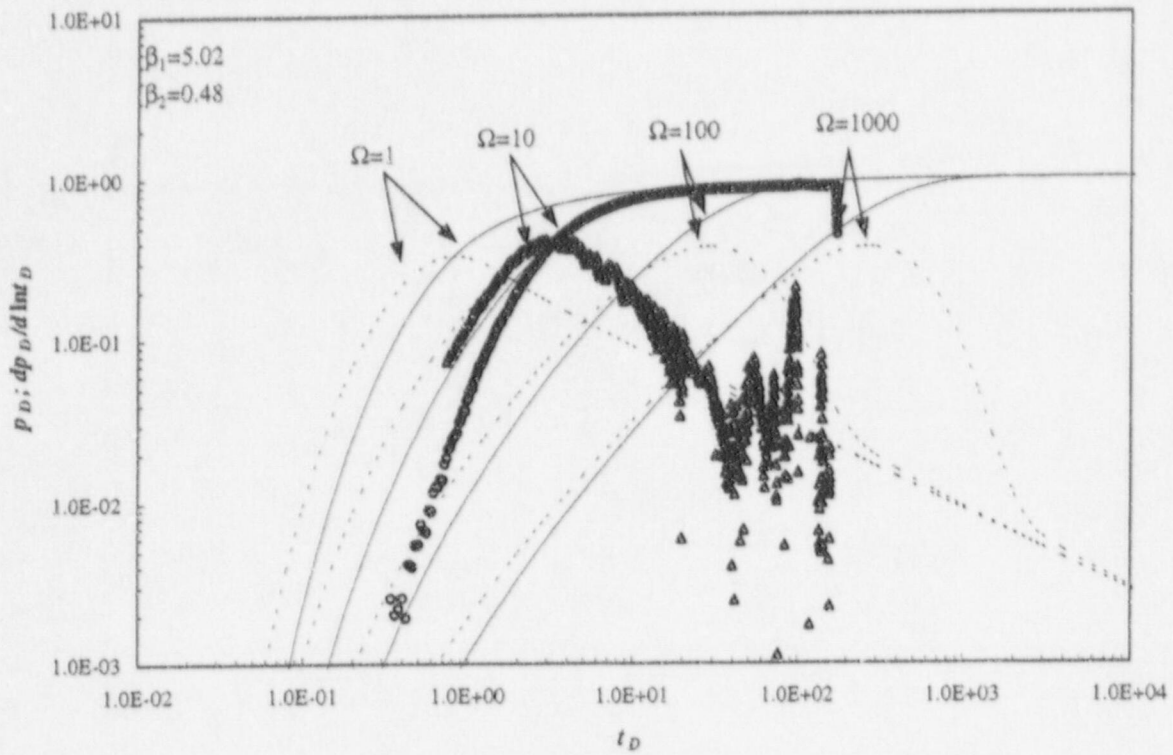
Figure 5.39: Type curve match of pressure data from monitoring interval X2M
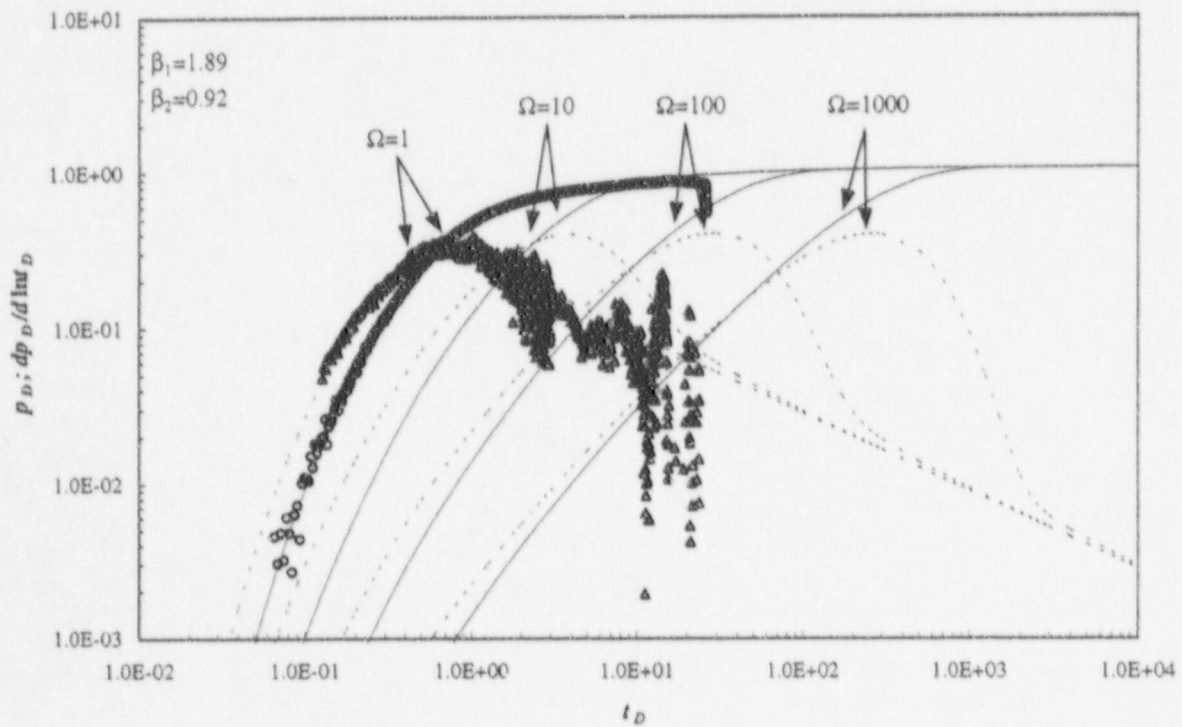
Figure 5.40: Type curve match of pressure data from monitoring interval X2B
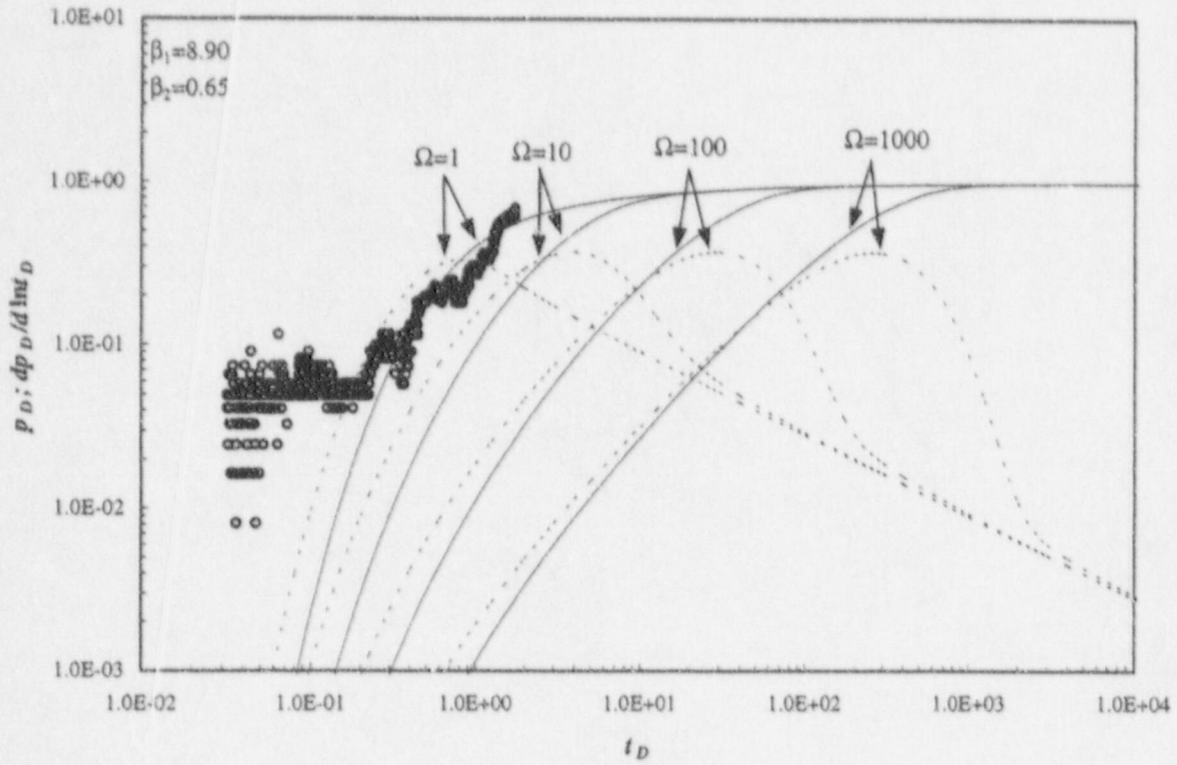
Figure 5.41: Type curve match of pressure data from monitoring interval Y1U
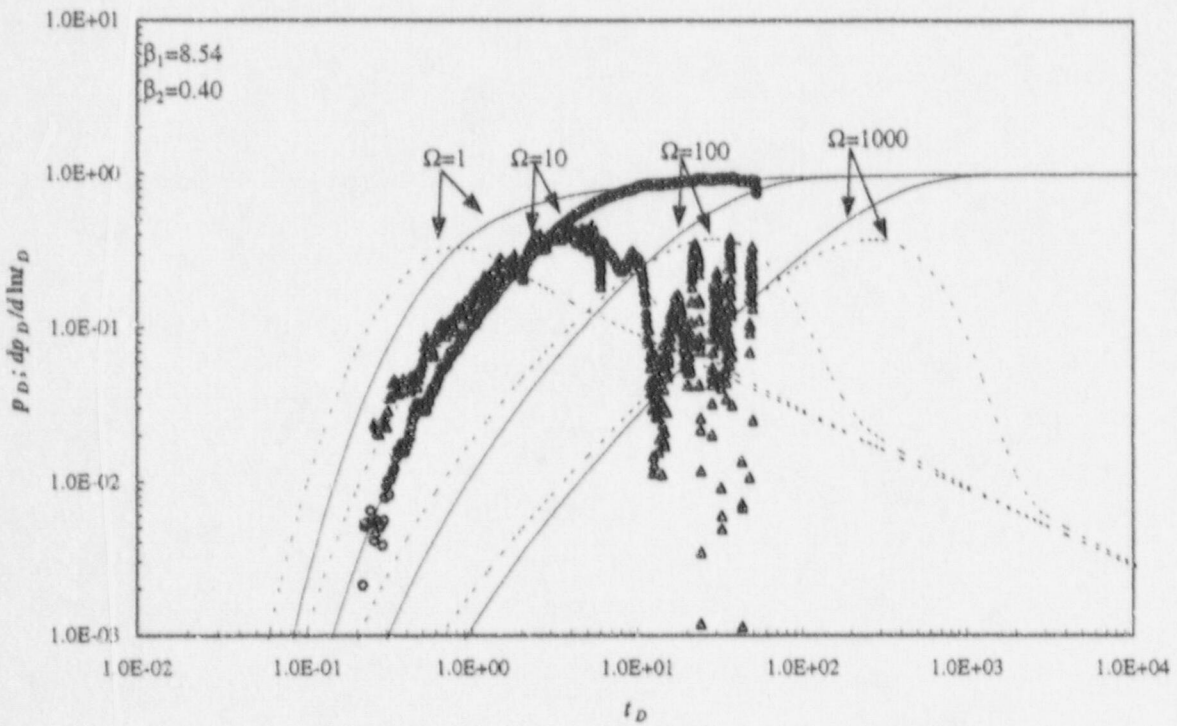
Figure 5.42: Type curve match of pressure data from monitoring interval Y1M
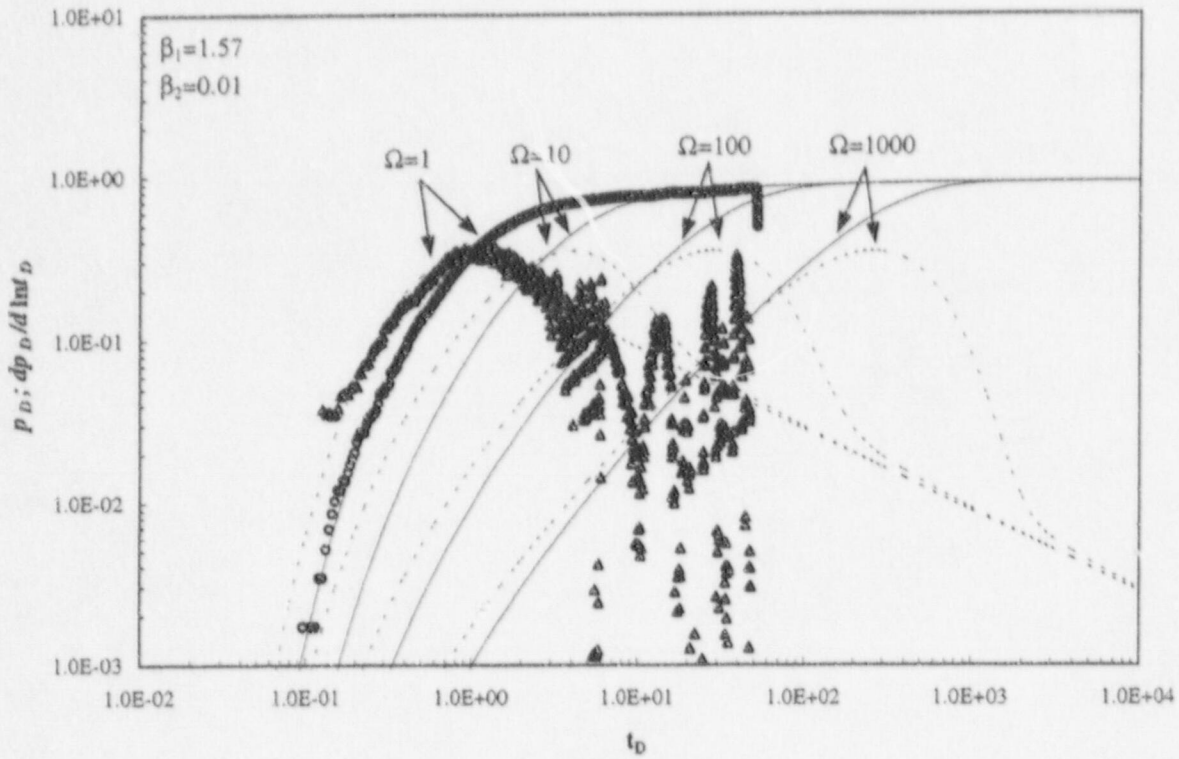
Figure 5.43: Type curve match of pressure data from monitoring interval Y2U
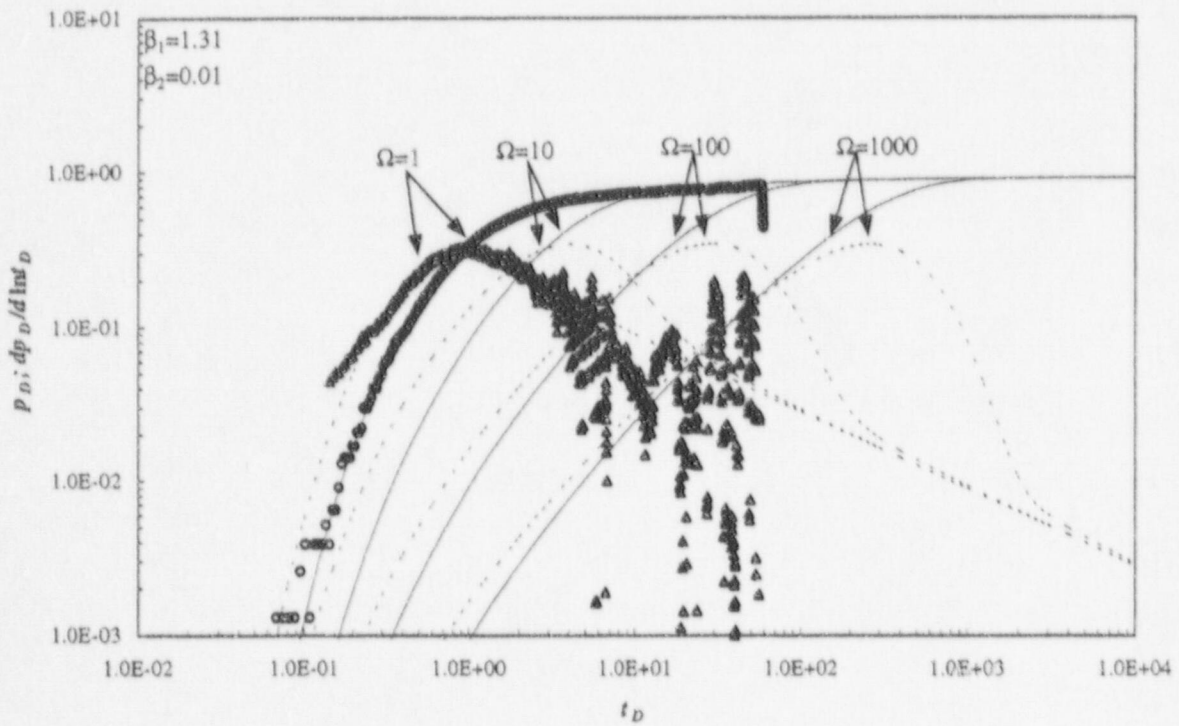
Figure 5.44: Type curve match of pressure data from monitoring interval Y2B
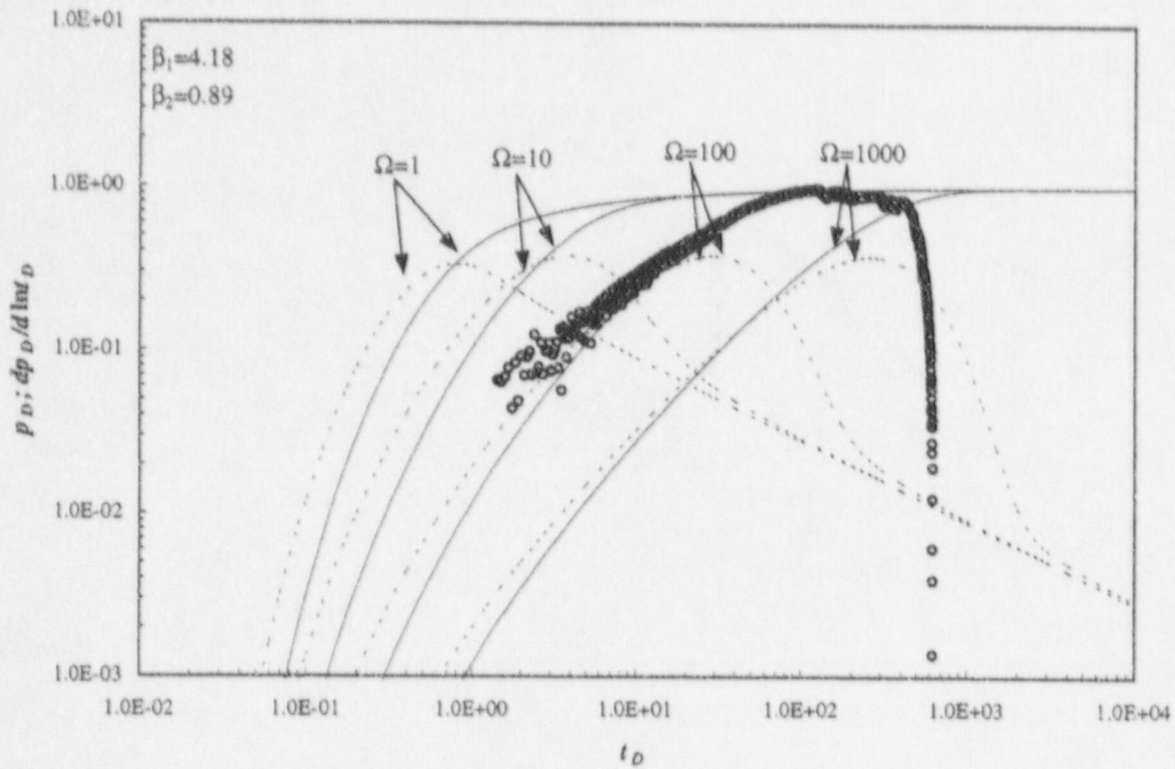
Figure 5.45: Type curve match of pressure data from monitoring interval Y3U
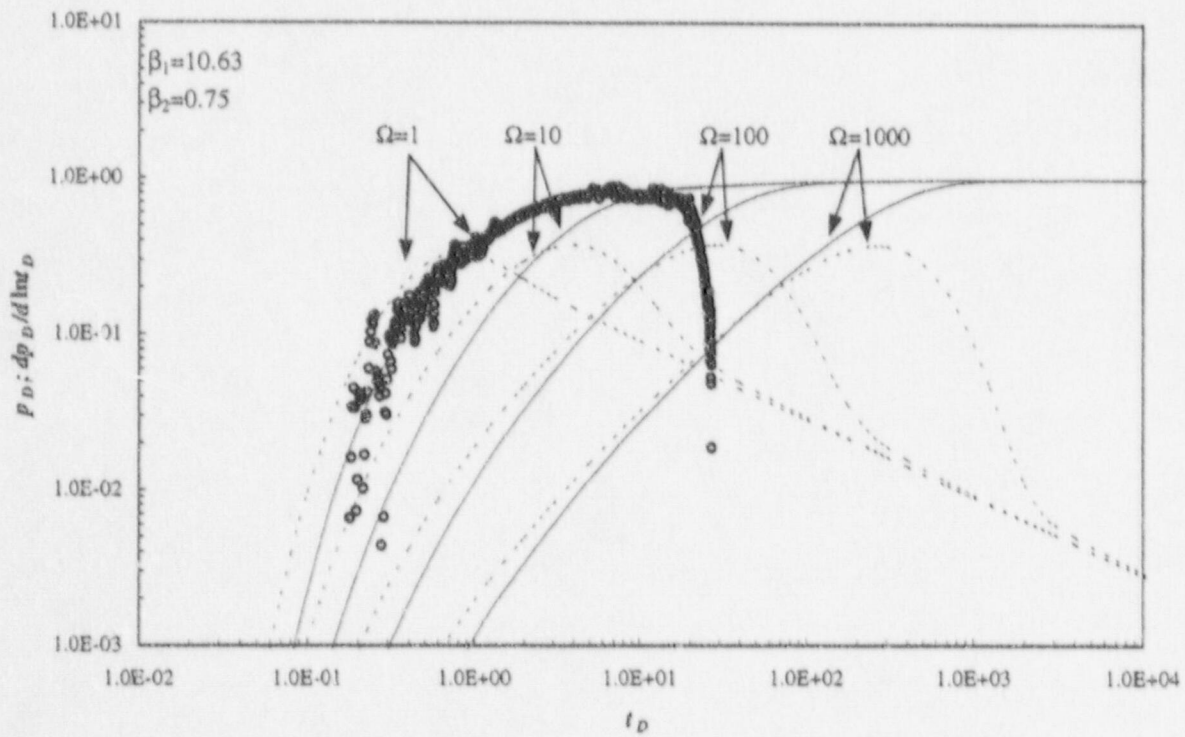
Figure 5.46: Type curve match of pressure data from monitoring interval Y3M

NUREG/CR-5559
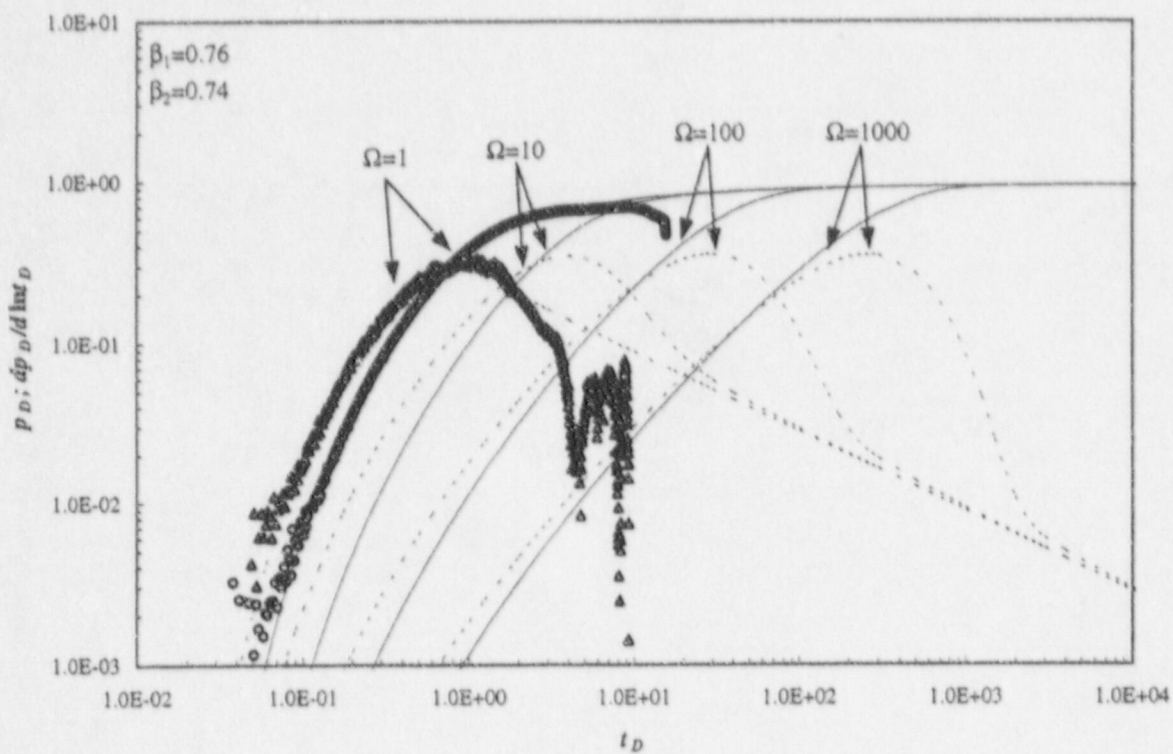
Figure 5.47: Type curve match of pressure data from monitoring interval Y3B
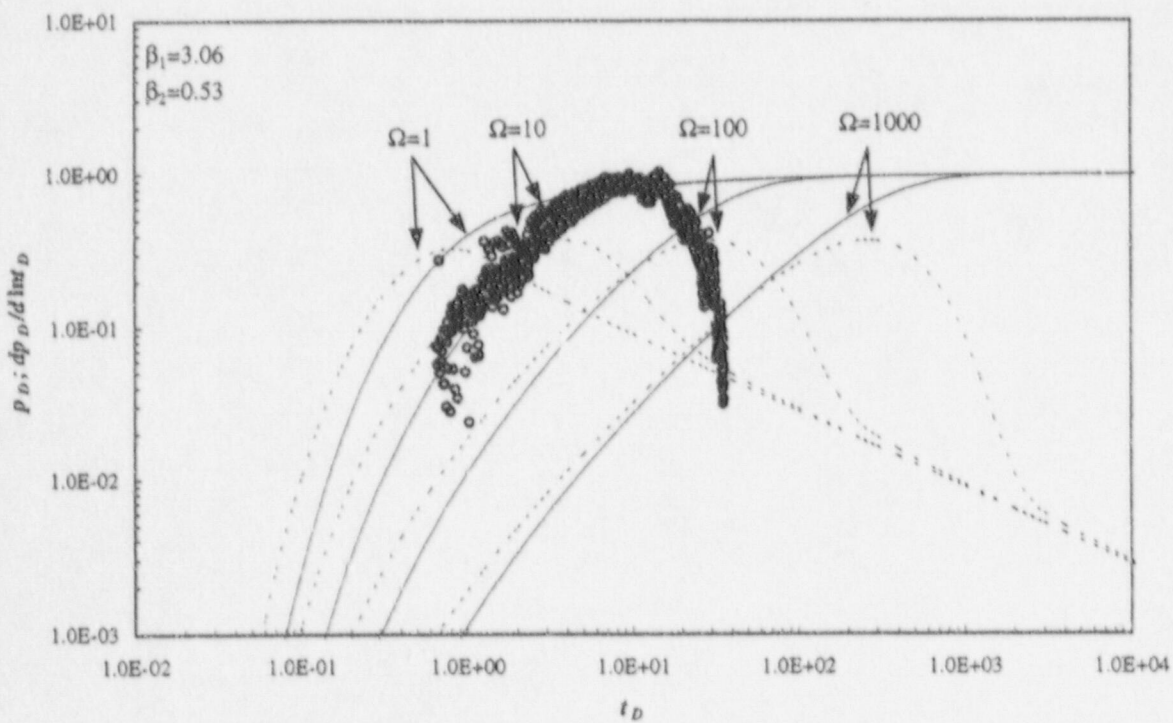
Figure 5.48: Type curve match of pressure data from monitoring interval Z1
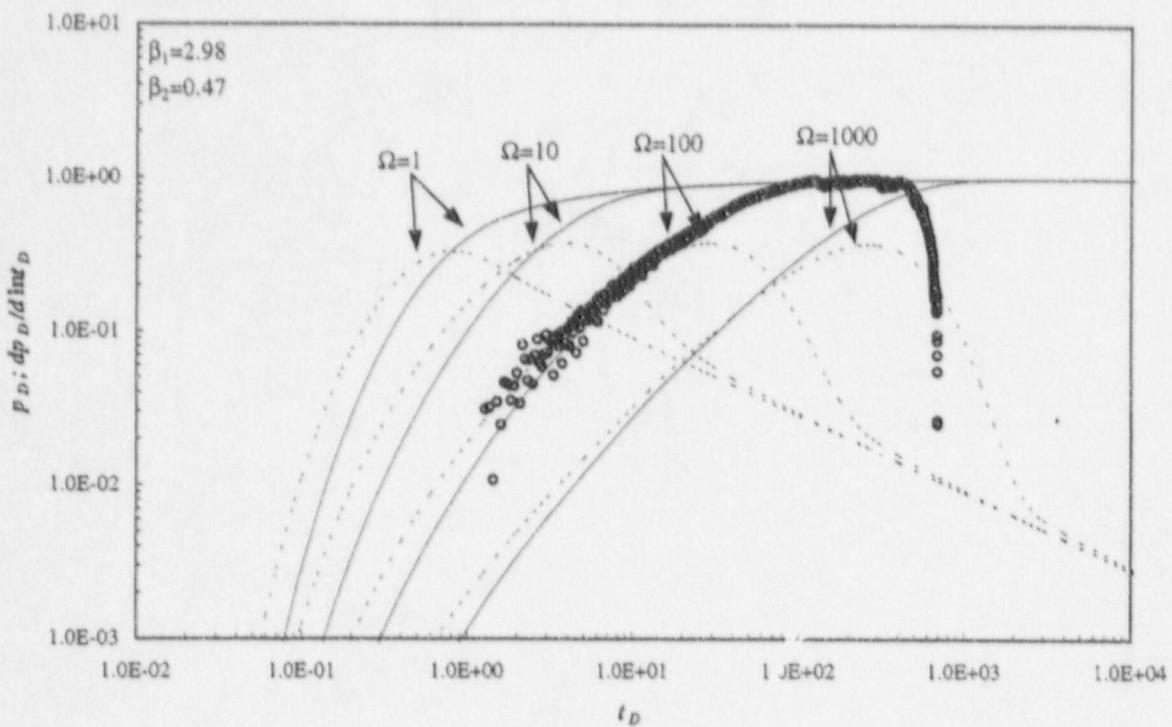
Figure 5.49: Type curve match of pressure data from monitoring interval Z2U
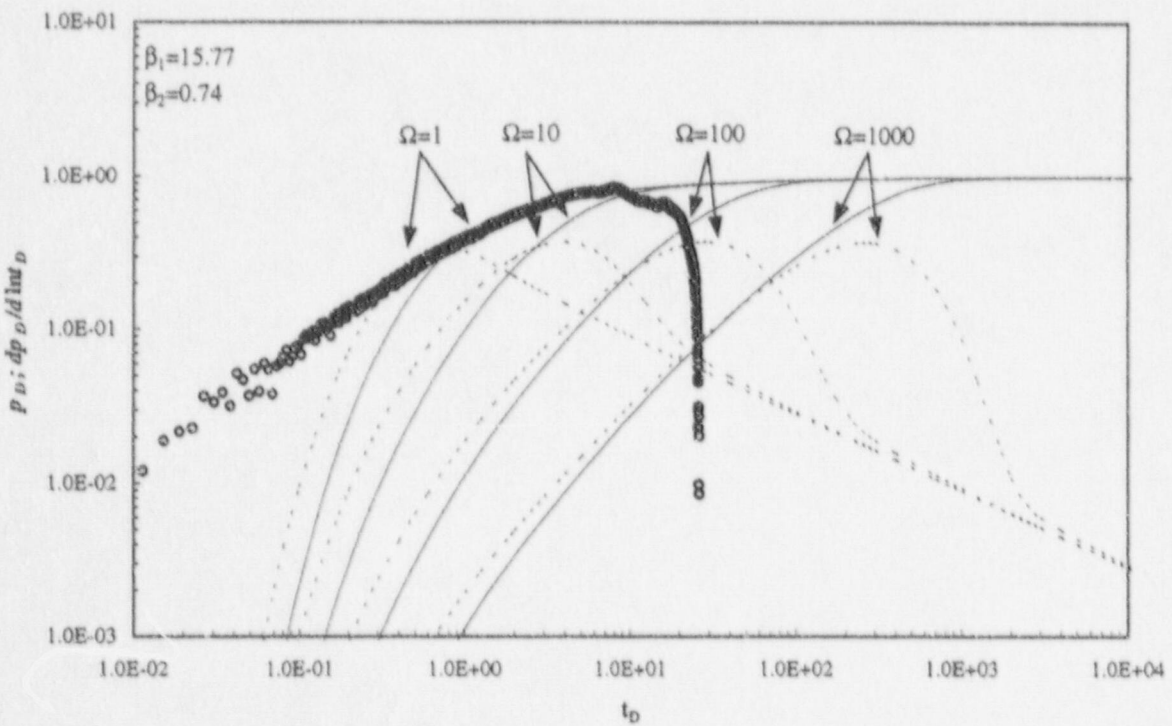
Figure 5.50: Type curve match of pressure data from monitoring interval Z2M
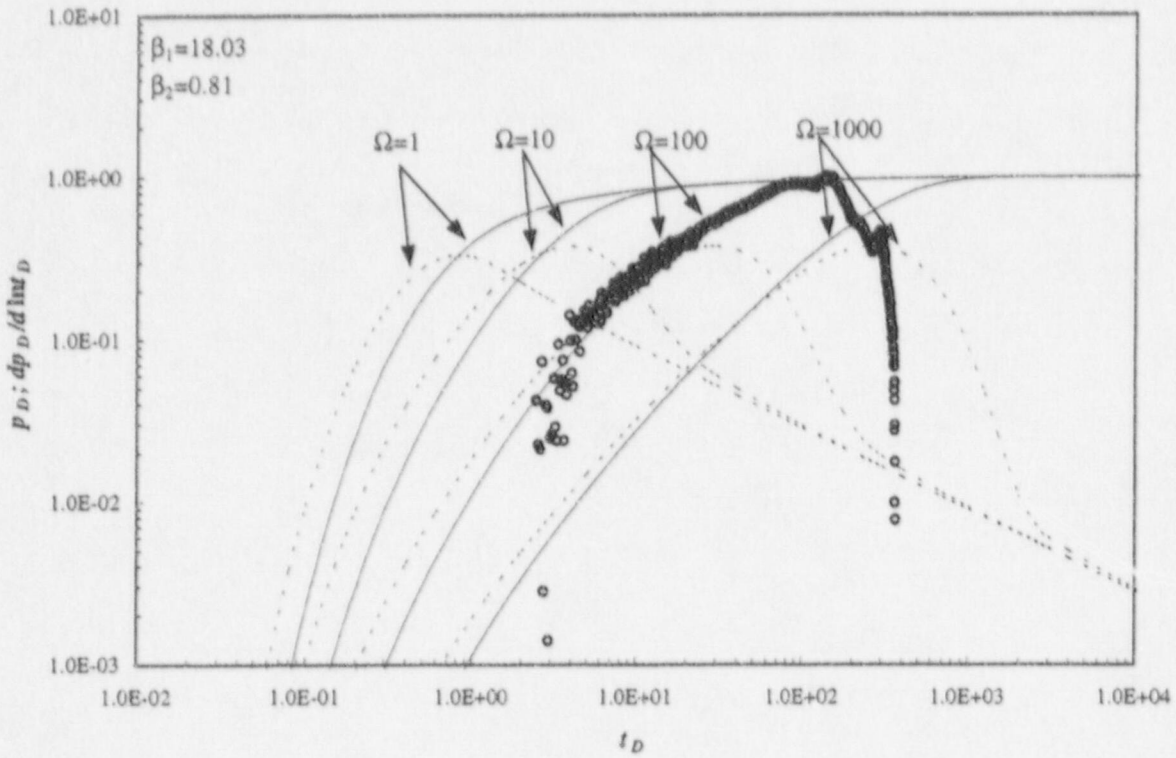
Figure 5.51: Type curve match of pressure data from monitoring interval Z2L
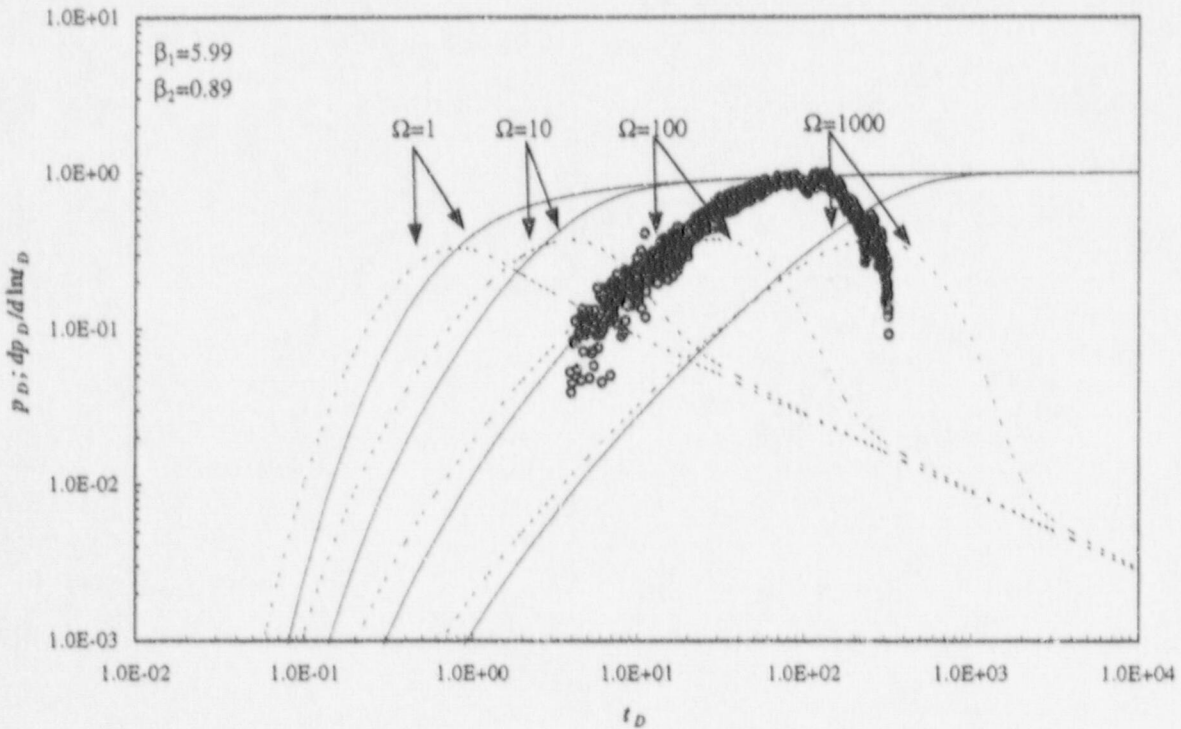
Figure 5.52: Type curve match of pressure data from monitoring interval Z2B
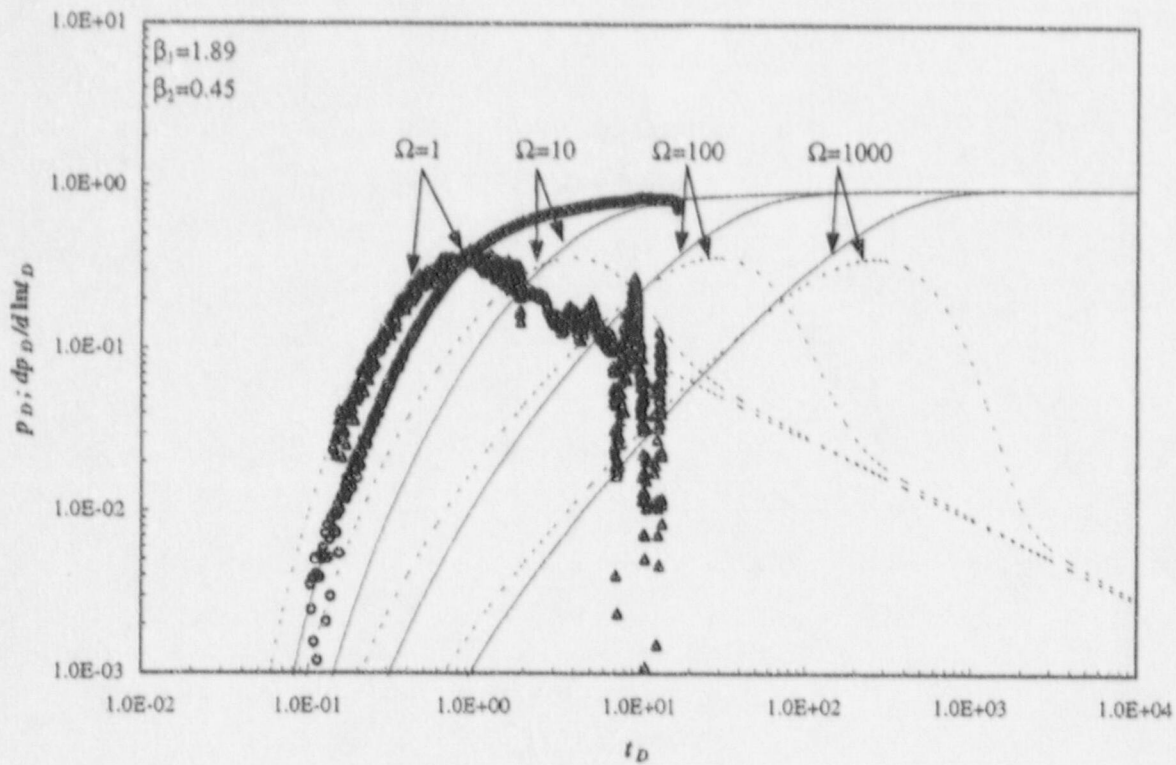
Figure 5.53: Type curve match of pressure data from monitoring interval Z3U
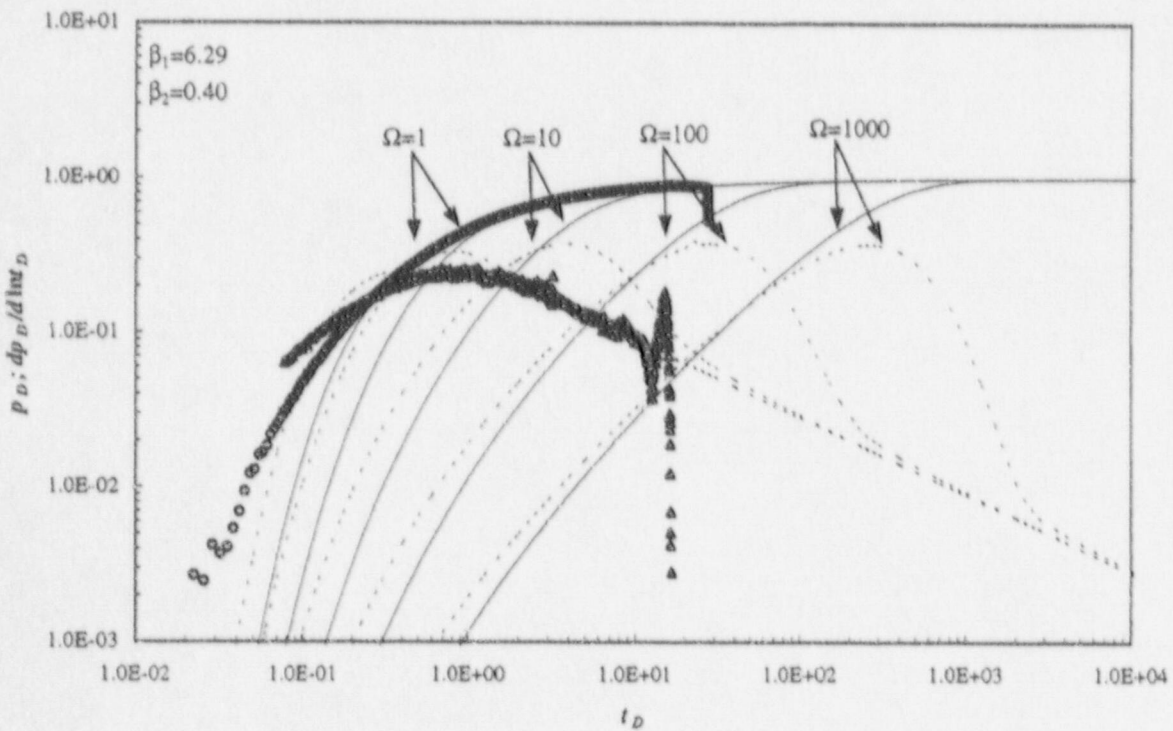
Figure 5.54: Type curve match of pressure data from monitoring interval Z3M

121
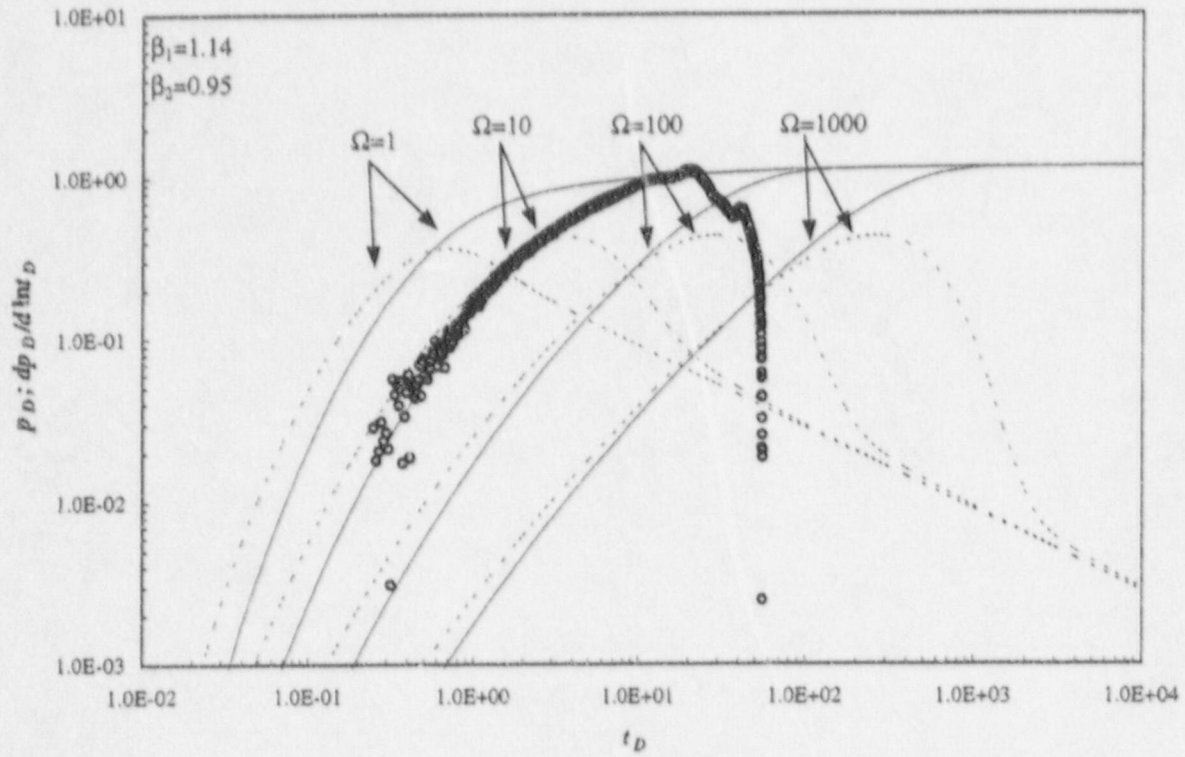
Figure 5.55: Type curve match of data from monitoring interval Z3B

6. INTERPRETATION OF PNEUMATIC INJECTION TEST DATA BY INVERSE MODELING

6.1 NUMERICAL SIMULATION OF CROSS-HOLE TESTS

6.1.1 Codes Used in the Analysis

To complement our type-curve analyses of cross-hole tests at the ALRS, we simulated these tests on the computer using a three-dimensional finite volume code, FEHM, developed at Los Alamos National Laboratory by Zyvoloski *et al.* (1988, 1996, 1997). Coupling FEHM with an inverse code, PEST (Doherty *et al.*, 1994), allowed us to estimate automatically the pneumatic parameters of the rock. For consistency with the type-curve analyses, we treated the fracture network at the site as a porous continuum. Likewise, we simulated only the single-phase flow of air. Our decision to use FEHM was based in part on the ability of this code to simulate two-phase flow of air and water in dual porosity and/or permeability continua, and to account for discrete fractures, should the need to do so arise. We were able to achieve success without activating these features of the code.

FEHM is coupled to a code X3D (Trease *et al.*, 1996) which automatically subdivides a three-dimensional domain into tetrahedral elements in a manner that enhances the computational efficiency of the simulator. We have supplemented these codes with a series of pre- and post-processors developed by us to facilitate the handling, analysis, and visualization of massive input and output data files, and to allow direct coupling between FEHM and PEST.

6.1.2 Computational Grid

The computational grid we employed in our analysis of cross-hole test data measures 63 *m* in the *x* direction, 54 *m* in the *y* direction, and 45 *m* in the *z* direction (Figures 1.2 and 1.3), encompassing a rock volume of 153,090 *m³* (Figure 6.1). The computational grid is illustrated for the case of cross-hole test PP4, during which injection takes place into borehole Y2, by means of two-dimensional images in Figures 6.2 and 6.3. Figure 6.2 shows three views of the grid perpendicular to the *x*-*y*, *x*-*z* and *y*-*z* planes. As the grid in the vicinity of boreholes is relatively fine, the corresponding areas appear dark in the figures. Figure 6.3 shows four cross-sectional views of the grid along vertical planes that contain selected boreholes. Since the grid is three-dimensional, its intersections with these planes do not necessarily occur along nodal points (*i.e.*, what may appear as nodes in the figure need not be such).

The grid is divided into three parts: a regular grid at the center of the modeled area, which measures 30 x 20 x 25 (15000) *m³* and has a node spacing of 1 *m*, equal to the nominal support of air permeability data from most available single-hole injection tests; a surrounding regular grid having a node spacing of 3 *m*; and a much finer and more complex unstructured grid surrounding each borehole. The grid includes a total of 39,264 nodes and 228,035 tetrahedral elements.
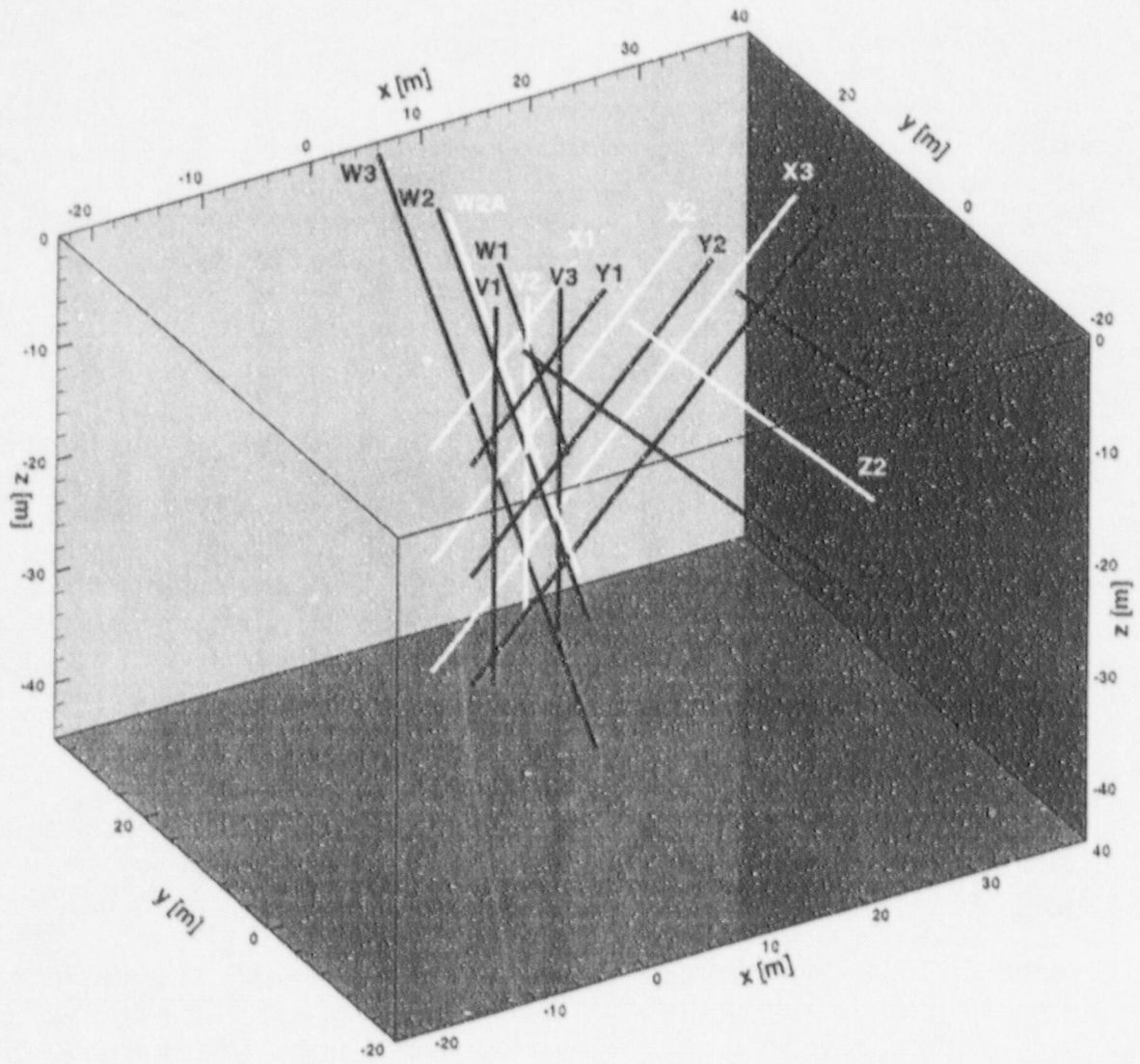
Figure 6.1: Boundaries of computational region.
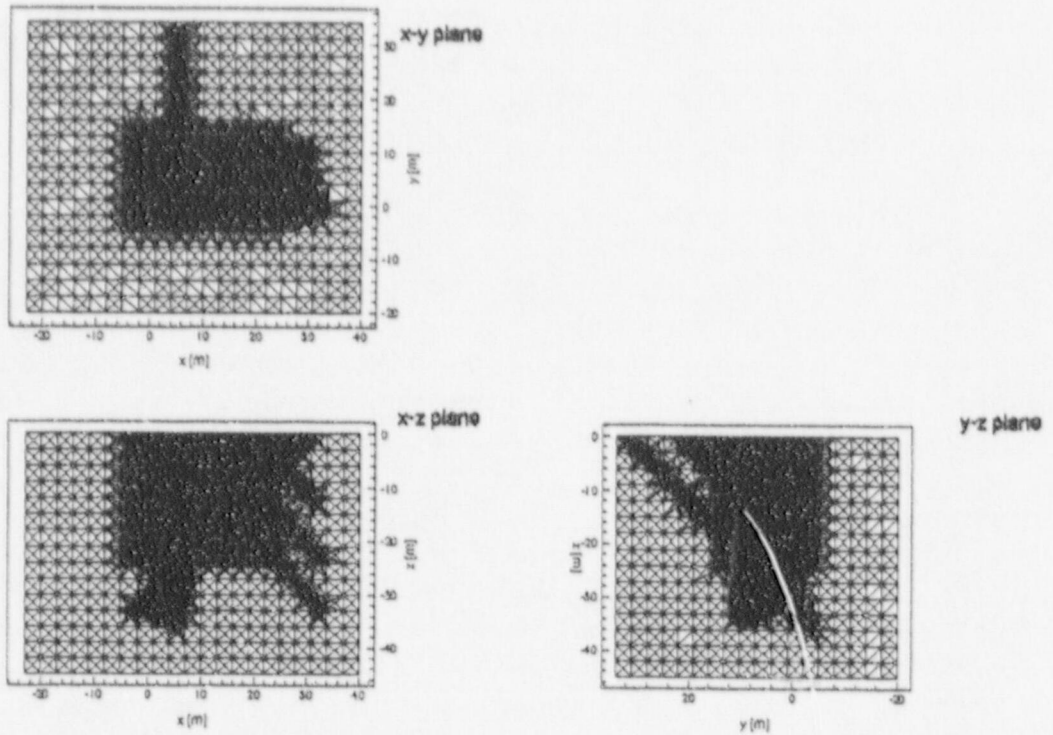
Figure 6.2: Side views of computational grid.
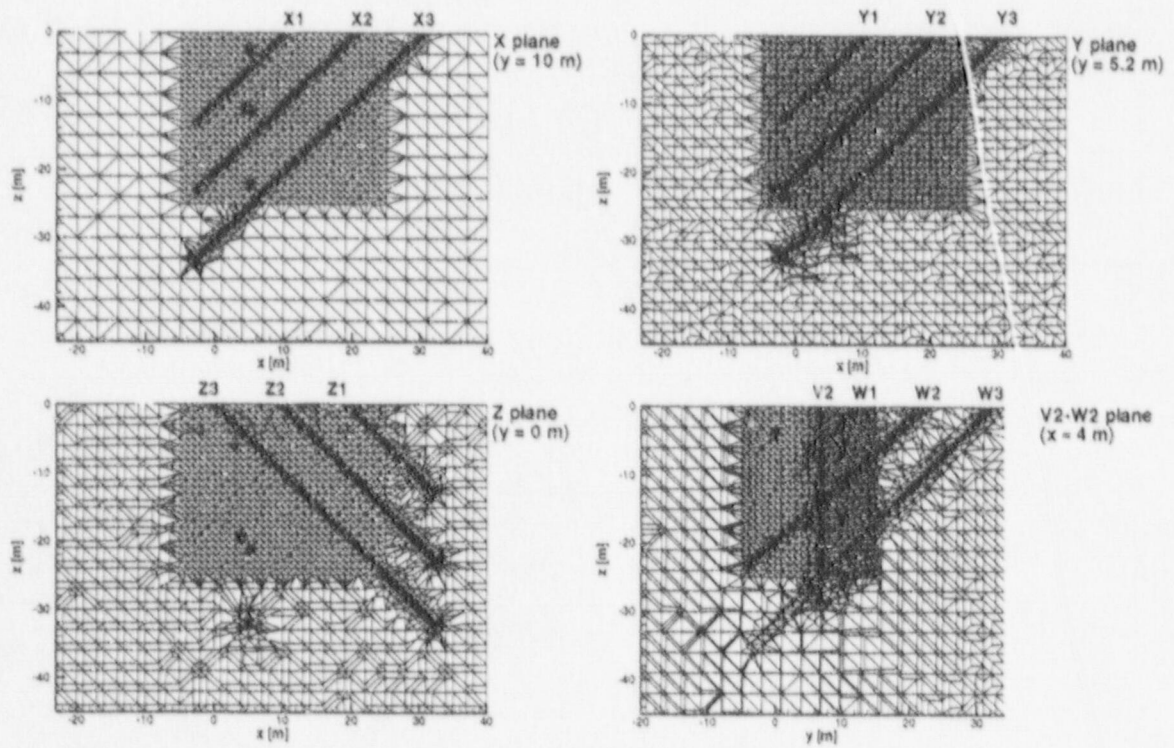
Figure 6.3: Vertical cross-sections through computational grid.

FEHM is a node-based finite volume code in which parameters are defined at nodes, not at elements. A nodal parameter is viewed as an average over a control volume associated with the node. This volume is defined using three-dimensional Voronoï diagrams based on Delaunay tesseilation (Watson, 1981). Numerical calculations are based on finite difference expressions, which represent local mass balance over each such finite volume.

Boreholes are treated in our numerical model as porous media having much higher permeability and porosity than the surrounding rock. The permeability and porosity of open borehole intervals are set to 3.23×10^{-4} m^2 and 1.0, respectively. These correspond to an ideal tube with radius equal to that of a typical borehole. The permeability and porosity of instrumented borehole segments are set to 3.23×10^{-5} m^2 and 0.5, respectively. The intersection of monitoring intervals V2B and W2 is assigned a lower permeability of 10^{-10} m^2 to avoid numerical difficulties; this value is still orders of magnitude higher than that of the surrounding rock. Packers are assigned zero permeability and a porosity of 10^{-5}. Each borehole is represented by a line of nodes, spaced 0.5 m apart, that are associated with parameters representing the properties of the borehole. This line forms the axis of a computational grid circumscribed by a cylinder with a hemispherical bottom. The radius of the cylinder and hemisphere, which define the grid that surrounds the injection borehole (Y2 in the case of cross-hole test PP4), is 1.52966 m. The radius of the cylinder and hemisphere which define the grid that surrounds each monitoring borehole is 0.499256 m. The grid associated with the injection borehole is wider and finer than those associated with monitoring boreholes so as to allow accurate resolution of the relatively high pressure gradients that develop around the former.

The cross-section of each borehole is represented numerically as a hexahedron centered about the borehole axis. A hexahedral plane passes through each node along this axis. The vertices of each hexahedral plane are designated as nodal points. Each such plane is circumscribed by a circle of radius 0.096755 m. This radius is calculated so as to insure that the sum of computational volumes associated with all nodes along the borehole axis is close to the actual volume of the borehole. The line segments, which connect nodes along the borehole axis, form the edges of tetrahedral elements. Where boreholes are located close to each other (as in the cases of V2 and the W-series of boreholes; W2A and W2; W1 and Y1; W3 and Y3), the grid between them is made finer in order to resolve correctly processes that take place within this grid volume. The most complicated of the grid structures is that representing the region between boreholes V2 and W2, which intersect each other (Figure 6.3).

Within each borehole grid, additional nodes are located along radii that form extensions of line segments which connect nodes along the borehole axis with nodes along the vertices of hexagonal planes lying perpendicular to this axis. The intervals between these nodes grow sequentially with distance from the borehole axis by a factor of 1.6, thus forming a geometric series. The number of rays and nodes associated with the injection borehole are larger that those associated with monitoring boreholes. Each borehole grid is additionally made finer near the soil surface so as to obtain an accurate resolution of conditions near this atmospheric boundary. The net result is a complex three-dimensional grid which represents quite accurately the geometry, flow properties, and storage capabilities of vertical and inclined boreholes at the ALRS study area; is

capable of resolving medium heterogeneity on a support scale of 1-*m* across the site; is able to represent, with a high degree of resolution, steep gradients around the injection test interval, as well as pressure interference between boreholes, no matter how closely spaced; and assures smooth transition between fine borehole grids having radial structures and surrounding coarser grids having regular structures.

6.1.3 Initial and Boundary Conditions

As we consider only single-phase airflow the saturation of air, and associated pneumatic properties of the rock, remain constant during each simulation. The only initial condition we need to specify is air pressure, which we take to be the average barometric pressure of 0.1 *MPa*. The side and bottom boundaries of the flow model are impermeable to airflow. Our results suggest that these boundaries are sufficiently far from injection boreholes to have virtually no effect on simulated cross-hole tests. The top boundary coincides with the soil surface and is maintained at a constant and uniform barometric pressure of 0.1 *MPa*. Though barometric pressure fluctuated during each cross-hole test, these fluctuations were small during the first two days of test PP4 and we therefore concentrate our analysis on pressure data obtained during these first two days.

6.1.4 Input Parameters

The numerical model requires that air permeability and air-filled porosity be specified at each node; these initial values are later modified by the parameter estimation code PEST so as to conform to pneumatic pressures recorded during injection tests. Any model input parameter assigned to a node represents an average over a control volume associated with that node. Our initial assignment of air permeabilities was based on geostatistical interpolation and extrapolation (kriging) of 1-*m* and 3-*m* scale data from steady state analyses of single-hole pneumatic tests across the entire computational grid (the kriging we described in the Introduction involved a much smaller rock volume). Permeabilities were first kriged on a regular gird and then projected onto the nodes of our irregular computational grid by interpolation. The corresponding distributions of air permeabilities along four vertical sections that contain boreholes are illustrated in Figure 6.4, which also show the permeabilities we assigned to boreholes. Open borehole intervals are shown to be of high permeability, and packers of low permeability. Figure 6.5 shows that the kriged estimation variance of log-transformed air permeabilities increases with distance from boreholes along which measurements are available.

Initial air-filled porosities were obtained by subtracting kriged estimates of water content from those of porosity. Once again, kriging was conducted on a regular grid and the results projected onto the nodes of our irregular computational grid by interpolation. The corresponding distributions of air-filled porosity along four vertical sections that contain boreholes are illustrated in Figure 6.6. Open borehole intervals are seen to have high air-filled porosity, and packers low porosity. Air-filled porosity is seen to decrease with depth; we arbitrarily disallowed it from falling below 1×10^{-3}. The estimation variance of log-transformed air-filled porosity in Figure 6.7 was calculated as the sum of corresponding variances of log-transformed porosity and water content. It increases with distance from boreholes along which all measured values are located.
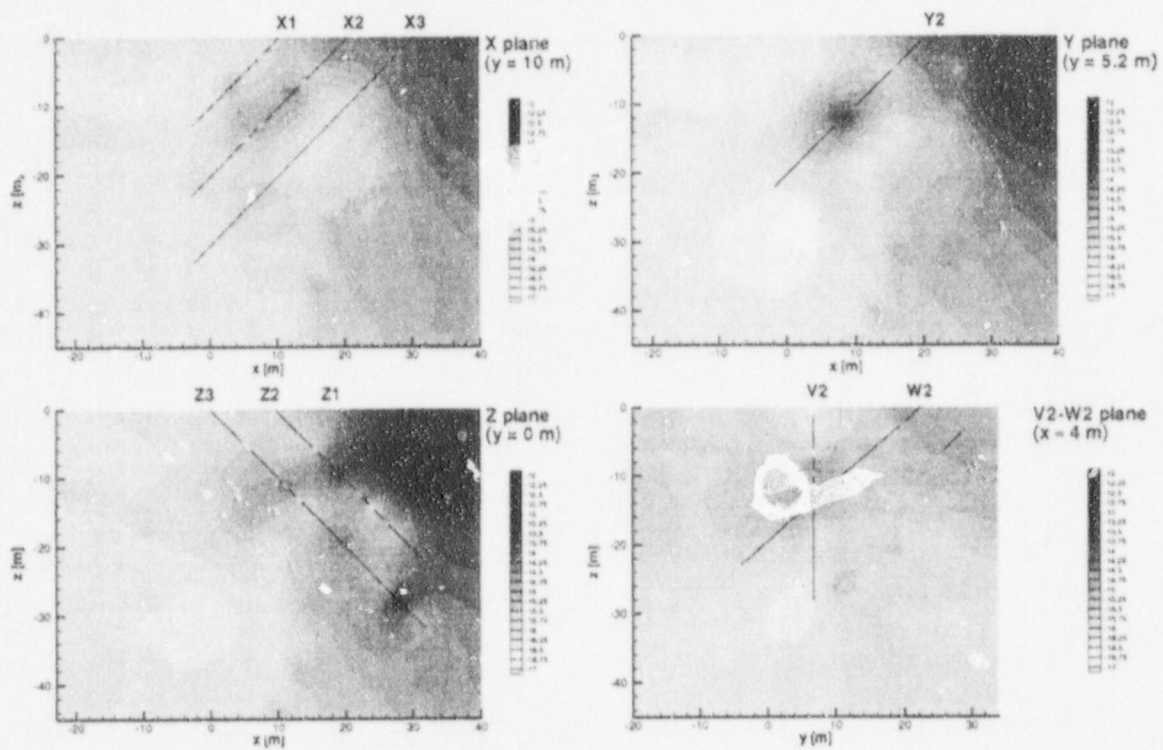
Figure 6.4: Kriged log k within computational region.
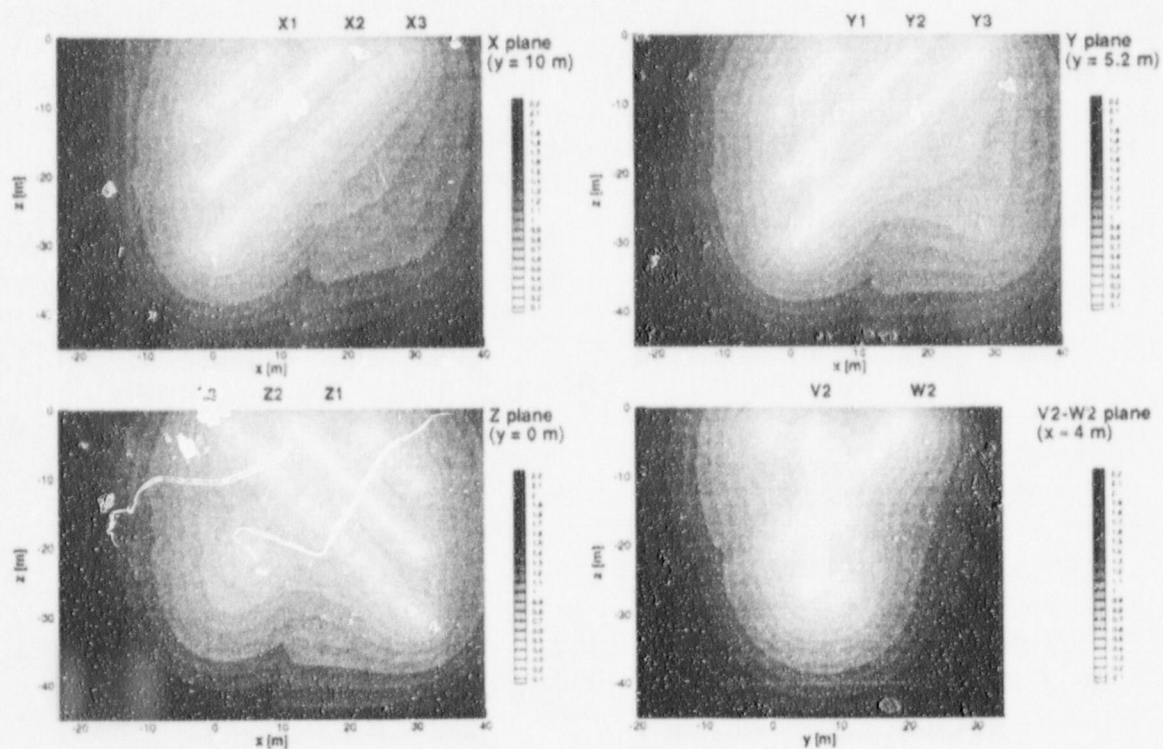
Figure 6.5: Kriged variance of log k within computational region.
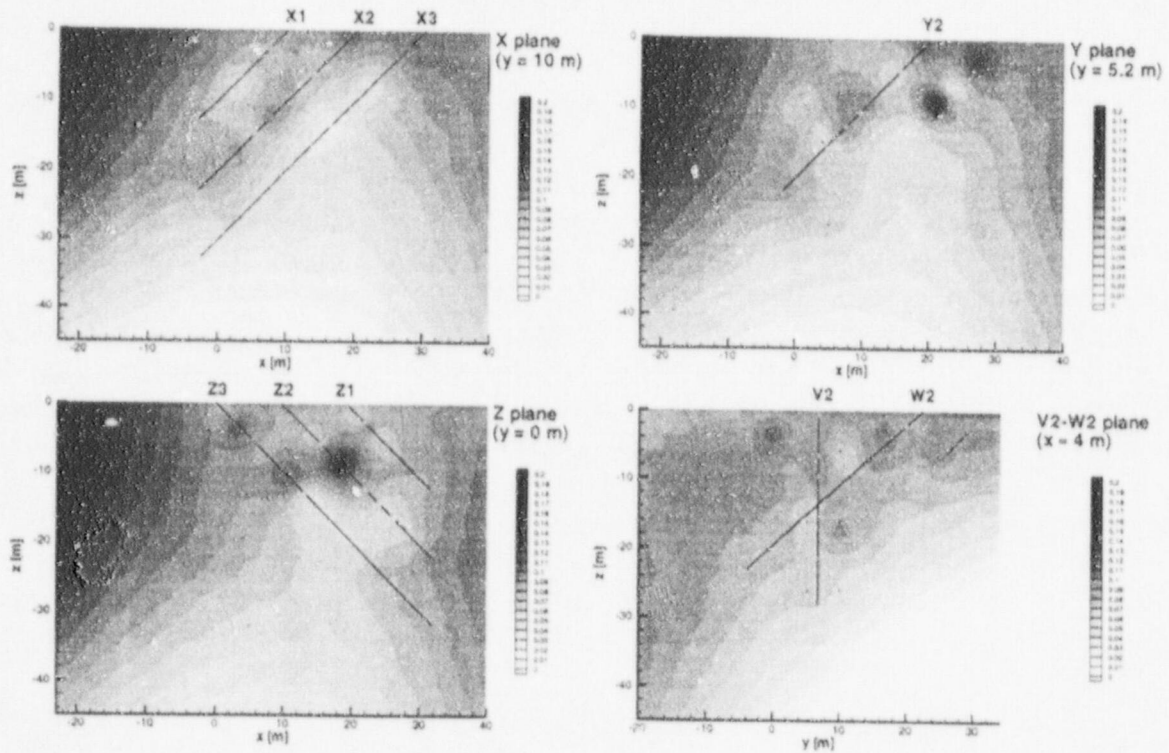
Figure 6.6: Kriged air-filled porosity within computational region.
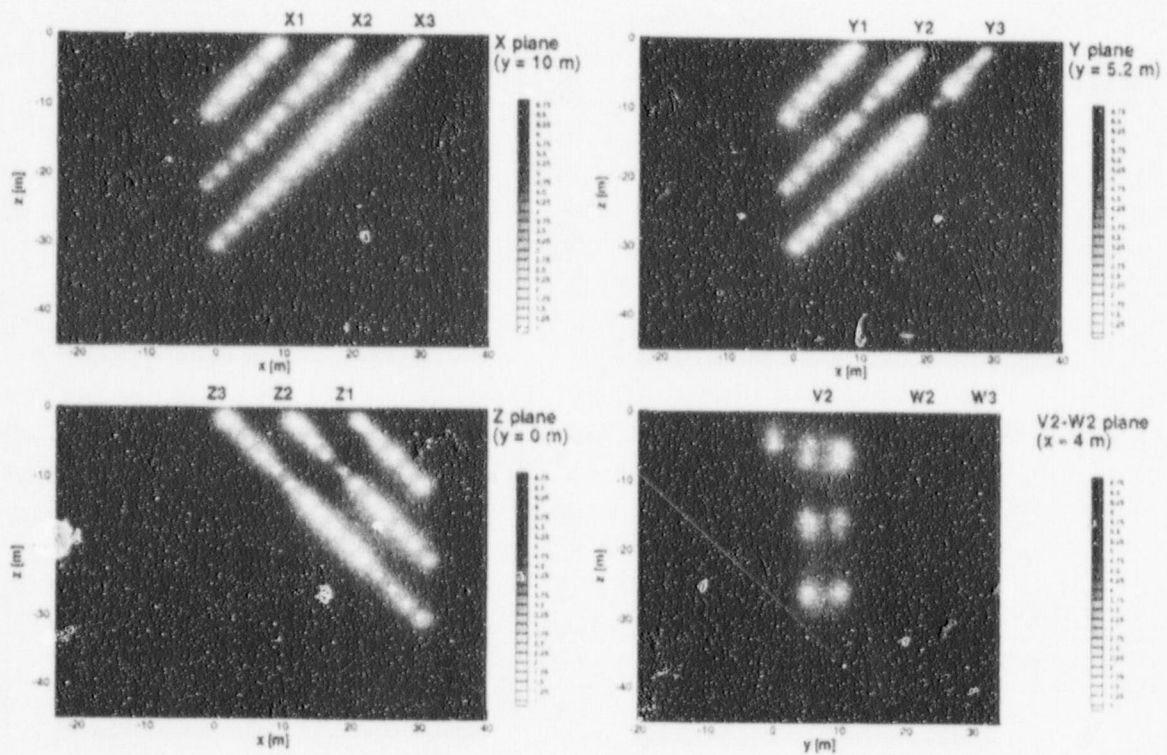
Figure 6.7: Kriged variance of air-filled porosity within computational region.

6.2 SIMULATION OF CROSS-HOLE TEST PP4

For reasons listed in Chapter 5, we focus on the numerical simulation and interpretation of cross-hole test PP4. Descriptions of this test and corresponding pressure responses were given in the same chapter. Pressure responses (heavy solid curves) in injection and monitoring borehole intervals, obtained by simulating test PP4 using kriged permeabilities and air-filled porosities without accounting for the effect of boreholes on flow, are compared with measured data (light solid curves) in Figure 6.8. The calculated pressure responses are evidently very different from those observed in the field. An attempt to improve the fit between calculated and observed pressures by model calibration using trial and error proved to be difficult and only partially successful. It nevertheless indicated that the fit could be improved significantly (though not sufficiently) upon increasing the initial permeability, and decreasing the air-filled porosity, by one order of magnitude across the entire grid. The corresponding pressure responses (dashed) are compared with actual data (light solid curves) in Figure 6.9. This served as a preliminary indication that air permeabilities from single-hole tests are generally lower than their cross-hole test counterparts, and air-filled porosities based (primarily) on matrix data are generally higher than their fracture counterparts, both by about one order of magnitude.

There is little information in the literature about the effect that open borehole intervals may have on pressure propagation, and response, during interference tests. Paillet (1993) noted that the drilling of an additional observation borehole had an effect on drawdowns created by an aquifer test. We likewise anticipated that open borehole intervals might impact the interpretation of our pneumatic cross-hole tests due to preferential airflow through, and enhanced storage within, these intervals. To examine this issue, we repeated the simulation, which led to the dashed curve in Figure 6.8 by accounting for all open borehole intervals in the model. The corresponding pressure responses are shown by heavy solid curves in Figure 6.9. It is clear that the presence of open borehole intervals has a considerable effect on pressure propagation through the site, and on pressure responses within boreholes. These responses can be either higher or lower than those calculated without open borehole intervals, and would be difficult to predict without a model such as ours. The discrepancy between pressures calculated with and without open borehole intervals is especially large in borehole X3, and within interval Z3B, which appear to have enhanced pneumatic connections to the atmosphere.

The distribution of pressures across two-dimensional vertical sections through the numerical model four days after the start of test PP4 are shown in Figures 6.10 for the case where open borehole intervals are not accounted for, and in Figure 6.11 for the case where they are. The open borehole intervals, packers, and their effects on pressure distribution are clearly evident in Figure 6.11. Both figures show how the atmospheric boundary causes the pressure distributions to exhibit vertical asymmetry. The effects of lateral and bottom no-flow boundaries on pressure are seen to be slight. It is evident that boreholes X2, X3 and Z3 are venting the system.
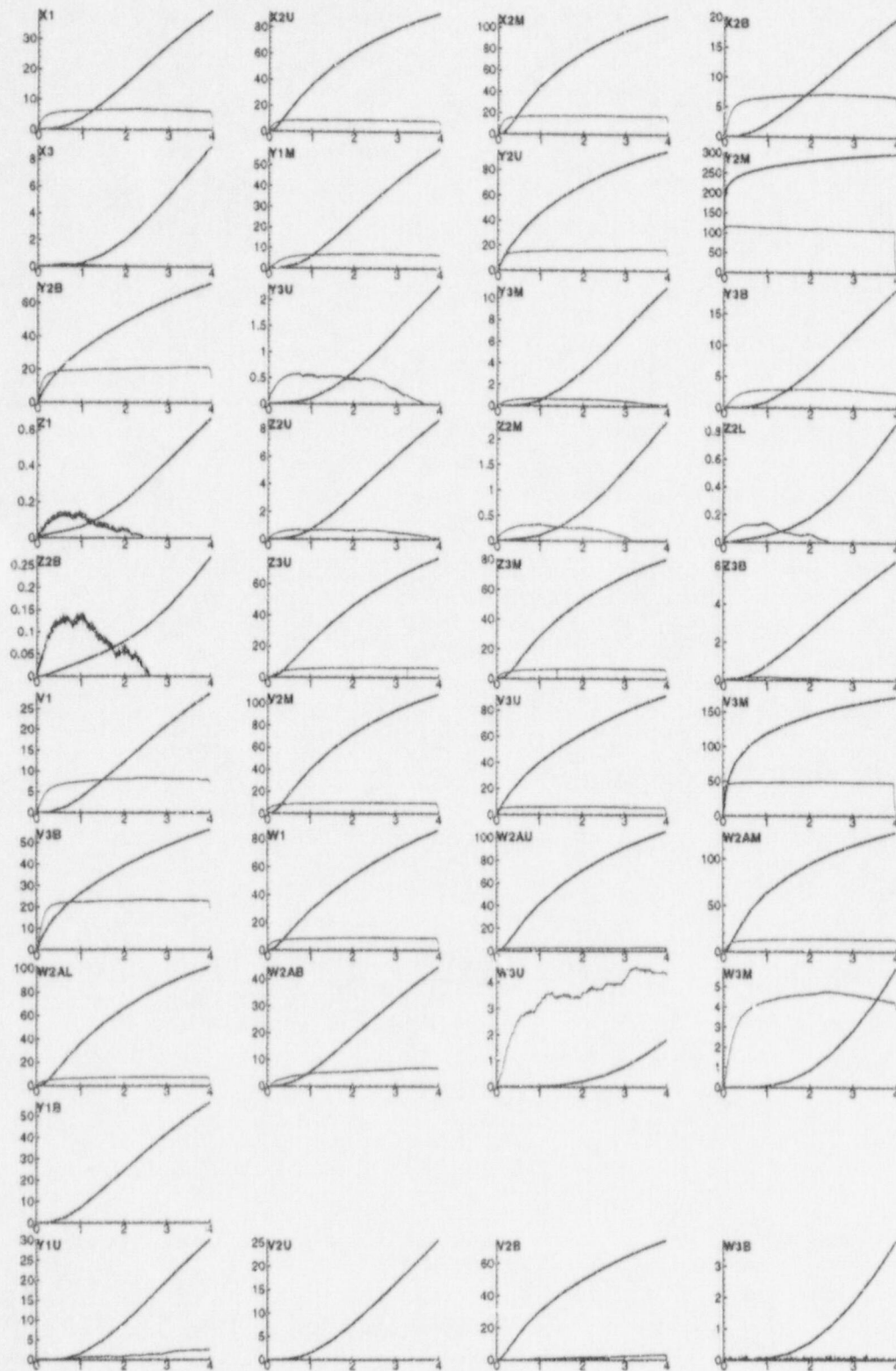
Figure 6.8: Observed (thin curve) and simulated (thick curve) pressure responses (*kPa*, vertical axes) versus time (*days*, horizontal axes) during cross-hole test PP4 using kriged air permeability and air-filled porosity without parameter estimation.
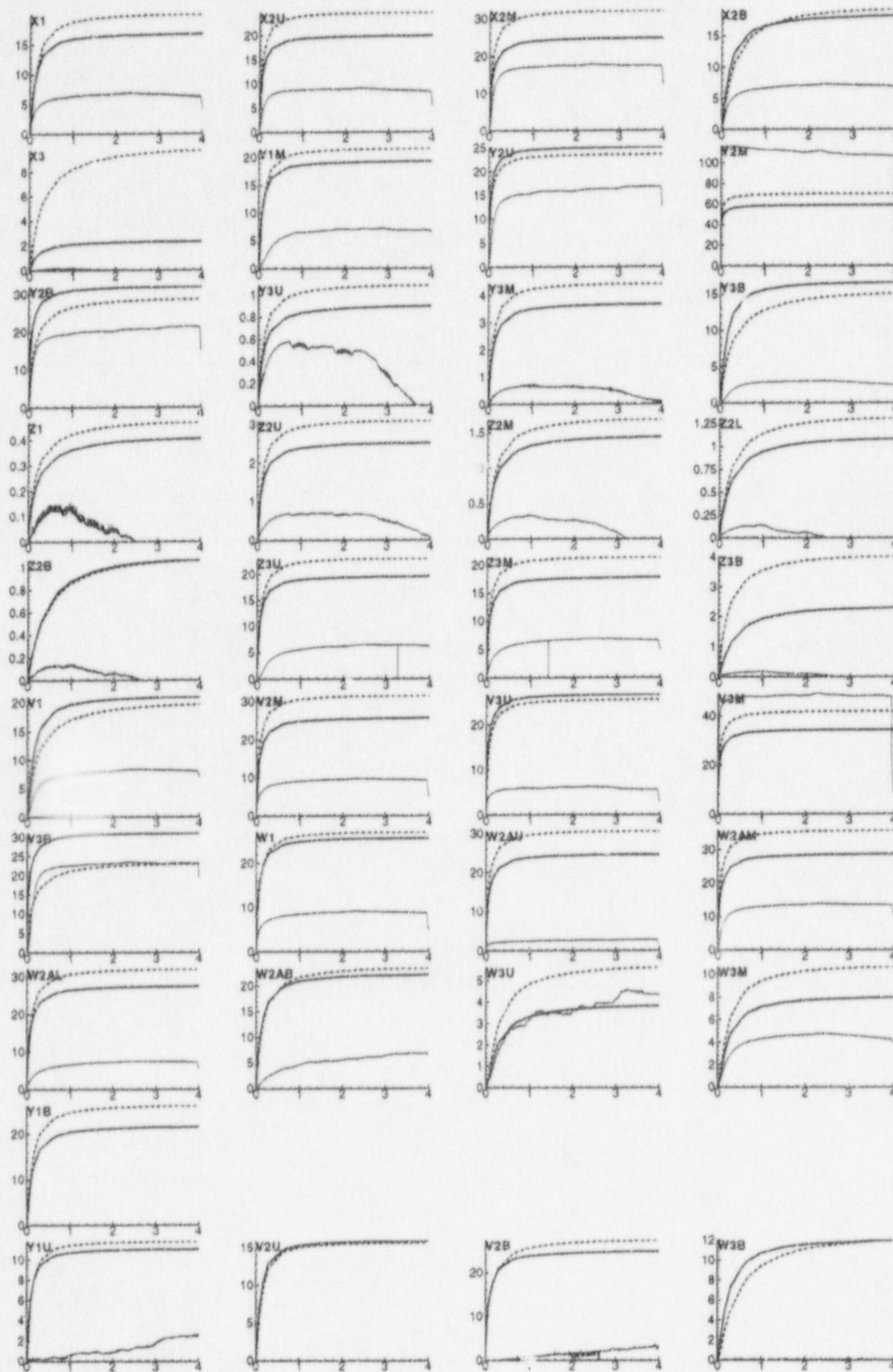
Figure 6.9: Observed (thin curve) and simulated (thick curve) pressure responses (*kPa*, vertical axes) versus time (*days*, horizontal axes) during cross-hole test PP4 using modified values of kriged air permeability and air-filled porosity without (dashed) and with (solid) inclusion of borehole effect.
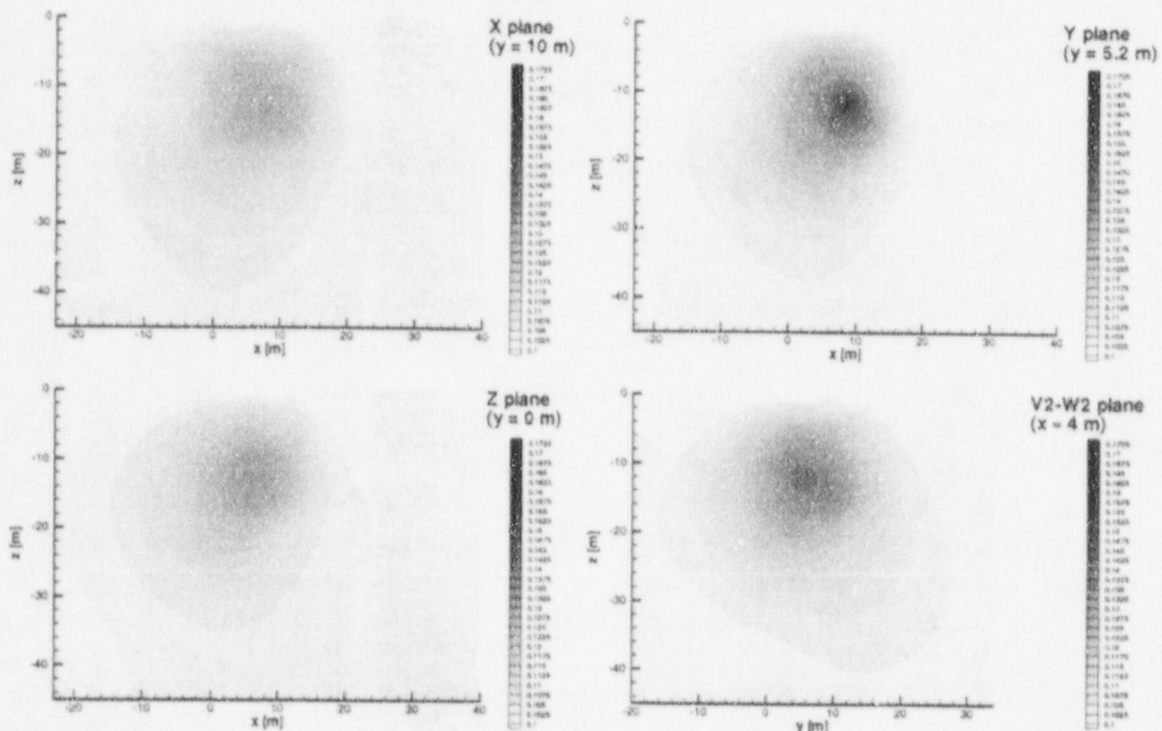
Figure 6.10: Simulated air pressure [*MPa*] in computational region 4 days after start of PP4 without borehole effect.
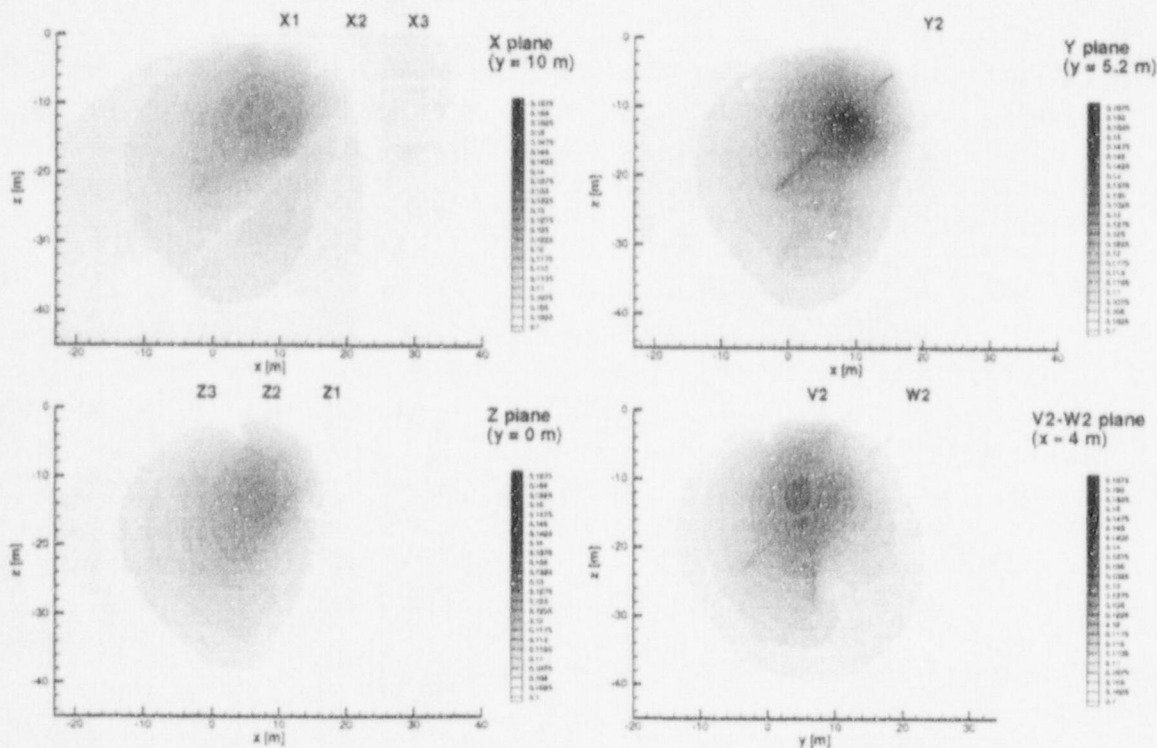
Figure 6.11: Simulated air pressure [*MPa*] in computational region 4 days after start of PP4 with borehole effect.

6.3 INVERSE MODELING OF CROSS-HOLE TEST PP4

To obtain a better fit between computed and measured pressures during cross-hole test PP4, we employed the parameter estimation code PEST (Doherty *et al.*, 1994). This code interacts automatically with FEHM with the aim of minimizing a weighted square difference, $\Phi(\beta)$, between calculated and observed pressures,

$$\Phi(\beta) = \sum_{j=1}^{P} \sum_{i=1}^{Q} w_{ij} \left(p_{ij}^* - p_{ij}(\beta) \right)^2 \tag{6.1}$$

where β is a vector of parameters to be adjusted; P is the number of pressure observation data in space; Q is the number of pressure observation data in time; w_{ij} is a relative weight ascribed to data point ij in space time; p_{ij}^* is the corresponding observed pressure value; and $p_{ij}(\beta)$ is its value calculated with parameters β. In our model we set the weights for all data included in the analysis equal to 1.

PEST uses a variant of the Gauss-Marquardt-Levenberg (Marquardt, 1963) algorithm to estimate the parameters β, which minimize $\Phi(\beta)$. PEST also calculates corresponding estimation covariance and correlation coefficient matrices; their normalized eigenvectors and eigenvalues; and 95% confidence limits for the optimized parameters. These calculations assume that (a) the data are mutually uncorrelated; (b) their weights represent their inverse normalized variances; (c) the estimation errors are Gaussian; and (d) they can be assessed with the aid of a linear model. In our case, these assumptions are not expected to be fulfilled and we therefore consider confidence limits calculated by PEST merely as crude approximations.

In our application of PEST to cross-hole test PP4, we relied on pressure data collected in one injection interval and thirty-six monitoring intervals. Though pressures were recorded separately in monitoring intervals V2B and W2, the latter are interconnected, and we therefore treat them as a single interval designated V2B. Computed and observed pressure responses are compared at 0.1, 0.3, 0.7 and 1.0 days following the start of the test in all monitoring intervals except Y1U, V2U, V2B and W3B whose pressure records are deemed unreliable, and at 2.0, 3.0 and 4.0 days in all monitoring intervals but the former and X3, Y3U, Y3M, Z1, Z2U, Z2M, Z2L, Z2B and Z3B which are visibly affected by a barometric pressure drop on these days. The maximum number of pressure data included in the analysis is thus 192.

We performed an inverse analysis of test PP4 twice, once treating the medium as if it was spatially uniform and once ascribing to it a heterogeneity pattern identical to that determined earlier by kriging. The two analyses are described below. In each case, the vector β consisted of only two parameters, one related to permeability and the other to air-filled porosity. On average, each analysis required about fifty sequential simulations of the cross-hole test by means of FEHM, and took about four hours on The University of Arizona supercomputer, SGI Origin 2000. Both the number of simulations, and computer time, increase sharply as the number of parameters increases.

6.3.1 Analysis Treating the Medium as Spatially Uniform

In this analysis the medium was treated as uniform with a distinct but unknown permeability and air-filled porosity. The analysis was performed twice, once by considering pressure data from each monitoring interval separately and once by

considering pressure data from all such intervals simultaneously. The results of the first approach are directly comparable to those we obtain in Chapter 5 on the basis of type-curve analyses. Any major difference between these two sets of results would appear to stem from the manners in which our type-curve and numerical models handle boreholes. Whereas our type-curves consider the injection interval to be a point, our numerical model assigns to it a realistic volume. Whereas our type-curves account indirectly for the storage of air in pressure monitoring intervals, our numerical model does so directly and in all open segments of each borehole (not only those in which pressure is monitored). Whereas our type curves assume that pressure equalizes instantaneously along each monitoring interval, our numerical model allows for rapid airflow and pressure equalization within each open borehole interval by modeling it more realistically as a high-permeability and high-porosity medium. Our numerical model additionally accounts for the effect of an atmospheric boundary at the soil surface, though at the expense of introducing artificial no-flow boundaries at the sides and the bottom of the modeled rock volume.

Table 6.1 lists air permeability and air-filled porosity estimates obtained by the matching of computed and recorded pressures in one monitoring interval at a time. The table also lists the associated 95% confidence limits calculated for these estimates by PEST, and some relevant statistics. The corresponding matches of computed (heavy solid curves) and recorded (light solid curves) pressures are shown in Figure 6.12. With the exception of pressure records (or portions thereof) that are visibly affected by temporal variations in barometric pressure, these matches may be regarded as being reasonably good.

Estimates of air permeability in Table 6.1 range from 4.3×10^{-15} to $4.6 \times 10^{-12} \ m^2$ with a mean of $3.5 \times 10^{-13} \ m^2$, variance of 9.6×10^{-25}, and coefficient of variation equal to 2.8. The mean, variance, and coefficient of variation of log-transformed permeability are -13.52 (corresponding to $3.0 \times 10^{-14} \ m^2$), 7.2×10^{-1}, and -6.3×10^{-2}, respectively. The mean, variance, and coefficient of variation of corresponding type-curve results are -13.46 (corresponding to $3.5 \times 10^{-14} \ m^2$), 3.2×10^{-1}, and -2.4×10^{-2}, respectively (Tables 5.4 and 5.5). The type-curve analysis excluded intervals X3 and Y2M but included interval Y1U, which was not considered in the inverse analysis. The inverse and type-curve analyses yield similar mean permeabilities but different variances. Monitoring intervals Z1, Z2M, Z2L, Z2B and Z3B respond weakly due to apparent pneumatic communication with the atmosphere. If we exclude these and consider only pressure data that have been interpreted by both methods, we obtain mean log-transformed permeability values of -13.90 and -13.66 from inverse and type-curve analyses, respectively, with corresponding variances of 1.1×10^{-1} and 1.4×10^{-1} that are smaller than before. The two sets of air permeability values are compared in Figure 6.13. Though type-curve results consistently exceed numerical results by a factor of about 1.7, the two sets of data correlate quite well if one ignores intervals Z1, Z2M, Z2L, Z2B and Z3B, with an r^2 of 0.92. When open monitoring boreholes are excluded from the numerical model, the systematic difference between the two sets of results is reduced from 1.7 to 1.4. This suggests that type-curve analysis compensates for its inability to consider high-permeability boreholes by assigning higher permeabilities to the rock.

The mean, variance, and coefficient of variation of combined 1-m and 3-m log-transformed air permeabilities from steady state analyses of single-hole tests (which

include data corresponding to all monitoring intervals for cross-hole test PP4) are -15.22 (corresponding to $6.0 \times 10^{-16} \ m^2$), 8.7×10^{-1} and -6.1×10^{-2}, respectively. The corresponding cross-hole test results have a mean that is larger by two orders of magnitude, but a variance of comparable magnitude. The available single-hole and cross-hole test results at the ALRS thus reveal a pronounced increase in permeability with scale, and a corresponding but lesser decrease in variance with scale.

Air-filled porosity estimated by our inverse model on the basis of pressure data from injection interval Y2M during cross-hole test PP4 is highly uncertain, as implied by the correspondingly wide confidence interval in Table 6.1; we attribute this to a very rapid pressure buildup in this interval. The large air-filled porosity estimates (0.9) obtained on the basis of pressure data from monitoring intervals X3, Z2L, Z2B and Z3B are equal to the upper limit of values allowed in our inverse model. We consider these estimates to be highly unlikely due to poor fits between calculated and observed pressure responses in these intervals (Figure 6.12), which appear to be pneumatically well-connected to the atmosphere and therefore strongly influenced by barometric pressure fluctuations. Upon excluding air-filled porosity values obtained from these five borehole intervals, the range of this parameter narrows down to $2.0 \times 10^{-3} - 9.5 \times 10^{-2}$. Their arithmetic mean, variance, and coefficient of variation are then 3.3×10^{-2}, 6.7×10^{-4} and 7.9×10^{-1}, respectively. The mean, variance, and coefficient of variation of log-transformed air-filled porosities are -1.65 (corresponding to 2.2×10^{-2}), 1.8×10^{-1} and -2.6×10^{-1}, respectively. Log-transformed air-filled porosities from type-curve analyses (Tables 5.4 and 5.5) have mean -2.18 (corresponding to 6.6×10^{-3}), variance 3.0×10^{-1}, and coefficient of variation -4.0×10^{-1}. Type-curve analysis thus yields a mean air-filled porosity that is lower by a factor of about three, and a higher variance, than do corresponding inverse results. Upon excluding monitoring intervals Z2L, Z2B and Z3B and comparing only pressure records analyzed by both methods, we obtain from inverse and type-curve analyses mean values of -1.65 and -2.20, and variances of 1.8×10^{-1} and 2.2×10^{-1}, respectively. The corresponding two sets of air-filled porosities are compared in Figure 6.14 and are seen to agree poorly, with a coefficient of correlation $r^2 = 0.33$. Results obtained by inverse analysis consistently exceed those from type-curve analysis by a factor of about three.

An attempt was also made to analyze pressure buildup records from all monitoring intervals simultaneously while treating the rock as uniform and isotropic. Pressure buildup in the injection interval was much larger than in the monitoring intervals and we therefore excluded it from this inverse analysis. The corresponding best fits between calculated (heavy solid curves) and observed (light solid curves) monitoring pressures are shown in Figure 6.15. These simultaneous fits are clearly not as good as the individual pressure matches in Figure 6.12. The obvious reason is that the medium is highly nonuniform as well as anisotropic and must be so modeled to simultaneously reproduce all pressure records. The simultaneous matching exercise gave a uniform pneumatic permeability estimate of $7.3 \times 10^{-15} \ m^2$ with a 95% confidence range of $\pm 0.9 \times 10^{-15} \ m^2$, and a corresponding air-filled porosity estimate of $4.8 \times 10^{-2} \pm 6.0 \times 10^{-3}$. The simultaneous permeability estimate is about one fourth the geometric mean of individual estimates listed in Table 6.1, and the simultaneous porosity estimate is about two times higher than the geometric mean of corresponding individual estimates.

Table 6.1: Numerically identified parameters for cross-hole test PP4 treating the medium as spatially uniform. Values in bold are excluded from computation of descriptive sample statistics.

Borehole interval	Permeability [m²]	95% confidence limits	Log-transformed permeability [m²]	Porosity [m³/m³]	95% confidence limits	Log-transformed porosity [m³/m³]
X1	7.9E-15	2.6E-16	-14.10	7.6E-03	9.9E-04	-2.12
X2U	1.1E-14	7.0E-16	-13.94	2.3E-02	5.8E-03	-1.65
X2M	5.5E-15	6.5E-16	-14.26	8.7E-03	4.7E-03	-2.06
X2B	9.0E-15	1.6E-15	-14.04	7.3E-03	3.8E-03	-2.14
X3	4.3E-13	1.1E-14	-12.37	**9.0E-01**	5.1E-03	**-0.05**
Y1M	8.8E-15	3.5E-16	-14.06	5.8E-02	4.3E-03	-1.23
Y2U	9.6E-15	5.8E-16	-14.02	4.5E-02	1.5E-02	-1.34
Y2M	2.2E-14	5.6E-16	-13.65	**1.0E-05**	1.1E-01	**-5.00**
Y2B	5.6E-15	6.2E-16	-14.25	9.1E-03	6.6E-03	-2.04
Y3U	5.1E-14	2.5E-16	-13.29	2.3E-02	7.2E-04	-1.64
Y3M	6.8E-14	4.1E-15	-13.17	9.5E-02	2.6E-03	-1.02
Y3B	2.3E-14	3.1E-15	-13.63	5.3E-02	5.5E-03	-1.28
Z1	6.1E-13	6.3E-15	-12.21	6.2E-02	2.8E-03	-1.21
Z2U	5.9E-14	1.6E-14	-13.23	5.6E-02	2.3E-02	-1.26
Z2M	2.9E-13	1.6E-14	-12.54	2.9E-02	9.1E-03	-1.54
Z2L	4.6E-12	5.7E-13	-11.33	**9.0E-01**	1.8E-01	**-0.05**
Z2B	2.2E-12	2.9E-14	-11.66	**9.0E-01**	1.3E-01	**-0.05**
Z3U	1.4E-14	1.0E-15	-13.87	9.1E-02	1.7E-04	-1.04
Z3M	1.5E-14	1.1E-16	-13.82	4.2E-02	9.6E-04	-1.38
Z3B	2.6E-12	3.1E-15	-11.59	**9.0E-01**	6.8E-03	**-0.05**
V1	7.4E-15	6.4E-16	-14.13	1.1E-02	8.4E-04	-1.94
V2M	1.0E-14	5.1E-17	-13.99	1.5E-02	3.8E-04	-1.82
V3U	2.2E-14	1.6E-16	-13.66	3.5E-02	1.9E-03	-1.45
V3M	6.2E-15	1.3E-16	-14.21	2.0E-03	2.1E-03	-2.70
V3B	4.3E-15	1.1E-16	-14.37	1.3E-02	3.7E-03	-1.88
W1	1.1E-14	1.2E-16	-13.98	1.9E-02	1.0E-03	-1.72
W2AU	4.3E-14	1.7E-15	-13.37	2.8E-02	1.0E-02	-1.55
W2AM	8.0E-15	1.0E-15	-14.10	2.6E-02	9.9E-03	-1.59
W2AL	1.5E-14	2.4E-16	-13.83	4.7E-02	2.3E-03	-1.33
W2AB	1.2E-14	5.2E-16	-13.94	6.1E-02	6.2E-03	-1.22
W3U	6.8E-15	9.8E-16	-14.17	6.9E-03	2.8E-03	-2.16
W3M	9.7E-15	2.0E-15	-14.01	6.0E-03	3.3E-03	-2.22
Min:	4.3E-15	5.1E-17	-14.37	2.0E-03	1.7E-04	-2.70
Max:	4.6E-12	5.7E-13	-11.33	9.5E-02	1.8E-01	-1.02
Mean:	3.5E-13	2.1E-14	-13.52	3.3E-02	1.8E-02	-1.65
Variance:	9.6E-25	1.0E-26	7.2E-01	6.7E-04	1.7E-03	1.8E-01
CV:	2.8E+00	4.8E+00	-6.3E-02	7.9E-01	2.3E+00	-2.6E-01

Figure 6.12: Separate matches between simulated (thick curve) and observed (thin curve) pressures (*kPa*, vertical axes) versus time (*days*, horizontal axes) in individual intervals during cross-hole test PP4 using uniform parameter values.

Figure 6.13: Analytically versus numerically derived air permeabilities for cross-hole test PP4. Thin regression line excludes intervals Z1, Z2M, Z2L, Z2B, and Z3B.

Figure 6.14: Analytically versus numerically derived air-filled porosities for cross-hole test PP4. Thin regression line excludes intervals Z2L, Z2B, and Z3B.

Figure 6.15: Simultaneous matches between simulated (thick curve) and observed (thin curve) pressures (*kPa*, vertical axes) versus time (*days*, horizontal axes) in individual intervals (excluding Y2M) during cross-hole test PP4 using uniform parameter values.

Figure 6.16: Simultaneous matches between simulated (thick curve) and observed (thin curve) pressures (*kPa*, vertical axes) versus time (*days*, horizontal axes) in individual intervals (excluding Y2M and V3M) during cross-hole test PP4 using uniform parameter values.

For comparison with results discussed in the next section, we include in Figure 6.16 pressure fits obtained upon excluding from the analysis the pressure record of monitoring interval V3M, which is closest to the injection interval and shows correspondingly high-pressures. The matches in Figure 6.16 are somewhat better than those in Figure 6.15. They yield a pneumatic permeability estimate of $1.0 \times 10^{-14} \pm 9.8 \times 10^{-16} m^2$, and an air-filled porosity estimate of $3.0 \times 10^{-2} \pm 5.5 \times 10^{-3}$, which are closer to the mean values of individual estimates than was the case when data from V3M had been included in the analysis.

6.3.2 Analysis Treating the Medium as Spatially Nonuniform

To account for medium heterogeneity, we performed inverse analyses of cross-hole test PP4 based on kriged values of pneumatic permeability and air-filled porosity as described in Section 1.2 of the Introduction. Each kriged field was multiplied by a single factor the value of which was estimated by our inverse model. The total number of unknown parameters (factors or multipliers) was therefore two, as in the uniform case. The results of analyzing each pressure monitoring record separately in this manner are listed in Table 6.2 and illustrated in Figure 6.17. The quality of the matches in Figure 6.17 constitutes a slight improvement over those of the corresponding uniform case in Figure 6.12, primarily at late time. The estimated permeability factor ranges from 4.3 to 8.2×10^2, with a mean of 7.8, variance of 2.6×10^4, and coefficient of variation equal to 2.0. Excluding the highly unlikely porosity values calculated by PEST for borehole intervals X3, Y2M, Z2L, Z2B and Z3B, for reasons discussed earlier, we find the porosity factor to range from 1.6×10^{-2} to 1.6 with a mean of 6.0×10^{-1}, variance of 2.1×10^{-1}, and coefficient of variation equal to 7.6×10^{-1}. Clearly our kriged images of air permeability and air-filled porosity do not provide an accurate description of site heterogeneity which appears to be much less smooth.

The mean log permeability of the kriged field is -15.42. The mean corresponding to any given multiplier of permeability is therefore equal to -15.42 plus the logarithm of this multiplier. The mean values of log permeability obtained in this manner for each test interval are listed in Table 6.2. These range from -14.79 to -12.51 with mean, variance and coefficient of variation equal to -13.88 (corresponding to $2.1 \times 10^{-14} m^2$), 2.3×10^{-1} and -3.5×10^{-2}, respectively. Uniform estimates in Section 6.3.1 had mean, variance and coefficient of variation equal to -13.52 (corresponding to $3.0 \times 10^{-14} m^2$), 7.2×10^{-1} and -6.3×10^{-2}, respectively. The large variance associated with uniform values, relative to that of corresponding mean non-uniform values, stems from the inability of uniform values to account for large contrasts in permeability between the injection and some of monitoring intervals. A comparison between pneumatic permeability values obtained by treating the medium as uniform, and mean field values obtained by treating the medium as non-uniform, is presented in Figure 6.18. It is evident that mean permeabilities estimated from data recorded in intervals Z1, Z2M, Z2L, Z2B, and Z3B are much lower than corresponding uniform values. This notwithstanding, the mean non-uniform and uniform values correlate quite well.

The logarithm of air-filled porosity ϕ was estimated geostatistically by subtracting kriged water content from kriged log-transformed matrix porosity, yielding a mean of -1.18. Corresponding mean field estimates obtained by the inverse model using pressure records from individual test intervals are listed in Table 6.2 (log-transformed mean air-

Table 6.2: Numerically identified parameters for cross-hole test PP4 treating the medium as spatially nonuniform. Values in bold are excluded from computation of descriptive sample statistics.

Borehole interval	Permeability factor	95% confidence limits	Log-transformed permeability factor	Mean log-transformed permeability [m^2] in the model region	Porosity factor	95% confidence limits	Log-transformed porosity factor	Mean log-transformed porosity [m^3/m^3] in the model region
X1	2.7E+01	5.2E-01	1.43	-13.99	2.4E-01	2.0E-02	-0.63	-1.81
X2U	2.3E+01	4.7E-01	1.36	-14.06	3.2E-01	3.1E-02	-0.50	-1.68
X2M	1.4E+01	9.0E-01	1.16	-14.26	1.8E-01	5.6E-02	-0.75	-1.93
X2B	2.8E+01	4.2E-01	1.44	-13.98	2.3E-01	1.4E-02	-0.64	-1.82
X3	4.8E+02	7.2E+01	2.68	-12.74	**1.0E+03**	2.2E+00	**3.00**	*-0.05*
Y1M	2.7E+01	4.1E+00	1.43	-13.99	9.4E-01	4.0E-01	-0.03	-1.21
Y2U	1.6E+01	5.9E-01	1.20	-14.22	3.9E-01	5.6E-02	-0.41	-1.59
Y2M	4.3E+00	3.1E-01	0.63	-14.79	**1.0E-10**	1.2E-01	**-10.00**	*-5.00*
Y2B	1.6E+01	8.9E-01	1.20	-14.22	2.7E-01	5.4E-02	-0.57	-1.75
Y3U	1.4E+01	2.0E+00	1.15	-14.27	1.9E-01	8.6E-02	-0.71	-1.89
Y3M	5.5E+01	1.6E-01	1.74	-13.68	1.1E+00	8.1E-03	0.06	-1.12
Y3B	6.0E+01	4.6E-01	1.78	-13.64	1.0E+00	4.1E-02	0.00	-1.18
Z1	4.9E+01	4.4E+00	1.69	-13.73	1.6E+00	2.0E-01	0.20	-0.98
Z2U	3.5E+01	2.0E+00	1.55	-13.87	6.5E-01	8.4E-02	-0.19	-1.37
Z2M	6.0E+01	3.2E+00	1.78	-13.64	8.9E-01	9.9E-02	-0.05	-1.23
Z2L	1.2E+02	9.6E+00	2.09	-13.33	**8.7E+00**	1.4E-01	**0.94**	**-0.24**
Z2B	2.0E+02	4.8E+00	2.29	-13.13	**1.4E+01**	2.5E-01	**1.14**	**-0.04**
Z3U	2.9E+01	8.8E-01	1.46	-13.96	1.5E+00	1.3E-01	0.18	-1.00
Z3M	2.7E+01	5.3E-02	1.44	-13.98	6.7E-01	6.2E-03	-0.18	-1.36
Z3B	8.2E+02	3.9E+02	2.91	-12.51	**1.0E+03**	6.2E-01	**3.00**	*-0.05*
V1	2.8E+01	1.0E+00	1.44	-13.98	3.8E-01	2.4E-02	-0.42	-1.60
V2M	3.0E+01	1.2E-01	1.48	-13.94	3.1E-01	4.9E-03	-0.51	-1.69
V3U	5.1E+01	8.5E-03	1.70	-13.72	4.0E-01	5.1E-04	-0.39	-1.57
V3M	6.7E+00	8.4E-02	0.83	-14.59	1.6E-02	8.2E-03	-1.79	-2.97
V3B	1.3E+01	3.9E-01	1.12	-14.30	3.7E-01	2.8E-02	-0.43	-1.61
W1	3.2E+01	5.3E-01	1.51	-13.91	3.6E-01	3.2E-02	-0.45	-1.63
W2AU	1.2E+02	7.7E-02	2.07	-13.35	9.1E-01	5.3E-03	-0.04	-1.22
W2AM	2.2E+01	4.0E-01	1.34	-14.08	4.8E-01	2.4E-02	-0.32	-1.50
W2AL	4.2E+01	3.1E-02	1.62	-13.80	1.1E+00	1.6E-03	0.02	-1.16
W2AB	3.5E+01	2.8E-01	1.55	-13.87	1.5E+00	4.4E-02	0.18	-1.00
W3U	9.0E+00	6.9E-01	0.96	-14.46	1.4E-01	2.3E-02	-0.85	-2.03
W3M	1.7E+01	2.2E-01	1.24	-14.18	1.6E-01	6.5E-03	-0.80	-1.98
Min:	4.3E+00	8.5E-03	0.63	-14.79	1.6E-02	5.1E-04	-1.79	-2.97
Max:	8.2E+02	3.9E+02	2.91	-12.51	1.6E+00	2.2E+00	0.20	-0.98
Mean:	7.8E+01	1.6E+01	1.54	-13.88	6.0E-01	1.5E-01	-0.37	-1.55
Variance:	2.6E+04	4.8E+03	2.3E-01	2.3E-01	2.1E-01	1.5E-01	1.8E-01	1.8E-01
CV:	2.0E+00	4.4E+00	3.1E-01	-3.5E-02	7.6E-01	2.6E+00	-1.2E+00	-2.8E-01
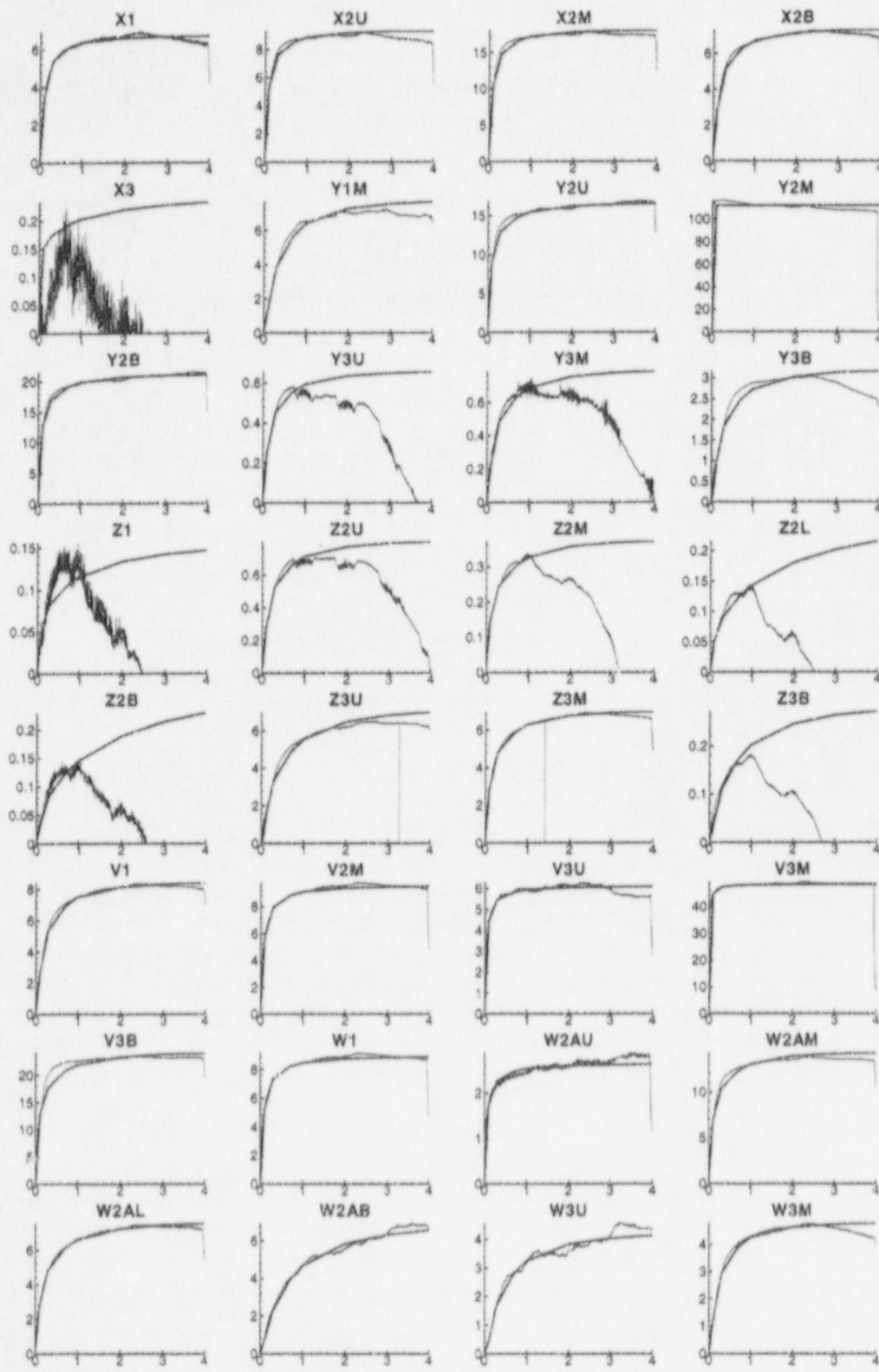
Figure 6.17: Separate matches between simulated (thick curve) and observed (thin curve) pressures (*kPa*, vertical axes) versus time (*days*, horizontal axes) in individual intervals during cross-hole test PP4 using nonuniform parameter values.
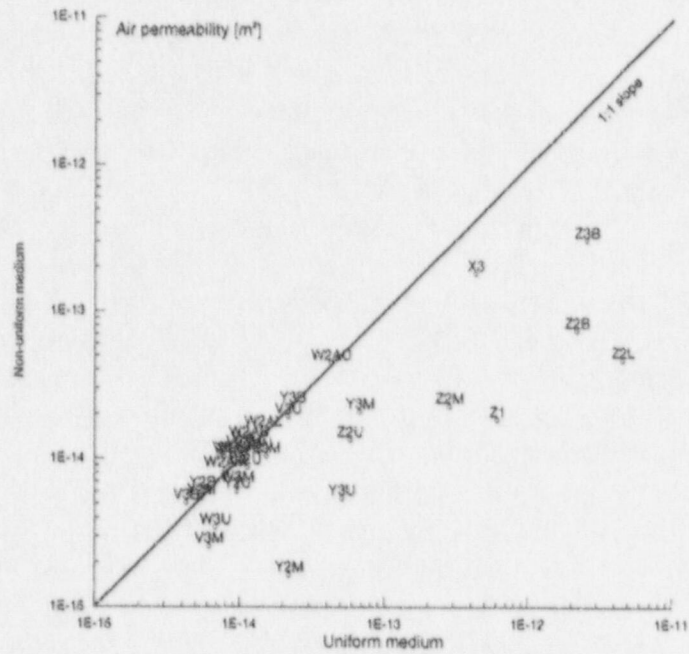
Figure 6.18: Numerically derived mean air permeabilities using uniform and non-uniform medium.
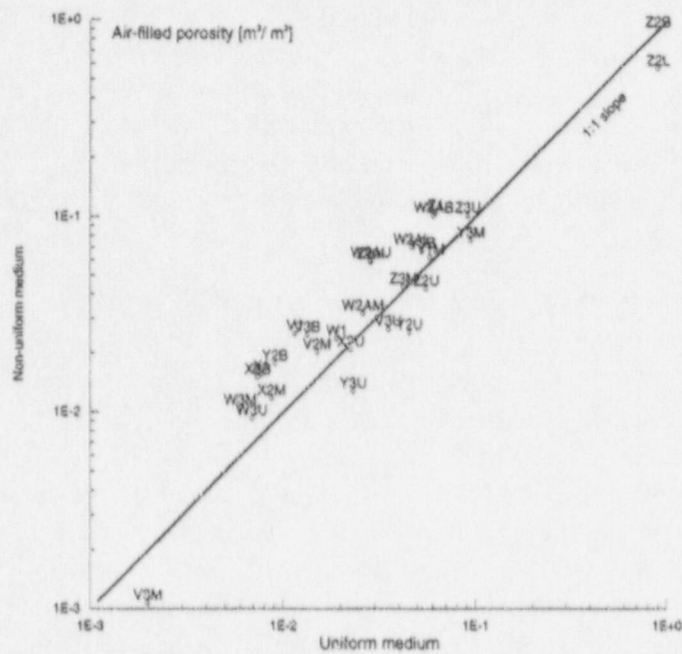
Figure 6.19: Numerically derived mean air-filled porosities using uniform and non-uniform medium (intervals X3, Y2M, and Z3L and not presented on figure).

filled porosity values for intervals X3, Y2M and Z3B were set equal to -0.05, -5.0 and -0.05, respectively; these define the lowest and highest value allowed in our inverse analysis). Upon excluding results corresponding to intervals X3, Y2M, Z2L, Z2B and Z3B for reasons discussed earlier, mean log ϕ ranges from -2.97 to -0.98 with mean, variance and coefficient of variation equal to -1.55 (corresponding to 2.82×10^{-2}), 1.8×10^{-1} and -2.8×10^{-1}, respectively. These are very similar to values of -1.65 (corresponding to 2.2×10^{-2}), 1.8×10^{-1} and -2.6×10^{-1} that we had obtained for a uniform medium. A comparison between air-filled porosity values obtained by treating the medium as uniform, and mean field values obtained by treating the medium as non-uniform, is presented in Figure 6.19 with the exclusion of results corresponding to intervals X3, Y2M and Z3B, which are deemed to be unrealistic. The two sets of air-filled porosity estimates are seen to correlate quite well.

A simultaneous fit of all pressure monitoring records with the exclusion of that corresponding to the injection interval, Y2M, leads to the matches depicted in Figure 6.20. These matches are again much less satisfactory than were the individual matches in Figure 6.17. Excluding V3M leads to considerable improvement in the resulting pressure fits (Figure 6.21), which are additionally better than those corresponding to the uniform case in Figure 6.16.

Finally, we present in Figure 6.22 results obtained by treating permeability as a spatially nonuniform field in the above manner, and air-filled porosity as uniform, while excluding the pressure records of Y2M and V3M. The results are very similar to those in Figures 6.21, suggesting that accounting for spatial variations in porosity does not have a significant effect on the quality of simultaneous matches. The corresponding permeability factor is close to that associated with Figure 6.21 and the porosity is very close to that calculated earlier for the simultaneous uniform case. Including the pressure record of V3M in the analysis brings about a reduction in the quality of the match, as is evident in Figure 6.20.

6.4 INVERSE MODELING OF SINGLE-HOLE TESTS

We used our inverse model to analyze four of the single-hole tests described in Chapter 4. All four tests had been conducted in borehole Y2 and are listed in Table 6.3. As in the case of cross-hole test PP4, we analyzed each test with and without considering the effect of boreholes on compressible air storage and pressure propagation through the system. We considered borehole effects twice, once including all open borehole intervals, and once only the injection interval.

Between 11 and 13 match points were considered in the analysis of each single-hole pressure record. In addition to air permeability k and air-filled porosity ϕ, we also estimated in some cases the effective porosity ϕ_w of the injection interval. The latter is allowed to take on values in excess of 1 as a means of accounting for effective borehole volumes larger than those originally built into the computational grid.

The 2-m injection interval of single-hole test JG0921A is offset downward from that of cross-hole test PP4 by 0.1 m, but otherwise the two intervals coincide. The parameters we have estimated from pressure buildup data recorded during this single-hole test by various method are listed in Table 6.4. Corresponding matches of computed and measured pressure data are depicted in Figure 6.23.
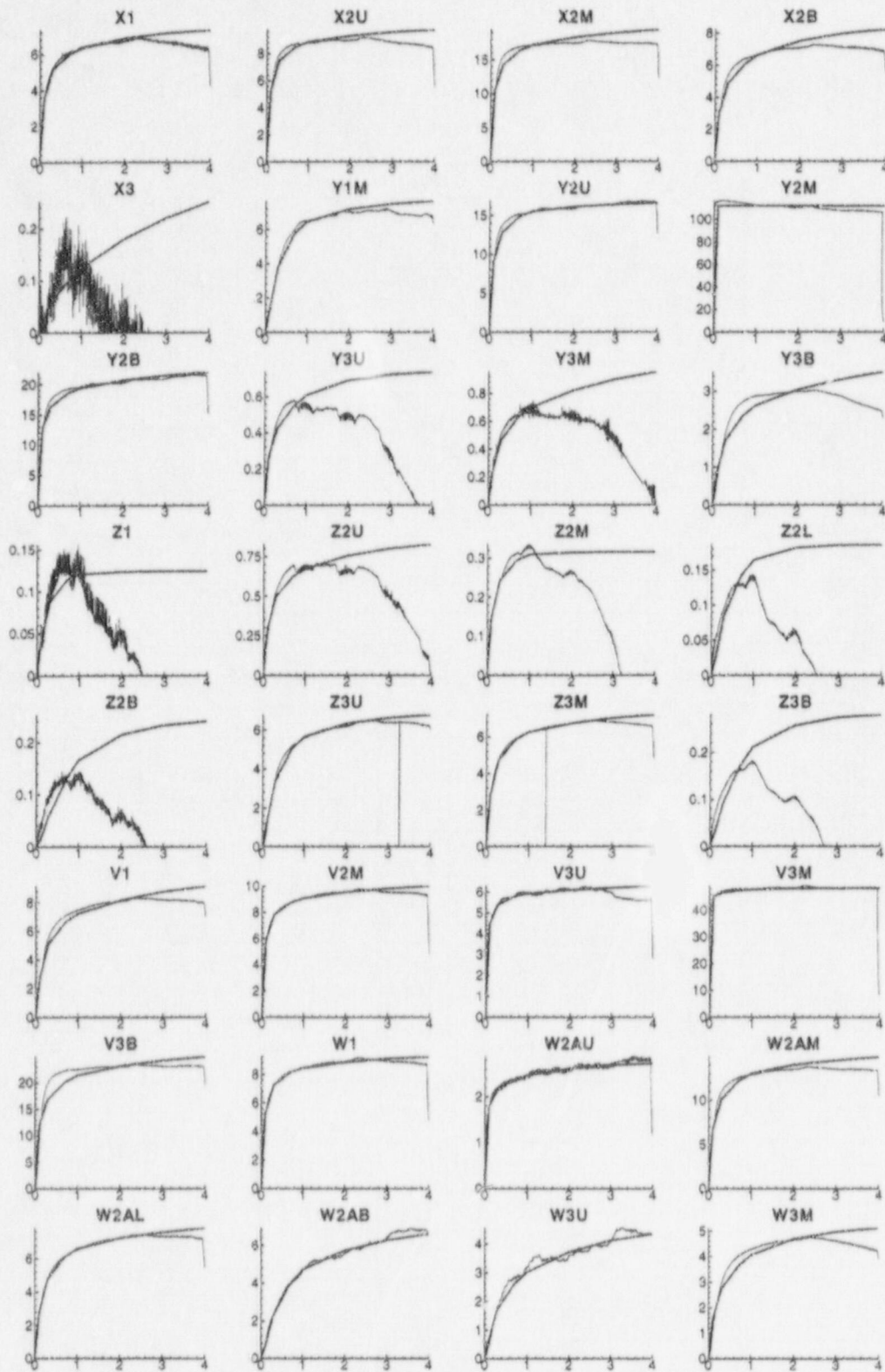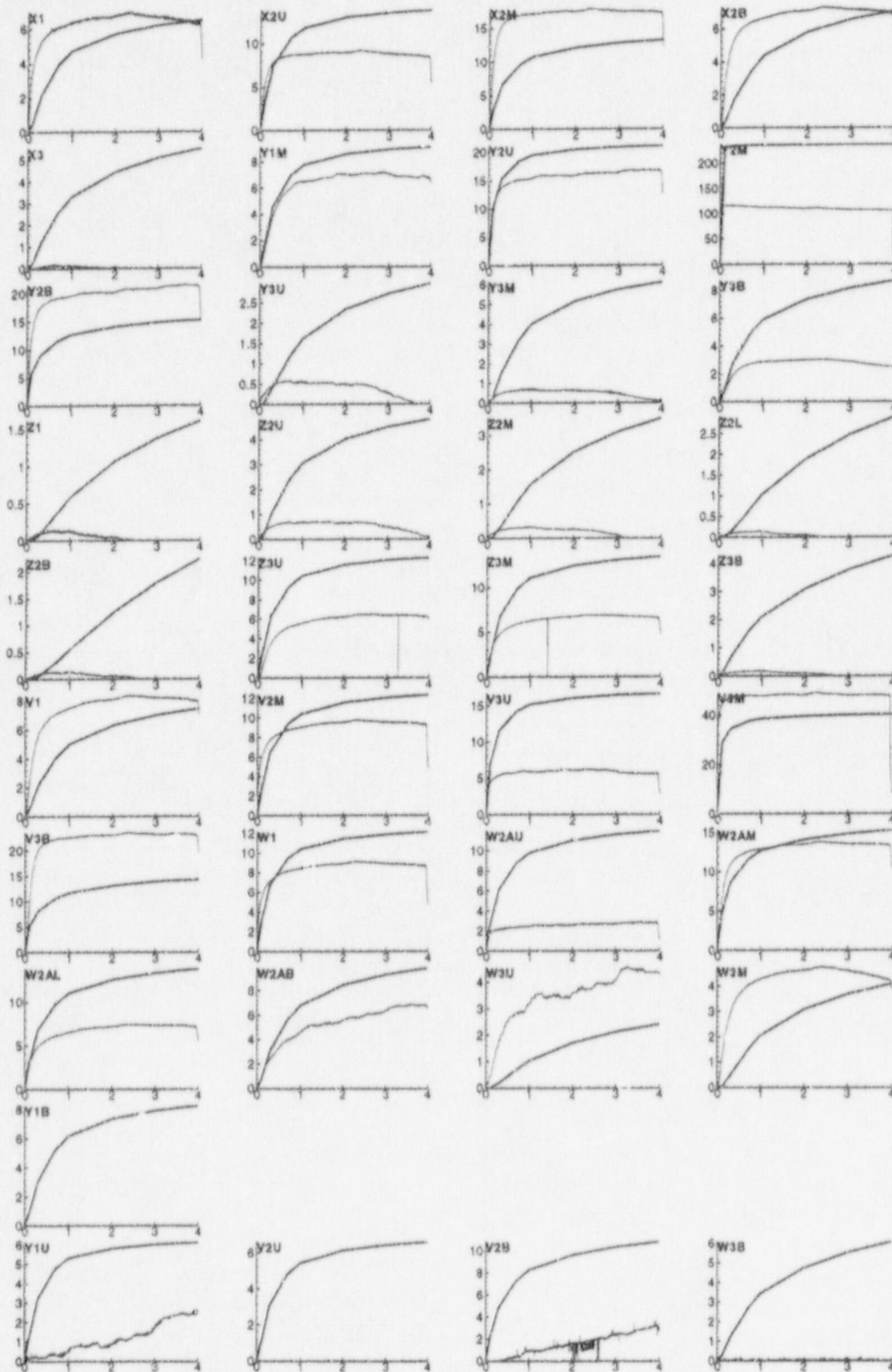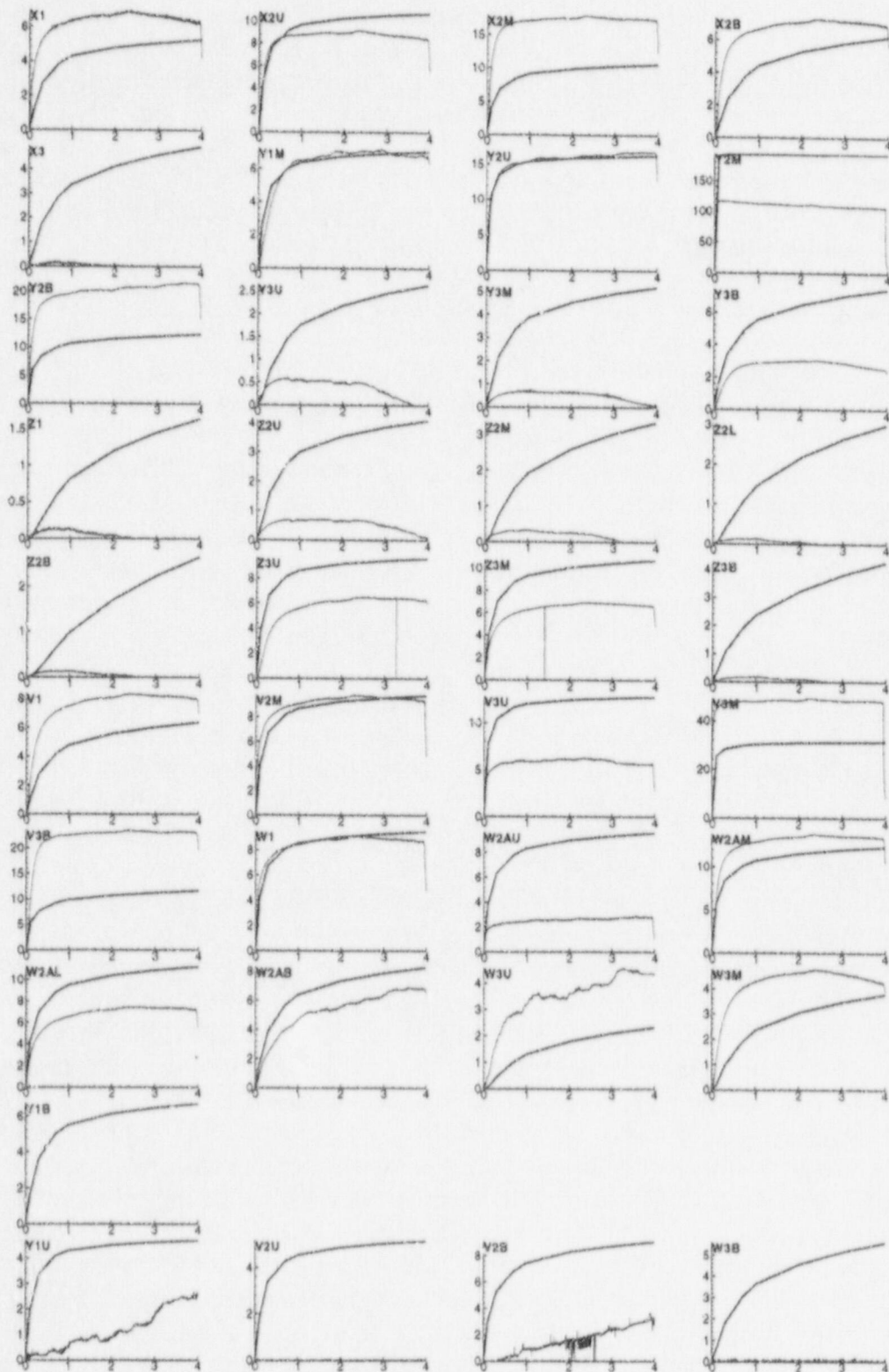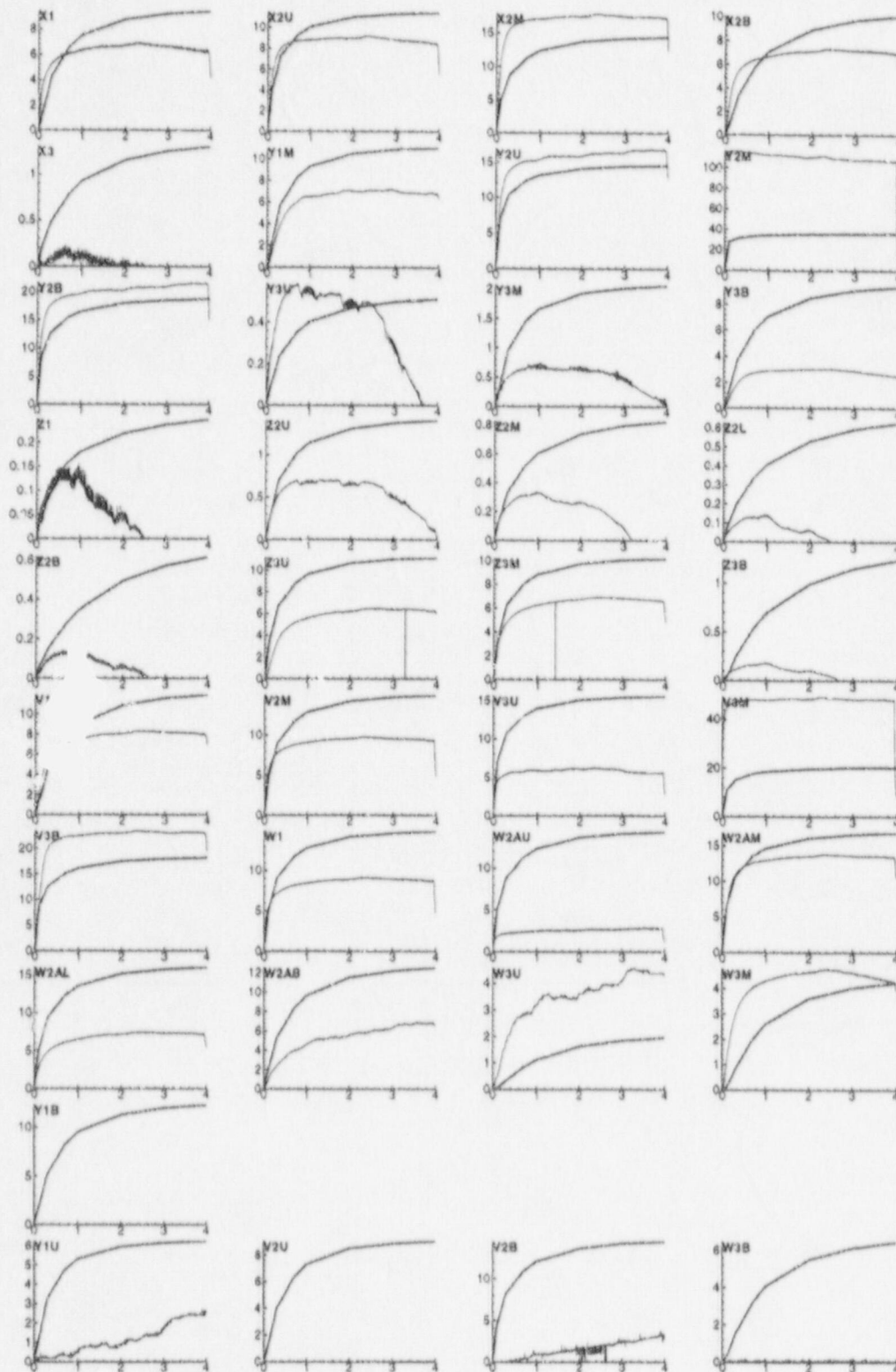
Figure 6.20: Simultaneous matches between simulated (thick curve) and observed (thin curve) pressures (*kPa*, vertical axes) versus time (*days*, horizontal axes) in individual intervals (excluding Y2M) during cross-hole test PP4 using nonuniform parameter values.
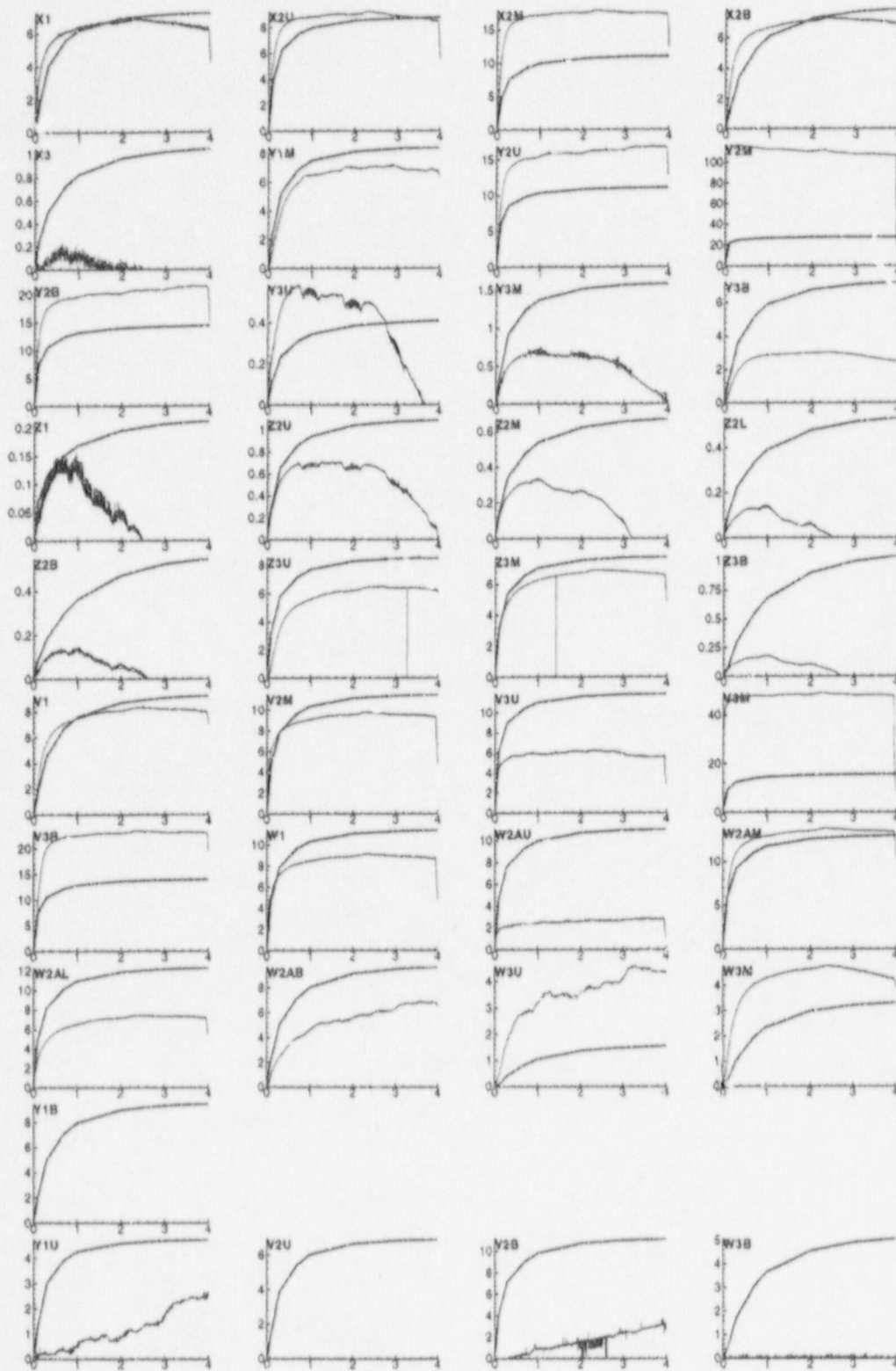
Figure 6.21: Simultaneous matches between simulated (thick curve) and observed (thin curve) pressures (*kPa*, vertical axes) versus time (*days*, horizontal axes) in individual intervals (excluding Y2M and V3M) during cross-hole test PP4 using nonuniform parameter values.
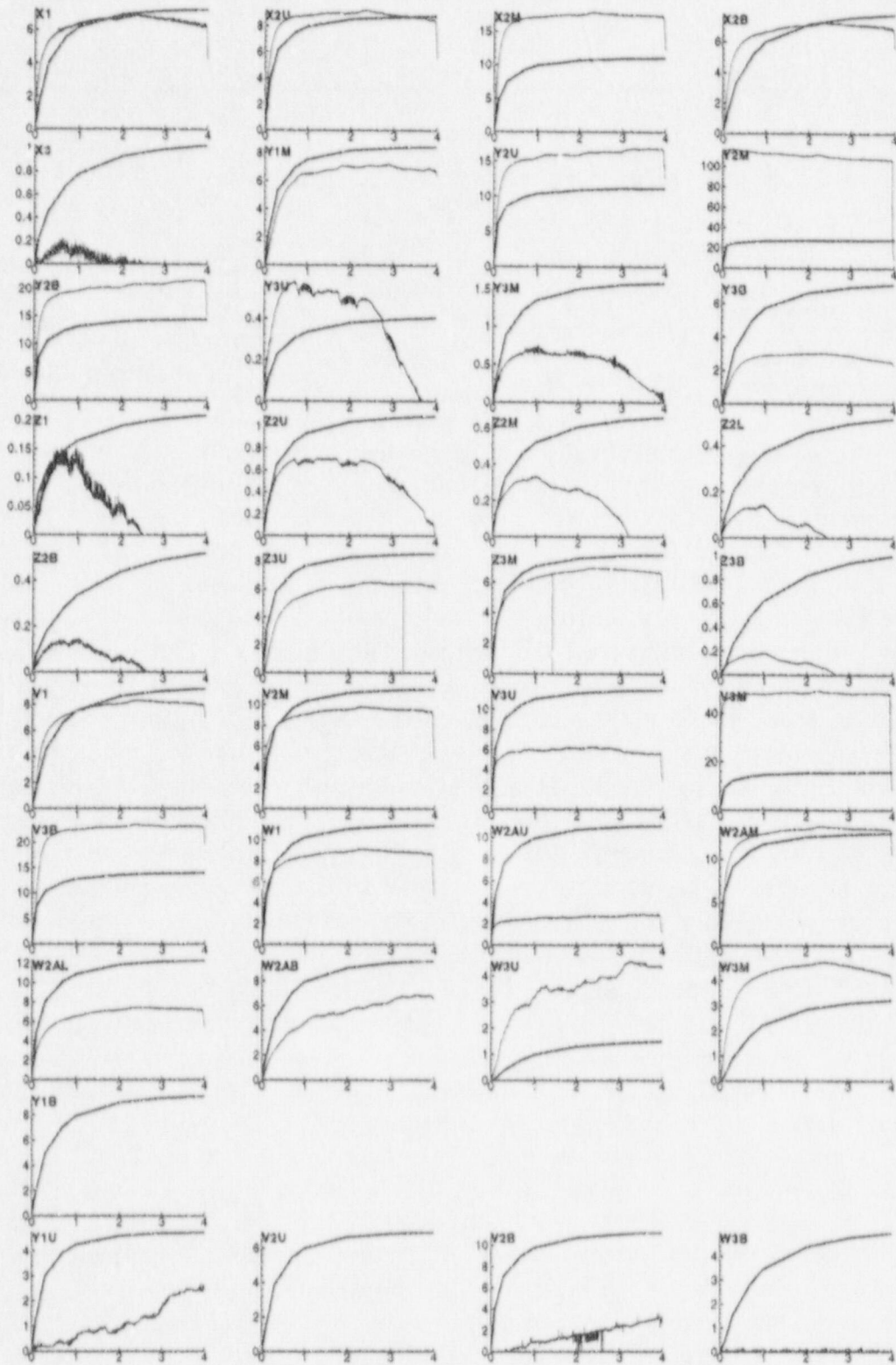
Figure 6.22: Simultaneous matches between simulated (thick curve) and observed (thin curve) pressures (*kPa*, vertical axes) versus time (*days*, horizontal axes) in individual intervals (excluding Y2M and V3M) during cross-hole test PP4 using nonuniform air permeability and uniform air-filled porosity.

Table 6.3: Single-hole tests analyzed by inverse modeling.

Single-hole test	Length of air-injection interval [m]	Distance from top of Y2 to center of injection interval [m]	Air-injection rate [cm³/min]	Air-injection rate [kg/s]
JG0921A	2	16.10	400.68	8.0136×10^{-6}
JGC0609A	1	13.85	499.20	9.984×10^{-6}
JHB0612A	1	15.81	502.30	1.0046×10^{-5}
JJA0616A	1	17.77	300.30	6.0006×10^{-6}

A steady-state interpretation of single-hole test JG0921A by means of an analytical formula (Guzman *et al.*, 1996) gave a pneumatic permeability of 2.8×10^{-14} m^2; our transient, p^2-based type-curve analysis using a spherical flow model gave 2.6×10^{-14} m^2 (Table 4.3); none were capable of yielding air-filled porosity estimates. Our numerical inverse model yields, without considering borehole effects, a permeability of $2.3 \times 10^{-14} \pm 2.6 \times 10^{-16}$ m^2 and an air-filled porosity of $4.5 \times 10^{-1} \pm 1.9 \times 10^{-3}$. If only the steady-state pressure data are used, the corresponding estimates are 2.8×10^{-14} m^2 and $\phi = 4.6 \times 10^{-3}$, respectively. In this case, the model's ability to estimate porosity is based entirely on information about the time (about 0.008 *days*) at which steady state has been established (as represented by the first pressure value that the model is asked to consider; see Figure 6.23); the model was thus relatively insensitive to ϕ and unable to associate it with meaningful confidence limits. When the effects of all boreholes are included, an inverse analysis of the complete (transient and steady state) pressure record yields a permeability estimate $k = 2.2 \times 10^{-14} \pm 1.6 \times 10^{-16}$ m^2 and a porosity estimate $\phi = 1.6 \times 10^{-2} \pm 1.9 \times 10^{-3}$. To obtain a satisfactory match against early data which are strongly affected by borehole storage, we found it necessary to include the effect of the injection interval. The inverse model then gave $k = 2.2 \times 10^{-14} \pm 4.4 \times 10^{-16}$ m^2, $\phi = 6.7 \times 10^{-3} \pm 4.7 \times 10^{-3}$ and $\phi_w = 7.0 \times 10^{-1} \pm 6.7 \times 10^{-3}$. The wide confidence interval associated with the latter porosity estimate stems from the relatively short time interval during which transient pressures are relatively free of borehole storage effects. Our earlier inverse analysis of injection pressure data during cross-hole test PP4, which had been conducted at the much higher injection rate of 1×10^{-3} *kg/s* (5×10^{1} *cm³/s*), gave a uniform permeability estimate of $2.2 \times 10^{-14} \pm 5.6 \times 10^{-16}$ m^2 (Figure 6.24, Table 6.1), which is highly consistent with all the above values and is a further indication that airflow behaves linearly under all test conditions encountered by us at the ALRS; the same analysis failed to yield a reliable value of air-filled porosity for the injection interval.

As in Chapter 3, we characterize borehole storage by a dimensionless coefficient, C_D, defined as

$$C_D = \frac{C_w \overline{p}}{4 V_w \phi} = \frac{V_s}{4 V_w \phi}, \tag{6.2}$$

where V_w is the nominal volume of a borehole interval and V_s is its effective volume. In our inverse model V_s is the product of V_w and ϕ_w, so that

$$C_D = \frac{\phi_w}{4\phi}. \qquad (6.3)$$

This yields a C_D of 2.6×10^1 for single-hole test JG0921A.

The results of analyzing pressure buildup data from single-hole test JGC0609A by various methods are listed in Table 6.5, and corresponding matches between measured and calculated pressures are depicted in Figure 6.25. The steady-state analysis of Guzman *et al.* (1996) gave a pneumatic permeability of 2.0×10^{-15} m^2; our p^2-based transient type-curve analysis using a spherical model gave $k = 2.9 \times 10^{-15}$ m^2 (Table 4.3,); our numerical inverse model yields, in the absence of borehole effects, $k = 1.8 \times 10^{-15} \pm 3.9 \times 10^{-15}$ m^2 and $\phi = 5.0 \times 10^{-1} \pm 4.2 \times 10^{-2}$; upon incorporating the injection interval, it yields a much improved fit to the early pressure data with $k = 1.6 \times 10^{-15} \pm 2.6 \times 10^{-17}$ m^2, $\phi = 4.8 \times 10^{-3} \pm 9.4 \times 10^{-3}$ and $\phi_w = 1.3 \pm 2.6 \times 10^{-2}$; and, upon incorporating all boreholes, $k = 1.6 \times 10^{-15} \pm 1.3 \times 10^{-17}$ m^2, $\phi = 5.5 \times 10^{-3} \pm 4.7 \times 10^{-3}$ and $\phi_w = 1.3 \pm 1.7 \times 10^{-2}$. A borehole porosity in excess of 1 implies that the effective volume V_S of the injection interval is larger than its nominal volume V_w. As in the case of single-hole test JG0921A, the wide confidence intervals of porosity reflect the very short time period during which transients pressures are relatively unaffected by borehole storage.

Table 6.6 lists parameters obtained by various methods of analysis from pressure buildup data recorded during single-hole test JHB0612A, and Figure 6.26 depicts corresponding matches between computed and measured pressure values. The steady state analysis of Guzman *et al.* (1996) yields a pneumatic permeability of 4.8×10^{-14} m^2; our transient, p^2-based type-curve analysis using a spherical model gives $k = 6.5 \times 10^{-14}$ m^2 (Table 4.3); our inverse analysis without boreholes gives $k = 5.2 \times 10^{-14} \pm 1.1 \times 10^{-16}$ m^2 and $\phi = 5.0 \times 10^{-1} \pm 1.2 \times 10^{-3}$; the same analysis incorporating the injection interval yields a much improved fit to the early pressure data with $k = 4.0 \times 10^{-14} \pm 4.4 \times 10^{-16}$ m^2, $\phi = 8.1 \times 10^{-2} \pm 1.6 \times 10^6$ and $\phi_w = 1.2 \pm 3.4 \times 10^6$ (the huge confidence intervals reflecting a virtual lack of sensitivity to ϕ and ϕ_w, which are negatively and almost perfectly correlated with each other); and upon considering all boreholes, the inverse model yields a good fit with $k = 4.1 \times 10^{-14}$ m^2, $\phi = 8.8 \times 10^{-2}$ and $\phi_w = 1.2$ (PEST was unable to calculate confidence limits for porosities in this case, but their values are strongly correlated and highly uncertain).

Corresponding results for single-hole test JJA0616A are given in Table 6.7 and Figure 6.27. The steady-state analysis of Guzman *et al.* (1996) gives $k = 5.6 \times 10^{-15}$ m^2; our p^2-based type-curve analysis of transient pressure data using a spherical flow model gives a relatively poor fit with $k = 8.0 \times 10^{-15}$ m^2 (Table 4.3, Figure 4.15); a similar analysis using a radial flow model gives an equally poor fit with $k = 7.1 \times 10^{-15}$ m^2, $\phi = 3.1 \times 10^{-2}$ and $C_D = 1.0 \times 10^{+1}$ (Figure 4.16); the numerical inverse model yields, in the absence of borehole effects, $k = 5.4 \times 10^{-15} \pm 7.9 \times 10^{-16}$ m^2 and $\phi = 5.0 \times 10^{-1} \pm 3.9 \times 10^{-2}$; it yields a much improved fit to early pressure data when one considers the effect of the injection interval, with $k = 4.0 \times 10^{-15} \pm 7.8 \times 10^{-17}$ m^2, $\phi = 1.3 \times 10^{-1} \pm 5.8 \times 10^{-3}$ and $\phi_w = 1.1 \pm 5.2 \times 10^{-2}$; and an equally good fit when one incorporates all boreholes with $k = 4.1 \times 10^{-15} \pm 7.1 \times 10^{-17}$ m^2, $\phi = 1.3 \times 10^{-1} \pm 6.4 \times 10^{-3}$ and $\phi_w = 1.1 \pm 3.9 \times 10^{-2}$. In all three cases, the inverse model yields parameter estimates with relatively narrow confidence intervals.

Table 6.4: Parameter estimates for single-hole test JG0921A.

TYPE OF ANALYSIS	$k\ [m^2]$	$\phi\ [m^3/m^3]$	$\phi_w\ [m^3/m^3]$	$C_D\ [-]$
Analytical steady-state interpretation	2.8E-14			
Analytical transient interpretation				
Spherical flow model	2.6E-14			
Inverse modeling				
No boreholes	2.3E-14	4.5E-01		
No boreholes (steady-state data)	2.8E-14	4.6E-03		
All boreholes (2 parameters)	2.2E-14	1.6E-02	5.0E-01	7.8E+00
All boreholes (3 parameters)	2.2E-14	6.7E-03	7.1E-01	2.6E+01

Table 6.5: Parameter estimates for single-hole test JGC0609A.

TYPE OF ANALYSIS	$k\ [m^2]$	$\phi\ [m^3/m^3]$	$\phi_w\ [m^3/m^3]$	$C_D\ [-]$
Analytical steady-state interpretation	5.6E-15			
Analytical transient interpretation				
Spherical flow model	2.9E-15			
Inverse modeling				
No boreholes	1.8E-15	5.0E-01		
Injection interval	1.6E-15	4.8E-03	1.3E+00	6.8E+01
All boreholes	1.6E-15	5.5E-03	1.3E+00	5.9E+01

Table 6.6: Identified parameters for single-hole test JHB0612A.

TYPE OF ANALYSIS	$k\ [m^2]$	$\phi\ [m^3/m^3]$	$\phi_w\ [m^3/m^3]$	$C_D\ [-]$
Analytical steady-state interpretation	4.8E-14			
Analytical transient interpretation				
Spherical flow model	6.5E-14			
Inverse modeling				
No boreholes	5.2E-14	5.0E-01		
Injection interval	4.0E-14	8.1E-02	1.2E+00	3.7E+00
All boreholes	4.1E-14	8.8E-02	1.2E+00	3.4E+00

Table 6.7: Identified parameters for single-hole test JJA0616A.

TYPE OF ANALYSIS	$k\ [m^2]$	$\phi\ [m^3/m^3]$	$\phi_w\ [m^3/m^3]$	$C_D\ [-]$
Analytical steady-state interpretation	5.6E-15			
Analytical transient interpretation				
Spherical flow model	8.0E-15			
Radial flow model	7.1E-15	3.1E-02		1.0E+01
Inverse modeling				
No boreholes	5.4E-15	5.0E-01		
Injection interval	4.0E-15	1.3E-01	1.1E+00	2.1E+00
All boreholes	4.1E-15	1.3E-01	1.1E+00	2.1E+00
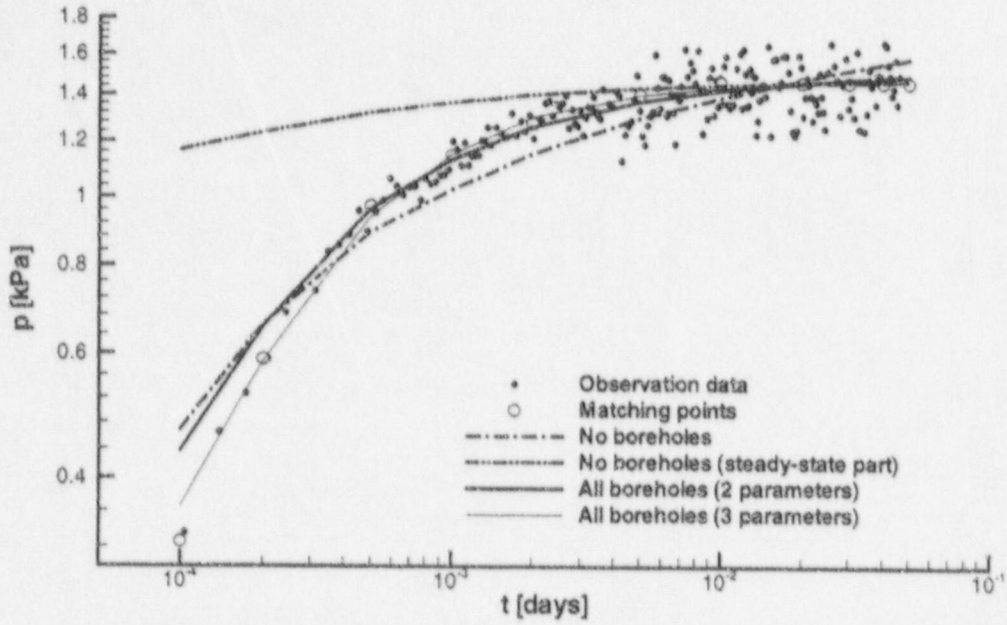
Figure 6.23: Pressure data from single-hole test JG0921A interpreted by various inverse models.
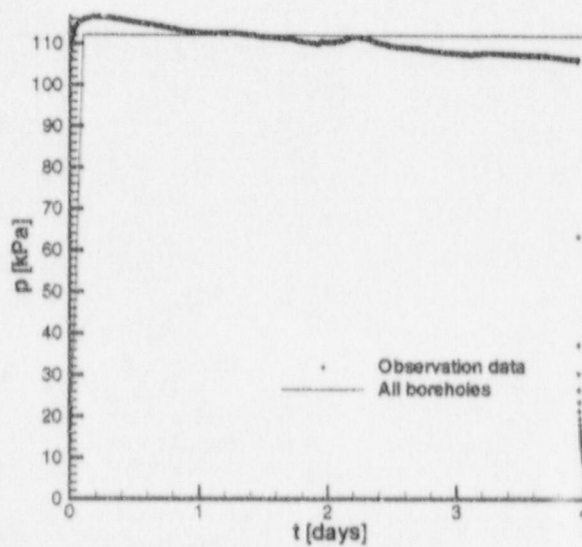
Figure 6.24: Pressure response in injection-interval during cross-hole test PP4 interpreted by inverse models.
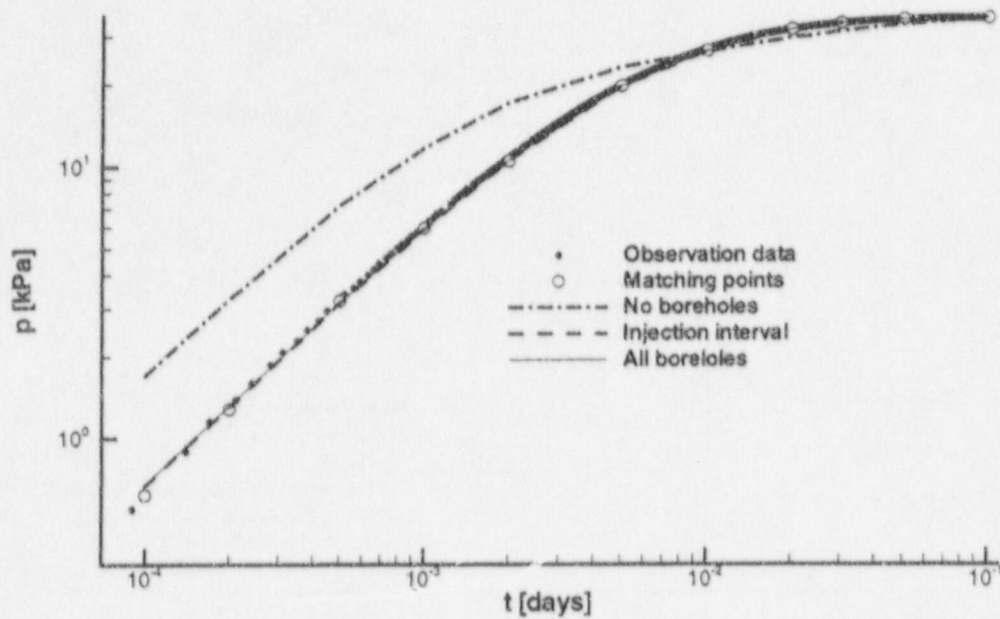
Figure 6.25: Pressure data from single-hole test JGC0609A interpreted by various inverse models.
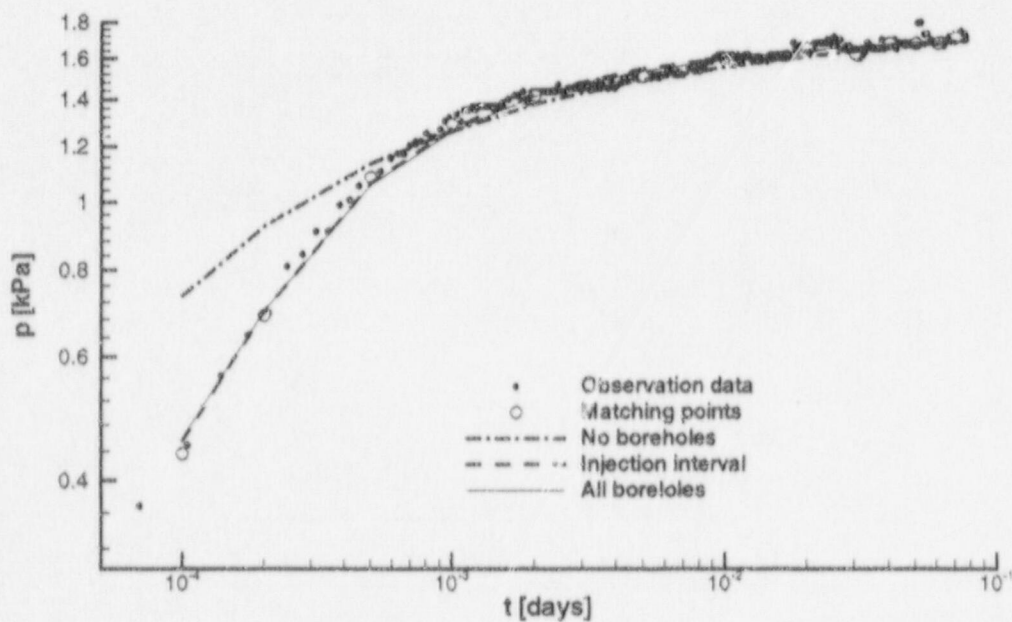
Figure 6.26: Pressure data from single-hole test JHB0612A interpreted by various inverse models.
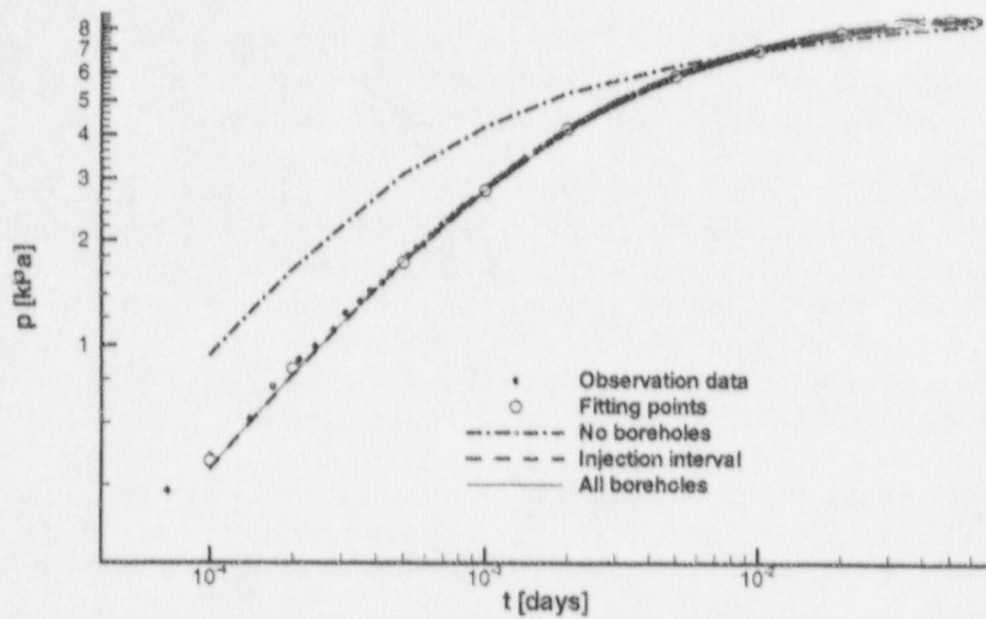
Figure 6.27: Pressure data from single-hole test JJA0616A interpreted by various inverse models.

7. CONCLUSIONS

Our work, together with earlier studies concerning the pneumatic behavior of unsaturated fractured tuffs at the ALRS, most notably those by Guzman et al. (1994, 1996) and Guzman and Neuman (1996), lead to the following major conclusions:

1. Issues associated with the site characterization of fractured rock terrains, the analysis of fluid flow and contaminant transport in such terrains, and the efficient handling of contaminated sites are typically very difficult to resolve. A major source of this difficulty is the complex nature of the subsurface "plumbing systems" of pores and fractures through which flow and transport in rocks take place. There is at present no well-established field methodology to characterize the fluid flow and contaminant transport properties of unsaturated fractured rocks.

2. In order to characterize the ability of unsaturated fractured rocks to conduct water, and to transport dissolved or suspended contaminants, one would ideally want to observe these phenomena directly by conducting controlled field hydraulic injection and tracer experiments within the rock. In order to characterize the ability of unsaturated fractured rocks to conduct non-aqueous phase liquids such as chlorinated solvents, one would ideally want to observe the movement of such liquids under controlled conditions in the field. In practice, there are severe logistical obstacles to the injection of water into unsaturated geologic media, and logistical as well as regulatory obstacles to the injection of non-aqueous liquids. There also are important technical reasons why the injection of liquids, and dissolved or suspended tracers, into fractured rocks may not be the most feasible approach to site characterization when the rock is partially saturated with water. Many of these limitations can be overcome by conducting field tests with gases rather than with liquids, and with gaseous tracers instead of chemicals dissolved in water.

3. The University of Arizona has conducted successfully numerous single-hole and cross-hole pneumatic injection tests in unsaturated fractured tuffs at the Apache Leap Research Site (ALRS) near Superior, Arizona, under the auspices of the U.S. Nuclear Regulatory Commission (NRC). These tests were part of confirmatory research in support of NRC's role as the licensing agency for a potential high-level nuclear waste repository in unsaturated fractured tuffs at Yucca Mountain. However, unsaturated fractured porous rocks similar to tuffs are found at many locations, including some low-level radioactive waste disposal sites, nuclear decommissioning facilities and sites contaminated with radioactive as well as other hazardous materials. The test methodologies we have developed, and the understanding we have gained concerning the pneumatic behavior and properties of tuffs at the ALRS, are directly relevant to such facilities and sites.

4. We found it possible to interpret both single-hole and cross-hole pneumatic injection tests at the ALRS by means of analytically derived type-curves, and a numerical inverse model, which account only for single-phase airflow through the rock while treating water as if it was immobile. Our type-curves are additionally based on

linearized versions of the nonlinear partial differential equations that govern single-phase airflow in uniform, isotropic porous continua under three regimes: three-dimensional flow with spherical symmetry, two-dimensional flow with radial symmetry, and flow in a continuum with an embedded high-permeability planar feature (a major fracture). The particular method of linearization appears to have only a minor impact on the results of our type-curve analyses. Included in our type-curves are effects of compressible air storage and skin in the injection interval during single-hole tests, and in monitoring intervals during cross-hole tests. Our analytical tools include type-curves of pressure derivative versus the logarithm of time, which accentuate phenomena that might otherwise be missed, help diagnose the prevailing flow regime, and aid in constraining the calculation of corresponding flow parameters. Our numerical inverse model represents pneumatic test conditions at the site more realistically than do our type-curves, yet the two methods of interpretation yield comparable results.

5. Steady state type-curve interpretations of single-hole pneumatic tests yield air permeability values for the rock in the immediate vicinity of the test interval. Transient type-curve analyses of   tests provide additional information about the dimensionality of the correspond   ow regime, skin factors and compressible air storage effects. Under radial flow, or in the absence of a significant borehole storage effect, transient type-curve analyses may also yield values of air-filled porosity. At the ALRS, air permeabilities obtained from steady state and transient type-curve interpretations of single-hole pneumatic injection tests, conducted in borehole intervals of 1-m, agree closely with each other but correlate poorly with fracture density data. Airflow around the vast majority of these relatively short test intervals appears to be three-dimensional; borehole storage due to air compressibility is pronounced; and skin effects are minimal. The combined effects of three-dimensional flow and borehole storage make it difficult to obtain reliable air-filled porosity values from these tests by means of type-curves, but do allow obtaining such values by means of our inverse model.

6. During a pneumatic injection test, air moves primarily through fractures most of which contain relatively little water, and the test therefore yields permeabilities and porosities which reflect closely the intrinsic properties of the surrounding fractures. This is so because capillary forces tend to draw water from fractures into porous (matrix) blocks of rock, leaving the fractures saturated primarily with air, and making it difficult for air to flow through matrix blocks. Since the fractures contain some residual water, the corresponding pneumatic permeabilities and air-filled porosities tend to be somewhat lower than their intrinsic counterparts. The former nevertheless approach the latter as the rate of injection goes up. This is due to displacement of water by air which, under a constant rate of injection, manifests itself in a rapid increase in pressure within the injection interval, followed by a gradual decrease. Two-phase flow of water and air additionally causes air permeabilities from single-hole pneumatic injection tests to exhibit a hysteretic variation with applied pressure.

7. In most single-hole pneumatic injection tests at the ALRS, pneumatic permeabilities increase systematically with applied pressure as air displaces water under two-phase flow. In a few single-hole tests, where the injection intervals are intersected by widely open fractures, air permeabilities decrease with applied pressure due to inertial effects. This pressure-dependence of air permeability suggests that it is advisable to conduct single-hole air injection tests at several applied flow rates and/or pressures. Pneumatic parameters derived from pressure data recorded in monitoring intervals during cross-hole tests appear to be much less sensitive to the rate of injection, suggesting that two-phase flow and inertial phenomena decay rapidly with distance from the injection interval. Enhanced permeability due to slip flow (the Klinkenberg effect) appears to be of little relevance to the interpretation of single-hole or cross-hole air injection tests at the ALRS.

8. Flow in the vicinity of most 1-m single-hole pneumatic test intervals at the ALRS appears to be three-dimensional regardless of the number or orientation of fractures in the surrounding rock. We interpret this to mean that such flow is controlled by a single continuum, representative of a three-dimensional network of interconnected fractures, rather than by discrete planar features. Indeed, most single-hole and cross-hole pneumatic test data at the ALRS have proven amenable to analysis by means of a single fracture-dominated continuum representation of the fractured-porous tuff at the site. Only in a small number of single-hole test intervals, known to be intersected by widely open fractures, have the latter dominated flow as evidenced by the development of an early half-slope on logarithmic plots of pressure versus time; unfortunately, the corresponding data do not fully conform to available type-curve models of fracture flow. Some pressure records conform to the radial flow model during early and intermediate times, but none do so fully at late time.

9. It is generally not possible to distinguish between the permeabilities of individual fractures, and the bulk permeability of the fractured rock in the immediate vicinity of a test interval, by means of pneumatic injection tests. Hence there is little justification for attempting to model flow through individual fractures at the site. The explicit modeling of discrete features appears to be justified only when one can distinguish clearly between layers, faults, fracture zones, or major individual fractures on scales not much smaller than the domain of interest.

10. Air permeabilities obtained from single-hole tests are poorly correlated with fracture densities, as is known to be the case for hydraulic conductivities at many water-saturated fractured rock sites worldwide (Neuman, 1987). This provides further support for Neuman's conclusion that the permeability of fractured rocks cannot be reliably predicted from information about fracture geometry (density, trace lengths, orientations, apertures and their roughness) but must be determined directly by means of hydraulic and/or pneumatic tests.

11. Core and single-hole measurements, conducted over short segments of a borehole, provide information only about a small volume of rock in the immediate vicinity of each measurement interval. Available data from the ALRS indicate that rock

properties, measured on such small scales, vary erratically in space in a manner which renders the rock randomly heterogeneous and pneumatically anisotropic. Local-scale air permeabilities from single-hole tests vary by orders of magnitude between test intervals across the site; their spatial variability is much more pronounced than their dependence on applied pressure. We found it possible to interpolate some of the core and single-hole measurements at the ALRS between boreholes by means of geostatistical methods, which view the corresponding variables as correlated random fields defined over a continuum. This was especially true about air permeability, porosity, fracture density, water content, and the van Genuchten water retention parameter α, for each of which we possess enough measurements to constitute a workable geostatistical sample. To differentiate between geostatistical models that appear to fit these data equally well, we used formal model discrimination criteria based on maximum likelihood and the principle of parsimony (which places a premium on simplicity). Standard geostatistical analysis provides best (minimum variance) linear unbiased estimates of how each such quantity varies in three-dimensional space, together with information about the quality of these estimates. Our finding supports the application of continuum flow and transport theories and models to unsaturated fractured porous tuffs at the ALRS on scales of one meter or more.

12. Estimates of hydrogeologic variables, obtained by geostatistical methods such as kriging, are smooth relative to their random counterparts. We found it possible to generate less smooth and more realistic images of log air permeability, fracture density, log porosity, water content, and log α values in three dimensions that honor the available data, by means of a sequential Gaussian conditional simulation code.

13. Cross-hole pneumatic injection test data from individual monitoring intervals at the ALRS have proven amenable to analysis by type-curve and numerical inverse models which treat the rock as a uniform and isotropic fractured porous continuum. Analyses of pressure data from individual monitoring intervals by the two methods gave comparable results concerning pneumatic connections between injection and monitoring intervals, corresponding directional air permeabilities, and air-filled porosities. All of these quantities were found to vary considerably from one monitoring interval to another in a given cross-hole test on scales ranging from a few to over 20 meters. Thus, even though our type-curve analysis treats the rock as if it was pneumatically uniform and isotropic, it ultimately yields information about the spatial and directional dependence of pneumatic permeability and connectivity across the site.

14. Some cross-hole pressure records reveal an inflection that is characteristic of dual continuum behavior. The prevailing interpretation of dual continua is that one represents the fracture network and the other embedded blocks of rock matrix. We take the broader view that multiple (including dual) continua may represent fractures on a multiplicity of scales, not necessarily fractures and matrix.

15. The pneumatic permeabilities of unsaturated fractured tuffs at the ALRS vary strongly with location, direction and scale. In particular, the mean of pneumatic permeabilities increases, and their variance decreases, with distance between packers in a single-hole injection test, and with distance between injection and monitoring intervals in cross-hole injection tests. This scale effect is most probably due to the presence in the rock of various size fractures that are interconnected on a variety of ales.

REFERENCES

Agarwal, R. G., R. Al-Hussainy, H. J. Ramey Jr., An Investigation of Wellbore Storage and Skin Effect in Unsteady Liquid Flow: 1. Analytical Treatment, AIME *Trans.*, 279-290, 1970.

Akaike, H., A new look at statistical model identification, *IEEE Trans. Automat. Control*, AC-19, pp.716-722, 1974.

Akaike, H., On entropy maximization principle. In: *Application of Statistics*, P.R.Krishnaiah ed., North-Holland, Amsterdam, 1977.

Al-Hussainy R. and H. J. Ramey Jr., The Flow of Real Gases Through Porous Media, *J. Pet. Tech.*, 624-636, 1966.

Alzaydi, A. A., C. A. Moore, and I. S. Rai, Combined Pressure and Diffusional Transition Region Flow of Gases in Porous Media, *AIChE Journal*, 24(1), pp.35 – 43, 1978.

Ando, K., Continuum stochastic modeling of flow and transport in a crystalline rock mass, M.S. thesis, The University of Arizona, Tucson, 1995.

Arnofsky, J. S. and R. Jenkins, A Simplified Analysis of Unsteady Radial Gas Flow, *Trans.*, AIME, 201, 149, 1954.

Barenblatt, G. I., Y. P. Zheltov, and I. N. Kochina, Basic concepts in the theory of seepage of homogeneous liquids in fissured rocks, *Jour. Appl. Math. Mech.*, English Transl., 24, 1286-1303, 1960.

Bassett, R. L., S. P. Neuman, T. C. Rasmussen, A. Guzman, G.R. Davidson, and C. L. Lohrstorfer, *Dvalidation Studies for Assessing Unsaturated Flow and Transport Through Fractured Rock*, NUREG/CR-6203, 1994.

Bassett, R. L., S. P. Neuman, P. J. Wierenga, G. Chen, G. R. Davidson, E. L. Hardin, W.A. Illman, M. T. Murrell, D. M Stephens, M. J. Thomasson, D. L. Thompson, E. G. Woodhouse, *Data Collection and Field Experiments at the Apache Leap Research Site, May 1995-1996*, NUREG/CR-6497, 1997.

Bear, J, *Dynamics of Fluids in Porous Media*, Dover Publications, Inc., 764 pp., 1972.

Berkowitz, B., J. Bear, and C. Braester, Continuum models for contaminant transport in fractured porous formations, *Water Resour. Res.*, 24(8), 1225-1236, 1988.

Bibby, R., Mass transport of solutes in dual-porosity media, *Water Resour. Res.*, 17(4), 1075-1081, 1981.

Birkhölzer, J., H. Rubin, H. Daniels, and G. Rouvé, Contaminant advection and spreading in a fractured permeable formation, 2, Numerical simulation, *J. Hydrology*, 144, 35-38, 1993.

Black J. H. and K. L. Kipp Jr., Observation Well Response Time And Its Effect Upon Aquifer Test Results, *J. Hydrology*, 34: 297-306, 1977.

Burcik, E. J., *Properties of Petroleum Reservoir Fluids*, International Human Resources Development Coorporation, 1957.

Cacas, M. C., E. Ledoux, G. de Marsily, A. Barbreau, P. Calmels, B. Gaillard, and R. Margritta, Modelling fracture flow with a stochastic discrete fracture network: Calibration and validation, 1, The flow model, *Water Resour. Res.*, 26(3), 479-489, 1990a.

Cacas, M. C., E. Ledoux, G. de Marsily, A. Barbreau, P. Calmels, B. Gaillard, and R. Margritta, Modelling fracture flow with a stochastic discrete fracture network: Calibration and validation, 1, The transport model, *Water Resour. Res.*, 26(3), 491-500, 1990b.

Carrera, J. and S.P. Neuman, Estimation of aquifer parameters under transient and steady state conditions: 1. Maximum likelihood method incorporating prior information, *Water Resour. Res.*, 22(2), 199-210, 1986a.

Carrera, J. and S.P. Neuman, Estimation of aquifer parameters under transient and steady state conditions: 2. Uniqueness, stability, and solution algorithm, *Water Resour. Res.*, 22(2), 212-227, 1986b.

Carrera, J. and S.P. Neuman, Estimation of aquifer parameters under transient and steady state conditions: 3. Application to synthetic and field data, *Water Resour. Res.*, 22(2), 228-242, 1986c.

Carrera, J., J. Heredia, S. Vomvoris, and P. Hufschmied, Modeling of flow in a small fractured monzonitic gneiss block, pp. 115-167 in Neuman, S.P. and I. Neretnieks, *Hydrogeology of Low Permeability Environments*, Hydrogeology, Selected Papers, 2, Verla Heinz Heise, Hannover, Germany, 1990.

Carter R. D., Solutions of Unsteady-State Radial Gas Flow, *J. Pet. Tech*, 549-554, 1962.

Chen G, S.P. Neuman, and P.J. Wierenga, *4. Infiltration tests in Fractured Porous Tuffs at the ALRS*, in Bassett, R.L., S.P. Neuman, P.J. Wierenga, G. Chen, G.R. Davidson, E.L. Hardin, W.A. Illman, M.T. Murrell, D.M Stephens, M.J. Thomasson, D.L. Thompson, E.G. Woodhouse, *Data Collection and Field Experiments at the Apache Leap Research Site, May 1995-1996*, NUREG/CR-6497, 1997.

Chuang, Y., W. R. Haldeman, T. C. Rasmussen, and D. D. Evans, *Laboratory Analysis of Fluid Flow and Solute Transport Through a Variably Saturated Fracture Embedded in Porous Tuff*, NUREG/CR-5482, 328 pp., 1990.

Cinco-Ley, H, H.J. Ramey, Jr., and F.G. Miller, Unsteady-State Pressure Distribution Created by a Well With an Inclined Fracture, paper SPE 5591 presented at the SPE-AIME 50th Annual Fall Technical Conference and Exhibition, Dallas, Sept. 28-Oct. 1, 1975.

Cinco-Ley, H., Samaniego-V. F., and Dominguez, A. N., Transient Pressure Behavior for a Well with a Finite Conductivity Vertical Fracture, *Soc. Pet. Eng. J.*, 253-264., 1978.

CRC, *Handbook of Chemistry and Physics*, David R. Lide (editor-in-chief), 73 rd. ed., CRC Press, 1992-1993.

Dachler, Time Lag and Soil Permeability in Groundwater Observations, Bulletin 36, U.S. Army, Eng. Waterways Exp. Sta., Vicksburg, Miss., 1936.

De Hoog F. R., Knight, and Stokes, A. N., An Improved Method for Numerical Inversion of Laplace Transforms, *SIAM J. Sci. Stat. Comp.*, 3(3), 357 – 366, 1982.

Dershowitz, W., P. Wallman, and S. Kindred, Discrete Fracture Modeling for the Stripa Site Characterization and Validation Drift Inflow Predictions, Stripa Project Technical Report 91-16, SKB Swedish Nuclear Fuel and Waste Management Co., Stockholm, Sweden, 1991.

Doherty, J., L. Brebber, P. Whyte, *PEST: Model Independent Parameter Estimation*, Watermark Computing, 1994.

Duguid, J.O. and P.C.Y. Lee, Flow in fractured porous media, *Water Resour. Res.*, 13, 558-566, 1977.

Dullien, F. A. L., *Porous Media - Fluid Transport and Pore Structure*, 2nd ed., Academic Press, Inc., 574 pp., 1992.

Dverstorp, B., J. Andersson, and W. Nordqvist, Discrete fracture network interpretation of field tracer migration in sparsely fractured rock, *Water Resour. Res.*, 28(9), 2327-2343, 1992.

Dykhuizen, R. C., A new coupling term for dual porosity models, *Water Resour. Res.*, 26, 351-356, 1990.

Evans, D. D., *Unsaturated Flow and Transport Through Fractured Rock – Related to High-Level Waste Repositories*, NUREG/CR-3206, 231 pp., 1983.

Evans, D. D. and T. C. Rasmussen, *Unsaturated Flow and Transport Through Fractured Rock Related to high-Level Waste Repositories, Final Report – Phase III*, NUREG/CR-5581, pp. 75, 1991.

Geddis, A. M., Rapid estimate of solid volume in large tuff cores using a gas pycnometer, M.S. thesis, The University of Arizona, Tucson, AZ, 1994.

Gerke, H. H. and M. T. van Genuchten, A dual-porosity model for simulating the preferential movement of water and solutes in structured porous media, *Water Resour. Res.*, 29, 305-319, 1993a.

Gerke, H. H. and M. T. van Genuchten, Evaluation of a first-order water transfer term for variably saturated dual-porosity models, *Water Resour. Res.*, 29, 1225-1238, 1993b.

Glover, R. E., Flow from a Test-Hole Above Groundwater level, in *Theory and problems of Water Percolation*, U.S. Bureau of Reclamation Engineering Monograph No. 8, 66-71, 1953.

Góméz-Hernández, J. J., A stochastic approach to the simulation of block conductivity values conditioned upon data measured at a smaller support, Ph D. dissertation, Stanford University, California, 1991.

Gomez-Hernandez, J. J., and E. F. Cassiraga, The Theory of Practice of Sequential Simulation, In: *Geostatistical Simulations*, M. Armstrong and P. A. Dowd (editors), 111-124, Kluwer Academic, Norwell Mass, 1994.

Gradshteyn, I. S., and Rhyzhik, I. M., *Table of Integrals, Series, and Products*, Academic Press, Inc., 1204 pp., 1965.

Green, R. T. and D. D. Evans, *Radionuclide Transport as Vapor Through Unsaturated Fractured Rock*, NUREG/CR-4654, 163 pp., 1987.

Gringarten, A.C., H. J. Ramey, Jr., and R. Raghavan, Unsteady-State Pressure Distributions Created by a Well With a Single Infinite-Conductivity Vertical Fracture. *Soc. Pet. Eng. Journ.*, 347-360; *Trans.*, AIME, 257, 1974.

Gringarten, A.C. and H. J. Ramey Jr., Unsteady-state pressure distributions created by a well with a single horizontal fracture, partial penetration, or restricted entry. *Soc. Pet. Eng. Journ.*, 413-426; *Trans.*, AIME, 257., 1974.

Gringarten, A. C., Flow Test Evaluation of Fractured Reservoirs, Symp. On Recent Trends in Hydrology, Berkeley, CA, February 8-11, 1979.

Gringarten, A. C., Flow Test Evaluation of Fractured Reservoirs, Geological Society of America, Special Paper 189, 237-263, 1982.

Guzman, A. G. and S. P. Neuman, Field Air Injection Experiments, pp. 52-94 in Rasmussen, T. C., S. C. Rhodes, A. Guzman, and S. P. Neuman, *Apache Leap Tuff INTRAVAL Experiments: Results and Lessons Learned*, NUREG/CR-6096, 1996.

Guzman, A. G., S. P. Neuman, C. Lohrstorfer, and R. Bassett, pp. 4-1 through 4-58 in Bassett, R. L., S. P. Neuman, T. C. Rasmussen, A. G. Guzman, G. R. Davidson, and C. L. Lohrstorfer, *Validation Studies for Assessing Unsaturated Flow and Transport Through Fractured Rock*, NUREG/CR-6203, 1994.

Guzman, A. G., A. M. Geddis, M. J. Henrich, C. Lohrstorfer, and S. P. Neuman, *Summary of Air Permeability Data From Single-Hole Injection Tests in Unsaturated Fractured Tuffs at the Apache Leap Research Site: Results of Steady-State Test Intepretation*, NUREG/CR-6360, 1996.

Hannan, E. S., The estimation of the order of an ARMA process, *Ann. Stat.*, v.8, 197-181, 1980.

Harleman, D. R. E., P.F. Mehlhorn, and R. R. Rumer, Dispersion-permeability correlation in porous media, *J. Hydrau. Div. Amer. Soc. Civil Eng.*, No. HY2, 89, 67-85 1963.

Hsieh, P. A. and S. P. Neuman, Field Determination of the Three-Dimensional Hydraulic Conductivity Tensor of Anisotropic Media, 1. Theory, *Water Resour. Res.*, 21(11): 1655-1665, 1985a.

Hsieh, P. A., S. P. Neuman, G. K. Stiles, and E. S. Simpson, Field Determination of the Three-Dimensional Hydraulic Conductivity Tensor of Anisotropic Media, 2. Methodology and Application to Fractured Rocks, *Water Resour. Res.*, 21(11): 1667-1676, 1985b.

Huang, C. and D. D. Evans, *A 3-Dimensional Computer Model to Simulate Fluid Flow and Contaminant Transport Through a Rock Fracture System*, NUREG/CR-4042, 109 pp., 1985.

Hvorslev J., *Time Lag and Soil Permeability in Ground-Water Observations*, Bulletin No, 36, Waterways Experiment Station, Corps of Engineers, U.S. Army, 50 pp., 1951.

Joseph, J. A., Unsteady-State Cylindrical, Spherical, and Linear Flow in Porous Media, Ph.D Dissertation, Univ. of Missouri-Rolla, 517 pp., 1984.

Joseph, J. A., and L. F. Koederitz, Unsteady-State Spherical Flow With Storage and Skin, *Soc. Pet. Eng. Journ.*, pp.804 – 822, 1985.

Journel, A.G., Fundamentals of geostatistics in five lessons, Short course in geology, 8, Am. Geophys. Union, Washington, D.C., 1989.

Kazemi, H., Pressure transient analysis of naturally fractured reservoirs with uniform fracture distribution, *Trans. Soc. Petrol. Engin. AIME*, 246, 451-462, 1969.

Kashyap, R.L., Optimal choice of AR and MA parts in autoregressive moving average models, *IEEE Trans. Pattern Anal. Mach. Intel. PAMI*, 4, 99-104, 1982.

Keidser, A. and D. Rosbjerg, A Comparison of Four Inverse Approaches to Groundwater Flow and Transport Identification, *Water Resour. Res.*, 27(9), 2219-2232, 1991.

Kirchhoff, G., Vorlesungen über de theorie der Wärme, Barth, Leipzig, 1894.

Klinkenberg, L. J., The permeability of porous media to liquids and gases, Am. Pet. Inst., *Drilling and Production Practice*, 200-213, 1941.

Knudsen, M., *The Kinetic Theory of Gases*, Methuen, London, 1950.

Kostner, A., Geostatistical and numerical analysis of flow in a crystalline rock mass, M.S. thesis, The University of Arizona, Tucson, 1993.

LeCain, G. D., Pneumatic testing in 45-degree-inclined boreholes in ash-flow tuff near Superior, Arizona, U.S. Geological Survey Water-Resources Investigations Report 95-4073, 1995.

LeCain, G. D., Air-injection testing in vertical boreholes in welded and nonwelded tuff, Yucca Mountain, Nevada, U.S. Geological Survey Milestone Report 3GUP610M, Denver, Colorado, 1996.

Long, J. C. S., P. Gilmour, and P. A. Witherspoon, A model for steady fluid flow in random 3-D network of disc shaped fractures, *Water Resour. Res.*, 21(8), 1105-1115, 1985.

Marquardt, D. W., An algorithm for least-squares estimation of nonlinear parameters, *Journal of the Society of Industrial and Applied Mathematics*, v. 11(3), 431-441, 1963.

Massmann, J. W., Applying Groundwater Flow Models In Vapor Extraction System Design, *Journ. of Env. Eng.*, 115(1), 129–149, 1989.

Mendoza, C.A., and E.O. Frind, Advective-dispersive transport of dense organic vapors in the unsaturated zone, 1, Model Development, *Water Resour. Res.*, 26(3), 379-387, 1990.

Mishra, S., G.S. Bodvarsson, and M.P. Attanayake, Injection and Falloff Test Analysis to Estimate Properties of Unsaturated Fractured Fractures, in *Flow and Transport Through Unsaturated Fractured Rock*, eds. D.D. Evans and T.J. Nicholson, American Goephysical Union, Geophysical Monograph 42, 1987.

Moench, A.F., Double-porosity models for a fissured groundwater reservoir with fracture skin, *Water Resour. Res.*, 20, 831-846, 1984.

Montazer, P.M., *Permeability of Unsaturated, Fractured Metamorphic Rocks Near An Underground Opening*, Ph. D thesis, Colorado School of Mines, Golden, Colorado, 1982.

National Research Council, *Rock Fractures and Fluid Flow: Contemporary Understanding and Applications*, National Academy Press, Washington, D.C., 1996.

Moran, J. H. and E. E. Finklea, Theoretical Analysis of Pressure Phenomena Associated with the Wireline Formation Tester, *J. Pet. Tech.*, 899-908, 1962.

Neuman, S. P. and E. A. Jacobson, Analysis of Noninstrinsic Spatial Variability by Residual Kriging with Application to Regional Groundwater Levels, *Math. Geology*, 16, 491-521, 1984.

Neuman, S. P., Stochastic continuum representation of fractured rock permeability as an alternative to the REV and fracture network concepts. In: I.W. Farmer, J.J.K. Dalmen, C.S.Desai, C.E.Glass and S.P. Neuman (Editors), *Rock Mechanics, Proc. Of the 28th U.S. Symposium*. Balkema, Rotterdam, pp.533-561, 1987.

Neuman, S. P., A proposed conceptual framework and methodology for investigating flow and transport in Swedish crystalline rocks, Arbetsrapport 88-37, 39 pp., SKB Swedish Nuclear Fuel and Waste Management Co., Stockholm, September 1988.

Neuman, S. P. and J. S. Depner, Use of Variable-Scale Pressure Test Data to Estimate the Log Hydraulic Conductivity Covariance and Dispersivity of Fractured Granites Near Oracle, Arizona, *J. Hydrology*, 102, 475-501, 1988.

Neuman, S. P. and D. A. Gardner, Determination of Aquitard/aquiclude hydraulic properties from arbitrary water level fluctuations by deconvolution, *Groundwater*, 27(1), 66-76, 1989.

Neuman, S.P., Stochastic approach to subsurface flow and transport: A view to the future, in Dagan, G. and S.P. Neuman (editors), *Subsurface Flow and Transport: A Stochastic Approach*, Cambridge University Press, Cambridge, United Kingdom, 1997.

Neuman, S.P. and V. Di Federico, Correlation, flow and transport in multiscale permeability fields, in *Scale Dependence and Scale Invariance in Hydrology*, edited by G. Sposito, Cambridge University Press, New York, New York, 1998.

Nisle, R. G., The Effect of Partial Penetration on Pressure Build-Up in Oil Wells, *Trans.*, AIME, *213*, 85, 1958.

Odeh, A. A., Unsteady-state behavior of naturally fractured reservoirs, *Soc. Pet. Eng. J.*, 60-66, 1965.

Paillet, F. L., Using borehole geophysics and cross-borehole flow testing to define hydraulic connections between fracture zones in bedrock aquifers, *J. App. Geoph.*, 20: pp. 261-279, 1993.

Papadopulos, I. S. and Cooper Jr., H. H., Drawdown in a Well of Large Diameter, *Water Resour. Res.*, 3(1): 241-244, 1967.

Peters, R. R. and E. A. Klavetter, A continuum model for water movement in an unsaturated fractured rock mass, *Water Resour. Res.*, 24, 416-430, 1988.

Peterson, D. W., *Dacitic Ash-Flow Sheet Near Superior and Globe, Arizona*, Ph.D. Dissertation, Stanford University, Palo Alto, CA, 1961.

Philip, J. R., Approximate Analysis of the Borehole Permeameter in Unsaturated Soil, *Water Resour. Res.*, 21(7), 1025-1033, 1985.

Present, R. D., *Kinetic Theory of Gases*, McGraw-Hill Book Company, Inc., 280 pp., 1958.

Pruess, K. and T. N. Narasimhan, A practical method to modeling fluid and heat flow in fractured porous media, *Soc. Petrol. Eng. J.*, 25(1), 14-26, 1985.

Pruess, K., J. S. Y. Wang, and Y. W. Tsang, On thermohydrologic conditions near high-level nuclear waste emplaced in partially saturated fractured tuff: 2. Effective continuum approximation, *Water Resour. Res.*, 26, 1249-1261, 1990.

Pruess, K., A general purpose numerical simulator for multiphase fluid and heat flow, Lawrence Berkeley Laboratory Report LBL-29400 UC-251, May, 1991.

Raghavan, R., Some Practical Considerations in the Analysis of Pressure Data, *J. Pet. Tech.*, 97-104; *Trans.*, AIME, 261, 1976.

Raghavan, R., Pressure Behavior of Wells Intercepting Fractures, *Proc.*, Invitational Well-testing Symposium, Berkeley (Oct. 19-21, 1977).

Raghavan R., A. Uraiet, and G. W. Thomas, Vertical fracture height: Effect on transient flow behavior, *Soc. Pet. Eng. J.*, 265-277, 1978.

Raghavan, R., *Well Test Analysis*, Prentice Hall Petroleum Engineering Series, Prentice-Hall Inc., 558 pp., 1993.

Rasmussen, T. C. and D. D. Evans, *Unsaturated Flow and Transport Through Fractured Rock-Related to High-level Waste Repositories*, NUREG/CR-4655, 474 pp., 1987.

Rasmussen T. C. and D. D. Evans, *Fluid Flow and Solute Transport Modeling Through Three-Dimensional Networks of Variably Saturated Discrete Fractures*, NUREG/CR-5239, 193 pp., 1989.

Rasmussen, T. C., D. D. Evans, P. J. Sheets, and J. H. Blanford, *Unsaturated Fractured Rock Characterization Methods and Data Sets at the Apache Leap Tuff Site*, NUREG/CR-5596, 125 pp., 1990.

Rasmussen, T. C. and D. D. Evans, *Nonisothermal Hydrologic Transport Experimental Plan*, NUREG/CR-5880, 41 pp., 1992.

Rasmussen, T. C., D. D. Evans, P. J. Sheets, and J. H. Blanford, Permeability of Apache Leap Tuff: Borehole and Core Measurements Using Water and Air, *Water Resour. Res.*, 29(7), 1997-2006, 1993.

Samper, F. J., Neuman, S. P., Estimation of Spatial Structures by Adjoint State Maximum Likelihood Cross Validation: 1. Theory, *Water Resour. Res.*, 25(3), 351-362, 1989.

Samper, F. J., Neuman, S. P., Estimation of Spatial Structures by Adjoint State Maximum Likelihood Cross Validation: 2. Synthetic Experiments, *Water Resour. Res.*, 25(3), 363-372, 1989b.

Samper, F.J. and S.P. Neuman, Estimation of spatial covariance structures by adjoint state maximum likelihood cross-validation: 3. Application to hydrochemical and isotopic data, *Water Resour. Res.*, 25(3), 373-384, 1989c.

Scheidegger, A.E., *The physics of flow through porous media*, 3rd. ed., University of Toronto Press, 352 pp., 1974.

Schrauf, T. W. and D. D. Evans, *Relationship Between the Gas Conductivity and Geometry of a Natural Fracture*, NUREG/CR-3680, 131 pp., 1984.

Scott, D.S., and Dullien, F. A. L., *AIChE J.* 8, 293, 1962a.

SKB, Annual Report 1992, SKB Tech. Rep. 92-46, Swedish Nuclear Fuel and Waste Management Co., Stockholm, Sweden, May 1993.

Tidwell, V. C., T. C. Rasmussen, and D. D. Evans, Saturated hydraulic conductivity estimates for fractured rocks in the unsaturated zone, in *Proceedings of International Conference and Workshop on the Validation of Flow and Transport Models for the Unsaturated Zone*, edited by P.J. Wierenga, New Mexico State University, Las Cruces, N.M., 1988.

Tongpenyai, Y. and R. Raghavan, The effect of wellbore storage and skin on interference test data, *J. Pet. Tech.*, 151-160, 1981.

Trauz, R. C., *Rock Fracture Aperture and Gas Conductivity Measurements In-Situ*, Topical Report, Contract No. NRC-04-81-224, 1984.

Trease, H. E., D. George, C. W. Gable, J. F. A. Kuprat, A. Khamyaseh, The X3D Grid Generation System, In: *Numerical Grid Generation in Computational Fluid Dynamics and Related Fields*, B. K. Soni, J. F. Thompson, H. Hausser and P. R. Eiseman (editors), Engineering Research Center, Mississippi State Univ. Press, 1996.

Tsang, C. F. and S. P. Neuman, Introduction and general comments on INTRAVAL Phase 2, Working Group 2, Test Cases, in The International Intraval Project, Phase 2, NEA/OEC-D, Paris, France, in press, 1995.

Tsang, Y. W., C. F. Tsang, F. V. Hale, and B. Dverstorp, Tracer transport in a stochastic continuum model of fractured media, *Water Resour. Res.*, 32(10): 3077-3092, 1996.

van Everdingen, A. F., and Hurst, W., The Application of the Laplace Transformation to Flow Problems in Reservoirs, *Trans.* AIME, 186, 305-324, 1949.

van Genuchten, M. T., A Closed-Form Equation for Predicting the Hydraulic Conductivity of Unsaturated Soils, *Soil Sci. Soc. Am. J.*, 44, p. 892-898, 1980.

Vasserman, A. A., Kazavchinskii, Ya. Z., and Rabinovich V.A., *Thermophysical Properties of Air and Air Components*, Academy of Sciences of the USSR, Edited by A.M. Zhuravlev, Translated from Russian by Israel Program for Scientific Translations, Jerusalem 1971, 1966.

Vickers, B. C., S. P. Neuman, M. J. Sully, and D. D. Evans, Reconstruction Geostatistical Analysis of Multiscale Fracture Apertures in a Large Block of Welded Tuff, *Geoph. Res. Let.*, 19(10), 1029-1032, 1992.

Vogt, G. T., Porosity, Pore-Size Distribution and Pore Surface Area of the Apache Leap Tuff Near Superior, Arizona using Mercury Porosimetry, M.S. Thesis, University of Arizona, pp. 130, 1988

Warren, J. E. and P. J. Root, The behavior of naturally fractured reservoirs, *S. Pet. Eng. J.*, 3, 245-255, 1963.

Watson, D. F., Computing the N-Dimensional Delaunay Tessellation with Application to Voroni Polytopes, *The Computer Journal*, v.24, Heyden & Son Ltd, London, England, pp. 167-172, 1981.

Yeh, T. C., T. C. Rasmussen, and D. D. Evans, *Simulation of Liquid and Vapor Movement in Unsaturated Fractured Rock at the Apache Leap Tuff Site -- Models and Strategies*, NUREG/CR-5097, 73 pp., 1988,

Zimmerman, R.W., G. Chen, T. Hadgu, and G.S. Bodvarsson, A numerical dual-porosity model with semianalytical treatment of fracture/matrix flow, *Water Resour. Res.*, 29(7), 2127-2137, 1993.

Zyvoloski, G. A., Z. V. Dash, S. Keikar, FEHM: Finite Element Heat and Mass Transfer, LA-11224-MS, Los Alamos National Laboratory, 1988.

Zyvoloski G. A., B. A. Robinson, Z. V. Dash, L. L. Trease, Users Manual for the FEHMN Application, LA-UR-94-3788, Los Alamos National Laboratory, 1996.

Zyvoloski G. A., B. A. Robinson, Z. V. Dash, L. L. Trease, Summary of the Models and Methods for the FEHM Application - A Finite-Element Heat- and Mass-Transfer Code, LA-13307-MS, Los Alamos National Laboratory, 1997.

APPENDIX A: AIR COMPRESSIBILITY AND VISCOSITY IN RELATION TO PRESSURE AND TEMPERATURE AT THE ALRS

In this appendix we include a sample calculation of the compressibility factor Z for air under standard conditions, tables of pressures and temperatures encountered during single-hole pneumatic injection tests over 1-m intervals at the ALRS, and a table of air viscosity values under a range of temperatures.

The compressibility factor for gas is defined in (2.1-9) as

$$Z = \frac{pV_s}{RT} \tag{A-1}$$

where $V_s = V/n$. To assess Z for air, we note from Table A-1 (CRC Handbook, 1992-1993) that the molecular weight of standard atmospheric air in the United States is 28.96443 g/mol. Its specific volume is therefore (Vasserman *et al.*, 1966) $V_s = 1.246629 \cdot 10^{-2} \, m^3/mol$. As the universal gas constant is $R = 8.31441 \, Nm/^\circ K \, mol$ we find that, under standard conditions of $p = 200 \, kPa$ and $T = 300^\circ K$,

$$Z = \frac{(200,000 \, Pa)\left(1.246629 \times 10^{-2} \, m^3/mol\right)}{(8.314510 \, Nm/^\circ Kmol)(300^\circ K)} \cong 1.0$$

Otherwise Z varies with p and T as shown in Figure 2-1. Table A-2 lists the minimum, maximum, average and range of stable injection pressures attained in each borehole within which single-hole pneumatic injection tests took place over 1-m intervals at the ALRS. Table A-3 shows the same for temperatures.

Table A-4 lists values of dynamic viscosity for air over a range of pressures and temperatures comparable to those encountered at the ALRS. The same data are shown graphically in Figure 2-2.

Table A.1: Gaseous composition of U.S. standard atmosphere
(CRC Handbook, 1992-1993)

Gas Species	Molecular Weight [kg/kmol]	Fractional Volume [dimensionless]	Fractional Molecular Weight [g/mol]
N_2	28.0134	0.78084	21.87398
O_2	31.9988	0.209476	6.702981
Ar	39.948	0.00934	0.373114
CO_2	44.00995	0.000314	0.013819
Ne	20.183	0.00001818	0.000367
He	4.0026	0.00000524	2.1e-5
Kr	83.8	0.00000114	9.55e-5
Xe	131.3	0.000000087	1.14e-5
CH_4	16.04303	0.000002	3.21e-5
H_2	2.01594	0.0000005	1.01e-6
Total			28.96443

Table A.2: Data concerning stable pressures encountered during 1-m scale single-hole pneumatic injection tests at the ALRS (summarized from Guzman et al., 1996)

Borehole	Minimum Pressure [Pa]	Maximum Pressure [Pa]	Mean Pressure [Pa]	Range of Pressures [Pa]
V2	88886.04	248592.9	159460.9	159706.9
W2A	88419.42	240073.6	147661.9	151654.2
X2	89805.97	265058.3	144005.1	175252.3
Y2	89632.65	233380.9	146031.9	143748.2
Y3	88379.42	361610.3	162972.3	273230.9
Z2	90072.61	240273.6	152740.5	150201.0

Table A.3: Data concerning temperatures encountered during 1-m scale single-hole pneumatic injection tests at the ALRS (summarized from Guzman et al., 1996)

Borehole	Minimum Temp (°K)	Maximum Temp (°K)	Mean Temp (°K)	Range of Temps (°K)
V2	293.09	300.90	294.40	7.81
W2A	292.57	299.07	293.40	6.50
X2	293.04	302.60	294.82	9.56
Y2	288.50	293.93	293.14	5.43
Y3	288.10	298.93	293.02	10.83
Z2	291.32	302.74	294.22	11.42

Table A.4: Variation of air dynamic viscosity with temperature and pressure (adapted from Vasserman et al., 1966)

p (kPa)	T (°K) T = 270°K	T (°K) T = 280°K	T (°K) T = 290°K	T (°K) T = 300°K	T (°K) T = 310°K	T (°K) T = 320°K
1.0E+02	1.6960E-05	1.7460E-05	1.7960E-05	1.8460E-05	1.8960E-05	1.9450E-05
1.0E+03	1.7110E-05	1.7600E-05	1.8100E-05	1.8590E-05	1.9100E-05	1.9580E-05
2.0E+03	1.7280E-05	1.7770E-05	1.8260E-05	1.8740E-05	1.9230E-05	1.9710E-05
3.0E+03	1.7480E-05	1.7950E-05	1.8430E-05	1.8910E-05	1.9390E-05	1.9860E-05
4.0E+03	1.7690E-05	1.8160E-05	1.8630E-05	1.9100E-05	1.9570E-05	2.0030E-05
5.0E+03	1.7930E-05	1.8380E-05	1.8830E-05	1.9290E-05	1.9760E-05	2.0210E-05
6.0E+03	1.8190E-05	1.8620E-05	1.9060E-05	1.9510E-05	1.9960E-05	2.0400E-05
7.0E+03	1.8460E-05	1.8880E-05	1.9300E-05	1.9730E-05	2.0170E-05	2.0610E-05
8.0E+03	1.8750E-05	1.9140E-05	1.9550E-05	1.9970E-05	2.0400E-05	2.0820E-05
9.0E+03	1.9070E-05	1.9440E-05	1.9830E-05	2.0230E-05	2.0640E-05	2.1050E-05
1.0E+04	1.9410E-05	1.9760E-05	2.0120E-05	2.0500E-05	2.0890E-05	2.1290E-05

APPENDIX B: SLIP FLOW

Consider single-phase flow of a Newtonian fluid in a porous or fractured medium. Knudsen (1934) defined a dimensionless number $K_n = \lambda/d$ (called Knudsen number) where λ is the mean free path of fluid molecules (average distance between molecules) and d is a characteristic length. In porous or fractured media, d is typically a measure of pore diameter or fracture aperture (Present, 1958; Bear, 1972). When $K_n < 0.01$, the fluid behaves (on the pore or fracture aperture scale) as a viscous continuum and satisfies the Navier-Stokes equation. At sufficiently small Reynolds numbers, a linear Stokes regime develops within pores or fractures in which viscous forces are large in comparison to nonlinear inertia so that the latter can be disregarded. The fluid continuum satisfies a no-slip, or zero velocity, condition at its contact with the solid walls of pores or fractures. On a macroscopic scale that includes many pores or fracture apertures the Stokes regime, under the no-slip condition, manifests itself in the form of Darcy's law. As the Knudsen number increases toward 1, viscosity and drag along solid walls diminish sufficiently to allow slippage of fluid past solid walls to occur. This allows flow rate to be higher than predicted by Darcy's law, a phenomenon known as slip flow or the Klinkenberg (1941) effect. As K_n increases further, the fluid behaves less and less as a viscous continuum and more and more as a diffusing collection of free-flowing molecules. When $K_n > 1$, Knudsen diffusion becomes dominant. As the mean free path of gas molecules is much larger than that of liquid molecules, the former is associated with much larger Knudsen numbers and one must therefore consider the possibility that gas may exhibit the Klinkenberg effect or, less commonly, be subject to Knudsen diffusion.

A decrease in gas pressure brings about an increase in the mean free path of its molecules and a concomitant increase in the Knudsen number. If one uses Darcy's law to describe the associated Klinkenberg effect, one finds that permeability appears to increase as pressure decreases. Indeed, based on an analogy to gas flow in a capillary tube, Klinkenberg (1941) proposed that the apparent permeability of gas varies according to

$$k_a = k\left(1 + \frac{4c\lambda}{r}\right) = k\left(1 + \frac{m}{p}\right) \tag{B-1}$$

where k is intrinsic permeability at high pressures (small Knudsen numbers), $c \approx 1$ is a proportionality factor, r is the radius of the capillary tube, and m is an empirical coefficient valid for porous media that depends on λ and pore size. As pore size and permeability are related, m can be considered a function of k. Though such inverse relationship between apparent permeability and pressure is often observed in the laboratory, it was pointed out by Aronofsky (1954) that the Klinkenberg effect seldom affects the interpretation of gas well tests in the field. We mentioned in the Introduction (section 1.2.3) that, according to Guzman et al. (1994), Knudsen diffusion and the Klinkenberg effect play virtually no role in the observed pressure dependence of air permeabilities obtained from single-hole pneumatic injection tests at the ALRS; the observed decrease in apparent permeability with pressure is due to inertia effects, and the observed increase is due to two-phase flow.

Most pneumatic injection tests at the ALRS "see" fractures, which have mean apertures that are considerably larger than the mean pore diameter of intact matrix at the

site (see Table B.1 for pore size distribution and Figure B.1 for mean pore sizes of intact matrix cores). We suspect that this is a major reason why these tests appear to be unaffected by the Klinkenberg effect. To understand how this effect is related to pore size, we consider the work of Scott and Dullien (1962a) who proposed the following quasi-Darcian relationship for gasflow,

$$\mathbf{F} = -\left(\frac{r^2 p}{8\mu} + \frac{4rRT}{3MV_m} \right) \frac{1}{RT} \nabla p \tag{B-2}$$

where $\mathbf{F}$ is molar flux of gas $[molL^{-2}T^{-1}]$, r is mean pore radius $[L]$, M is molecular weight $[Mmol^{-1}]$, and V_m is mean molecular velocity $[LT^{-1}]$. Volume flux is related to molar flux via (Massmann, 1989)

$$\mathbf{q} = \frac{M\mathbf{F}}{\rho} \tag{B-3}$$

This, coupled with the Boyle-Mariotte law for real gases (Burcik, 1957)

$$\rho = \frac{pM}{ZRT} \tag{B-4}$$

transform (B-2) into

$$\mathbf{q} = -\left(\frac{Zr^2}{8\mu} + \frac{4rZRT}{3MV_m p} \right) \nabla p \tag{B-5}$$

In the absence of slip flow, (B-5) reduces to Darcy's law in the form

$$\mathbf{q} \approx -\frac{Zr^2}{8\mu} \nabla p \tag{B-6}$$

The first term on the right hand sides of (B-2) and (B-5) accounts for Darcian flow and the second for slip flow. These equations imply that (a) as r becomes large, the importance of slip flow relative to Darcian flow diminishes; (b) the opposite happens as r becomes small; and (c) gas-flow involving light molecules that travel at low velocities through large pores can exhibit a large slip component.

According to Harleman et al. (1963), intrinsic permeability is proportional to the square of mean pore diameter d,

$$k = cd^2 \tag{B-8}$$

where c is a constant. Therefore, eq. (B-6) can be rewritten as

$$\mathbf{q} = -\frac{k}{\mu} \nabla p \tag{B-9}$$

which is Darcy's law expressed in terms of pressure when the flowing gas is assumed to be ideal $(Z \cong 1)$.

Table B.1: Cumulative mercury intrusion volume as a function of equivalent pore diameter (adapted from Rasmussen et al., 1990)

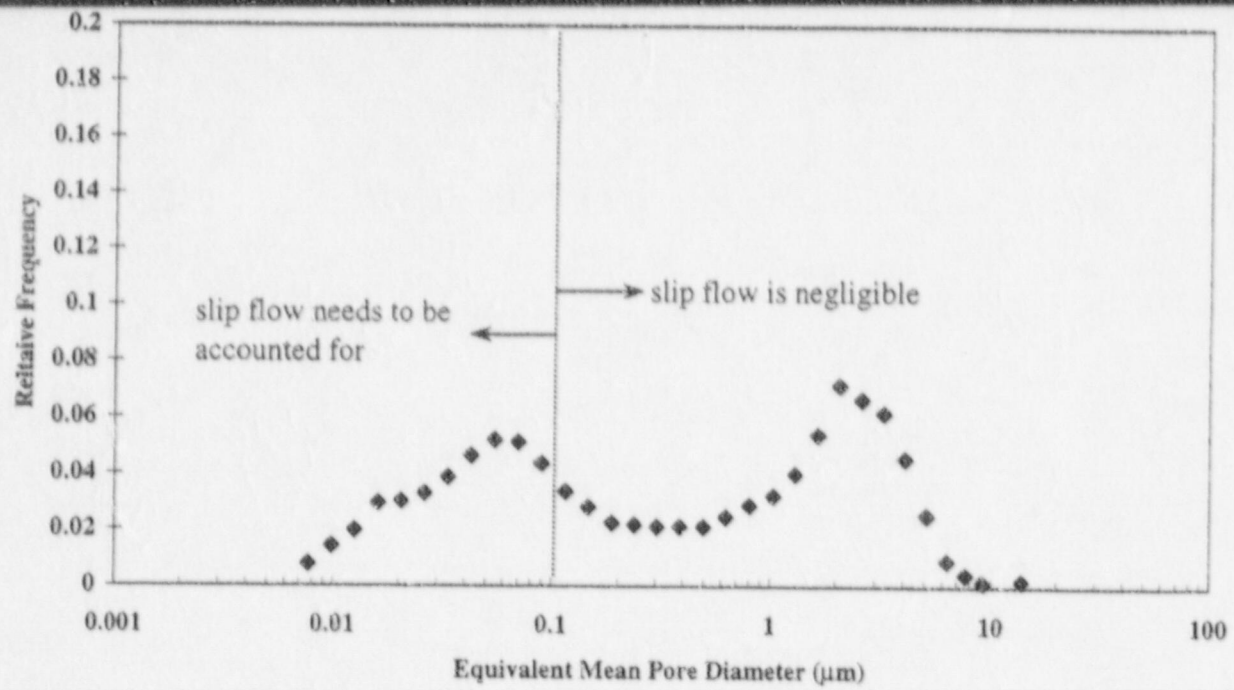| Pore Size [μm]	Cumulative Volumetric Porosity [m^3/m^3]	Volumetric Porosity [m^3/m^3]	Relative Frequency
13.8	0.0003	0.0003	0.002101
9.19	0.0005	0.0002	0.001401
7.64	0.0011	0.0006	0.004202
6.3	0.0024	0.0013	0.009104
5.08	0.006	0.0036	0.02521
4.06	0.0125	0.0065	0.045518
3.27	0.0213	0.0088	0.061625
2.61	0.0308	0.0095	0.066527
2.07	0.041	0.0102	0.071429
1.65	0.0487	0.0077	0.053922
1.3	0.0544	0.0057	0.039916
1.03	0.059	0.0046	0.032213
0.802	0.0631	0.0041	0.028711
0.627	0.0666	0.0035	0.02451
0.494	0.0696	0.003	0.021008
0.385	0.0726	0.003	0.021008
0.302	0.0756	0.003	0.021008
0.237	0.0787	0.0031	0.021709
0.187	0.0819	0.0032	0.022409
0.146	0.0859	0.004	0.028011
0.115	0.0907	0.0048	0.033613
0.0896	0.0969	0.0062	0.043417
0.07	0.1042	0.0073	0.05112
0.0548	0.1116	0.0074	0.051821
0.0429	0.1182	0.0066	0.046218
0.0336	0.1237	0.0055	0.038515
0.0262	0.1284	0.0047	0.032913
0.0205	0.1327	0.0043	0.030112
0.016	0.1369	0.0042	0.029412
0.0125	0.1397	0.0028	0.019608
0.0098	0.1417	0.002	0.014006
0.0077	0.1428	0.0011	0.007703
	Sum	0.1428	1

Figure B.1: Relative frequency of equivalent mean pore diameter plotted on semi-logarithmic scale, showing bimodal distribution of pores in tuff matrix at the ALRS.

APPENDIX C: DERIVATION OF SINGLE-PHASE GAS FLOW EQUATION

The continuity equation for single-phase gas flow in a rigid porous medium is

$$-\nabla \cdot (\rho \mathbf{q}) = \phi \frac{\partial \rho}{\partial t} \qquad \text{(C-1)}$$

Substituting the Boyle-Mariotte relationship (Burcik, 1957)

$$\rho = \frac{pM}{ZRT} \qquad \text{(C-2)}$$

and Darcy's law (2.1-2) for a gas into (C-1) yields

$$\nabla \cdot \left(\frac{M}{RT} \frac{p}{Z} \frac{k}{\mu} \nabla p \right) = \phi \frac{\partial}{\partial t} \left(\frac{M}{RT} \frac{p}{Z} \right) \qquad \text{(C-2)}$$

As M and R are constant for a homogeneous gas, and T is constant under isothermal conditions, this reduces to

$$\nabla \cdot \left(\frac{p}{Z} \frac{k}{\mu} \nabla p \right) = \phi \frac{\partial}{\partial t} \left(\frac{p}{Z} \right) \qquad \text{(C-3)}$$

The latter form of the single-phase gas flow equation is found, for example, in Al-Hussainy et al. (1966) and Bear (1972, p. 200, eq. 6.2.26). In a medium with uniform permeability,

$$\nabla \cdot \left(\frac{p}{\mu Z} \nabla p \right) = \frac{\phi}{k} \frac{\partial}{\partial t} \left(\frac{p}{Z} \right) \qquad \text{(C-4)}$$

which can be written as

$$\nabla \cdot \left(\frac{1}{2\mu Z} \nabla p^2 \right) = \frac{\phi}{k} \frac{\partial}{\partial t} \left(\frac{p}{Z} \right) \qquad \text{(C-5)}$$

Expanding the left-hand-side of (C-5) yields

$$\nabla \left(\frac{1}{2\mu Z} \right) \cdot \nabla p^2 + \frac{1}{2\mu Z} \nabla^2 p^2 = \frac{\phi}{k} \frac{\partial}{\partial t} \left(\frac{p}{Z} \right) \qquad \text{(C-6)}$$

Multiplying both sides by $2\mu Z$ gives

$$\mu Z \left(\nabla \left(\frac{1}{\mu Z} \right) \cdot \nabla p^2 \right) + \nabla^2 p^2 = \frac{2\phi \mu Z}{k} \frac{\partial}{\partial t} \left(\frac{p}{Z} \right) \qquad \text{(C-7)}$$

Remembering that μZ is pressure dependent, we note that

$$\frac{\partial}{\partial x} \left(\frac{1}{\mu Z} \right) = \frac{d}{dp^2} \left(\frac{1}{\mu Z} \right) \frac{\partial p^2}{\partial x} = \frac{d}{d(\mu Z)} \left(\frac{1}{\mu Z} \right) \frac{d(\mu Z)}{dp^2} \frac{\partial p^2}{\partial x}$$

$$= -\frac{1}{(\mu Z)^2} \frac{d(\mu Z)}{dp^2} \frac{\partial p^2}{\partial x} \qquad \text{(C-8)}$$

$$\frac{d}{dp^2} (\mu Z) = \mu Z \frac{d}{dp^2} [\ln(\mu Z)] \qquad \text{(C-9)}$$

and therefore

$$\frac{\partial}{\partial x}\left(\frac{1}{\mu Z}\right) = -\frac{1}{(\mu Z)}\frac{d\ln(\mu Z)}{dp^2}\frac{\partial p^2}{\partial x} \qquad (C\text{-}10)$$

It follows from (C-7) and (C-10) that

$$\nabla^2 p^2 - \frac{d\ln(\mu Z)}{dp^2}\nabla p^2 \cdot \nabla p^2 = \frac{2\phi\mu Z}{k}\frac{\partial}{\partial t}\left(\frac{p}{Z}\right) \qquad (C\text{-}11)$$

Upon taking $\mu =$ constant and $Z \approx 1$,

$$\nabla^2 p^2 \approx \frac{2\phi\mu}{k}\frac{\partial p}{\partial t} \qquad (C\text{-}12)$$

which is the same as (2.1-11) and a form found in Scheidegger [1974]. Defining the compressibility of air as

$$c(p) = \frac{1}{\rho}\frac{d\rho}{dp} \qquad (C\text{-}13)$$

we obtain from (C-2) and (C-13), for isothermal conditions,

$$c(p) = \frac{Z(p)RT}{pM}\frac{d}{dp}\left(\frac{pM}{Z(p)RT}\right) = \frac{Z(p)}{p}\frac{d}{dp}\left(\frac{p}{Z(p)}\right) \qquad (C\text{-}14)$$

This simplifies to

$$c(p) = \frac{1}{p} - \frac{1}{Z(p)}\frac{dZ(p)}{dp} \qquad (C\text{-}15)$$

If Z is a weak function of pressure, air behaves almost ideally and compressibility can be approximated by

$$c(p) \approx \frac{1}{p} \qquad (C\text{-}16)$$

Otherwise, it follows from (C-14) that

$$\frac{\partial}{\partial t}\left(\frac{p}{Z(p)}\right) = \frac{pc(p)}{Z(p)}\frac{\partial p}{\partial t} \qquad (C\text{-}17)$$

Substitution of (C-17) into (C-11) yields (Raghavan, 1993, p. 27, eq. 3.21)

$$\nabla^2 p^2 - \frac{d\ln(\mu Z)}{dp^2}\nabla p^2 \cdot \nabla p^2 = \frac{\phi\mu c(p)}{k}\frac{\partial p^2}{\partial t} \qquad (C\text{-}18)$$

APPENDIX D: TYPE-CURVE SOLUTION OF SPHERICAL GASFLOW

In a manner analogous to Joseph and Koederitz (1985) who dealt with a liquid, we consider the injection of gas at a constant mass rate Q from a spherical source of radius r_{sw} into a uniform, isotropic continuum of infinite extent. The flow is spherically symmetric so that surfaces of equal pressure (isobars) form concentric spheres about the source. Pseudopressure is then governed by

$$\frac{\partial^2 w}{\partial r^2} + \frac{2}{r}\frac{\partial w}{\partial r} = \frac{1}{\alpha}\frac{\partial w}{\partial t} \tag{D-1}$$

where r is radial distance from the center of the source.

In our case the source is closer to a cylinder of length L and radius r_w. Under steady state, the isobars around such a cylinder can be closely approximated by prolate-spheroids or confocal ellipsoids (Moran and Finklea, 1962, Culham, 1974, and Joseph, 1984). It is convenient to view the source as the innermost ellipsoid with semi axes a and $b = c$. The radius r_{sw} of a sphere having similar volume is then given by Joseph and Koedertiz (1985) as

$$r_{sw} = \frac{L}{2\ln\left(L/r_w\right)} \tag{D-2}$$

Equation (D-1) is solved subject to the initial and outer boundary conditions

$$w(r,0) = 0; \qquad r \geq r_{sw} \tag{D-3}$$

$$\lim_{r \to \infty} w(r,t) = 0; \qquad t > 0 \tag{D-4}$$

Mass balance within the injection interval (Figure D.1) is written in terms of pressure as

$$Q_{in}\rho_{in} - Q_w\rho_w = \rho_w C_w \frac{dp_w}{dt} \tag{D-5}$$

where the subscripts in and w refer to the injection line and injection interval, respectively, and C_w is a borehole storage coefficient $[L^4 T^2 M^{-1}]$.
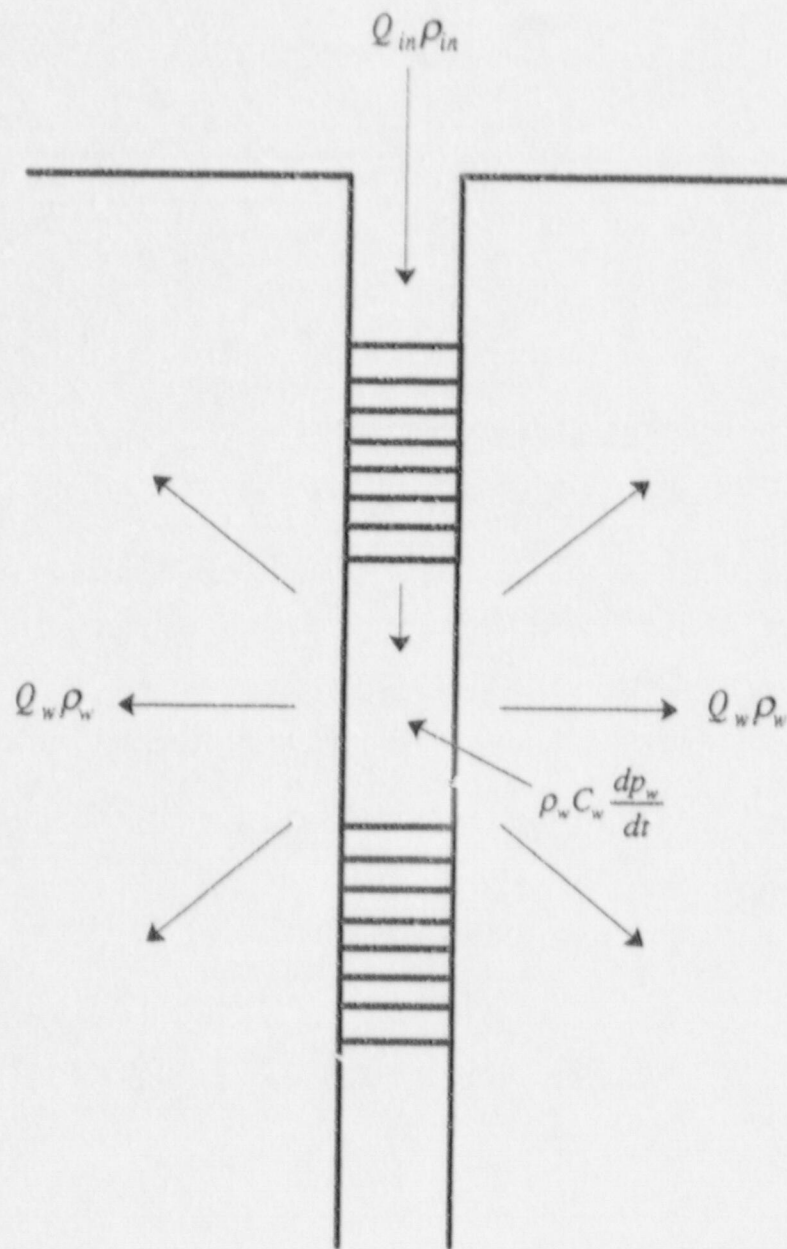
Figure D.1: Mass conservation in injection system.

Mass flow rate from a spherical source into the surrounding rock is given in terms of pressure by Darcy's law, in combination with (C-2), as

$$Q_w \rho_w = -4\pi k \frac{M}{RT} \left(\frac{p}{\mu Z} r^2 \frac{\partial p}{\partial r} \right)_{r_w} \tag{D-6}$$

For a low pressure system such as ours, eq. (2.1-16) implies that

$$\frac{\partial w}{\partial r} \approx \frac{2p}{\mu Z} \frac{\partial p}{\partial r}$$

$$\frac{\partial w}{\partial t} \approx \frac{2p}{\mu Z} \frac{\partial p}{\partial t}$$

so that (D-6) can be written in terms of pseudopressure as

$$Q_w \rho_w = -2\pi k \frac{M}{RT} \left(r^2 \frac{\partial w}{\partial r} \right)_{r_w} \tag{D-7}$$

By virtue of (B-4), the rate at which mass within the interval increases with time can be re-written in terms of pseudopressure as

$$\rho_w C_w \frac{dp_w}{dt} = \frac{p_w M}{ZRT} C_w \frac{\mu Z}{2 p_w} \frac{dw_w}{dt} = C_w \frac{\mu M}{2RT} \frac{dw_w}{dt} \tag{D-8}$$

Substituting (D-7) and (D-8) into (D-5) yields the inner boundary condition in terms of pseudopressure,

$$C_w \frac{\mu M}{2RT} \cdot \frac{dw_w}{dt} - 2\pi k \frac{M}{RT} \left(r^2 \frac{\partial w}{\partial r} \right)_{r_w} = Q_{in} \rho_{in} \tag{D-9}$$

If air density in the injection system and in the formation are the same $(\rho_{in} \approx \rho_w)$, (D-9) simplifies to

$$C_w \frac{\mu Z}{2 p_w} \frac{dw_w}{dt} - 2\pi k \frac{Z}{p_w} \left(r^2 \frac{\partial w}{\partial r} \right)_{r_w} = Q_{in} \tag{D-10}$$

Equation (3.1-5),

$$Q = \frac{Q_{sc} T p_{sc} Z}{T_{sc} p} \tag{D-11}$$

allows rewriting (D-10) as

$$C_w \frac{\mu T_{sc}}{2 Q_{sc} T p_{sc}} \frac{p_{in}}{p_w} \frac{dw_w}{dt} - 2\pi k \frac{T_{sc}}{Q_{sc} T p_{sc}} \left(r^2 \frac{\partial w}{\partial r} \right)_{r_w} = 1 \tag{D-12}$$

An infinitesimal skin may cause pressure and pseudopressure differences

$$\Delta p_s = p_{wf} - p_w \tag{D-13}$$

$$\Delta w_s = w_{wf} - w_w \tag{D-14}$$

to develop across it, as shown schematically in Figure D.2, where the subscripts s and wf represent skin and the rock just outside the skin, respectively. As the skin is infinitesimally thin, it cannot store gas and therefore the pressure drop across it is constant, as required by the Laplace equation. This allows defining a constant dimensionless skin factor s through

$$\Delta w_s = \frac{Q_{sc}}{2\pi k r_{rw}} \left(\frac{Tp_{sc}}{T_{sc}} \right) s \qquad (D\text{-}15)$$

where s is a dimensionless skin factor. Substituting (D-15) into (D-14) yields the auxiliary inner boundary condition

$$w_{wf} = w_w + \frac{Q_{sc}}{2\pi k r_{rw}} \left(\frac{Tp_{sc}}{T_{sc}} \right) s \qquad (D\text{-}16)$$

The complete mathematical problem for spherical flow with storage and skin effects consists of the governing diffusion equation (D-1), initial condition (D-3), outer boundary condition (D-4), inner boundary condition (D-12) and auxiliary inner boundary condition (D-16).
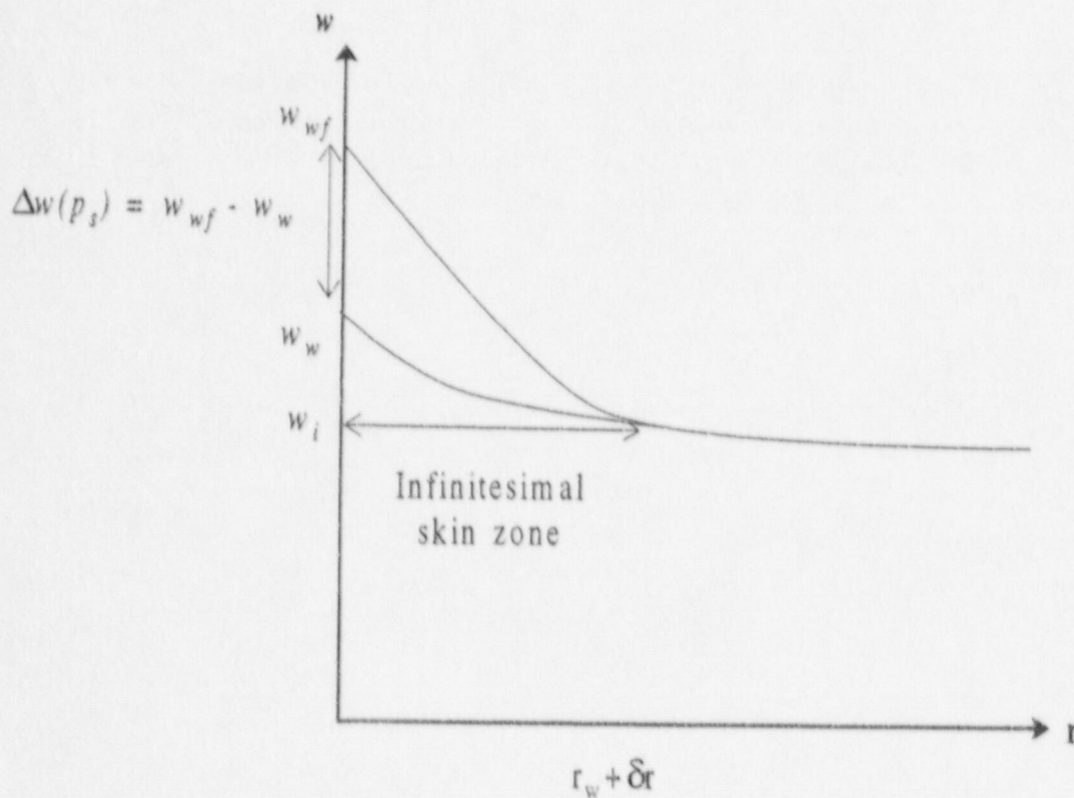

Figure D.2 : Impact of positive skin on pseudopressure around the injection interval.

The following dimensionless variables reduce the dimensional boundary value problem into a dimensionless form:

$$w_D = \frac{2\pi k r_{rw}}{Q_{sc}} \left(\frac{T_{sc}}{Tp_{sc}} \right) w$$

$$t_D = \frac{k r_{rw}^2 t \, \overline{p}}{\phi \mu r^4} ; \qquad r \geq r_{rw}$$

$$r_D = 1 - \frac{r_{sw}}{r}; \qquad r \geq r_{sw} \tag{D-17}$$

The dimensionless form of the complete mathematical problem is

$$\frac{\partial^2 w_D}{\partial r_D^{\,2}} = \frac{\partial w_D}{\partial t_D} \tag{D-18}$$

$$w_D(r_D, t_D = 0) = 0 \, ; \; 0 \leq r_D \leq 1 \tag{D-19}$$

$$\lim_{r_D \to 1}\left\{ w_D(r_D, t_D) \right\} = 0 \, ; \; t_D > 0 \tag{D-20}$$

$$C_* \frac{dw_{wD}}{dt_D} - \left[\frac{\partial w_D}{\partial r_D} \right]_{r_D = 0} = 1 \tag{D-21}$$

$$w_{wD}(t_D) = w_D(r_D = 0, t_D) - \left(\frac{\partial w_D}{\partial r_D} \right)_{r_D = 0} (s) \tag{D-22}$$

where $C_D = C_w \bar{p} / 4\pi \phi r_{sw}^3$ is a dimensionless wellbore storage coefficient. Note that the dimensionless form of the boundary value problem is virtually identical to that of liquid flow given in Joseph and Koederitz (1985). The definition of the radial flow boundary value problem follows in a similar manner to the above development.

APPENDIX E: MODIFICATION OF HSIEH AND NEUMAN (1985a) SOLUTION TO ACCOUNT FOR STORAGE AND SKIN IN MONITORING INTERVALS

In this appendix we modify the cross-hole solution of Hsieh and Neuman (1985a) to account for storage and skin effects in monitoring intervals by following an approach originally proposed by Black and Kipp (1977).

Mass balance in the monitoring interval can be expressed as

$$Q_{ow} = C_{ow} \frac{dp_{ow}}{dt} \tag{E-1}$$

where Q_{ow} is volumetric flow rate into the interval, $C_{ow} = V/p_{ow}$ is storage coefficient $[L^4 T^2 M^{-1}]$ associated with an interval of volume V, and p_{ow} is pressure in the interval $[ML^{-1}T^{-2}]$. Hvorslev (1951) expresses volumetric flow rate into the observation interval as

$$Q_{ow} = \frac{Fk_s \Delta p}{\mu} \tag{E-2}$$

where F is a shape factor $[L]$, k_s is permeability $[L^2]$ which we take to represent a skin, and $\Delta p = p - p_{ow}$ where p is pressure in the rock outside the skin. Substituting (E-2) into (E-1) and rearranging yields

$$\Delta p = \frac{C_{ow}\mu}{Fk_s} \frac{dp_{ow}}{dt} \tag{E-3}$$

This can be rewritten as

$$p = p_{ow} + t_. \frac{dp_{ow}}{dt} \tag{E-4}$$

where $t_B = C_{ow}\mu/Fk_s$ is basic time lag $[T]$ as defined by Hvorslev. The latter is a characteristic constant of the monitoring interval, which reflects its response time (lag) to changes in pressure within the rock. If t_B is known, one can use (E-4) to calculate pressure in the rock outside the skin, based on measurements of pressure within the monitoring interval. Note that when the latter is stable. the two pressures are equal unless t_B is infinite due to an impermeable skin. The basic time lag can be determined by means of a pressurized slug test in the monitoring interval according to a graphical method proposed by Hvorslev (1951).

For known p, (E-4) is an ordinary differential equation in terms of p_{ow}. In the case where $p_{ow} = p$ at $t = 0$, its solution is

$$p_{ow} = \frac{1}{t_B} \exp\left(-\frac{t}{t_B} \right) \int_0^t \exp\left(\frac{\eta}{t_B} \right) p(\eta) d\eta \tag{E-5}$$

Now suppose that p is given by the solution of Hsieh and Neuman (1995a) described in Section 3.4. Dimensionless pressure is defined in equation 3.4-4 as $p_D = 4\pi pkR/Q\mu$. Equation 3.4-5 defines dimensionless time for this case as $t_D = kt\bar{p}/\phi\mu R^2$ where R is distance between the centroids of the injection and monitoring intervals. Introducing a new variable $\xi = \phi\mu R^2/4k \bar{p}\eta$ then transforms (E-5) into

$$p_{ow} = \frac{1}{\Omega}\left(\frac{Q\mu\sigma}{k}\right)\exp\left(-\frac{1}{\Omega u}\right)\int_u^\infty \exp\left(\frac{1}{\Omega\xi}\right)p_D(\xi)\frac{a\xi}{\xi^2} \tag{E-6}$$

where $u = 1/4t_D$, $\Omega = 4k_s t_B / S_G \mu R^2$ is a dimensionless well response time, $S_G = \phi/\overline{p}$ is a gas storage factor defined in equation 2.1-23, and $p_D(\xi)$ acts as the kernel of a Fredholm integral equation of the 2nd kind. For the case of point-injection/line-observation, the solution of Hsieh and Neuman (1985a, p. 1658, eq. 27) reads

$$p_D = \frac{\beta_1}{4}\int_{u=1/4t_D}^{u=\infty}\frac{1}{u}\exp\left[-\left(1-\beta_2^2\right)u\right]\cdot\left\{erf\left[u^{1/2}(\beta_2 + 1/\beta_1)\right] - erf\left[u^{1/2}(\beta_2 - 1/\beta_1)\right]\right\}du$$

$$\tag{E-7}$$

Substituting this into (E-6) gives (3.4-10) and (3.4-11).

1. REPORT NUMBER (Assigned by NRC, Add Vol., Supp., Rev., and Addendum Numbers, if any.)
NUREG/CR-5559

2. TITLE AND SUBTITLE

Single- and Cross-Hole Pneumatic Tests in Unsaturated Fractured Tuffs at the Apache Leap Research Site: Phenomenology, Spatial Variability, Connectivity and Scale

3. DATE REPORT PUBLISHED	
MONTH	YEAR
November	1998

4. FIN OR GRANT NUMBER
JCN J5130/ W6388

5. AUTHOR(S)

Walter A. Illman, Dick L. Thompson, Velimir V. Vesselinov, Gouliang Chen and Shlomo P. Neuman

6. TYPE OF REPORT

Technical

7. PERIOD COVERED *(Inclusive Dates)*

May 1995 - May 1998

8. PERFORMING ORGANIZATION - NAME AND ADDRESS *(If NRC, provide Division, Office or Region, U.S. Nuclear Regulatory Commission, and mailing address; if contractor, provide name and mailing address.)*

Department of Hydrology & Water Resources
University of Arizona
Tucson, AZ 85721

9. SPONSORING ORGANIZATION - NAME AND ADDRESS *(If NRC, type "Same as above"; if contractor, provide NRC Division, Office or Region, U.S. Nuclear Regulatory Commission, and mailing address.)*

Division of Regulatory Applications
Office of Nuclear Regulatory Research
U.S. Nuclear Regulatory Commission
Washington, DC 20555

10. SUPPLEMENTARY NOTES

T.J. Nicholson, NRC Project Manager

11. ABSTRACT *(200 words or less)*

This report documents research results from a series of field experiments and analyses used to test interpretive models for investigating the role of fractures in fluid flow through unsaturated, fractured tuffs. The report summarizes the experimental design of single-hole and cross-hole pneumatic injection tests, including borehole configuration and testing schedules, data collection system, interpretive models developed and tested, data, and conclusions. Single-hole tests initially used steady-state analysis to obtain permeability values based solely on late pressure data, and subsequently used pressure and pressure-derivative type-curve analyses on the transient data. Air permeabilities determined from transient analysis agree well with those derived from steady-state analysis. Single- and cross-hole pneumatic tests were analyzed using a graphical matching procedure based on type-curves of pressure and pressure-derivatives, and an automatic parameter estimation method based on a three-dimensional, finite-volume code (FEHM) coupled with an inverse code (PEST). Analyses of pressure data from individual monitored intervals using these two methods, under the assumption that the rock acts as a uniform and isotropic fractured porous continuum, yield comparable results. These results include information about pneumatic connections between the injection and monitored intervals, corresponding directional air permeabilities, and air-filled porosities. Together with the results of earlier site investigations, single- and cross-hole test analyses reveal that, at the Apache Leap Research Site: (1) the pneumatic pressure behavior of fractured tuff is amenable to analysis by methods that treat the rock as a continuum on scales ranging from meters to tens of meters; (2) this continuum is representative primarily of interconnected fractures; (3) its pneumatic properties vary strongly with location, direction and scale, in particular, the mean of pneumatic permeabilities increases, and their variance decrease, with scale; (4) this scale effect is most probably due to the presence in the rock of various size fractures that are interconnected on a variety of scales; and (5) given a sufficiently large sample of spatially-varying pneumatic rock properties on a given scale of measurement, these properties are amenable to analysis by geostatistical methods, which treat them as correlated random fields defined over a continuum.

12. KEY WORDS/DESCRIPTORS *(List words or phrases that will assist researchers in locating the report.)*

connectivity
fractures
heterogeneity
inverse methods
permeability
pneumatic tests
porosity
scale
spatial variability
type-curve analysis
unsaturated tuffs

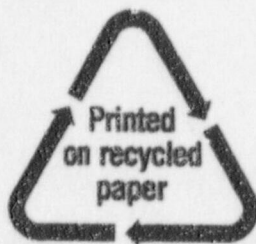| 13. AVAILABILITY STATEMENT |
|---|
| unlimited |

14. SECURITY CLASSIFICATION
(This Page)
unclassified
(This Report)
unclassified

15. NUMBER OF PAGES

16. PRICE

120555154486   1 1AN1RW1WD1WF1
US NRC-OCIO
DIV-INFORMATION MANAGEMENT
TPS-PDR-NUREG
2WFN-6F7
WASHINGTON   DC 20555